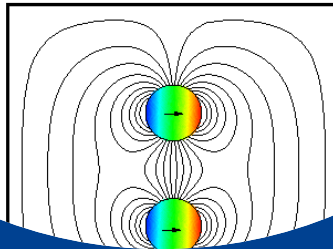
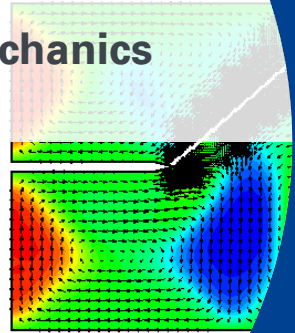
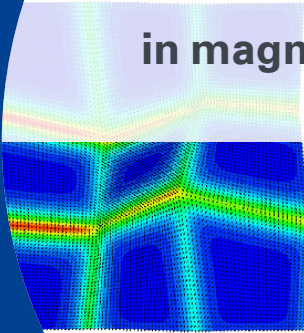




University of Stuttgart
Germany

Ashish
Sridhar

**Phase-field modeling of
microstructure and fracture evolution
in magneto-electro-mechanics**



5

Publication series of the
Institute of Applied Mechanics (IAM)

Phase-field modeling of microstructure and fracture evolution in magneto-electro-mechanics

Von der Fakultät Bau- und Umweltingenieurwissenschaften
der Universität Stuttgart zur Erlangung der Würde
eines Doktor-Ingenieurs (Dr.-Ing.)
genehmigte Abhandlung

von

Ashish Sridhar

aus Mumbai, Indien

Hauptberichter : Prof. Dr.-Ing. Marc-André Keip
Mitberichter : Prof. Dipl.-Ing. Björn Kiefer, Ph.D.
Vorsitzer : Prof. Dr.-Ing. habil. Manfred Bischoff

Tag der mündlichen Prüfung: 14. September 2020

Institut für Mechanik (Bauwesen) der Universität Stuttgart

2020

Publication series of the Institute of Applied Mechanics (IAM). Volume 5 Institute of Applied Mechanics
University of Stuttgart, Germany, 2020

Editors:

Prof. Dr.-Ing. Dr. h. c. W. Ehlers
Dr.-Ing. Dipl.-Math. techn. F. Fritzen
Prof. Dr.-Ing. M.-A. Keip
Prof. Dr.-Ing. H. Steeb

Organisation und Verwaltung:

Institut für Mechanik (Bauwesen)
Lehrstuhl für Materialtheorie
Universität Stuttgart
Pfaffenwaldring 7
70569 Stuttgart
Tel.: +49 (0)711 685-60046
Fax: +49 (0)711 685-66347

© Ashish Sridhar
Institut für Mechanik (Bauwesen)
Lehrstuhl für Materialtheorie
Universität Stuttgart
Pfaffenwaldring 7
70569 Stuttgart
Tel.: +49 (0)711 685-60046
Fax: +49 (0)711 685-66347

Alle Rechte, insbesondere das der Übersetzung in fremde Sprachen, vorbehalten. Ohne Genehmigung des Autors ist es nicht gestattet, dieses Heft ganz oder teilweise auf fotomechanischem Wege (Fotokopie, Mikrokopie) zu vervielfältigen.

ISBN 978-3-937399-53-9 (D 93 Stuttgart)

Acknowledgements

The present work is the culmination of my research during my stay at the Institute of Applied Mechanics (Civil Engineering) at the University of Stuttgart. I would like to take this opportunity and thank the people who have contributed to this work scientifically and personally while enriching my experience during this journey.

First and foremost I would like to pay my sincere and deepest gratitude to Professor Christian Miehe for his trust in me and providing me with this opportunity. He had an unparalleled dedication and enthusiasm, and to say that he was a stalwart in the field would be an understatement. I am truly privileged to have worked with him and his memories live with us forever.

I would also like to thank my supervisor Professor Marc-André Keip, for being my mentor, guide and friend. The times spent together with him collaborating on various research projects were truly amazing and one of the key highlights of my time at the institute. I will be forever thankful to him for providing me support and guidance even in difficult times. I would also sincerely thank Professor Björn Kiefer and Professor Manfred Bischoff for accepting to be co-referees of this thesis and their valuable inputs.

Furthermore, a note of thanks to all my colleagues from the Institute of Applied Mechanics for providing me such a wonderful, vibrant, warm and friendly atmosphere. I express my sincere gratitude here also to Gautam Ethiraj and Fadi Aldakheel not only for kindling my interest in his field and encouraging me to pursue further research but also for their friendship. I would like to thank Stephan Teichtmeister and Daniel Vallicotti for their contributions in this work. A big thanks to Matthias Rambausek, Omkar Nadgir, Elten Polukhov, Kheim Nguyen, Daniel Kienle, Felix Göküzüm, Aref Nateghi and Shreeraman Swamynathan for their contributions and friendship.

Moreover, I would like to thank my wife Ankitha Nagabushan for the motivation she provided, for her support and especially her patience and endurance during the last years. This would not have been possible without her. Thank you ! I am truly grateful to my parents (amma, appa) for their care and encouragement and always believing in me and motivating me. I would like to also thank my brother Rohan Sridhar (chotu!) for always being there for me as my friend. I thank also Ankitha's parents for believing in me and providing me support and guidance. I would like to thank also Swaroop Gaddikere Nagaraja, for being my dear friend and companion in the computational mechanics world. I will truly cherish our COMMAS days together. Last but not the least, I am extremely grateful to my son Riaan Ashish for being the joy of my life.

Stuttgart, September 2020

Ashish Sridhar.

Table of Contents

Abstract	v
Zusammenfassung	vii
1. Introduction	1
1.1. Magnetomechanical Coupling Phenomena	1
1.2. Electromechanical Coupling Phenomena	4
1.3. Phase-Field Modeling in Continuum Mechanics	4
1.4. State of the Art	6
1.4.1. Homogenization and Finite Deformation in Micromagnetics	6
1.4.2. Anisotropic Fracture in Piezoelectric and Ferroelectric Ceramics	9
1.4.3. Objectives and Overview	12

I Continuum Mechanics, Electromagnetism and Fracture

2. Fundamentals of Continuum Mechanics and Electromagnetism	17
2.1. Fundamentals of Continuum Mechanics	17
2.1.1. Introduction and Motivation	18
2.1.2. Motion of a Continuum Body	19
2.1.3. The Deformation Gradient: Line, Area and Volume Maps	20
2.1.4. Metric Tensors, Stretch and Cauchy-Green Stretch	22
2.1.5. Velocity, Velocity gradient and Lie Rate	23
2.1.6. Cauchy Stress Theorem and Stress Measures	24
2.1.7. Mechanical Power Expressions	26
2.2. Fundamentals of Electromagnetism	27
2.2.1. Lorentz Force on a Moving Charge Particle	27
2.2.2. Gauss Law for Electricity	28
2.2.3. Gauss Law for Magnetism	29
2.2.4. Maxwell Faraday Equation	29
2.2.5. Ampère Circuital Law	30
2.3. Maxwell Equations in Ponderable Media	31
2.3.1. Dielectric Materials and Polarization	31

2.3.2.	Ferromagnetic Materials and Magnetization	33
2.3.3.	Special Case of Electro-Magneto-Statics	35
2.3.4.	Geometrical Transformations of Electromagnetic Objects	36
2.3.5.	Boundary Conditions at Interfaces Between Materials	37
3.	Coupled Anisotropic Electromechanical Fracture	39
3.1.	Fundamental Definition of Fracture in Solids	39
3.1.1.	Griffith Energetic Fracture Approach	39
3.1.2.	Geometric Crack in a 1-D Bar	41
3.1.3.	Phase-Field Approximation of Anisotropic Crack Topology	42
3.2.	Coupled Electromechanical Fracture in Piezoelectrics	44
3.2.1.	Crack Face Electrical Boundary Conditions	44
II	Micromagnetics: Homogenization and Finite Deformation	
4.	Variational Homogenization of Micro-Magneto-Elasticity	49
4.1.	Variational Formulation of Macroscopic Response	49
4.1.1.	Introduction of Macroscopic Fields	50
4.1.2.	Macroscopic Rate-type Variational formulation	50
4.1.3.	Macroscopic Incremental Variational Formulation	51
4.1.4.	Space-Time Discrete Incremental Variational Principle	52
4.2.	Variational Homogenization of Micro-Magneto-Elasticity	53
4.2.1.	Introduction of Microscopic Fields	53
4.2.2.	Microscopic Rate-Type Variational Principle of Homogenization	54
4.2.3.	Microscopic Incremental Variational Principle	56
4.2.4.	Staggered Solution Scheme of Micromagnetic Evolution Problem	57
4.2.5.	Space-Time Discretization of Staggered Solution Scheme	58
4.2.6.	Algorithmic Homogenized Quantities	59
4.3.	Functionals in Micro-Magneto-Elasticity	60
4.3.1.	Energy Density and Dissipation Potential Functionals	60
4.3.2.	Energy-Enthalpy Function of Micro-Magneto-Elasticity	63
4.3.3.	Dissipation Potential for Magnetization Evolution	63
4.4.	Numerical Examples	63
4.4.1.	Problem 1: Homogenization of a Galfenol Single Crystal	64
4.4.2.	Problem 2: Homogenization of a NdFeB Permanent Magnet	68
4.4.3.	Problem 3: Homogenization of a Two-Phase Magnet	69
5.	Variational Finite Strain Micro-Magneto-Mechanics	73
5.1.	Functionals in Finite Strain Micromagnetics	73
5.1.1.	Deformation, Magnetization and Magnetic Potential	73

5.1.2.	Gradients of the Primary Fields	75
5.1.3.	Objective State Variables and Material Symmetry Conditions	75
5.2.	Magnetic energy, Loading and Dissipation Potential Functional	76
5.2.1.	Contributions to Energy Density Function	77
5.2.2.	Coupled Magnetomechanical Loading Functional	79
5.2.3.	Magnetic energy Functional of Micro-Magneto-Elasticity	80
5.2.4.	Objective Dissipation Potential Functional	80
5.3.	Variational Formulation of Finite Strain Micromagnetics	81
5.3.1.	Space-Time Discrete Formulation of Finite Micromagnetics	83
5.4.	Numerical Examples	83
5.4.1.	Normalization of parameters	84
5.4.2.	Problem 1: Standard Micromagnetic Problem	84
5.4.3.	Problem 2: Behavior Under Superimposed Rigid body Motions	85
5.4.4.	Problem 3: Circular inclusions Embedded in Elastomeric Matrix	86
5.4.5.	Problem 4: Circular inclusions in a chain formation	90

III Electromechanical Fracture: Piezoelectrics and Ferroelectrics

6.	Phase-Field Anisotropic Fracture in Piezoelectrics	95
6.1.	Crack Conditions and Local Damage Model	95
6.1.1.	Electromechanical Energy and Degradation Functions	96
6.1.2.	Electromechanical Driving Force and Damage Evolution	100
6.2.	Variational Principle of Phase Field Fracture in Piezoelectrics	102
6.2.1.	Primary Fields for Fracture in Piezoelectrics	102
6.2.2.	Variational Principle and Euler-Lagrange Equations	103
6.2.3.	Irreversible Evolution of Fracture	104
6.3.	Degrading Energy Functional with Fracture Evolution	105
6.3.1.	Stored Electromechanical Energy Functional	105
6.3.2.	Tension-Compression Split of Energy	106
6.3.3.	Electromechanical Energy Split and Crack Driving Force	107
6.4.	Numerical examples	108
6.4.1.	Problem 1: Isotropic Electromechanical Crack Propagation	108
6.4.2.	Problem 2: Anisotropic Electromechanical Crack Propagation	110
6.4.3.	Problem 3: Three-dimensional electromechanical crack propagation	113
7.	Phase-Field Anisotropic Fracture in Ferroelectrics	117
7.1.	Local Ferroelectric Damage Model	117
7.1.1.	Thermodynamic Formulation of Local Damage	117
7.1.2.	Ferroelectric Energy Function for Local Damage	118
7.1.3.	Driving Force and Damage Evolution	119

7.2. Diffuse Electromechanical Fracture in Ferroelectrics	121
7.2.1. Primary Fields for Ferroelectric Fracture	121
7.2.2. Variational Principle and Euler-Lagrange Equations	122
7.3. Degrading Energy Functional Due to Fracture Evolution	123
7.3.1. Stored Ferroelectric Energy Functional	123
7.3.2. Tension-Compression Split of Energy	124
7.3.3. Rate of Energy Functional and Crack Driving Force	124
7.4. Numerical examples	125
7.4.1. Problem 1: Isotropic Crack Propagation in Ferroelectrics	126
7.4.2. Problem 2: Anisotropic Crack Propagation in Ferroelectrics	127
8. Conclusion	131
Bibliography	133

Abstract

Functional or smart materials have been known to mankind since the discovery of magnetism in ancient Greece and India around 500 BC. Over the millennia their use was restricted to very specific applications due to our lack of understanding. With the advent of Maxwell's equations in the mid 19th century, research and understanding of these materials grew. The understanding of ferromagnetic and piezoelectric materials in specific, led to the dawn of electronic age in the 20th century. Today, in the 21st century, the need for more reliable, robust, compact and highly efficient materials has led to an ever increasing interest and demand for such materials. Functional materials now encompass a wide variety of solid, fluid, organic, inorganic, nano and fluid matter that interact with externally applied electric, magnetic, optic, chemical, hydro and thermal fields. These materials typically find applications in sensors, actuators, micro-electro-mechanical systems (MEMS), memory storage devices, display devices and medical devices among many others. The focus of this work is on electromagnetic functional materials specifically ferromagnets, magnetorheological elastomers (MREs) and piezoelectric ceramics. The overarching theme of the present contribution is to use appropriate *phase-field formulations* to better predict and understand the behavior of these materials. Two main topics are covered in this context

- **Variational micromagnetic framework** : is used to capture nonlinear magnetomechanical coupling in ferromagnetic materials. It is presented in a homogenization context to predict the aggregate behavior of single and polycrystals. The micromagnetic framework is then extended to large deformations to capture the behavior of magnetorheological elastomers. The order parameter or phase-field in these formulations is the *magnetization director* M , that controls domain evolution on microscale.
- **Coupled electromechanical fracture** : is presented in the context of analyzing anisotropic crack propagation in piezoelectric ceramics. Appropriate choice of crack driving force and degradation functions are employed to model crack electrical boundary conditions. This framework is then extended to model crack propagation in ferroelectrics. The *damage field* α and the *polarization field* P are employed as phase-field in this formulation.

Ferromagnetic materials are materials that respond to an external applied magnetic field. Some examples of these materials are iron, cobalt, nickel and other neodymium magnets, which exhibit linear and nonlinear coupling phenomena as well as hysteresis under cyclic loading. The applications of these materials include memory storage devices, electromagnets, generators, transformers among many others. At the atomistic scale, these materials show a resultant magnetization stemming from the spin and orbital motion of electrons. On the microscale, these materials are composed of several homogeneously magnetized regions, called magnetic domains. The time evolution of these domains is driven by external magnetic fields and stresses applied to the sample. The evolution and interaction of these domains in response to external stimuli governs the macroscopic nonlinear magnetomechanical coupling seen in these materials. In order to directly link microstructure evolution with macroscopic response, a *computational homogenization* framework for

dissipative magnetomechanical behavior is presented. A staggered solution scheme is proposed to numerically satisfy the unity constraint on the magnetization director, which is a unique property of the *Landau-Lifschitz* equation. Two- and three-dimensional numerical simulations are presented to analyze micromagnetic domain evolution as well as associated hysteretic response of ferromagnetic materials for macroscopic strain and magnetic field driven scenarios.

Today ferromagnetic materials are all around us, but these materials have their short coming as they are hard materials that show very small deformations. Magnetorheological elastomers on the other hand, are materials where micron sized ferromagnetic inclusions are embedded in a soft non-magnetic matrix substrate. The inclusions realign under the influence of an external applied magnetic field, in turn causing large deformations of the substrate material. The magnetomechanical coupling in this case stems from magnetic properties of the inclusion and mechanical properties of the matrix. A large deformation micromagnetic formulation can capture the ferromagnetic behavior of the magnetic inclusions and thus help better understand and accurately predict the behavior of such materials. In this context a *large deformation micromagnetic* model is proposed that can accurately capture the microscopic response of such materials. Exploitation of rate type variational principles keeping in mind objectivity restrictions in a large deformation scenario gives Euler equations of the problem. Specific numerical examples are presented, where the capability of the proposed framework to capture physically observable phenomenon without any prior assumptions are highlighted.

Piezoelectric ceramics are the other class of materials that are analyzed in this work. Piezoelectrics like the naturally occurring quartz crystal respond to an external electrical stimulus and show nonlinear electromechanical coupling that has been exploited in sensors and actuators. The structural reliability analysis of these materials needs the modeling of failure under coupled electromechanical conditions. A dissipative framework with the fracture phase field driven by only the mechanical part of the coupled electromechanical driving force is presented. Appropriate degradation functions account for different crack electrical boundary conditions. A three field variational framework is presented that accounts for anisotropic crack propagation. A *Ginzburg-Landau* type evolution equation accounts for the irreversibility condition of the fracture phase field. The influence of electric field on fracture behavior is shown by means of various benchmark problems. The anisotropic fracture framework is then extended to the case of ferroelectric materials like Barium Titanate that show a spontaneous polarization under the Curie temperature. An additional phase field parameter that is polarization is employed to capture the behavior of these materials. This requires the solution of an additional Euler equation for the time-dependent solution of polarization field. Influence of applied electric field on polarization itself and additionally on fracture behavior is analyzed by means of traditional benchmark problems.

Zusammenfassung

Funktionale oder intelligente Materialien sind der Menschheit seit der Entdeckung des Magnetismus im antiken Griechenland und Indien um 500 v. Chr. bekannt. Im Laufe der Jahrtausende war ihr Einsatz aufgrund unserer mangelnden Kenntnisse auf sehr spezifische Anwendungen beschränkt. Mit dem Aufkommen der Maxwell Gleichungen in der Mitte des 19. Jahrhunderts wuchs Forschung und Kenntnis für diese Materialien. Das Verständnis von ferromagnetischen und piezoelektrischen Materialien war im 20. Jahrhundert der Startschuss des elektronischen Zeitalters. Heute, im 21. Jahrhundert, hat der Bedarf an zuverlässigeren, robusteren, kompakteren und hocheffizienteren Materialien zu einem immer größer werdenden Interesse und der Nachfrage nach solchen Materialien geführt. Funktionsmaterialien umfassen jetzt eine Vielzahl von festen, flüssigen, organischen, anorganischen und nano Stoffen, die mit extern aufgebracht elektrischen, magnetischen, optischen, chemischen, hydro- und thermischen Feldern interagieren. Diese Materialien finden typischerweise Verwendung in Sensoren, Aktoren, mikroelektromechanischen Systeme (MEMS), Speichergeräten, Anzeigegegeräten, medizinischen Geräten und vielem mehr. Der Schwerpunkt dieser Arbeit liegt auf elektromagnetischen Funktionsmaterialien, insbesondere ferromagneten, Magnetorheologischen Elastomeren (MREs) und piezoelektrischen Keramiken. Das übergeordnete Thema ist hierbei die Verwendung geeigneter Phasenfeldformulierungen, um das Verhalten dieser Materialien besser verstehen und vorherzusagen zu können. In diesem Zusammenhang werden zwei Hauptthemen behandelt:

- **Variational mikromagnetisch Rahmen** : wird verwendet, um nichtlineare magnetomechanisch Kopplungen in ferromagnetischen Materialien zu erfassen. Es wird über einen Homogenisierungskontext beschrieben, um das Aggregatverhalten von Einzel- und Polykristallen vorherzusagen. Die mikromagnetischen Erkenntnisse werden dann auf große deformation ausgedehnt, um das Verhalten von magnetorheologischen Elastomeren zu erfassen. Der Ordnungsparameter, oder das Phasenfeld, ist der *Magnetisierungsdirektor* M , der die Domänenevolution auf Mikroskala steuert.
- **Der gekoppelte elektromechanische Bruch** : wird im Rahmen der Analyse anisotroper Rissausbreitungen in piezoelektrischen Keramiken dargestellt. Es wird eine geeignete Wahl der Rissantriebskraft und der Degradierungsfunktionen zur Modellierung der elektrischen Randbedingungen des Risses dargestellt. Dieses framework wird dann erweitert, um die Rissausbreitung in der Ferroelektrik zu modellieren. Das *Schadensfeld* α und das *Polarisationsfeld* P wird in dieser Formulierung als Phasenfeld eingesetzt.

Ferromagnetische Materialien sind Materialien, die auf ein extern angelegtes Magnetfeld reagieren. Beispiele für solche Materialien sind Eisen, Kobalt, Nickel und Neodym-Magnete, die lineare und nichtlineare Kopplungsphänomene sowie Hysterese bei zyklischer Belastung aufweisen. Die Anwendungen dieser Materialien umfassen Speichergeräte, Elektromagnete, Generatoren, Transformatoren unter vielen anderen. Auf atomistische skala diese Materialien eine Magnetisierung die aus einer Spin- und Orbitalbewegung der Elektronen resultieren. Im Mikro-Skala bestehen diese Materialien aus mehreren homogen magnetisierten Bereichen, sogenannten magnetischen Domänen. Die zeitliche Evolution

dieser Domänen wird durch externe Magnetfelder und an der Probe angelegte Spannungen bestimmt. Die Evolution und der Interaktion dieser Domänen mit der Reaktion auf externe Felder steuert die makroskopische nichtlineare magnetomechanische Kopplung, die in diesen Materialien zu sehen ist. Um die Evolution der Mikrostruktur direkt mit der makroskopischen Reaktion zu verknüpfen, wird ein *computational Homogenisierungsframework* für dissipatives magnetomechanisches Verhalten vorgeschlagen. Es wird ein staggered Lösungsschema vorgeschlagen, um die Einheits Constraint für den Magnetisierungsdirektor numerisch zu erfüllen, was eine einzigartige Eigenschaft der *Landau-Lifschitz-Gleichung* ist. Zwei- und dreidimensionale numerische Simulationen werden zur Analyse präsentiert Evolution mikromagnetischer Domänen sowie zugehörige hysteretische Reaktion ferromagnetischer Materialien für makroskopische Dehnungs- und Magnetfeldgesteuerte Szenarien.

Heute ferromagnetische Materialien sind überall um uns herum, aber diese Materialien haben ihre kurze kommen, da sie harte Materialien sind, die sehr kleine Verformungen. Magnetorheologische Elastomere sind dagegen Materialien, bei denen ferromagnetische Materialien in Mikrometergröße in ein nichtmagnetisches Matrixsubstrat eingebettet sind. Die Einschlüsse richten sich unter dem Einfluss eines extern angelegten Magnetfelds aus, was wiederum zu starken Verformungen des Substratmaterials führt. Die magnetomechanische Kopplung beruht in diesem Fall auf den magnetischen Eigenschaften des Einschlusses und den mechanischen Eigenschaften der Matrix. Die mikromagnetische Formulierung zum Erfassen des ferromagnetischen Verhaltens der magnetischen Einschlüsse kann verwendet werden, um das Verhalten solcher Materialien besser zu verstehen und genauer vorherzusagen. In diesem Zusammenhang wird ein *mikromagnetisches Modell mit großen Verformungen* vorgeschlagen, das die mikroskopische Reaktion solcher Materialien genau erfassen kann. Die Ausnutzung von raten-Variationsprinzip unter Berücksichtigung der Objektivitäts constraint in einem großen Deformationsszenario ergibt die Euler-Gleichungen der Formulierungen. Es werden spezifische numerische Beispiele vorgestellt, bei denen die Fähigkeit des vorgeschlagenen Rahmens zur Erfassung physikalisch beobachtbarer Phänomene ohne vorherige Annahmen hervorgehoben wird.

Die andere Klasse solcher Materialien, die in dieser Arbeit analysiert werden, sind Piezoelektrische-Keramiken. Beispiele hierfür, wie der natürlich vorkommende Quarzkristall, reagieren auf einen externen elektrischen Feld und zeigen eine nichtlineare elektromechanische Kopplung, die in Sensoren und Aktoren genutzt wird. Es wird ein dissipatives framework mit dem Bruchphasenfeld vorgestellt, das nur durch den mechanischen Teil der gekoppelten elektromechanischen Antriebskraft angetrieben wird. Geeignete Degradationsfunktionen berücksichtigen unterschiedliche risslektrische Randbedingungen. Es wird ein Drei-Feld-Variationsrahmen vorgestellt, der die Ausbreitung anisotroper Brüche berücksichtigt. Eine Evolutionsgleichung vom Typ *Ginzburg-Landau* berücksichtigt den irreversiblen Zustand des Bruchphasenfeldes. Der Einfluss des elektrischen Feldes auf das Bruchverhalten wird anhand verschiedener Benchmark-Probleme gezeigt. Das anisotrope Bruch framework wird dann auf ferroelektrische Materialien wie Barium Titanate erweitert, die unter der Curie-Temperatur eine spontane Polarisierung zeigen. Ein zusätzlicher Phasenfeldparameter, nämlich die Polarisierung, wird verwendet, um das Verhalten dieser Materialien zu erfassen. Dies erfordert die Lösung einer zusätzlichen Euler-Gleichung für die zeitabhängige Lösung des Polarisierungsfeldes. Der Einfluss des angelegten elektrischen Feldes auf die Polarisierung selbst und zusätzlich auf das Bruchverhalten wird anhand herkömmlicher Benchmark-Probleme analysiert.

Introduction

Functional materials have been around for a very long time in human history. However in recent years with increasing demand for reliability, efficiency, robustness and miniaturization of machines, interest and research has piqued in this field. These materials are pivotal in the development of modern age computing, piezoelectric sonar devices, smart apparels, liquid crystal displays and artificial muscles just to name a few. Functional or smart materials are materials that react to external stimuli besides mechanical stress such as temperature, moisture, chemical, electric fields, magnetic fields or light. The ability to significantly influence the property of these materials without mechanical input has revolutionized modern age technology. Even though there has been significant development in finding new materials for high-tech and high performance applications, in many cases understanding and modeling capabilities have lagged far behind. With advancements in computational power, the need to accurately capture, predict and in turn improve the capabilities of these materials has taken center stage.

1.1. Magnetomechanical Coupling Phenomena

It has been shown that magnetism in materials originates due to orbital and spin motions of electrons and how these electrons interact with each another. Most materials are magnetic in nature, however there are only some materials where magnetic moments on the atomic scale interact strongly to show a macroscopic magnetic response. Various magnetic materials are seen in nature such as ferromagnetic, ferrimagnetic, diamagnetic, paramagnetic and antiferromagnetic materials. They are characterized based on the interaction of neighboring magnetic moments with each other. Among these, ferromagnetic and ferrimagnetic materials show tangible magnetomechanical coupling on macroscopic scale. SPALDIN [224], provides a good introduction and overview into this field. Ferromagnetic materials exhibit a spontaneous magnetization in the absence of an applied magnetic field that align parallel to each other, for example cobalt (Co) and iron (Fe) at room temperature. This spontaneous magnetization is responsible for the well known phenomenon of *magnetization hysteresis* under applied magnetic loading. The overall hysteretic response of a ferromagnet is based on the formation and evolution of complex

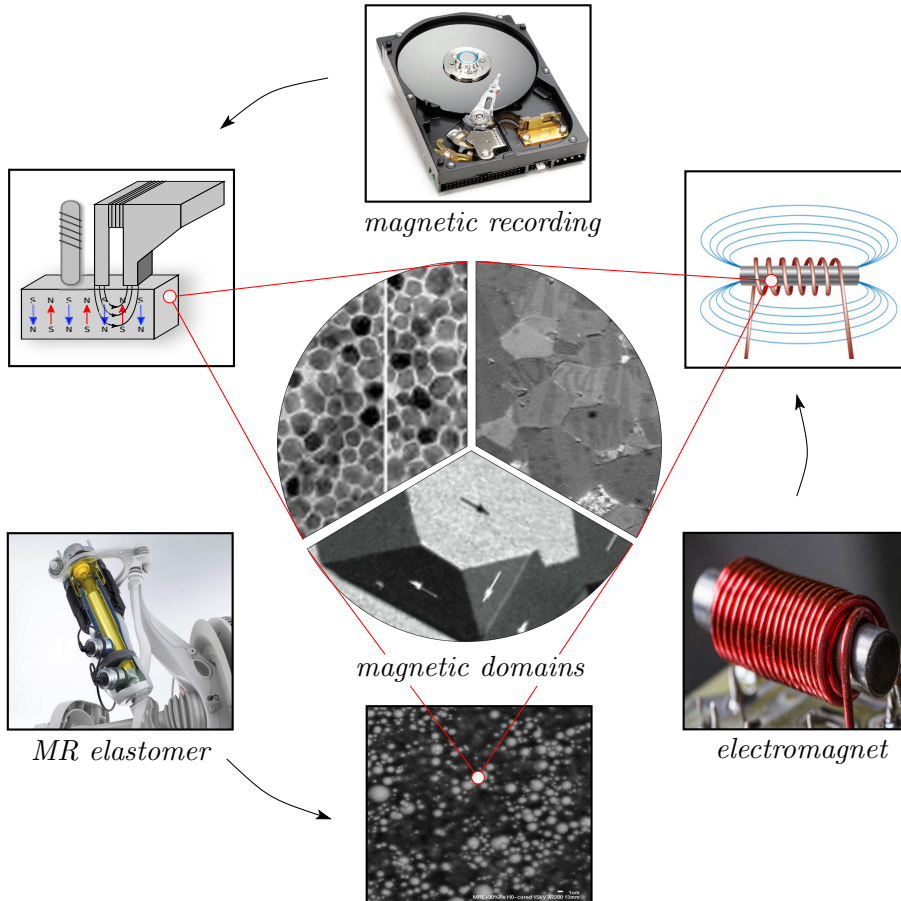


Figure 1.1: *Applications of ferromagnetic materials and underlying importance of magnetic domains.* Ferromagnetic materials are used as magnetic recording media to store data by classifying magnetization *up* or *down* states as bits (image courtesy: Hitachi, Ltd.), electromagnetic devices where a ferromagnetic core enhances the magnetic field (image courtesy: Tesla Institute and howstuffworks.com) and as composite materials such as magnetorheological fluids/elastomers used for variable damping (image courtesy: Porsche MagnerideTM TANNER [234] and KALLIO [112]). The magnetic phenomenon is governed by *magnetic domains* on the microscale (image courtesy: Wikipedia, R. Schäfer (magnetism.eu) and VARAPRASAD ET AL. [246]).

magnetic domains at a microscopic level (HUBERT & SCHÄFER [103]). Due to their advantageous properties, ferromagnetic materials have found many applications in industry, mainly in/as magnetic recording media (BERTRAM [18], GREAVES [81]) and as high-performance permanent magnets (GOLL & KRONMÜLLER [80], SCHREFL ET AL. [214]). Spontaneous magnetization generally leads to development of *spontaneous deformation* in material. This phenomenon is called *magnetostriction*. In order to technologically exploit the magnetostrictive effect, the associated strains have to be significant. The highest magnetostrictive strains that could be measured so far were obtained with rare-earth alloys such as Terfenol-D ($\text{Tb}_x\text{Dy}_{1-x}\text{Fe}_2$ with $x = 0.3$), Galfenol ($\text{Ga}_x\text{Fe}_{1-x}$ with $0.1 < x < 0.4$) or cobalt iron oxide (CoFe_2O_4) (ABBUNDI & CLARK [1], SANDLUND ET AL. [207], CLARK ET AL. [43]). Due to these “large” deformations, these materials are also termed *giant* magnetostrictive materials. These materials are attractive for applications especially in the field of sensor and actuator technology (CLAEYSSSEN ET AL. [42], OLABI & GRUNWALD [187]). New applications of ferromagnetic materials include magnetorheological fluids and elastomers. These materials are characterized by a het-

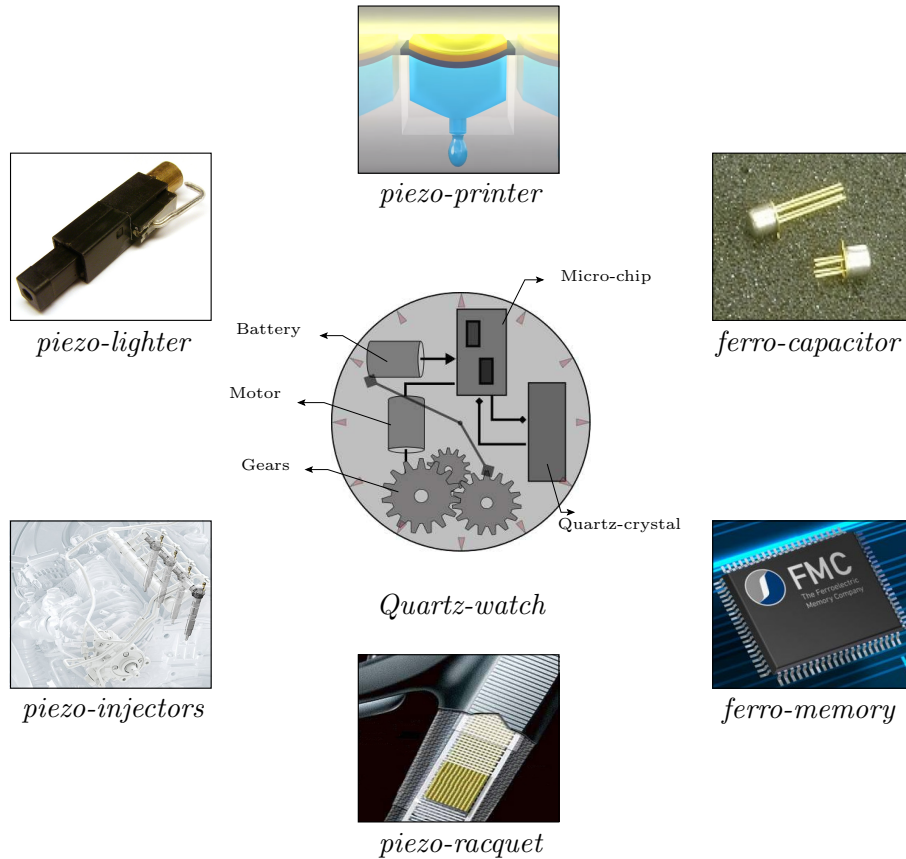


Figure 1.2: *Applications of piezoelectric materials.* Piezoelectric ceramics find a wide variety of applications as sensors and actuators. Most common day to day applications of these materials include the Quartz watch and piezoelectric lighter. Advanced applications use the high-frequency and high precision of the piezoelectric effect in controlling diesel injection (BOSCH piezo inline injector, product name: Piezo-Injektor CRI3-27), controlling the ink flow in inkjet printing (EPSON Micro Piezo Printheads and TFP technology using MEMS www.epson.com) and in vibration control of tennis racquets (IntellifiberTM system www.head.com/tennis/). Ferroelectric applications on the other hand exploit the non-linear hysteresis response in these materials with applications as ferro-memory (FMC company: www.ferroelectric-memory.com) and ferro-capacitor (Radiant Technologies: www.ferrodevices.com).

erogeneous microstructure that consists of a fluid substrate or soft elastic matrix and embedded magnetic inclusions. Due to the combination of magnetic properties of inclusion and elastic softness of substrate, magnetorheological elastomers (MREs) specifically exhibit magnetomechanical coupling at finite strains. These soft materials can then be used as actuators (BÖSE ET AL. [26]), variable vibration damping devices (WATSON [252], ALBANESE & CUNEFARE [7] and BLOM & KARI [21] among others) and in novel applications such as seismic applications (DYKE ET AL. [60]). MREs in general are cheap and easy to manufacture and are soft materials compared to the brittle properties seen in classical magnetostrictive materials. Experiments have shown that, microstructure of these materials can greatly influence their overall macroscopic properties. The microstructure can be influenced during the curing process such that the ferromagnetic inclusions are dispersed isotropically or, if a magnetic field is applied during the process, show an anisotropic microstructure (KALLIO [112]). Over and above, particle shape and optimized microstructures also play a crucial role in these materials (GALIPEAU & PONTE CASTAÑEDA [75], GALIPEAU & PONTE CASTAÑEDA [76], METSCH ET AL. [163] and

KALINA ET AL. [111]). Magnetorheological fluids are already widely used in the industry especially in the much acclaimed MagnerideTM variable vibration systems used by General Motors, Porsche, Audi and other automobile manufacturers (TANNER [234]). MREs possess advantageous properties over MR-fluids but are still in the nascent stage of development, which has sparked many experimental investigations in this field (JOLLY ET AL. [110], BEDNAREK [17], DANAS ET AL. [47] and VARGA ET AL. [247]). Some applications of ferromagnetic materials, their working and the underlying magnetic domain structures are shown in Figure 1.1.

1.2. Electromechanical Coupling Phenomena

Piezoelectric materials are another class of functional materials. They show electromechanical coupling in the presence of an applied electric field. Most non-centrosymmetric crystalline materials show linear *piezoelectricity*. Piezoelectric effect is the phenomenon in which some materials develop an electric charge under the influence of an external mechanical stress. The inverse piezoelectric effect is also seen in these materials where an applied electric field generates a mechanical deformation. This phenomenon occurs due to positive and negative charge centers in the unit cells of these materials do not coincide under external influence. Naturally occurring piezoelectric materials are quartz (SiO_2), berlinite (AlPO_4), lead zirconate titanate (PZT), lead titanate (PbTiO_3) and barium titanate (BaTiO_3). Lead titanate and barium titanate specifically show *ferroelectric* response due to the development of *spontaneous polarization* under Curie temperature. Ferroelectric materials, in addition to linear piezoelectric response under small electric fields and stresses, exhibit non-linear “dielectric” and “butterfly” hysteresis effects under cyclic loading. Typical applications are in adaptive and control systems such as actuators, sensors, motors, micro-electro-mechanical systems (MEMS), fuel injectors, ink-jet printers, ferroelectric memory and capacitor devices (JAFFE ET AL. [107], LINES & GLASS [151], MOULSON & HERBERT [178]). In fact piezoelectric materials are ubiquitous in daily life with applications in wrist watches and lighters. Some applications of these materials are shown in Figure 1.2. Similar to ferromagnetic materials, ferroelectric materials also show electric domain walls on the nano-scale. This non-linear polarization behavior contributes to the non-linear behavior observed on the macro-level.

1.3. Phase-Field Modeling in Continuum Mechanics

The generic phase-field approach can be traced back to diffuse interface descriptions derived by VAN DER WAALS [244, 245]. The modern term “phase-field” originates from the traditional use of such methods in solidification, where it was employed to track the different “phases” (LANGER [147]). This method has been recently used in many computational approaches to model and predict microstructure evolution. The microstructure of a material evolves to reduce the total free energy that may include the bulk interface energy, elastic-strain energy, magnetostatic and electrostatic energy, and/or applied external fields such as mechanical stress, electrical field, temperature, and magnetic field. It has to be noted that the microstructure can be separated into local domains with varying elastic properties, magnetization orientation, polarization orientation, grain ori-

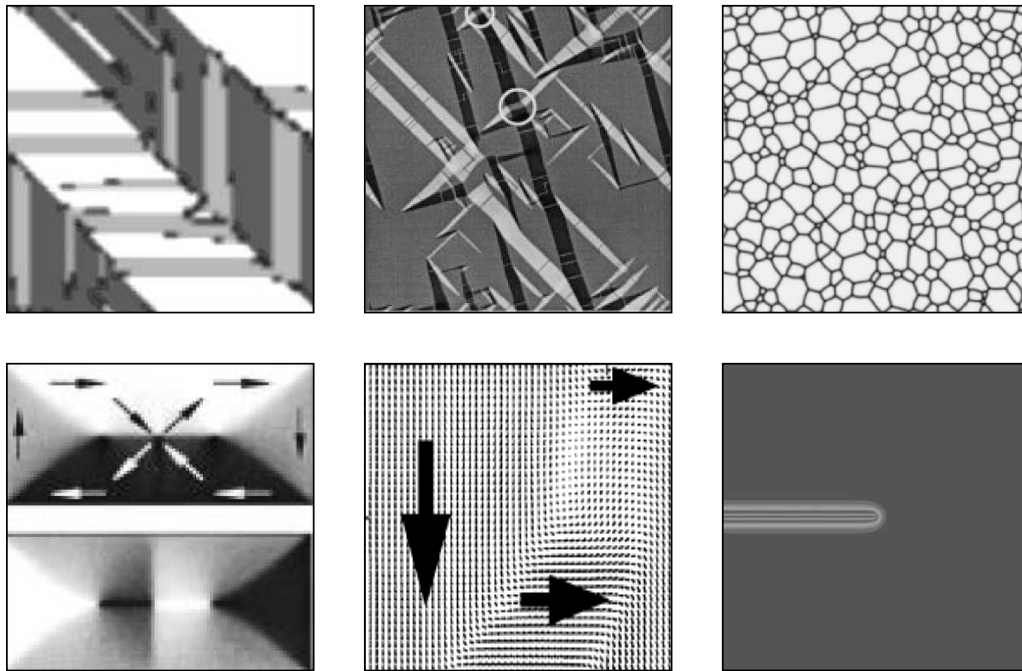


Figure 1.3: Applications of phase field methods to model microstructure evolution in various materials. Phase field methods are used in computational framework in a wide variety of applications to model complex non-linear microstructural evolution that affects macroscopic response of these materials. Traditionally “phase-field” refers to the identification of phases in a solidification process. More commonly, phase-field formulation employs additional variable/s (which may or may not have physical meaning) into the formulation that are used to differentiate between “phases”. These methods have found a wide variety of applications such as Martensitic phase transformation (ARTEMEV ET AL. [11]), hexagonal to orthorhombic phase transformation (WEN ET AL. [253]), isotropic and anisotropic grain growth (KAZARYAN ET AL. [120]), ferromagnetic domain evolution (RAVE [199]), ferroelectric domain evolution (ZHANG & BHATTACHARYA [262]) and fracture evolution (MIEHE ET AL. [172]), just to name a few.

entation or crystal structures. Due to the highly non-linear nature of such microstructure evolution processes, numerical methods are employed to better understand these effects. However, traditional approaches of tracking various interfacial conditions are practically applicable only for small calculations due to their high computational cost. On the other hand, phase-field methods describe a microstructure by employing additional field variables that are continuous across interfacial regions while converging to the sharp interface for vanishing length scales. In most cases, temporal and spatial evolution of these field variables is governed by the *Cahn-Hilliard* and *Allen-Cahn* type equations (CAHN & HILLIARD [37], CAHN & ALLEN [36]). These additional variables can in general be variables used solely for the purpose of tracking multiple phases as in the case of solidification processes or they can be related to physical variables like magnetization or polarization, that act as order parameters in the formulation. The advantage of these methods lies in the fact that given the correct thermodynamic and dynamic information, phase-field methods are able to predict complex non-linear behavior without the need to explicitly track the position of interfaces. Applications of such methods include solidification processes, cubic-tetragonal phase transformation, martensitic phase transformations, grain growth in single- and two-phase materials, ferroelectric and ferromagnetic domain motions among numerous others (ARTEMEV ET AL. [11], WEN ET AL. [253], KAZARYAN ET AL. [120], RAVE [199], MIEHE & ETHIRAJ [168], ZHANG & BHATTACHARYA [263],

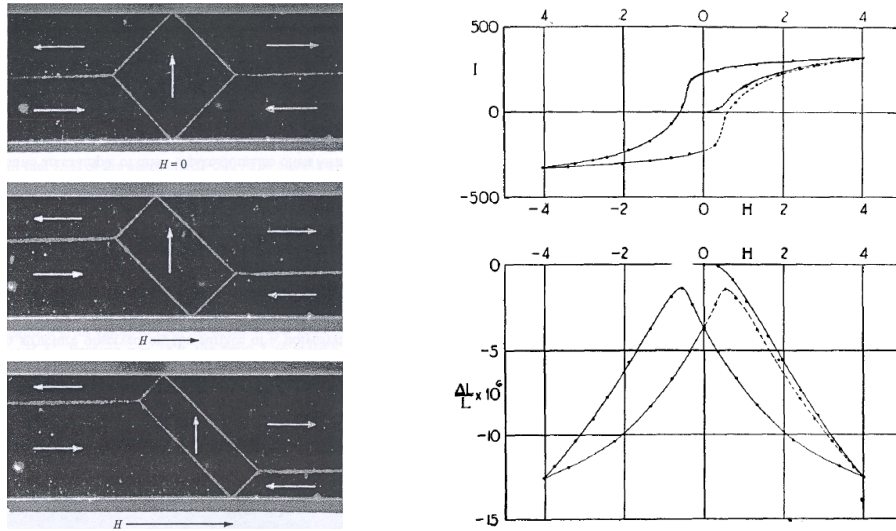


Figure 1.4: *Experimental observations of domain structure and associated hysteresis in ferromagnetic materials.* Ferromagnetic materials show magnetic domains on the micro-scale, which are regions with homogeneous magnetization (DEBLOIS & GRAHAM [50]). These domains evolve under the influence of external magnetic fields, resulting in non-linear magnetic and coupled magnetomechanical hysteresis behavior seen on macroscopic level (MCKEEHAN [157]).

MIEHE ET AL. [176], BOURDIN ET AL. [29] and MIEHE ET AL. [172]). For a general overview of phase-field methods refer to CHEN [39].

1.4. State of the Art

1.4.1. Homogenization and Finite Deformation in Micromagnetics

As discussed previously, ferromagnetic materials show complex domain wall motions on the microscale that affects its macroscopic response. In order to describe the behavior of these materials, it is necessary to develop reliable and accurate models that reflect the complex magnetomechanically coupled nature of the material. The field of electromagnetism and its connection to traditional mechanics has been a topic of research for a long time, due to its apparent technological relevance (TOUPIN [239], TRUESDELL & TOUPIN [241], ERINGEN [64], PAO [190], MAUGIN [155], KOVETZ [134]). Specific development of microscopic models to capture the domain evolution effects was initiated with the *domain theory* of magnetization (LANDAU & LIFSHITZ [142]). Several years later variational principles for the basis of *micromagnetics* were derived (BROWN [33]). Approaches to *dynamic theories of domain evolution* consider the Landau-Lifshitz-Gilbert equation (LLG equation), which describes the time-dependent evolution of magnetization (GILBERT [79]). Recent formulations based on the LLG equation are found in (SHU ET AL. [221], ZHANG & CHEN [259], ZHANG & CHEN [260], HU ET AL. [99], LANDIS [143]) as well as more recently in (LIANG ET AL. [150], YI & XU [257] and MIEHE & ETHIRAJ [168]). Microscopic aspects of ferromagnetic materials, origins of magnetization, statistical models and microstructures are addressed in (CULLITY [45], KITTEL [132], SPALDIN [224] and HUBERT & SCHÄFER [103]). The micromagnetic theory is quite successful in capturing and predicting the complex non-linear behavior of ferromagnetism. However, the inherent length scale restrictions and resulting high computational cost for large bodies still remain

a challenge. *Macroscopic phenomenological models* have been developed to predict the coupled magnetomechanical behavior of ferromagnetic materials to overcome such limitations (SABLIK & JILES [206], HIRSINGER ET AL. [92], SMITH ET AL. [223], KANKANALA & TRIANTAFYLIDIS [118], LINNEMANN ET AL. [152], MIEHE ET AL. [174] and MIEHE ET AL. [175]). However phenomenological approaches do not allow for the investigation of microstructural material properties and mechanism.

It has to be noted that the numerical implementation of the Landau-Lifshitz-Gilbert equation with the consistent update of magnetization as the order parameter has been an active field of research for many years. The exact update of magnetization is not straightforward from the numerical perspective as special updates are generally required to satisfy the unity constraint on the magnetization director. Exact implementations for the evolution of magnetization usually require non-linear rotational updates. MIEHE & ETHIRAJ [168] proposed the nonlinear exponential rotational updates such that the geometric property is exactly preserved at the nodes of a corresponding finite element discretization. KRISHNAPRASAD & TAN [135] make use of the Cayley transformation to achieve consistent mappings. Special test functions for finite element interpolation, considering the unity constraint, have been proposed by FRANÇOIS & PASCAL [72] and GROHS ET AL. [85]. Alternatively, methods have been developed that enforce magnetization constraint numerically. Such methods are more widely used due to their ease of implementation. A Gauss-Seidel projection method was proposed by WANG ET AL. [251] that was also employed in the homogenization framework by ZHANG & CHEN [261]. A constrained optimization approach employing Lagrange multipliers or penalty formulation of the constraint have been presented in SZAMBOLICS ET AL. [232] and LANDIS [143], respectively. YI & XU [257] proposed a constraint free formulation, in which the azimuth angle of the magnetization is chosen as the order parameter instead of the magnetization vector itself. This approach requires special numerical treatment and is elaborated in DORNISCH ET AL. [58].

To address the limitations of conventional micromagnetic approach at large body limits, computational homogenization techniques are needed. The idea of such scale-bridging techniques is to attach a microstructure point wise to a macro-continuum. Such an approach defines the macroscopic response of the material based on microstructural information. Purely mechanical homogenization theories have been proposed by NEMAT-NASSER & HORI [183] and extended to variational-based homogenization in MIEHE [164, 165], BRUN ET AL. [34], LAHELLEC & SUQUET [141] and BRASSART ET AL. [30]. Extensions of homogenization to coupled material response have been explored in recent years. Applications in the area of electromechanics are given by SCHRÖDER [215], KUZNETSOV & FISH [140], SCHRÖDER & KEIP [216], PONTE CASTAÑEDA & SIBONI [195], ZÄH & MIEHE [258] and KEIP ET AL. [121, 125]. The homogenization of *magnetomechanical material behavior* has also been worked on by PISANTE [193], in a mathematical context, while DANIEL ET AL. [48, 49] have presented homogenization of a simplified microscale model. JAMES & KINDERLEHRER [108], DESIMONE [53], DESIMONE & JAMES [54], DESIMONE ET AL. [55], BARTEL ET AL. [14] and KIEFER & LAGOUDAS [128], KIEFER ET AL. [130], KIEFER & LAGOUDAS [129] treat the modeling of magnetic shape memory alloys (MSMAs) and ferromagnetic materials with domains in the large body limit by the use of *relaxation methods*. An overview in this topic is given in DESIMONE ET AL. [55].

In this context a consistent homogenization framework that incorporates *micromag-*

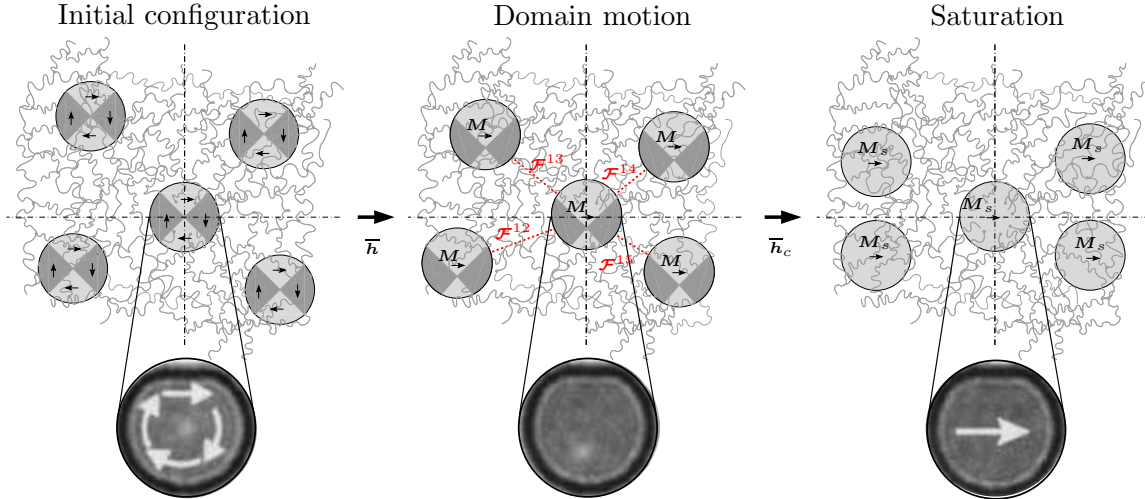


Figure 1.5: *Deformation mechanism of MREs under the application of an external magnetic field.* Under no applied magnetic field the embedded particles reside in a low-energy state, e.g. a classical vortex-type domain configuration. The particle–particle interactions are low. As soon as an external field is applied, the domain configuration changes. On the magnetic side, this causes a net magnetization of the individual particles which goes along with an effective magnetization of the MRE. The net magnetizations of the individual particles in turn causes stronger magneto-mechanical interactions (indicated by the red lines) that gives rise to deformations. Under large magnetic fields, the particles fully magnetize such that saturation of the magnetizations occurs along with deformation of the MRE saturate. Experimental observations show similar domain wall motions for micron and sub-micron sized ferromagnetic particles (SCHNEIDER ET AL. [210]).

netic domain evolution and its connection to *macroscopic material response* conceptually in line with the work of ZÄH & MIEHE [258] on micro-electro-elasticity, allows for the description of macroscopic ferromagnetic response in consideration of a dissipative microstructure. The microstructure could be described as a micro-magneto-elastic solid, where the magnetization is described by a *phase-field* (MIEHE & ETHIRAJ [168], ETHIRAJ ET AL. [69] and SRIDHAR ET AL. [227]).

MREs are characterized by a heterogeneous microstructure that consists of a soft elastic matrix and embedded magnetic inclusions. Due to the combination of magnetic properties and elastic softness, MREs exhibit magnetomechanical coupling at large elastic deformations. Figure 1.5 shows the deformation mechanism of an MRE under applied magnetic field, on the mesoscale. When no external field is applied, magnetization in the inclusions exist at a low energy state such that the net magnetization and in turn the magnetic self field is zero. Application of an external field causes domain wall motion in particles which in turn induces a net magnetization. These magnetizations then induce interaction forces between embedded particles, hence causing deformation of the matrix-particle composite as a whole (BORCEA & BRUNO [24]). When coercive field is reached, the magnetizations in the particles fully rotate in the direction of field such that both, the overall magnetization and deformation of the composite saturate. Experimentally, domain motion in micron and sub-micron sized ferromagnetic particles has been shown in SCHNEIDER ET AL. [210] and MRE deformation under various loads and conditions has been shown in JOLLY ET AL. [110] and DANAS [46], DANAS ET AL. [47, 47].

Advanced continuum approaches that account for these large deformations and non-linear Maxwell interactions have been developed to model the behavior of soft magnetoelastic materials. These theories mainly employ the deformation and magnetic poten-

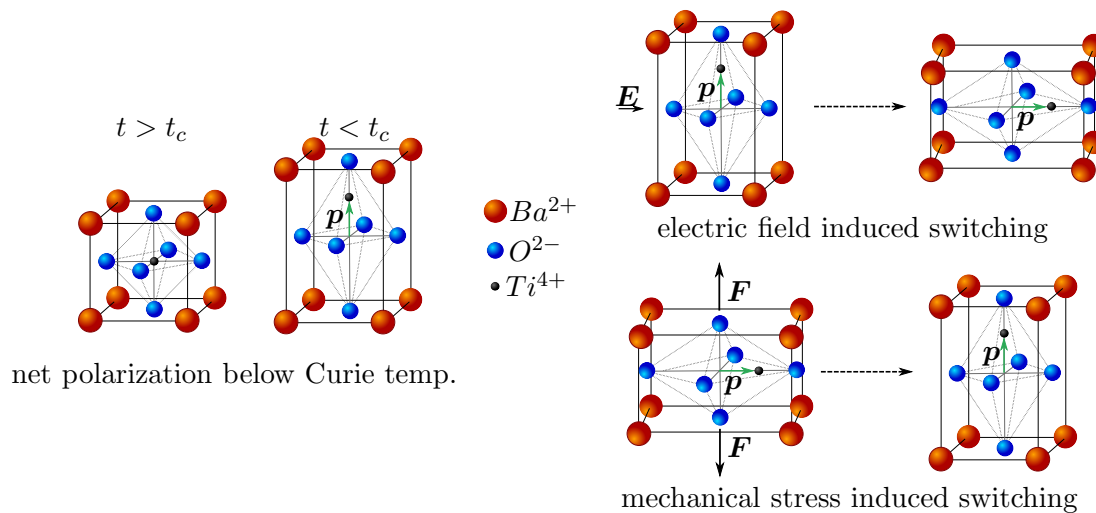


Figure 1.6: *Spontaneous polarization and electromechanical coupling in piezoelectric ceramics.* Ferroelectric materials like Barium Titanate are a special class of piezoelectric materials that show a spontaneous polarization below a certain temperature, known as the Curie temperature. This polarization can be influenced by application of external mechanical or electric field. This in turn gives rise to the electromechanical coupling in the form of piezoelectric or inverse piezoelectric effect respectively.

tial as primary fields (BRIGADNOV & DORFMANN [31], DORFMANN & OGDEN [57], STEIGMANN [228] and BUSTAMANTE ET AL. [35]). Complementary modeling approaches also incorporate magnetization as an additional variable (KANKANALA & TRIANTAFYLIDIS [118], DANAS ET AL. [47]). To account for the composite nature of MREs, analytical homogenization techniques have also been proposed in literature (PONTE CASTAÑEDA & GALIPEAU [194], GALIPEAU & PONTE CASTAÑEDA [76] and LEFÈVRE ET AL. [148]). Furthermore, and complementary to this, computational homogenization strategies were proposed by JAVILI ET AL. [109], MIEHE ET AL. [177], KEIP & RAMBAUSEK [122, 123] and DANAS [46]. However, the inherent information from dissipative and nonlinear domain evolution on microscopic level are not accounted for in such settings. Extensions of the micromagnetic framework to account for large deformations would enable the model to capture these non-linear aspects without any prior constitutive assumptions (KEIP & SRIDHAR [124]).

1.4.2. Anisotropic Fracture in Piezoelectric and Ferroelectric Ceramics

Similar to ferromagnetic materials, piezoelectric ceramics find multiple applications due to their electromechanical coupling capability, relatively low power requirements, and high generative forces. Common piezoelectric materials like lead zirconate titanate ($Pb[Zr_xTi_{1-x}]O_3$ with $0 \leq x \leq 1$ commonly known as PZT), exhibit linear electromechanical response due to charge separation under external influence. This charge separation results in an induced polarization which is the source of the electromechanical response in these materials. Most piezoelectrics however do not show a remnant polarization, that is inherently, there is no charge separation. A special class of these materials are ferroelectric materials, like barium titanate ($BaTiO_3$) that show spontaneous polarization below a certain Curie temperature, Figure 1.6 (JAFJE ET AL. [107]). This spontaneous polarization can be influenced by applying an appropriate electric and/or mechanical field. This

process is typically dissipative and rate dependent, accompanied by hysteretic effects in cyclic loading.

From the continuum modeling viewpoint *microscopically motivated phenomenological* models have been proposed in literature to capture these effects (CHEN & LYNCH [40], HUBER ET AL. [102], KAMLAH [115], HUBER [100], MCMEEKING & LANDIS [158], MCMEEKING ET AL. [162] among many other). These microscopic models, capture the constitutive behavior by employing energy arguments as switching criteria. Macroscopic phenomenological models on the other hand propose thermodynamically consistent formulations of the macroscopic hysteresis response. Some of the earliest works in this field can be seen in BASSIOUNY ET AL. [15, 16]. Following this thermodynamical framework, other *macroscopic models* were proposed to capture the hysteresis response similar to plasticity problems (KAMLAH & TSAKMAKIS [117], KAMLAH & BÖHLE [116], LANDIS [145, 146], MCMEEKING & LANDIS [158], HUBER & FLECK [101], SCHRÖDER & ROMANOWSKI [218] and KLINKEL [133]). Extensions in the context of variational rate-dependent formulations for magneto-electro-mechanical processes were proposed by MIEHE & ROSATO [170], MIEHE ET AL. [174, 175].

On the other hand, *phase-field and relaxation methods* have been employed with *polarization as the order parameter* to capture nonlinear and dissipative domain wall motion in ferroelectric materials (CAO & CROSS [38], HU & CHEN [98], WANG ET AL. [250], SHU & BHATTACHARYA [222], BHATTACHARYA & RAVICHANDRAN [19], ZHANG & BHATTACHARYA [263, 264], SU & LANDIS [229], SCHRADER ET AL. [212, 211, 213], CHOUDHURY ET AL. [41], MÜLLER ET AL. [179, 180], XU ET AL. [255], WANG & KAMLAH [248], XU ET AL. [256] and MIEHE ET AL. [176]). Traditionally, the polarization is chosen as an order parameter whose evolution is given by a time-dependent *Ginzburg-Landau* type evolution equation. Homogenization approaches in the context of electromechanically coupled problems have been considered in HORI & NEMAT-NASSER [97], SCHRÖDER [215], KHALAQUZZAMAN ET AL. [127], PONTE CASTAÑEDA & SIBONI [195], SCHRÖDER & KEIP [216], ZÄH & MIEHE [258].

Brittle materials experience dynamic fracture mechanism like multiple crack branching, crack arrest and crack kinking. These highly non-smooth effects appear in many engineering applications due to cyclic, impact or critical loading conditions. Experimental investigations of such fracture has been reported in RAVI-CHANDAR & KNAUSS [200, 201, 202, 203], RAMULU & KOBAYASHI [198], KALTHOFF [113], ZHOU ET AL. [267], ZHOU ET AL. [266] and KALTHOFF & WINKLER [114]. Theoretical foundations of the *classical theory of brittle fracture* in solids are outlined by seminal work of GRIFFITH [82] and GRIFFITH [83]. Griffith emphasized that a crack propagates in a solid, if the energy available to extend a crack, reaches a critical value which is called the *critical energy release rate*. Following this, studies in the field of brittle fracture were carried out by (IRWIN [104], IRWIN [105]). Irwin proposed the concept of *stress intensity factors*, where instead of considering the energy of the whole system, the crack is described by the intensity of stresses in the neighborhood of the crack tip. It has to be noted however that the stress intensity near the crack tip depend on the geometry and boundary conditions of the solid. Finally a *cohesive zone model* which models the separation of crack faces near the crack tip was proposed by BARENBLATT [13]. Variations of these theories in terms of the path independent *J-integral*, introduced by RICE [204], relates the energy release rate to the stresses and strains at the crack tip. Further, the description of crack in terms

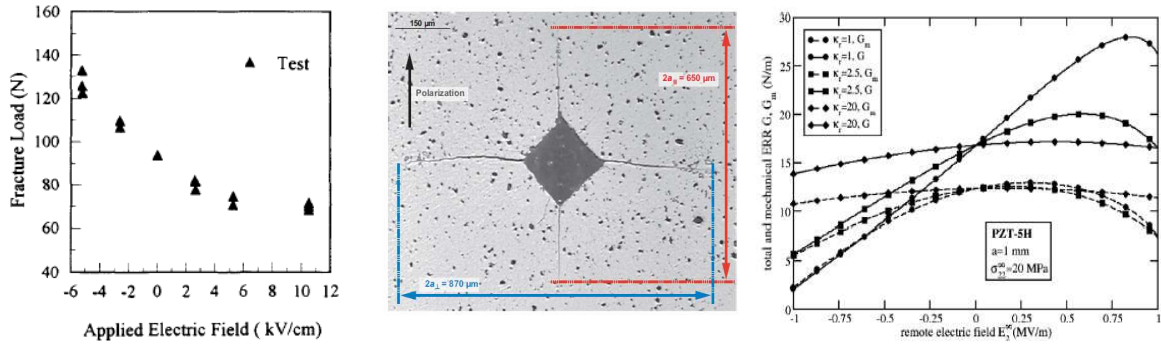


Figure 1.7: Influence of electric field loading on the fracture behavior of piezoelectric ceramics. Piezoelectric materials show a coupled electromechanical response which is also reflected in their fracture behavior. Experimental results show varied influence of a positive or negative applied electric field (PARK & SUN [191]). Indentation tests show that the length of the crack also depends on poling direction of the crystal (SCHNEIDER [209]). Theoretical prediction of energy release rates predict the influence of field loading on the fracture behavior (KUNA [139]).

of configurational forces was discussed in the works by ESHELBY [65, 66, 67], RICE [204], MIEHE ET AL. [171], MIEHE & GÜRSES [169], GÜRSES & MIEHE [86] and MAUGIN & TRIMARCO [154].

Variational formulations of the Griffith-type energy minimization problem was introduced by FRANCFORT & MARIGO [73] and BOURDIN ET AL. [29]. This was inspired by the work in image segmentation of MUMFORD & SHAH [181] which utilizes an auxiliary field to regularize the sharp crack discontinuity by a diffusive crack zone. This scalar auxiliary field can be considered as a phase-field which interpolates between the intact and fully broken phases. This phase-field is then governed by a traditional *Ginzburg-Landau* type evolution equation in the dynamic setting (HAKIM & KARMA [90], KUHN & MÜLLER [138], MIEHE ET AL. [172], BORDEN ET AL. [25] and HOFACKER & MIEHE [94, 95]). The above works describe crack propagation in isotropic solids. However many materials possess an inherent anisotropic structure that influences crack propagation. Such anisotropy can occur due to inherent material anisotropy, polycrystalline aggregate or composite microstructure. This has also been shown experimentally in the works by (RIEDLE & GUMBSCH [205], NIANDOU ET AL. [185], QIAO & ARGON [197], NASSERI & MOHANTY [182] and TAKEI ET AL. [233]). Extensions of the phase-field approach to account for anisotropic behavior have been proposed in recent years (EGGLESTON ET AL. [61], SEKERKA [219], HAKIM & KARMA [89], TORABI ET AL. [238], TORABI & LOWENGRUB [237], CLAYTON & KNAP [44], SHANTHRAJ ET AL. [220] and NGUYEN ET AL. [184]). Recently a general modular framework for phase-field modeling of fracture in anisotropic solids in large and small deformations was proposed by TEICHTMEISTER ET AL. [235]. Due to the aforementioned applications of piezoelectric ceramics, recently there has been much research interest in fracture and life cycle analysis of these materials. Experimental investigations in this regard were performed to check the influence of electric field on the fracture behavior (PARK & SUN [191], FU & ZHANG [74], PAK & TOBIN [189], DOS SANTOS E LUCATO ET AL. [59], LI ET AL. [149]). Experimental observations showed pronounced effects of the electric field on the fracture toughness of a piezoelectric material. This led to extensions of the fracture framework to the coupled electromechanical setting (PARTON [192], DEEG [51], PAK [188], SUO ET AL. [231], GAO ET AL. [77], McMEEKING [159], FANG ET AL. [70], ZHANG ET AL. [265]). In this context, the be-

behavior of electric field inside the crack gap was investigated in PARTON [192] and DEEG [51]. More recently, *energetically consistent boundary conditions* that take into account nonlinear Maxwell interactions were proposed by MCMEEKING [161] and LANDIS [144]. Computational modeling of electromechanical fracture for fixed cracks was investigated by WANG & ZHANG [249] and WANG & KAMLAH [248]. Phase-field approaches that capture nonlinear crack propagation under combined electromechanical loading are also proposed in MIEHE ET AL. [172], ABDOLLAHI & ARIAS [2, 3, 4, 5, 6], ARIAS ET AL. [10] and XU ET AL. [254]. An overview of fracture in piezoelectric ceramics is given in SCHNEIDER [209] and KUNA [139]. Anisotropic fracture propagation in the case of a coupled electromechanical behavior is a relatively new area. A phase-field approach to capture this coupled behavior was proposed in SRIDHAR & KEIP [226].

1.4.3. Objectives and Overview

This work deals with the development of variational electro-magneto-mechanically coupled *phase-field* models in the context of homogenization, finite strains and fracture mechanics. Three material classes are the focus of this work namely *ferromagnetic materials*, *magnetorheological elastomers (MREs)* and *ferroelectrics*. The work is mainly divided into three parts:

Part I deals with fundamentals of continuum mechanics, electromagnetism and fracture mechanics. **Chapter 2** starts with an elementary description of the finite strain formulation, which is a key aspect in the continuum modeling description presented later. Further the theory of electromagnetism is presented starting from the well known Maxwell equations. Modification of Maxwell equation to ponderable media, gives definition of polarization and magnetization in the material. The respective electric and magnetic quantities are then introduced in the finite strain setting. In **Chapter 3** fundamental fracture mechanics is introduced in a diffusive setting by introduction of a damage phase-field. Extension of the fracture phase-field method to account for anisotropy and electric field is briefly introduced.

Part II presents the micromagnetic theory, with magnetization as the phase-field, in the context of homogenization and finite strains. **Chapter 4** deals with the small strain formulation of the micromagnetic framework. A novel staggered solution scheme for the *Landau-Lifschitz* equation and a homogenization framework satisfying the Hill-Mandel condition is presented. The capability of the proposed framework to capture microscopic domain evolution in ferromagnetic materials and in turn predict macro response is shown by appropriate numerical examples. **Chapter 5** deals with extension of micromagnetic approach to the finite strain setting with the aim of modeling magnetorheological elastomers (MREs). MREs show a coupled magnetomechanical response in the presence of an applied field due to non-linear magnetic interactions between ferromagnetic inclusions. The small strain theory does not account for “Maxwell” interactions that play a critical role in these effects. A finite strain extension of the micromagnetic theory capable of capturing this phenomenon while having the microstructural information lends new insights into the behavior of such materials. Particular importance is given to satisfy objectivity restrictions and rate-type variational principles. Numerical examples showcase the capability of the model to capture domain evolution, satisfy objectivity restrictions and capture the physical effects of magnetic particles interacting in a non-magnetic substrate.

Part III deals with anisotropic fracture mechanics in a coupled electromechanical setting for piezo-/ferro-electrics. **Chapter 6** introduces the phase-field approach to anisotropic fracture in piezoelectric ceramics. A non-associative framework of the crack driving force is proposed after due comparison of the local constitutive response with experimental data. Appropriate degradation functions are proposed to capture various electrical conditions inside the crack gap. A three-field variational framework accounting for irreversibility of the crack and a tension-compression split is presented. Two- and three-dimensional examples are shown to analyze the influence of crack behavior under combined electromechanical loads. **Chapter 8** extends the fracture framework to ferroelectric ceramics. To account for the non-linear behavior of such materials an additional order parameter that is the polarization is introduced. The local constitutive response is presented in a one-dimensional setting and the influence of the polarization on the fracture behavior is presented. The variational framework proceeds similar to the case of piezoelectrics with an additional Euler equation for the polarization order parameter. Numerical examples showcase capability of the model to capture non-linear domain evolution of polarization and the influence of crack propagation on the same.

— Part I —

**Fundamentals of Continuum
Mechanics, Electromagnetism and
Fracture**

Fundamentals of Continuum Mechanics and Electromagnetism

This chapter provides the fundamentals of finite strain continuum mechanics, which is the basis for the continuum formulation of brittle materials. An introduction to electromagnetism is also presented in the continuum setting. A finite strain continuum formulation is introduced in a geometric setting and a physical description along with motivation for the same is presented. The stress and strain quantities linked to the reference and current configuration are presented in an intuitive fashion and metric tensors are introduced as a natural mapping between tangent and co-tangent spaces. This viewpoint is mainly adopted from the lectures on advanced mechanics held at the Institute of Applied Mechanics at the University of Stuttgart, presented by the late Prof. C. Miehe (MIEHE [166, 167]). In the second half of the section Maxwell equations and magnetic quantities are presented in the continuum setting. The introduction to electromagnetism is motivated from the lectures of Prof. R. L. Feynman (FEYNMAN ET AL. [71]).

2.1. Fundamentals of Continuum Mechanics

The mechanics of continuous media is a fundamental field of research used to describe certain phenomena in deforming solids and lays the groundwork for all advanced fields of applied mechanics. Kinematics in large strain continuum mechanics are based on the introduction of nonlinear deformation map, that describes the motion from Lagrangian to Eulerian manifold. The focus is on a geometric setting, using the nomenclature of co- and contravariant objects for description. Hence, material and spatial metric coefficients are introduced to connect tangent and cotangent spaces and act as index lowering or raising operators. This section is of introductory nature and is by no means complete. For further explanations including an introduction to tensor algebra and analysis, the interested reader is referred to classical textbooks of TRUESDELL & NOLL [240], GURTIN [87], MARSDEN & HUGHES [153], OGDEN [186], HOLZAPFEL [96], BAŞAR & WEICHERT [12], HAUPT [91], and GURTIN ET AL. [88] among many others.

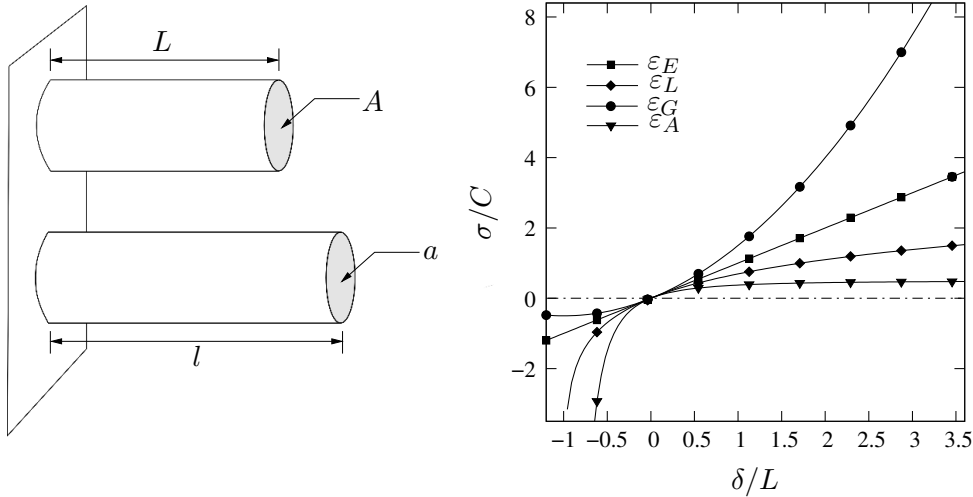


Figure 2.1: One dimensional deformation of an elastic rod with initial length L and area A along with deformed dimensions of length l and area a . The stress-strain behavior for a one dimensional elastic rod for various strain measures are plotted. Linear material law with modulus C is assumed. The behavior differs drastically depending on the strain measure chosen. It is however important to note that for small strains $\delta/L \rightarrow 0$, that is in the linearized regime, all the strains give the same result.

2.1.1. Introduction and Motivation

Continuum mechanics is a branch of mechanics that deals with the analysis of the kinematics and mechanical behavior of materials modeled as a continuous mass rather than as discrete particles. Solid mechanics, in specific is a branch of continuum mechanics that studies the behavior of solid materials, especially their motion and deformation under the action of forces, temperature changes, phase changes, and other external or internal agents. The infinitesimal strain theory is a mathematical approach to describe deformation of the solid body in which displacements of material particles are assumed to be much smaller than the physical dimensions of the body. However in most practical applications this is not the case and a generalized nonlinear finite strain theory is used to describe the material response. To illustrate the differences between linear and nonlinear theory an one dimensional bar example is presented in [Figure 2.1](#), adapted from BONET & WOOD [23].

The motion of a body is best described by strain measures that measure deformations in the solid. The simplest possible quantity that can be used to measure strain in the bar is the so called *engineering strain* ϵ defined as

$$\epsilon_E = \frac{l - L}{L}. \quad (2.1)$$

Other strain measures could also be used to describe the deformation of the body. For instance, a large strain measure can be obtained by adding all infinitesimal strain increments during deformation. This gives the *natural or logarithmic strain* ϵ_L as

$$\epsilon_L = \int_L^l \frac{dl}{L} = \ln \frac{l}{L}. \quad (2.2)$$

Other strain measures that are generally used in three dimensional setting are the *Green and Almansi strain* defined as,

$$\epsilon_G = \frac{l^2 - L^2}{2L^2} \quad \text{and} \quad \epsilon_A = \frac{l^2 - L^2}{2l^2}. \quad (2.3)$$

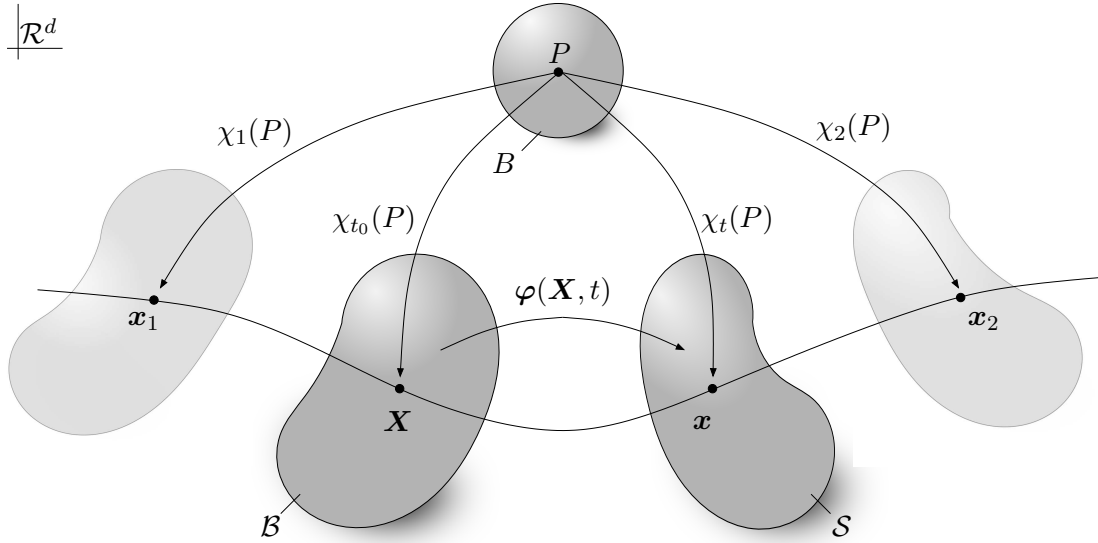


Figure 2.2: Motion of a body in Euclidean space and deformation map. The motion of the body \mathcal{B} in Euclidean space $\{\mathcal{R}^d\}_{d=1,2,3}$ can be characterized as a series of placements of the physical body B by a family of configurations $\chi_t : B \rightarrow \mathcal{B}_t \in \mathcal{R}^d$. The deformation of the body from reference configuration $\mathcal{B} := \chi_{t_0}(B)$ to the deformed configuration $\mathcal{S} := \chi_t(B)$ is described by deformation map $\varphi(\mathbf{X}, t)$.

All the strain measures introduced above, converge to the linear engineering strain for the case that the deformation is small $l \approx L$. For example performing the Taylor expansion of the logarithmic strain gives,

$$\varepsilon_L(l \approx L) = \ln(1) + \frac{(l - L)}{L} - \frac{1}{2L^2}(l - L)^2 + \frac{1}{3l^3}(l - L)^3 \approx \frac{l - L}{L}. \quad (2.4)$$

Stress in the bar under applied deformation can be defined as $\sigma = C\varepsilon$, where ε can be any strain measure and a stiffness constant C . Figure 2.1 shows load displacement plots for various strain measures. It can be clearly seen from the plots that different strain measures give different constitutive response. However, in the linear regime of infinitesimal deformations all the strain measures converge to the same result. The infinitesimal or small strain formulation is computationally less expensive however is valid strictly for the case where deformations are small. The finite strain theory on the other hand is computationally more expensive however it is capable of modeling the nonlinear behavior of materials under large deformations. In the following sections the continuum framework is presented for large deformation case.

2.1.2. Motion of a Continuum Body

A material body B is a physical object that occupies a region in the Euclidean space $\{\mathcal{R}^d\}_{d=1,2,3}$, as shown in Figure 2.2. The continuum body B can be defined as an open set of material points $P \in B$ with deformation considered as a continuous time sequence of events. The material body will occupy different configurations at different times. Then the configuration of the body $B \subset \mathcal{R}^d$, at any given time t can be defined by an injective function

$$\chi_t : \begin{cases} B \rightarrow \mathcal{B}_t \subset \mathcal{R}^d \\ P \rightarrow \mathbf{x}_t = \chi_t(P) \end{cases}. \quad (2.5)$$

The function χ_t , in (2.5), maps the material points P of the the body B to the coordinate triple $\mathbf{x}_t \in \mathcal{R}^d$ with respect to the global Cartesian basis $\{\mathbf{E}_i\}_{i=1,2,3}$. To characterize the deformations in a finite strain setting the placement of the body at time t_0 is referred to as *reference configuration* $\mathcal{B} = \chi_0(B)$. The reference state is generally chosen to be a undeformed and a stress-free state of the body. Similarly, the deformed state of the body is called *actual configuration* $\mathcal{S} = \chi_t(B)$. The reference configuration is also referred to as *material or Lagrangian* configuration and the actual configuration is denoted as *spatial or Eulerian* configuration. The material points P of the body B , consequently occupy the positions $\mathbf{X} = \chi_0(P)$ and $\mathbf{x} = \chi_t(P)$, in material and spatial configurations respectively. The motion of the body between time t_0 and time t , can be described by a nonlinear deformation map

$$\varphi_t : \begin{cases} \mathcal{B} \rightarrow \mathcal{S} \in \mathcal{R}^d \\ \mathbf{X} \rightarrow \mathbf{x} = \varphi_t(\mathbf{X}) := \chi_t \circ \chi_0^{-1}(\mathbf{X}). \end{cases} \quad (2.6)$$

Due to the one-to-one property of $\mathbf{X} = \chi_0(P)$, its inverse reads $P = \chi_0^{-1}(\mathbf{X})$ such that

$$\mathbf{x} = \chi_t(P) = \chi_t(\chi_0^{-1}(\mathbf{X})) = \chi_t \circ \chi_0^{-1}(\mathbf{X}) = \varphi(\mathbf{X}). \quad (2.7)$$

2.1.3. The Deformation Gradient: Line, Area and Volume Maps

An important quantity in finite deformation analysis is the *deformation gradient* \mathbf{F} which describes the relative spatial position of two neighboring particles after deformation in terms of their material position before deformation. As an example consider a curve parameterized by scalar quantity θ . Such a curve in the material setting can be given by a nonlinear map $\mathcal{C}(\theta) : \theta \rightarrow \mathbf{X} = \mathcal{C}(\theta)$ and in spatial setting as $\mathcal{c}(\theta) : \theta \rightarrow \mathbf{x} = \mathcal{c}(\theta)$. With the deformation map $\varphi(\mathbf{X}, t)$ (2.6), gives the relation

$$\mathbf{x} = \varphi(\mathbf{X}, t) \quad \rightarrow \quad \mathcal{c}(\theta) = \varphi(\mathcal{C}(\theta), t). \quad (2.8)$$

With this relation at hand chain rule could be used to describe the Eulerian tangent as,

$$\mathbf{t}(\theta) = \frac{d}{d\theta} \mathcal{c}(\theta) = \nabla_{\mathbf{X}} \varphi \cdot \frac{d}{d\theta} \mathcal{C}(\theta) := \mathbf{F}\mathbf{T}. \quad (2.9)$$

The deformation gradient is then given as derivative of the deformation map with respect to material coordinates

$$\mathbf{F}(\mathbf{X}) = \nabla_{\mathbf{X}} \varphi(\mathbf{X}, t) := \begin{cases} T_{\mathbf{X}}\mathcal{B} \rightarrow T_{\mathbf{x}}\mathcal{S} \\ \mathbf{T} \rightarrow \mathbf{t} = \mathbf{F}\mathbf{T} \end{cases}. \quad (2.10)$$

The deformation gradient provides a one-to-one mapping between the material manifold \mathbf{X} and spatial manifold \mathbf{x} . Mathematically, the deformation gradient \mathbf{F} is a mapping between material tangent space $\mathbf{T} \in T_{\mathbf{X}}\mathcal{B}$ and spatial tangent space $\mathbf{t} \in T_{\mathbf{x}}\mathcal{S}$ (Figure 2.3). Similar to the line element, the deformation gradient also plays a key role in the definition of volume and area elements of the deforming continuum. Consider the material and spatial volume elements

$$dV := d\mathbf{X}_1 \cdot (d\mathbf{X}_2 \times d\mathbf{X}_3) \quad \text{and} \quad dv := d\mathbf{x}_1 \cdot (d\mathbf{x}_2 \times d\mathbf{x}_3), \quad (2.11)$$

defined as the scalar triple product of the vectors $d\mathbf{X}_{i=1,2,3} \in T_{\mathbf{X}}\mathcal{B}$ and $d\mathbf{x}_{i=1,2,3} \in T_{\mathbf{x}}\mathcal{S}$, respectively. Then the volume map can be defined as

$$dv := \mathbf{F}d\mathbf{X}_1 \cdot (\mathbf{F}d\mathbf{X}_2 \times \mathbf{F}d\mathbf{X}_3) = \det[\mathbf{F}] dV = J dV, \quad (2.12)$$

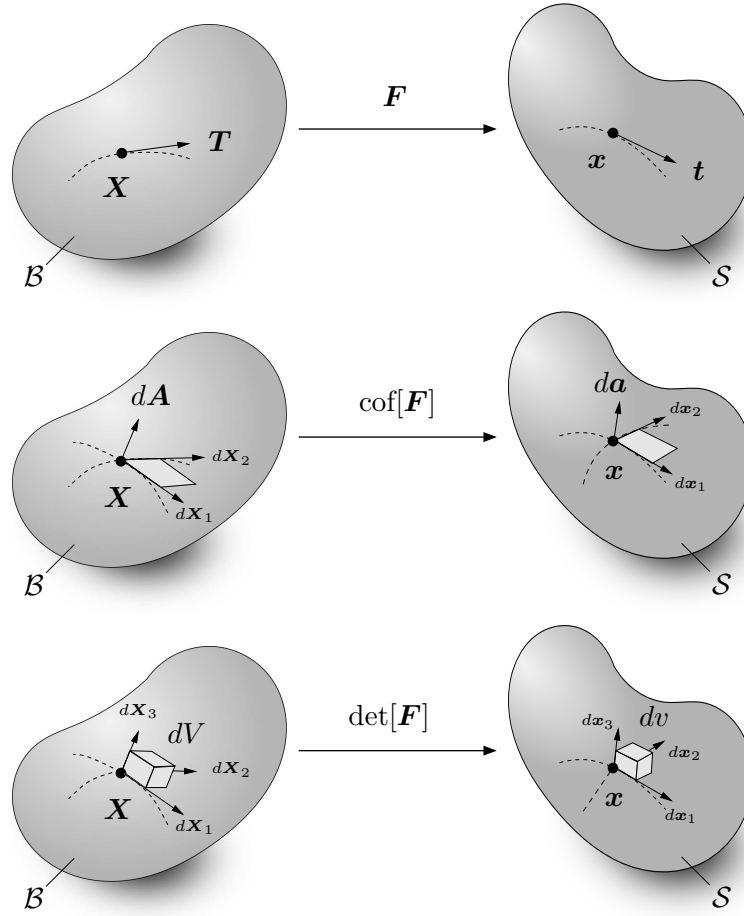


Figure 2.3: Tangent, area and volume maps of the body. The deformation gradient \mathbf{F} , its cofactor $\text{cof}[\mathbf{F}]$ and its determinant $J = \det[\mathbf{F}]$ define the mapping of the tangent, area and volume elements of the continuum respectively.

with the definition of the determinant of a second order tensor $J = \det[\mathbf{F}]$. The Jacobian is constrained to positive real numbers \mathcal{R}_+ in order to ensure material impenetrability. Mathematically we can express the volume map as,

$$J = \det[\mathbf{F}] : \begin{cases} \mathcal{R}_+ \rightarrow \mathcal{R}_+ \\ dV \rightarrow dv = \det[\mathbf{F}] dV. \end{cases} \quad (2.13)$$

The area map can consequently be derived from the volume map from (2.11). Defining area co-vectors $\mathbf{N} dA = d\mathbf{X}_2 \times d\mathbf{X}_3$ and $\mathbf{n} da = d\mathbf{x}_2 \times d\mathbf{x}_3$ in the referential and spatial setting respectively (2.11) can be rewritten as

$$J d\mathbf{X}_1 \cdot \mathbf{N} dA = d\mathbf{x}_1 \cdot \mathbf{n} da = \mathbf{F} d\mathbf{X}_1 \cdot \mathbf{n} da = d\mathbf{X}_1 \cdot \mathbf{F}^T \mathbf{n} da. \quad (2.14)$$

For arbitrary material tangent $d\mathbf{X}_1$, the above equality is satisfied for

$$\mathbf{n} da = \text{cof}[\mathbf{F}] \mathbf{N} dA \quad \text{with} \quad \text{cof}[\mathbf{F}] = \partial_{\mathbf{F}} \det[\mathbf{F}] = \det[\mathbf{F}] \mathbf{F}^{-T}. \quad (2.15)$$

The tensorial quantity for the area map is \mathbf{F}^{-T} , hence we consider \mathbf{F}^{-T} as the normal map transforming the co-vectors from the co-tangent space in the material $\mathbf{N} \in T_{\mathbf{X}}^* \mathcal{B}$ to the spatial manifold $\mathbf{n} \in T_{\mathbf{x}}^* \mathcal{S}$

$$\mathbf{F}^{-T} : \begin{cases} T_{\mathbf{X}}^* \mathcal{B} \rightarrow T_{\mathbf{x}}^* \mathcal{S} \\ \mathbf{N} \rightarrow \mathbf{n} = \mathbf{F}^{-T} \mathbf{N}. \end{cases} \quad (2.16)$$

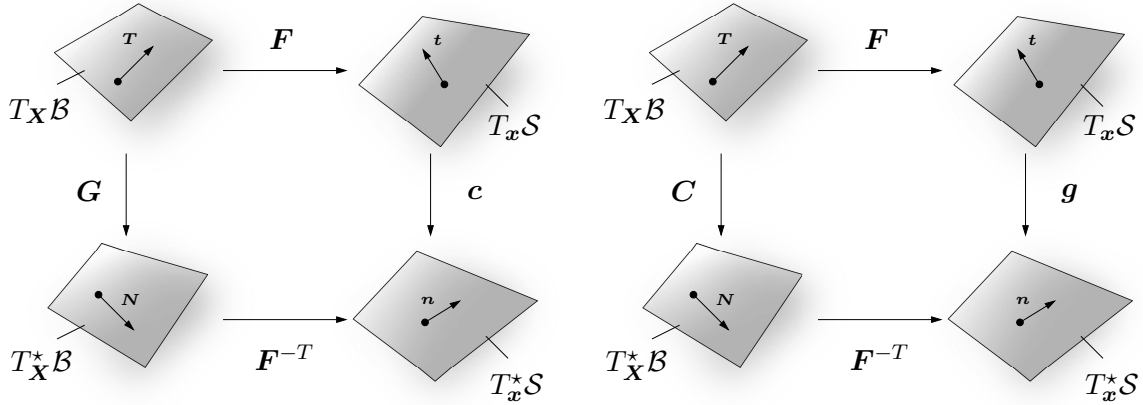


Figure 2.4: Commutative diagram and tensorial mapping between tangent and co-tangent spaces. The deformation gradient \mathbf{F} maps tangents between referential and spatial manifolds while the co-tangents are mapped via \mathbf{F}^{-T} . The referential metric tensor \mathbf{G} and spatial metric \mathbf{g} map the tangent and co-tangent spaces.

2.1.4. Metric Tensors, Stretch and Cauchy-Green Stretch

The definition of metric tensors is an integral part of continuum mechanics, such that the magnitude of vectors can be obtained with the aid of simple inner products. The metric tensors are chosen according to the local coordinate system. The natural metric tensors are defined by

$$\mathbf{G} = \delta_{AB} \mathbf{E}_A \otimes \mathbf{E}_B \quad \text{and} \quad \mathbf{g} = \delta_{ab} \mathbf{e}_a \otimes \mathbf{e}_b, \quad (2.17)$$

in referential and spatial Cartesian coordinate system. The Lagrangian metric \mathbf{G} and its Eulerian counterpart \mathbf{g} are considered as mappings between the tangent and co-tangent spaces respectively,

$$\mathbf{G} : \begin{cases} T_X \mathcal{B} \rightarrow T_X^* \mathcal{B} \\ \mathbf{T} \rightarrow \mathbf{N} = \mathbf{G}\mathbf{T} \end{cases} \quad \text{and} \quad \mathbf{g} : \begin{cases} T_x \mathcal{S} \rightarrow T_x^* \mathcal{S} \\ \mathbf{t} \rightarrow \mathbf{n} = \mathbf{g}\mathbf{t} \end{cases}. \quad (2.18)$$

The geometrical mappings between tangent and co-tangent spaces are depicted in [Figure 2.4](#). The metric tensors play a fundamental role in measuring basic deformations. To illustrate this, consider a Lagrangian tangent $\mathbf{T}(\mathbf{X})$ and an Eulerian tangent $\mathbf{t}(\mathbf{x})$ and define the stretch $\bar{\lambda}$, as ratio of the length of the deformed tangent to the reference tangent, i.e. $\bar{\lambda} := |\mathbf{t}|_{\mathbf{g}} / |\mathbf{T}|_{\mathbf{G}} = \sqrt{\mathbf{t} \cdot \mathbf{g}\mathbf{t}} / \sqrt{\mathbf{T} \cdot \mathbf{G}\mathbf{T}} > 0$. Setting $|\mathbf{T}|_{\mathbf{G}} = 1$ as the reference values, the stretch can be expressed as,

$$\bar{\lambda} = \sqrt{\mathbf{t} \cdot \mathbf{g}\mathbf{t}} = \sqrt{\mathbf{F}\mathbf{T} \cdot \mathbf{g}\mathbf{F}\mathbf{T}} = \sqrt{\mathbf{T} \cdot \mathbf{F}^T \mathbf{g}\mathbf{F}\mathbf{T}} = \sqrt{\mathbf{T} \cdot \mathbf{C}\mathbf{T}} =: |\mathbf{T}|_{\mathbf{C}} \quad (2.19)$$

in Lagrangian (material) description of the length deformation. This in turn gives the definition of convected spatial metric in the Lagrangian setting, the *right Cauchy-Green tensor*

$$\mathbf{C} := \varphi^*(\mathbf{g}) = \mathbf{F}^T \mathbf{g}\mathbf{F}. \quad (2.20)$$

With $\varphi^*(\cdot)$ representing the pull-back operation. On the other hand, setting $|\mathbf{t}|_{\mathbf{g}} = 1$ in Eulerian description of the deformation, the inverse stretch could be expressed as

$$\bar{\lambda}^{-1} = \sqrt{\mathbf{T} \cdot \mathbf{G}\mathbf{T}} = \sqrt{\mathbf{F}^{-1}\mathbf{t} \cdot \mathbf{G}\mathbf{F}^{-1}\mathbf{t}} = \sqrt{\mathbf{t} \cdot \mathbf{F}^{-T} \mathbf{G}\mathbf{F}^{-1}\mathbf{t}} = \sqrt{\mathbf{t} \cdot \mathbf{c}\mathbf{t}} =: |\mathbf{t}|_{\mathbf{c}} \quad (2.21)$$

in terms of *inverse left Cauchy-Green tensor*, as material metric in the spatial setting

$$\mathbf{c} := \varphi_*[\mathbf{G}] = \mathbf{F}^{-T} \mathbf{G} \mathbf{F}^{-1}. \quad (2.22)$$

With $\varphi_*(\cdot)$ representing the push-forward operation. The inverse of left Cauchy-Green tensor is also referred as the *finger tensor* $\mathbf{b} := \mathbf{c}^{-1} = \mathbf{F} \mathbf{G}^{-1} \mathbf{F}^T$. The geometric interpretation of these tensors leads us to commutative diagrams shown in [Figure 2.4](#). Note that in traditionally upper and lower indices, in the sense of co- and contravariant representations, are used for the tangent and co-tangent spaces respectively. This in turn leads to varied mappings for the geometric entities (also for the stress measures introduced later), by index lowering and raising operations in conjunction with the metric tensors. However, only Cartesian coordinate system is used in this work and in turn to keep the notation compact mappings are a priori assumed as shown in [Figure 2.4](#).

2.1.5. Velocity, Velocity gradient and Lie Rate

Nonlinear deformation may be time dependent, hence it is necessary to consider velocity and material *time derivatives* of various quantities. Even, if the process is not rate-dependent equilibrium equations may be expressed in terms of virtual velocities and virtual time dependent quantities. The usual motion of the body given by (2.6) could be reformulated in various settings as

$$\mathbf{x} = \underbrace{\varphi(\mathbf{X}, t)}_{\text{motion}} = \underbrace{\varphi_t(\mathbf{X})}_{\text{configuration}} = \underbrace{\varphi_{\mathbf{X}}(t)}_{\text{path}} \quad (2.23)$$

where the general motion of the body $\varphi(\mathbf{X}, t)$ is as defined before. The configuration $\varphi_t(\mathbf{X})$ of \mathcal{B} defines at a specific (frozen) time t the configuration, and path $\varphi_{\mathbf{X}}(t)$ of the particle P labeled by coordinate \mathbf{X} in the reference configuration. The *material velocity of a particle* \mathbf{V} then is defined as the time derivative of the motion $\varphi(\mathbf{X}, t)$ as,

$$\mathbf{V}(\mathbf{X}, t) = \frac{\partial}{\partial t} \varphi(\mathbf{X}, t) = \frac{d}{dt} \varphi_{\mathbf{X}}(t). \quad (2.24)$$

Observe that the velocity is a spatial vector in the *current configuration* \mathcal{S} despite the fact that the velocity field is expressed in the material coordinates of the particle \mathbf{X} . The *spatial velocity* \mathbf{v} then follows from the material velocity as,

$$\mathbf{v}(\mathbf{x}, t) = \mathbf{V}(\varphi_t^{-1}(\mathbf{x}), t) = \mathbf{V} \circ \varphi_t^{-1}(\mathbf{x}) \quad (2.25)$$

which is understood as vector field in the current configuration \mathcal{S} but in contrast to material velocity $\mathbf{V}(\mathbf{X}, t)$ is parameterized in Eulerian coordinates \mathbf{x} . Similar to spatial velocity many other fields in mechanics are more consistently expressed as a function of spatial position \mathbf{x} . In this context consider a tensor or scalar quantity \mathbf{g} , expressed in terms of material coordinates \mathbf{X} , then the time derivative of $\mathbf{g}(\mathbf{X}, t)$ is defined as,

$$\dot{\mathbf{g}} = \frac{d\mathbf{g}}{dt} = \frac{\partial}{\partial t} \mathbf{g}(\mathbf{X}, t). \quad (2.26)$$

This measures the change in \mathbf{g} associated with a specific particle initially located at \mathbf{X} with respect to time, it's known as the *material time derivative* of $\mathbf{g}(\mathbf{X}, t)$. Now when

the the same entity is expressed in spatial coordinates \mathbf{x} , the time derivative becomes a little more complicated. This complication arises due to the fact that the spatial position of the particle also changes as time progresses. This means then that the time derivative must take into account 1) the change in \mathbf{g} with time when the particle remains in the same spatial position and 2) change in \mathbf{g} due to the change in the spatial position of the particle. Then using the chain rule we can express the material time derivative of the spatial entity \mathbf{g} as

$$\dot{\mathbf{g}}(\mathbf{x}, t) = \frac{\partial \mathbf{g}(\mathbf{x}, t)}{\partial t} + \frac{\partial \mathbf{g}(\mathbf{x}, t)}{\partial \mathbf{x}} \frac{\partial \varphi(\mathbf{X}, t)}{\partial t} = \frac{\partial \mathbf{g}(\mathbf{x}, t)}{\partial t} + (\nabla \mathbf{g})\mathbf{v}, \quad (2.27)$$

with the second term being the *convective derivative* of $\mathbf{g}(\mathbf{x}, t)$. With the definition of the material time derivative at hand consider the deformed tangent $\mathbf{t} = \mathbf{F}\mathbf{T}$ and its time derivative of the form $\dot{\mathbf{t}} = \dot{\mathbf{F}}\mathbf{T}$. The time derivative of the deformation gradient $\dot{\mathbf{F}}$ is termed as the *material velocity gradient*

$$\dot{\mathbf{F}} = \frac{d}{dt}[\nabla_{\mathbf{X}}\varphi(\mathbf{X}, t)] = \nabla_{\mathbf{X}} \left[\frac{d}{dt}\varphi(\mathbf{X}, t) \right] = \nabla_{\mathbf{X}}\mathbf{V}(\mathbf{X}, t). \quad (2.28)$$

The time derivative of the tangent can be expressed purely in terms of spatial objects by using the relation $\mathbf{T} = \mathbf{F}^{-1}\mathbf{t}$,

$$\dot{\mathbf{t}} = \dot{\mathbf{F}}\mathbf{F}^{-1}\mathbf{t} =: \mathbf{l}\mathbf{t}. \quad (2.29)$$

This defines the *spatial velocity gradient* \mathbf{l} that represents a spatial, mixed-variant tensor field

$$\mathbf{l} = \nabla_{\mathbf{x}}\mathbf{v} = \dot{\mathbf{F}}\mathbf{F}^{-1}. \quad (2.30)$$

From the geometrical point of view, both material and spatial velocity can be interpreted as mappings of the form,

$$\dot{\mathbf{F}} : \begin{cases} T_{\mathbf{X}}\mathcal{B} \rightarrow T_{\mathbf{x}}\mathcal{S} \\ \mathbf{T} \rightarrow \dot{\mathbf{t}} = \dot{\mathbf{F}}\mathbf{T} \end{cases} \quad \text{and} \quad \mathbf{l} : \begin{cases} T_{\mathbf{x}}\mathcal{S} \rightarrow T_{\mathbf{x}}\mathcal{S} \\ \mathbf{t} \rightarrow \dot{\mathbf{t}} = \mathbf{l}\mathbf{t} \end{cases}. \quad (2.31)$$

Lastly one more measure is commonly employed for the time derivative of spatial objects, which is the *Lie-rate* of spatial objects. The Lie-rate is an objective time rate which measures time evolution of a spatial tensor. The Lie-rate is calculated in three steps, 1) *pull-back* operation of the Eulerian object \mathbf{g} onto its material representation $\mathfrak{G} = \varphi_t^*(\mathbf{g})$ is performed, 2) time derivative of the material representation $\dot{\mathfrak{G}} = \frac{d}{dt}\mathfrak{G}$, and 3) the material time derivative is pushed forward to the current configuration $\varphi_{t*}(\dot{\mathfrak{G}})$,

$$\mathcal{L}_{\mathbf{v}}(\mathbf{g}) = \varphi_{t*} \left[\frac{d}{dt} [\varphi_t^*(\mathbf{g})] \right]. \quad (2.32)$$

Note that the Lie derivative yields a priori objective rates of tensors, i.e. they are invariant under superimposed rigid body motions.

2.1.6. Cauchy Stress Theorem and Stress Measures

Consider a part $\mathcal{P}_{\mathcal{B}} \subset \mathcal{B}$ cut off from the reference body \mathcal{B} and it's spatial counterpart $\mathcal{P}_{\mathcal{S}} \subset \mathcal{S}$, with the boundaries $\partial\mathcal{P}_{\mathcal{B}}$ and $\partial\mathcal{P}_{\mathcal{S}}$ as depicted in [Figure 2.5](#). In the Eulerian setting the traction vector $\hat{\mathbf{t}}$ acts on the surface $\partial\mathcal{P}_{\mathcal{S}}$ and represents the action of the rest

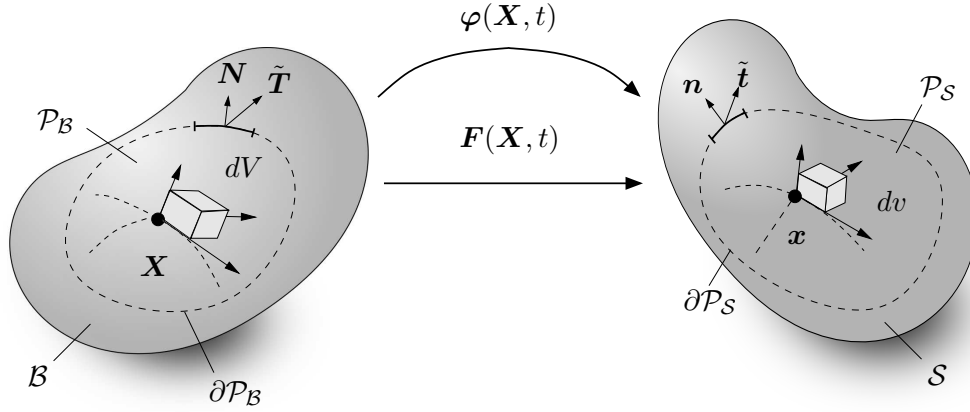


Figure 2.5: *Cauchy stress theorem and traction vectors.* The material traction vector $\tilde{\mathbf{T}}(\mathbf{X}, t, \mathbf{N})$ and its spatial counterpart $\tilde{\mathbf{t}}(\mathbf{x}, t, \mathbf{n})$ define the force acting at the vicinity of the cut (\mathcal{P}_B and \mathcal{P}_S respectively) due to the rest of the body.

of the body at the vicinity $\mathcal{P}_S \setminus \mathcal{S}$ on $\partial\mathcal{P}_S$ on $\partial\mathcal{P}_S$. The Cauchy stress theorem states that the spatial traction vector $\tilde{\mathbf{t}} \in T_x\mathcal{S}$ linearly depends on the spatial normal $\mathbf{n} \in T_x^*\mathcal{S}$ of the surface $\partial\mathcal{P}_S$, i.e.

$$\tilde{\mathbf{t}}(\mathbf{x}, t, \mathbf{n}) := \boldsymbol{\sigma}(\mathbf{x}, t)\mathbf{n}, \quad (2.33)$$

through the Cauchy (true) stress tensor $\boldsymbol{\sigma}(\mathbf{x}, t)$. In the geometrical framework outlined so far, Cauchy stress tensor can be understood as a mapping of the normals $\mathbf{n} \in T_x^*\mathcal{S}$ onto the tangent vectors $\tilde{\mathbf{t}} \in T_x\mathcal{S}$

$$\boldsymbol{\sigma} : \begin{cases} T_x^*\mathcal{S} \rightarrow T_x\mathcal{S} \\ \mathbf{n} \rightarrow \tilde{\mathbf{t}} = \boldsymbol{\sigma}\mathbf{n}. \end{cases} \quad (2.34)$$

The Cauchy stress is an Eulerian object that describes a mapping between two vector spaces. Another spatial stress measure, Kirchhoff stress tensor which is also known as the weighted Cauchy stress tensor is obtained by the scaling of the Cauchy (true) stress with the Jacobian J

$$\boldsymbol{\tau} := J\boldsymbol{\sigma} = \begin{cases} T_x^*\mathcal{S} \rightarrow T_x\mathcal{S} \\ \mathbf{n} \rightarrow \tilde{\mathbf{t}} = \boldsymbol{\tau}\mathbf{n}. \end{cases} \quad (2.35)$$

The Kirchhoff stress is more commonly used in the spatial description of stress power in terms of the spatial volume, however it maintains the geometrical properties of the Cauchy stress. Now considering force equality such that $\tilde{\mathbf{T}}dA := \tilde{\mathbf{t}}da$ the first Piola-Kirchhoff stress tensor can be defined in reference configuration by $\tilde{\mathbf{T}} = \mathbf{P}\mathbf{N}$, giving the relation $\mathbf{P}\mathbf{N}dA := \boldsymbol{\sigma}\mathbf{n}da$. Using the relation for the area map (2.15) this relation can be reformulated as

$$\mathbf{P}\mathbf{N}dA := \boldsymbol{\sigma}J\mathbf{F}^{-T}\mathbf{N}dA \rightarrow \mathbf{P} := J\boldsymbol{\sigma}\mathbf{F}^{-T} := \boldsymbol{\tau}\mathbf{F}^{-T}. \quad (2.36)$$

This gives the relation between the first Piola-Kirchhoff stress tensor and the spatial stress measures. Notice that \mathbf{P} is a two-point tensor possessing the geometrical mapping properties

$$\mathbf{P} : \begin{cases} T_{\mathbf{X}}^*\mathcal{B} \rightarrow T_x\mathcal{S} \\ \mathbf{N} \rightarrow \tilde{\mathbf{t}} = \mathbf{P}\mathbf{N}. \end{cases} \quad (2.37)$$

The first Piola-Kirchhoff stress is used for experimental investigations as it gives the relation between the current traction and the reference area element. The third fundamental

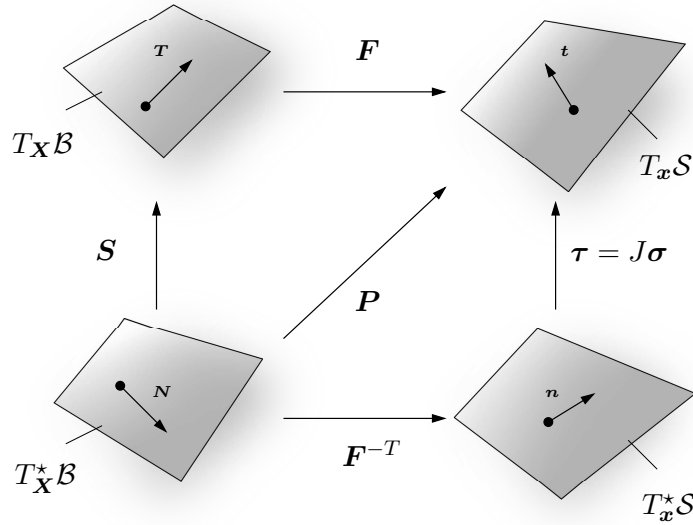


Figure 2.6: Mechanical stress tensors and the mapping in the tangent and co-tangent space. The Lagrangian second Piola-Kirchhoff stress tensor $\mathbf{S} : \mathbf{N} \rightarrow \tilde{\mathbf{T}} = \mathbf{S}\mathbf{N}$ and the Eulerian Kirchhoff stress $\boldsymbol{\tau} : \mathbf{n} \rightarrow \tilde{\mathbf{t}} = \boldsymbol{\tau}\mathbf{n}$, define the co-tangent to tangent maps respectively. The two point first Piola-Kirchhoff stress tensor $\mathbf{P} : \mathbf{N} \rightarrow \tilde{\mathbf{t}} = \mathbf{P}\mathbf{N}$, maps the Lagrangian co-tangent space to the Eulerian tangent space.

stress measure is the second Piola-Kirchhoff stress tensor \mathbf{S} defined as the mapping,

$$\mathbf{S} = \begin{cases} T_X^* \mathcal{B} \rightarrow T_X \mathcal{B} \\ \mathbf{N} \rightarrow \tilde{\mathbf{T}} = \mathbf{S}\mathbf{N}. \end{cases} \quad (2.38)$$

Incorporating the transformations introduced above, the second Piola-Kirchhoff stress tensor in terms of other stress measures can be expressed as,

$$\mathbf{S} := \boldsymbol{\varphi}^*(\mathbf{P}) = \mathbf{F}^{-1}\mathbf{P} \quad \text{and} \quad \mathbf{S} := \boldsymbol{\varphi}^*(\boldsymbol{\tau}) = \mathbf{F}^{-1}\boldsymbol{\tau}\mathbf{F}^{-T}, \quad (2.39)$$

pull-back of the two-point tensor \mathbf{P} and spatial tensor $\boldsymbol{\tau}$. The push-forward relations of reference tensor \mathbf{S} to the spatial tensors also holds true,

$$\boldsymbol{\tau} := J\boldsymbol{\sigma} = \boldsymbol{\varphi}_*(\mathbf{P}) = \mathbf{P}\mathbf{F}^T \quad \text{and} \quad \boldsymbol{\tau} = \boldsymbol{\varphi}_*(\mathbf{S}) = \mathbf{F}\mathbf{S}\mathbf{F}^T. \quad (2.40)$$

The push-forward and pull-back operations of the various stress measures are depicted in [Figure 2.6](#). Note that the Lagrangian stress tensor \mathbf{S} is a purely geometric object with no physical meaning.

2.1.7. Mechanical Power Expressions

The mechanical stress power \mathcal{P}^m per unit mass of reference configuration describes the work needed by the continuum to deform from the reference to current configuration in the time interval $[0, t]$ as

$$W := \int_{\mathcal{B}} w_0^t dV \quad \text{with} \quad w_0^t := \int_0^t \rho_0 \mathcal{P}^m d\tau, \quad (2.41)$$

with w being the work per unit reference volume. The stress power is defined as stress times the strain-rate in three different configurations introduced above. This leads to the necessity of dual stress and strain objects in respective geometric settings

$$\rho_0 \mathcal{P}^m := \underbrace{\mathbf{P} : \dot{\mathbf{F}}}_{\text{two point}} = \underbrace{\mathbf{S} : \frac{1}{2} \dot{\mathbf{C}}}_{\text{Lagrangian}} = \underbrace{\boldsymbol{\tau} : \frac{1}{2} \boldsymbol{\mathcal{L}}_v \mathbf{g}}_{\text{Eulerian}}. \quad (2.42)$$

As dual objects, one can identify in geometric setting the two-point first Piola-Kirchhoff stress \mathbf{P} and the deformation gradient \mathbf{F} . In referential setting the second Piola-Kirchhoff stress \mathbf{S} and the right Cauchy-Green tensor \mathbf{C} and in spatial setting the Kirchhoff stress $\boldsymbol{\tau}$ and the spatial metric \mathbf{g} as work conjugates. These are the basic ingredients for a constitutive modeling framework based on the second axiom of thermodynamics. Note that any constitutive model can be formulated in either of the three frameworks and can also be interchanged freely due to this geometric compatibility.

2.2. Fundamentals of Electromagnetism

Electromagnetism is a branch of physics which deals with the behavior of electric fields, magnetic fields and light. The electromagnetic force is one of the four fundamental forces of nature and the understanding of electromagnetism has broadened mankind's knowledge of the particle-wave behavior, relativistic theory, intermolecular forces and electric and magnetic behavior to name a few. Interestingly, electricity and magnetism were considered two separate forces until the publication of the work by JAMES CLARK MAXWELL [156] in 1873. Maxwell in this seminal work presented four equations which together completely describe the coupled electromagnetic phenomenon. It is important to note however that the theory and understanding of electricity and magnetism were present long before the Maxwell equations. In this section the general form of Maxwell equations are introduced to the reader.

2.2.1. Lorentz Force on a Moving Charge Particle

The basic electromagnetic fields required to describe Maxwell equations can be understood by looking at the force acting on a charged particle. Experimentally, it has been shown that the force that acts on a particular charge depends only on the position of that particular charge, on velocity of the charge and on the amount of charge. The *Lorentz force* at a position in space \mathbf{x} and time t for any given charge q is defined as,

$$\mathbb{F}(\mathbf{x}; t) = q[\mathbf{e}(\mathbf{x}; t) + \mathbf{v}(\mathbf{x}; t) \times \mathbf{b}(\mathbf{x}; t)], \quad (2.43)$$

where $\mathbf{e}(\mathbf{x}; t)$ and $\mathbf{b}(\mathbf{x}; t)$ are some electric and magnetic fields at that point and time, generated due to some external charges and currents. The charge is replaced by another *test charge* q' which is small enough to not alter the fields \mathbf{b} and \mathbf{e} such that

$$\mathbf{e}(\mathbf{x}; t) + \mathbf{v}(\mathbf{x}; t) \times \mathbf{b}(\mathbf{x}; t) = \lim_{q' \rightarrow 0} \frac{\mathbb{F}(\mathbf{x}; t)}{q'}. \quad (2.44)$$

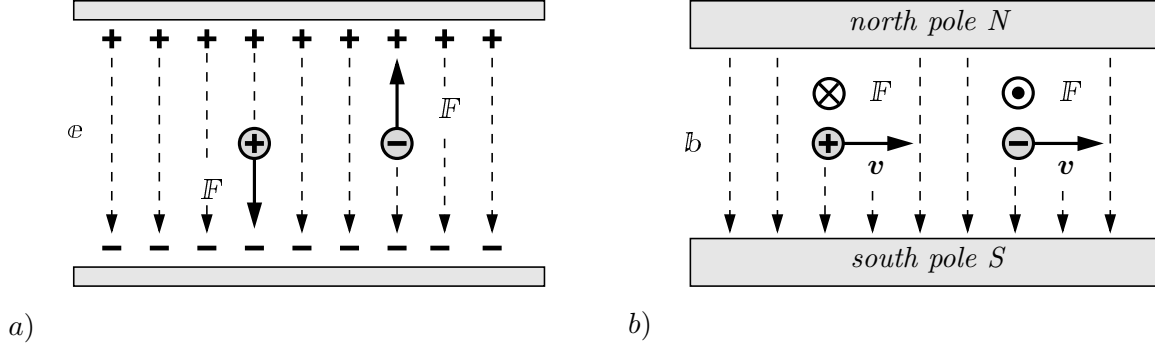


Figure 2.7: Lorentz's force acting on a moving charged particle. a) For a given electric field e , a charge q at position \mathbf{x} and time t in this field experiences an electric force proportional to the charge and the external field $\mathbb{F}(\mathbf{x}; t) = qe(\mathbf{x}; t)$. b) Similar to the electric force a charge moving with a velocity $\mathbf{v}(\mathbf{x}; t)$ in a magnetic induction field $b(\mathbf{x}; t)$ experiences a magnetic force given by $\mathbb{F}(\mathbf{x}; t) = q\mathbf{v}(\mathbf{x}; t) \times b(\mathbf{x}; t)$. The superposition principle then gives the complete electromagnetic force on a moving charge as $\mathbb{F}(\mathbf{x}; t) = q[e(\mathbf{x}; t) + \mathbf{v}(\mathbf{x}; t) \times b(\mathbf{x}; t)]$.

This gives the units of e as [N/C] or [V/m] known as the *spatial electric field* and b as [N/Am] known as the *spatial magnetic induction field*. The electric and magnetic fields satisfy the principle of superposition, such that the fields produced by individual sources (A and B) could be summed up to get the complete field at any given space and time

$$e(\mathbf{x}; t) = e(\mathbf{x}; t)_A + e(\mathbf{x}; t)_B \quad \text{and} \quad b(\mathbf{x}; t) = b(\mathbf{x}; t)_A + b(\mathbf{x}; t)_B. \quad (2.45)$$

These fields form the basic ingredients for the description of electromagnetism presented in Maxwell equations. The Lorentz force on a moving charge is depicted in Figure 2.7.

2.2.2. Gauss Law for Electricity

The first equation of Maxwell, also known as Gauss law of electric charges states that “the flux of an electric field through a closed surface is equal to the ratio of the charge enclosed by that surface and the permittivity of vacuum”. The flux of an electric field is the amount of electric field passing perpendicular to a given surface. For an infinitesimal area element $d\mathbf{a}$ shown in Figure 2.8 a) the flux can be defined as $\Phi^e = e \cdot d\mathbf{a}$. Then the flux through a closed surface $\partial\mathcal{S}$ is given in the integral as

$$\Phi^e(\mathbf{x}; t) = \int_{\partial\mathcal{S}} e(\mathbf{x}; t) \cdot d\mathbf{a}. \quad (2.46)$$

Note that the surface \mathcal{S} is any arbitrary *closed surface*. Then according to Gauss law this flux Φ^e must be proportional to the sum of charges enclosed inside the surface as

$$\Phi^e(\mathbf{x}; t) = \oint_{\partial\mathcal{S}} e(\mathbf{x}; t) \cdot d\mathbf{a} = \frac{1}{\epsilon_0} \sum_{i=1}^n q_i. \quad (2.47)$$

Electric permittivity of vacuum $\epsilon_0 = 8.854 \times 10^{-12}$ [C/Vm] is a universal constant. In the framework of continuum mechanics, it is convenient to consider a charge distribution instead of dealing with discrete charges. If the charges are distributed in \mathcal{S} with a volume density of $\rho^e(\mathbf{x})$ then the charge enclosed can be given as $q_{enc} = \int_{\mathcal{S}} \rho^e(\mathbf{x}) dv$. Substituting

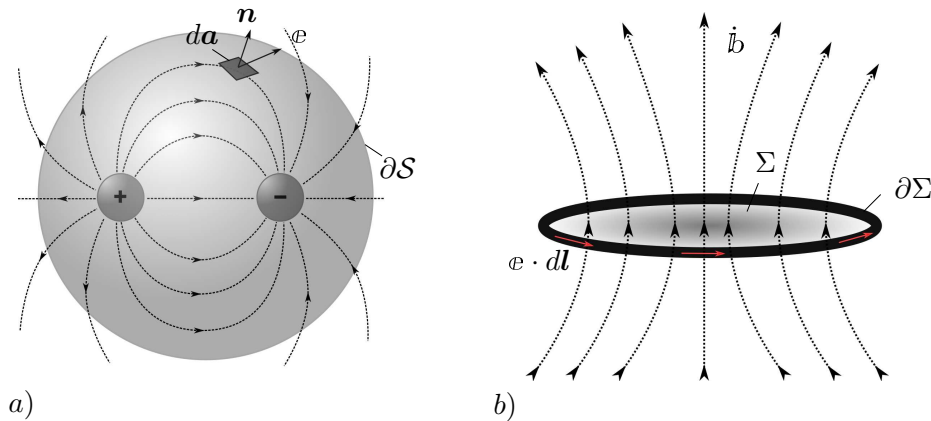


Figure 2.8: Gauss's law for electricity and the Faraday equation. a) The electric field \mathbf{e} generated by charges, with the positive charge acting as the source and negative as the sink. The electric flux Φ^e passing through the closed Gaussian surface $\partial\mathcal{S}$ is proportional to the charge enclosed. b) A changing magnetic induction \mathbf{b} through a closed loop surface Σ generates an electric field \mathbf{e} in the loop $\partial\Sigma$.

this in the above result and applying the divergence theorem gives the differential form of Gauss law as

$$\operatorname{div} \mathbf{e}(\mathbf{x}; t) = \frac{\rho^e}{\epsilon_0} \quad \text{in } \mathcal{S}. \quad (2.48)$$

2.2.3. Gauss Law for Magnetism

The second equation of Maxwell, is the Gauss law for magnetism which states that “the flux of the magnetic induction field through a closed surface is always equal to zero”. The structure of this equation is similar to the Gauss law for electricity, however as magnets always exist as a pair of North and South poles (magnetic monopoles or “magnetic charges” do not exist in nature) the right hand side of is always zero. The magnetic flux is then defined as

$$\Phi^m(\mathbf{x}) = \int_{\partial\mathcal{S}} \mathbf{b} \cdot d\mathbf{a}. \quad (2.49)$$

Proceeding as before the Gauss law for magnetism in integral and differential form are given as,

$$\Phi^m(\mathbf{x}) = \oint_{\partial\mathcal{S}} \mathbf{b}(\mathbf{x}; t) \cdot d\mathbf{a} = 0 \quad \rightarrow \quad \operatorname{div} \mathbf{b}(\mathbf{x}) = 0, \quad (2.50)$$

as visualized in [Figure 2.9 a](#)). The magnetic North and South poles act as source and sink of the magnetic induction field, which makes the flux passing through any closed surface equal to zero.

2.2.4. Maxwell Faraday Equation

The third equation of Maxwell is the so called Maxwell Faraday equation, which states that “the line integral of the electric field around a loop is equal to the time rate of the magnetic flux through the loop”. For any fixed surface Σ with a closed boundary $\partial\Sigma$,

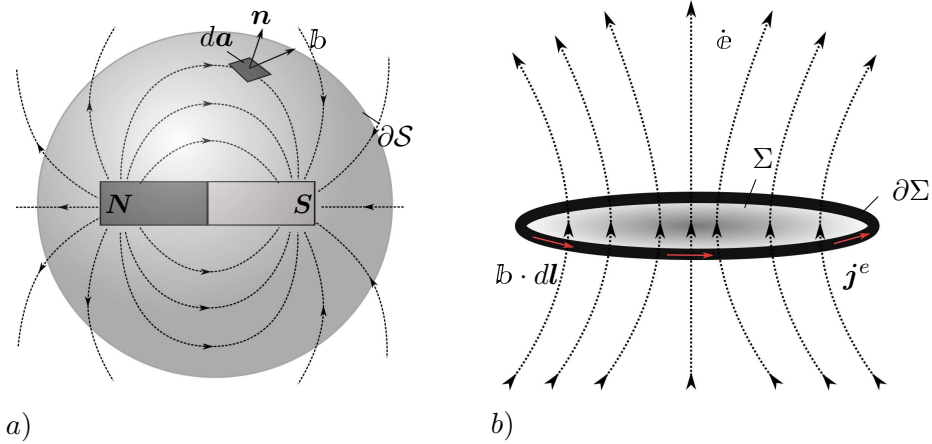


Figure 2.9: Gauss's law for magnetism and the Ampère circuital law. a) The magnetic flux Φ^m of a magnetic induction \mathbf{b} passing through the closed Gaussian surface $\partial\mathcal{B}$ is always equal to zero. b) A changing electric field \mathbf{e} through a closed loop Σ generates a magnetic induction \mathbf{b} in the loop.

shown in Figure 2.8 b) and represented as,

$$\oint_{\partial\Sigma} \mathbf{e} \cdot d\mathbf{l} = -\frac{d}{dt} \int_{\Sigma} \mathbf{b} \cdot d\mathbf{a}. \quad (2.51)$$

Applying Stokes theorem to the left hand side of the above equation the differential form of this equation can be written as,

$$\text{curl } \mathbf{e}(\mathbf{x}; t) = -\frac{\partial \mathbf{b}(\mathbf{x}; t)}{\partial t}. \quad (2.52)$$

This equation relates directly the electric and magnetic fields and shows that a changing magnetic field could produce an electric field.

2.2.5. Ampère Circuital Law

The final set of Maxwell equation relates magnetic induction \mathbf{b} to electric current density \mathbf{j}^e and electric field \mathbf{e} . It states that “the line integral of the magnetic induction around a loop is equal to the sum of the current flowing through the loop and the time rate of the electric flux through the loop”. This is expressed mathematically in integral form as

$$\oint_{\partial\Sigma} \mathbf{b} \cdot d\mathbf{l} = \mu_0 \left(\int_{\Sigma} \mathbf{j}^e \cdot d\mathbf{a} + \epsilon_0 \frac{d}{dt} \int_{\Sigma} \mathbf{e} \cdot d\mathbf{a} \right), \quad (2.53)$$

as visualized in Figure 2.9 b). Application of Stoke theorem leads us to differential form of the equation as,

$$\text{curl } \mathbf{b} = \mu_0 \left(\mathbf{j}^e + \epsilon_0 \frac{\partial \mathbf{e}}{\partial t} \right). \quad (2.54)$$

The above presented form of the Maxwell equations are valid universally as has been proved by numerous experimental observations. These equations are however quite general because the information regarding the material behavior is not included. These equations pertain rather to the complete charge ρ^e and current densities \mathbf{j}^e . A detailed discussion regarding this is presented in the next section.

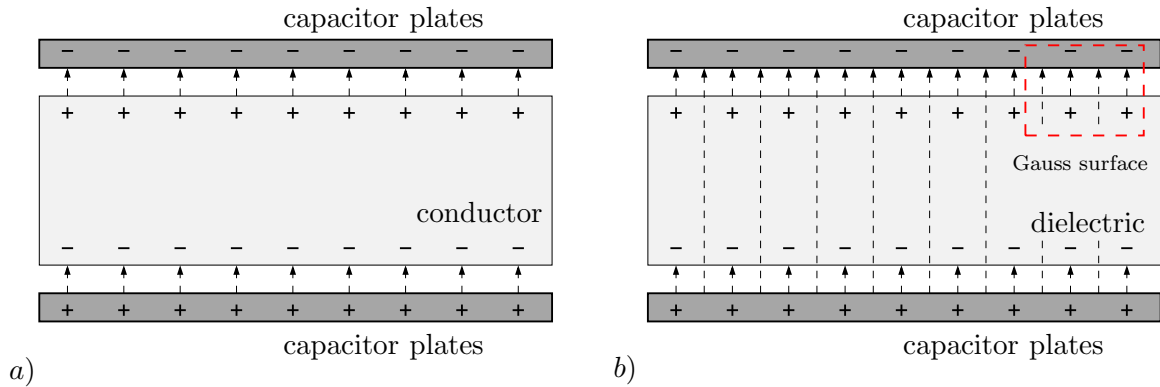


Figure 2.10: The electric field inside a parallel plate capacitor with a conductor or dielectric material inbetween the plates. a) The electric field lines for a parallel plate capacitor with a conductor inbetween is shown. The charges inside the conductor move such that the electric field inside the conductor is zero. b) The capacitance and hence the electric field of the capacitor varies due to the presence of the dielectric material. This was observed by Faraday in his experiments. Applying the Gauss’s law for electricity we see that this is not possible unless there is a charge creation inside the dielectric material. This charge is denoted by the bound charge density ρ_f^e .

2.3. Maxwell Equations in Ponderable Media

The Maxwell equations presented in the previous section are valid universally for vacuum or in ponderable media. However, application of these equations in case of dielectric or ferromagnetic materials is quite tricky due to the nature of these materials. As shown before the Maxwell equations depend on “total charge density” ρ^e and “total current density” \mathbf{j}^e , both of which are not necessarily known in case of these materials. In order to understand this a deeper understanding of these materials is required. In the following sections the behavior of these materials will be discussed reformulating the Maxwell equation and in turn introduce *polarization* and *magnetization* fields.

2.3.1. Dielectric Materials and Polarization

Dielectric materials are in general insulators, that is they are materials that do not conduct electricity. It is easy to believe that such materials do not respond to any applied electric fields. However, early experiments by Faraday showed that the capacitance of a parallel plate capacitor is increased when a dielectric material is placed between the plates. If the gap between parallel plate capacitor is completely filled by such a material, it was observed that the capacitance is increased by a factor of κ , the dielectric constant. The change of capacitance due to the dielectric means that the material essentially changes the electric field inside the parallel plates, even though the *free charges* ρ_f^e on the plates are constant. Applying the first equation of Maxwell (Gauss law for electricity) inside the dielectric only if there were some electric charges inside the dielectric material. This was an important observation that proves the existence of *bound charges* inside the dielectric material. The molecular behavior of dielectric materials plays a key role in the understanding of bound charges. [Figure 2.11](#) shows the behavior of the molecule in equilibrium and under applied electric field. As shown the atom is neutral and the electron cloud surrounding the nucleus is negatively charged. Under no applied electric field the positive and negative

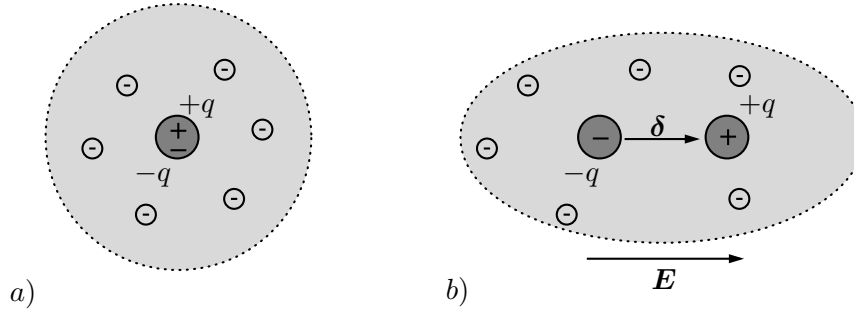


Figure 2.11: The polarization of electrically neutral dielectric atoms in an electric field. a) The positive and negative charge centers coincide in the absence of an external applied electric field. b) On application of an electric field the charge centers separate. There will be a resultant electric dipole moment $\tilde{\mathbf{p}} = q\boldsymbol{\delta}$.

charge centers coincide. However, under application of an external electric field the charge centers are separated, creating an electric dipole moment per atom. If there are N atoms per unit volume, using the principle of superposition the *polarization per unit volume* can be defined as,

$$\mathbb{P} = Nq \sum_i^N \boldsymbol{\delta}_i. \quad (2.55)$$

Note that the polarization \mathbb{P} is dependent on the electric field \mathbf{e} and is zero in the absence of the electric field¹. The bound charge density ρ_b^e inside the dielectric material and the polarization field are related as²

$$\rho_b^e = -\text{div } \mathbb{P}(\mathbf{x}; t). \quad (2.56)$$

Which states that the source and sink for polarization are the bound charges inside the material. So the total charge density that is needed in the Maxwell equations consists of the *free charges* which are given from outside the system and *bound charges* which are created in the material due to externally created field that is $\rho^e = \rho_f^e + \rho_b^e$. Using this in the first Maxwell equation (2.48),

$$\text{div} [\epsilon_0 \mathbf{e}(\mathbf{x}; t) + \mathbb{P}(\mathbf{x}; t)] = \text{div } \mathbf{d} = \rho_f^e. \quad (2.57)$$

Where the *electric displacement field* \mathbf{d} in units of [N/Vm] or [C/m²] is defined as,

$$\mathbf{d}(\mathbf{x}; t) = \epsilon_0 \mathbf{e}(\mathbf{x}; t) + \mathbb{P}(\mathbf{x}; t). \quad (2.58)$$

Such a reformulation of Maxwell equation is much more convenient as the only information required is the free charges that are prescribed on the system while the information of the bound charges are embedded in equations in terms of the polarization field $\mathbb{P}(\mathbf{x}, t)$ ³.

¹Dielectric (piezoelectric) materials have no spontaneous polarization i.e. the polarization under no electric field is zero. Ferroelectric materials however show spontaneous polarization.

²The relation of the bound charge density ρ_b^e and the polarization field \mathbb{P} can be mathematically proven FEYNMAN ET AL. [71] and dissertation work of D. ROSATO and D. ZÄH for more details. The derivation of the same has been skipped here for brevity.

³Note that the same reformulation of the Maxwell equations can be achieved even without the formal introduction of the polarization field \mathbb{P} . From a purely mathematical point of view it is a vector field created by the bound charges which can be used to explain Faraday experiments. The physical relevance of the field was identified later.

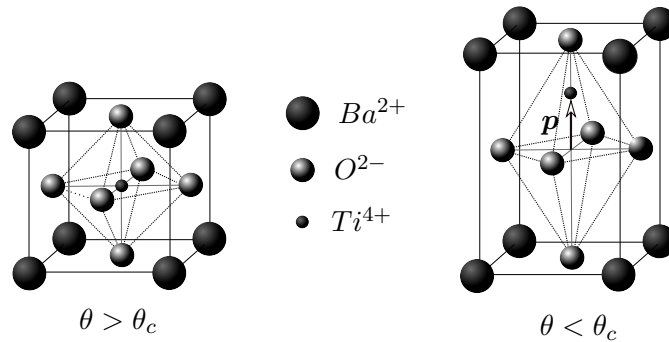


Figure 2.12: Spontaneous polarization in perovskite ferroelectric materials $BaTiO_3$ or $PbTiO_3$, below the Curie temperature. The shift of the charge centers creates spontaneous polarization which is influenced by external electric fields.

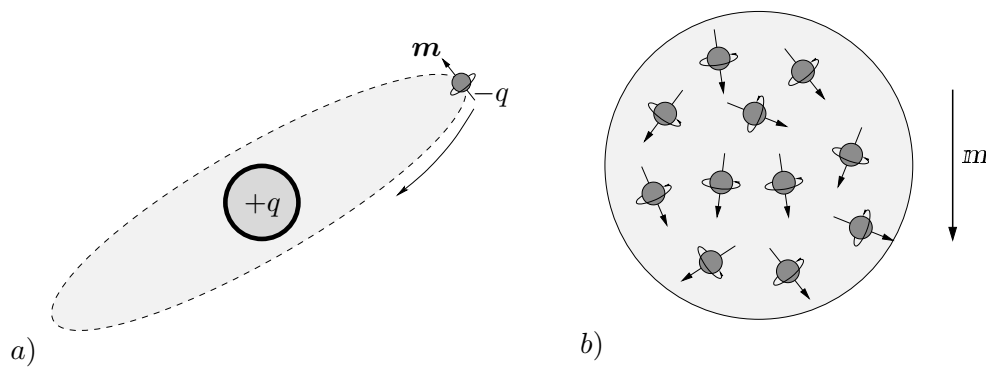


Figure 2.13: Magnetization in atoms and average magnetization. Spin and orbital motion of the valence electrons creates magnetization in the atoms of some transition elements. In ferromagnetic materials neighboring magnetization show tendency to align parallel to each other.

The polarization field \mathcal{P} , depends on electric field e . For simplicity a linear relation can be assumed such that

$$\mathcal{P} = (1 + \chi)\epsilon_0 e = \epsilon e. \quad (2.59)$$

Where ϵ is the permittivity of dielectric material and χ is the electric susceptibility. Such a formulation of polarization and electric field is used to model the electric behavior of dielectric materials in a linear theory. It has to be noted however that this is a linear approximation of the electromechanical behavior of dielectric materials and such approximation is valid only under small applied fields and for linear dielectrics. Ferroelectric materials are a special class of dielectrics that show spontaneous polarization and a non-linear polarization distribution as show in Figure 2.12. The spontaneous polarization in these materials occur due to the centers of positive and negative charges not coinciding under a certain temperature, known as the Curie temperature. The electromechanical description of these materials has to consider polarization as an independent variable.

2.3.2. Ferromagnetic Materials and Magnetization

To understand the origins of magnetization in magnetic materials, the concept of *charge conservation* has to be understood. The charge conservation equation is a direct corollary of the fourth Maxwell equation. Since a curl field is divergence free (2.48) and (2.54) can

be rewritten as,

$$\operatorname{div}[\operatorname{curl} \mathbf{b}] = \mu_0 \operatorname{div} \left[\mathbf{j}^e + \epsilon_0 \frac{\partial \mathbf{e}}{\partial t} \right] = 0 \rightarrow \operatorname{div} \mathbf{j}^e + \frac{\partial \rho^e}{\partial t} = 0. \quad (2.60)$$

The charge conservation states that for a closed isolated system the total charge is always conserved. The charge in a system consists of bound and free charges, $\rho^e = \rho_b^e + \rho_f^e$. This can be rewritten with (2.56) as,

$$\operatorname{div} \mathbf{j}^e - \frac{\partial \operatorname{div} \mathbf{p}}{\partial t} - \operatorname{div} \mathbf{j}_f^e = 0 \quad \text{with} \quad \operatorname{div} \mathbf{j}_f^e = -\frac{\partial \rho_f^e}{\partial t}. \quad (2.61)$$

Where the corollary that the source of free current density \mathbf{j}_f^e is the change in the free charge density ρ_f^e has been used. This equation can be satisfied assuming $\mathbf{j}_b^e = \mathbf{j}^e - \mathbf{j}_f^e = \frac{\partial \mathbf{p}}{\partial t}$, which means that the bound current density in a ponderable media is the change in the polarization in the material. It is important to note however that since a curl field is divergence free, (2.61) can also be satisfied by assuming

$$\mathbf{j}^e - \mathbf{j}_f^e = \frac{\partial \mathbf{p}}{\partial t} + \operatorname{curl} \mathbf{m}, \quad (2.62)$$

for any vector field $\mathbf{m}(\mathbf{x}, t)$. This vector term points to an additional contribution to the current inside the material in addition to polarization field. It was however unclear at the time of this discovery if this additional contribution had any physical motivation⁴. It was shown by EINSTEIN & DE HAAS [62] through the *Einstein-de Haas effect* that this additional contribution does indeed exist. It was found to arise in some materials due to their atomic structure. As shown in Figure 2.13 the electrons orbiting around the nucleus and revolving around it's axis are essentially moving charges (currents) which create magnetic fields. In most elements these quantum effects are negligible and the curl \mathbf{m} contribution to current density can be dropped on the continuum scale. However, some elements specifically transition elements Iron, Nickel, Cobalt and some of their alloys show what is called ferromagnetism due to specific energy difference in their electron valence orbits⁵. Due to their specific atomic structure, the valence electrons have a net magnetic moment. Calculating the atomic moment of each atom or molecule is extremely tedious. However, in an average sense the magnetization \mathbf{m} per unit volume of the material can be defined which gives the property of the material to react to applied magnetic fields⁶.

$$\operatorname{curl} \mathbf{b} = \mu_0 \left(\frac{\partial \mathbf{p}}{\partial t} + \operatorname{curl} \mathbf{m} + \mathbf{j}_f^e + \epsilon_0 \frac{\partial \mathbf{e}}{\partial t} \right). \quad (2.63)$$

⁴It is interesting to note that the vector field \mathbf{m} could also be introduced (mathematically) similar to the polarization by assuming $\rho_b^m = -\operatorname{div} \mathbf{m}$, where ρ_b^m are the "bound magnetic charges". Such a mathematical formulation would give analogous equations to the electric case. However, such magnetic charges (monopoles) have not been observed in nature and hence such an assumption is physically not feasible

⁵The focus of this work is on ferromagnetic materials, which show spontaneous magnetization with neighboring magnetizations tending to align parallel to each other due to energy requirements. In general, there are also diamagnetic, paramagnetic, ferrimagnetic and antiferromagnetic materials that naturally occur in nature and show varied magnetic properties.

⁶Note that in later chapters the magnetization per unit mass is denoted by the symbol \mathbf{m} while the magnetization director is represented by $\mathbf{m} \in \mathcal{S}^{d-1}$. The magnetization per unit mass is related to the magnetization director as $\mathbf{m} = m_s \mathbf{m}$, where m_s is a material constant. For ease of reading the symbol \mathbf{m} here is used for the magnetization per unit mass.

$$\operatorname{curl} \mathbf{h} = \mathbf{j}_f^e + \frac{\partial \mathbf{d}}{\partial t}. \quad (2.64)$$

$$\mathbf{h}(\mathbf{x}; t) = \frac{\mathbf{b}(\mathbf{x}; t)}{\mu_0} - \mathbf{m}(\mathbf{x}; t), \quad (2.65)$$

in terms of the spatial magnetic field \mathbf{h} with units of [A/m]. With the introduction of *polarization* and *magnetization* fields, the Maxwell equations for a general ponderable media can be rewritten in the form,

$$\begin{aligned} \text{Gauss law for electric charges} & \quad \operatorname{div} \mathbf{d}(\mathbf{x}; t) = \rho_f^e \\ \text{Gauss law for magnetism} & \quad \operatorname{div} \mathbf{b}(\mathbf{x}; t) = 0 \\ \text{Maxwell-Faraday equation} & \quad \operatorname{curl} \mathbf{e}(\mathbf{x}; t) = -\frac{\partial \mathbf{b}(\mathbf{x}; t)}{\partial t} \\ \text{Ampère's circuital law} & \quad \operatorname{curl} \mathbf{h} = \mathbf{j}_f^e + \frac{\partial \mathbf{d}}{\partial t} \end{aligned} \quad (2.66)$$

along with the constitutive definitions,

$$\begin{aligned} \text{Electric constitutive law} & \quad \mathbf{d}(\mathbf{x}, t) = \epsilon_0 \mathbf{e} + \mathbf{p} \\ \text{Magnetic constitutive law} & \quad \mathbf{b}(\mathbf{x}, t) = \mu_0 (\mathbf{h} + \mathbf{m}). \end{aligned} \quad (2.67)$$

These equations represent a more generalized setting, with the prescribed free charges ρ_f^e and the free current density \mathbf{j}_f^e .

2.3.3. Special Case of Electro-Magneto-Statics

The Maxwell equations presented in (2.67) are a set of partial differential equations which are used for the description of classical electromagnetism, optics and electrical circuits. The solutions of these equations are however in general quite time consuming and complicated. In this work the focus is on understanding the *material behavior* of electro- and magneto-mechanically coupled materials. A rather straight forward simplification to the Maxwell equations is to assume the absence of *time-varying effects* called the *static case*. Under this assumption, all of the terms in the Maxwell equations which are time derivatives of the fields are zero. This assumption is valid for low frequency applications (electric and magnetic fields do not change rapidly) considered in this work. In addition, no external current is provided into the system such that the free current density $\mathbf{j}_f^e = 0$. In such a case, equations (2.67) can then be rewritten in the form,

Electrostatics	$\operatorname{div} \mathbf{d}(\mathbf{x}; t) = \rho_f^e$	(2.68)
	$\operatorname{curl} \mathbf{e}(\mathbf{x}; t) = \mathbf{0}$ with	
Magnetostatics	$\operatorname{div} \mathbf{b}(\mathbf{x}; t) = 0$	
	$\operatorname{curl} \mathbf{h} = \mathbf{0}$ with	

yielding the pull-back of the Eulerian electric displacement field to the Lagrangian configuration as

$$\mathbb{D} = J\mathbf{F}^{-1}d \rightarrow \tilde{d} = Jd = \mathbf{F}\mathbb{D}. \quad (2.71)$$

Which is a typical inverse Piola transformation. A similar relationship for the Lagrangian magnetic induction field can be derived from (2.69)₄ as,

$$\mathbb{B} = J\mathbf{F}^{-1}b \rightarrow \tilde{b} = Jb = \mathbf{F}\mathbb{B}. \quad (2.72)$$

Now following the second equation of electrostatics (2.69)₂ for the Lagrangian description of the electric field using (2.10),

$$\oint_{\partial\Sigma} e(\mathbf{x}; t) \cdot d\mathbf{l} = \oint_{\partial\tilde{\Sigma}} e(\mathbf{x}; t) \cdot \mathbf{F}d\mathbf{L} = \oint_{\partial\tilde{\Sigma}} \mathbb{E}(\mathbf{x}; t) \cdot d\mathbf{L}, \quad (2.73)$$

which gives the pull back of the Eulerian electric field to Lagrangian configuration as

$$\mathbb{E} = \mathbf{F}^T e \rightarrow e = \mathbf{F}^{-T} \mathbb{E}. \quad (2.74)$$

Analogous to the electric field the transformation of the magnetic field can be defined as

$$\mathbb{H} = \mathbf{F}^T h \rightarrow h = \mathbf{F}^{-T} \mathbb{H}. \quad (2.75)$$

$$\int_S \rho_b^e dV = \int_{\partial S} \mathbb{P} \cdot d\mathbf{a} = \int_{\partial B} \mathbb{P} \cdot J\mathbf{F}^{-T} d\mathbf{A} = \int_{\partial B} \mathbb{P} \cdot d\mathbf{A}. \quad (2.76)$$

$$\mathbb{P} = J\mathbf{F}^{-1}p \rightarrow \tilde{p} = Jp = \mathbf{F}\mathbb{P}. \quad (2.77)$$

Following this geometric interpretation the definition of polarization needs to be modified as $\mathbb{P} = d - \epsilon_0 \mathbf{g}^{-1}e$ and in the Lagrangian setting as $\mathbb{P} = \mathbb{D} - \epsilon_0 J\mathbf{C}^{-1}\mathbb{E}$. Similarly for the magnetization mapping can be defined as

$$\mathbb{M} = J\mathbf{F}^{-1}m \rightarrow \tilde{m} = Jm = \mathbf{F}\mathbb{M}. \quad (2.78)$$

The geometric interpretations of the fields are depicted in Figure 2.14 and the magnetization field redefined as $m = b/\mu_0 - \mathbf{g}^{-1}h$ and $\mathbb{M} = \mathbb{B}/\mu_0 - J\mathbf{C}^{-1}\mathbb{H}$ in the Eulerian and Lagrangian setting respectively.

2.3.5. Boundary Conditions at Interfaces Between Materials

Consider a material interface where the respective materials 1 and 2 have varied electromagnetic properties as $\{e_i, d_i\}_{i=1,2}$ and $\{h_i, B_i\}_{i=1,2}$. Applying the curl equation of magnetostatics (2.69)₅ and electrostatics (2.69)₂ at such an interface the tangential boundary conditions can be derived as

$$(e_2 - e_1) \times \mathbf{n} = \mathbf{0} \quad \text{and} \quad (h_2 - h_1) \times \mathbf{n} = \mathbf{0}. \quad (2.79)$$

The normal jump conditions can be derived by Gauss law for electro- (2.69)₁ and magnetostatics (2.69)₄ as,

$$(d_2 - d_1) \cdot \mathbf{n} = \sigma_f^e \quad \text{and} \quad (b_2 - b_1) \cdot \mathbf{n} = 0. \quad (2.80)$$

Coupled Anisotropic Electromechanical Fracture

3.1. Fundamental Definition of Fracture in Solids

From a continuum mechanics perspective fracture in a body \mathcal{B} can be defined as a cut or a crack that essentially results in two opposite *crack surfaces* which may result in jumps in mechanical displacement field (and other primary fields) in between these surfaces. The relative motion of these opposite crack surfaces is often used to distinguish the crack opening. The crack opening modes depend on the loading direction in relation to the orientation of the crack surfaces. The different crack modes are depicted in [Figure 3.1](#). These crack opening modes are essentially local and are valid for the entire body only under special circumstances. However, a general crack opening can be described as a combination of the three failure modes. Solids can undergo in general brittle or ductile fracture. Brittle fracture is a phenomenon where fracture occurs without any prior plastic deformation while ductile fracture occurs after appreciable plastic deformation. This work focuses on fracture phenomena in piezoelectric materials which undergo brittle fracture.

3.1.1. Griffith Energetic Fracture Approach

The behavior of the crack is influenced by the jumps of the primary fields in the vicinity of the crack tip. Irwin in 1957, investigated these concentrations near the crack tip and introduced the *stress intensity factors* IRWIN [104, 105, 106], which form the basis of several crack criteria till date. These stress intensity factors however are dependent on the geometry of the body, crack, loading and material parameters. Griffith on the other hand, introduced the idea of the so-called *energy release rate* GRIFFITH [84, 83] for brittle materials in 1920. According to this theory, as soon as a critical energy release rate is reached, failure occurs. This critical value of the energy release rate is, in contrast to the stress intensity factors, independent of the geometry of the body. It is essentially a material property and can thus be treated as a material parameter. Griffith's theory can be interpreted as a *global approach* to fracture mechanics based on the balance of energy, where the critical energy release rate indicates the energy needed for the formation of the two crack surfaces. The first principle of thermodynamics states that the internal power

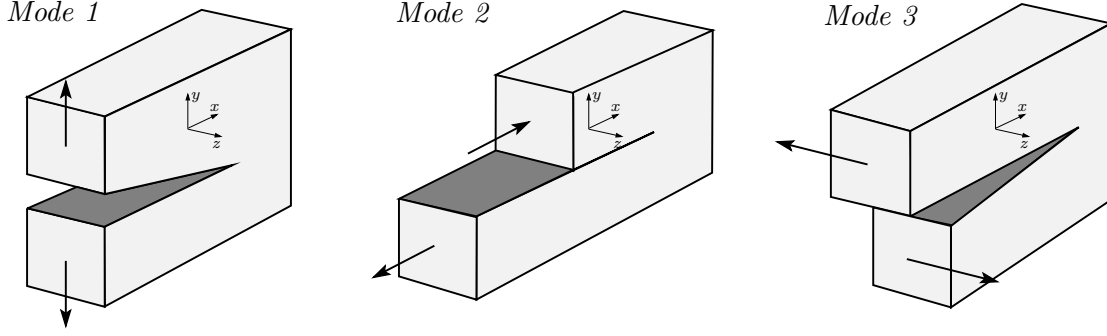


Figure 3.1: Various crack opening modes of brittle fracture in solids. *Mode 1* crack: Opening mode symmetric to the $\{x, z\}$ -plane. *Mode 2* crack: relative displacement of crack surfaces in x -direction. *Mode 3* crack: relative displacement of crack surfaces in z -direction. In general, fracture in brittle materials is a combination of these fracture modes.

$P_{int} = \mathcal{E} + \mathcal{K} + \mathcal{D}$, equals the power due to external loading $P_{ext} = \mathcal{P} + \mathcal{Q}$ i.e.

$$\mathcal{E} + \mathcal{K} + \mathcal{D} = \mathcal{P} + \mathcal{Q}, \quad (3.1)$$

where the rate of internal energy \mathcal{E} , rate of kinetic energy \mathcal{K} and dissipation \mathcal{D} constitute internal power contributions. The external loading contributions are considered via \mathcal{P} and thermal contribution through \mathcal{Q} . For a simple isothermal, quasi-static problem kinetic contribution \mathcal{K} can be neglected and external loading P_{ext} , represents the energy supply due to only mechanical loads

$$\mathcal{P} = P_{ext} = \int_{\mathcal{B}} \bar{\gamma} \cdot \dot{\mathbf{u}} \, dV + \int_{\partial \mathcal{B}_t} \bar{\mathbf{t}} \cdot \dot{\mathbf{u}} \, dA, \quad (3.2)$$

in terms of the body force per unit volume $\bar{\gamma}$ and the traction forces $\bar{\mathbf{t}}$. The rate of the internal energy \mathcal{E} is generally defined in terms of an energy function per unit volume ψ as

$$\mathcal{E} = \int_{\mathcal{B}} \rho \dot{\psi} \, dV. \quad (3.3)$$

The dissipation \mathcal{D} describes the energy dissipation during crack propagation in the solid. This dissipation can be related to the newly created crack surfaces A and material constant γ

$$\mathcal{D} = 2\gamma A. \quad (3.4)$$

For an elastic material under conservative loading, the rate of internal energy can be related to an internal potential $\mathcal{E} = \dot{\Pi}^{int}$ and the external loading may be related to the rate of a negative external potential $\mathcal{P} = -\dot{\Pi}^{ext}$ which decreases with the external power. Insertion into (3.1) yields,

$$-\dot{\Pi}^{ext} = \dot{\Pi}^{int} + \mathcal{D}. \quad (3.5)$$

For crack propagation between time t_1 and t_2 with a crack surface area A_1 and A_2 the energy difference is

$$-(\Pi_2^{ext} - \Pi_1^{ext}) = \Pi_2^{int} - \Pi_1^{int} + 2\gamma(A_2 - A_1). \quad (3.6)$$

With the relation $\Delta A = A_2 - A_1$ and summing up the internal potential and external potentials $\Pi = \Pi_{ext} + \Pi_{int}$, the energy balance can be rewritten as

$$-\frac{\Delta \Pi}{\Delta A} = \frac{\Delta \mathcal{D}}{\Delta A} = 2\gamma. \quad (3.7)$$

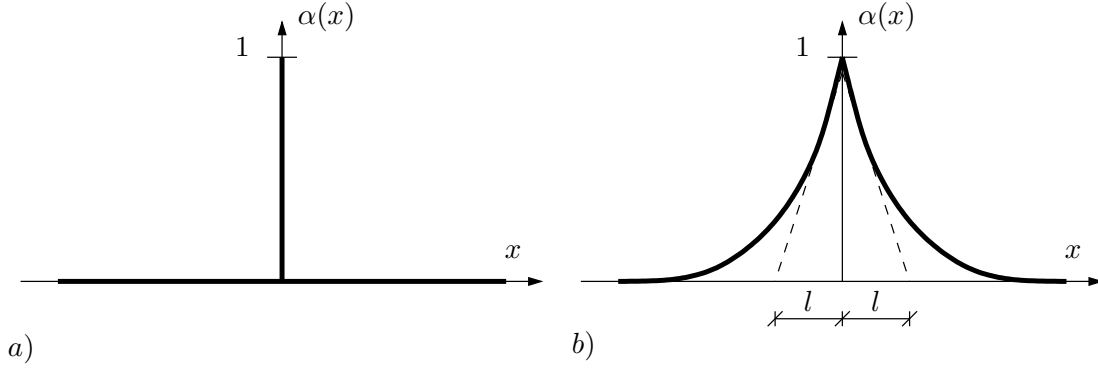


Figure 3.2: *Sharp crack topology and diffuse crack modeling approach.* a) sharp crack at $x = 0$ and b) diffusive crack at $x = 0$ modeled with the length scale l in terms of the crack phase field α . The phase field α represents intact material for $\alpha = 0$ and damaged body for $\alpha = 1$.

The energy required for crack propagation is represented by the left hand side of (3.7). The right hand side is the energy needed for crack propagation. The crack propagation occurs when the available energy equals the critical energy such that for an infinitesimal crack growth

$$G = g_c = 2\gamma = -\frac{d\Pi}{dA}. \quad (3.8)$$

The critical energy release rate g_c is a material parameter which corresponds to the energy needed for crack propagation. A detailed review regarding the same is given in SCHÄNZEL [208], HOFACKER [93].

3.1.2. Geometric Crack in a 1-D Bar

Mathematically and numerically describing of a sharp crack topology is not straight forward. The traditional Griffith's approach with sharp crack is unable to predict crack initiation, crack kinking and nonlinear crack paths. A *diffuse approach* to describe the sharp crack overcomes these drawbacks. The theory of fracture and crack propagation in a diffuse setting was developed by AMBROSIO & TORTORELLI [8], AMBROSIO ET AL. [9], BOURDIN ET AL. [27, 29] and later by MIEHE ET AL. [172]. The auxiliary *crack phase-field* $\alpha \in [0, 1]$ is introduced to model such a smooth transition. To motivate this approach an infinite bar with $L = [-\infty, \infty]$ and cross-section Γ such that $\mathcal{B} = \Gamma \times L$ is considered. If a crack exists at position $x = 0 \in L$, then a sharp crack can be written in terms of the crack phase-field α as,

$$\alpha(x) := \begin{cases} 1 & \text{for } x = 0 \\ 0 & \text{otherwise} \end{cases}, \quad (3.9)$$

where the crack phase-field approximates the unbroken material for $\alpha = 0$ and a fully broken material for $\alpha = 1$ as shown in Figure 3.2. From a continuum approach the crack can be approximated by an exponential function of the form,

$$\alpha(x) = \exp(-|x|/l) \quad \text{with} \quad \alpha(0) = 1 \quad \text{and} \quad \alpha(\pm\infty) = 0. \quad (3.10)$$

The exponential function smears the non-smooth crack by a regularized diffuse crack topology as shown in Figure 3.2. The length scale parameter l controls the approximation,

with $l \rightarrow 0$ representing the sharp crack topology. The exponential formulation (3.10) can be interpreted as a solution of the variational principle

$$\alpha = \arg \left\{ \inf_{\alpha \in \mathcal{W}} \Gamma_l(\alpha) \right\} \quad \text{with} \quad \mathcal{W} = \{ \alpha \mid \alpha(0) = 1, \alpha(\pm\infty) = 0 \}, \quad (3.11)$$

in terms of the crack functional and the crack phase-field α

$$\Gamma_l(\alpha) = \frac{1}{2l} \int_{\mathcal{B}} \{ \alpha^2 + l^2 \alpha'^2 \} dV. \quad (3.12)$$

With α' representing the spatial gradient of the phase-field α .

3.1.3. Phase-Field Approximation of Anisotropic Crack Topology

The idea of representing a sharp crack in a diffuse manner can be extended to a multi-dimensional setting following the framework presented above (MIEHE ET AL. [172, 173]). Consider $\mathcal{B} \subset \mathcal{R}^d$ represent the material body with dimension $d \in [1, 2, 3]$ in space and $\partial\mathcal{B} \subset \mathcal{R}^{d-1}$ its surface. Then for time $\mathcal{T} \in \mathcal{R}_+$ consider the crack phase-field as

$$\alpha : \begin{cases} \mathcal{B} \times \mathcal{T} \rightarrow [0, 1] \\ (\mathbf{x}, t) \mapsto \alpha(\mathbf{x}, t) \end{cases}, \quad (3.13)$$

defined in the solid \mathcal{B} . Then the regularized crack functional (3.12) reads

$$\Gamma_l(\alpha) = \int_{\mathcal{B}} \gamma_l(\alpha, \nabla\alpha) dV, \quad (3.14)$$

with the *crack surface density functional* per unit volume of the body defined as

$$\gamma_l(\alpha, \nabla\alpha) = \frac{1}{2l} \alpha^2 + \frac{l}{2} \nabla\alpha \cdot \nabla\alpha. \quad (3.15)$$

The crack surface density functional depends on the phase-field α and its spatial gradient $\nabla\alpha$. It is pivotal in the modeling of crack propagation. However, this representation is restricted to isotropic solids. In order to account for anisotropic effects the crack density function needs to be extended. Recently TEICHTMEISTER ET AL. [235] proposed the extension of such a functional to the case of anisotropic crack propagation. The first order anisotropic crack density function can be considered as

$$\gamma_l(\alpha, \nabla\alpha; \mathbf{A}) = \frac{1}{2l} \alpha^2 + \frac{l}{2} \nabla\alpha \cdot \mathbf{A} \cdot \nabla\alpha, \quad (3.16)$$

where \mathbf{A} is a generic second order structural tensor, that characterizes the anisotropic microstructure of the material. Note that the choice $\mathbf{A} = \mathbf{1} := \delta_{ij} \mathbf{e}_i \otimes \mathbf{e}_j$, recovers the isotropic function (3.15). For a transversely isotropic microstructure the tensor \mathbf{A} can be defined as,

$$\mathbf{A} := \mathbf{1} + \beta \mathbf{M} \quad \text{with} \quad \mathbf{M} := \mathbf{a} \otimes \mathbf{a}. \quad (3.17)$$

Here \mathbf{a} is a given structural director with $\|\mathbf{a}\| = 1$ and β is the anisotropy constant. A detailed summary of anisotropic formulations for orthotropic and cubic along with higher order formulations is discussed in the work TEICHTMEISTER ET AL. [235].

For a given anisotropic sharp crack $\Gamma(t) \subset \mathcal{B}$ inside a solid \mathcal{B} at time t , analogous to the

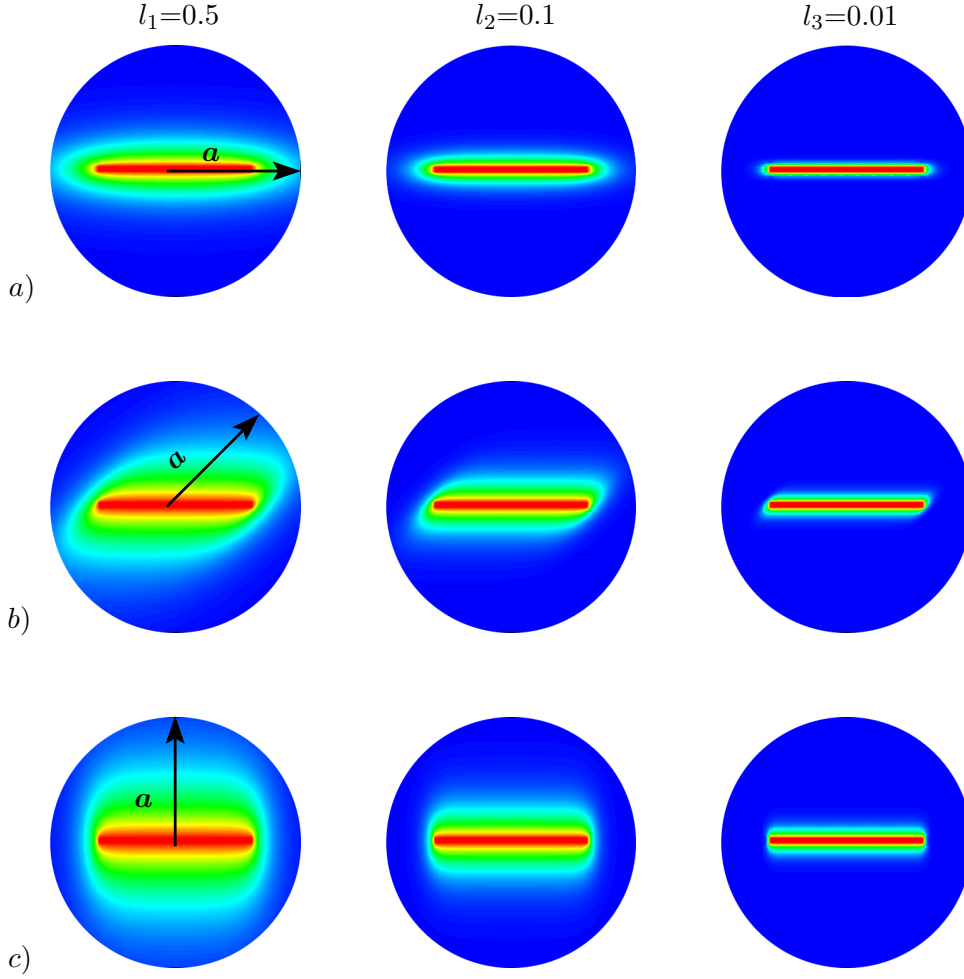


Figure 3.3: Anisotropic approximation of diffuse crack topology for various length scales. Solutions of the minimization principle (3.18) of diffuse crack topology for a transversely isotropic body \mathcal{B} with a pre-given sharp crack Γ . Crack phase field distribution for different length scales $l_1 > l_2 > l_3$ and different orientations of the structural director a) $\theta = 0^\circ$, b) $\theta = 45^\circ$ and c) $\theta = 90^\circ$, with respect to the horizontal axis. All computations done with anisotropy parameter $\beta = 5.0$.

one-dimensional case the regularized crack phase-field $\alpha(\mathbf{x}, t)$ can be obtained from the minimization principle of diffuse crack topology,

$$\alpha(\mathbf{x}, t) = \arg \left\{ \inf_{\alpha \in \mathcal{W}_{\Gamma(t)}} \Gamma_l(\alpha) \right\} \quad \text{with} \quad \mathcal{W}_{\Gamma(t)} = \{ \alpha \mid \alpha = 1 \text{ at } \mathbf{x} \in \Gamma(t) \}. \quad (3.18)$$

For the crack surface density function (3.16) formulated in terms of the second order structural tensor \mathbf{A} , the variational principle (3.18) yields the Euler equations,

$$\alpha - l^2 \operatorname{div}[\mathbf{A} \nabla \alpha] = 0 \text{ in } \mathcal{B} \quad \text{and} \quad [\mathbf{A} \nabla \alpha] \cdot \mathbf{n} = 0 \text{ on } \partial \mathcal{B}. \quad (3.19)$$

To ensure positive definiteness of the structural tensor and ensure elliptic partial differential equations the anisotropy parameter must satisfy $\beta > -1$. The standard finite element interpolations of the variational principle (3.18) is done and the results are plotted in Figure 3.4.

3.2. Coupled Electromechanical Fracture in Piezoelectrics

For a general electromechanical body \mathcal{B} undergoing fracture under the influence of mechanical and electrical loads the concept of energy release rate introduced in [Subsection 3.1.1](#) has to be revisited. The internal energy \mathcal{E} defined previously can for such a case be split

$$\mathcal{E} = \mathcal{E}^m + \mathcal{E}^{el}, \quad (3.20)$$

into a mechanical part \mathcal{E}^m and an electrical part \mathcal{E}^{el} . Similarly the external electric and mechanical loading could be identified such that

$$P_{ext} = P^m + P^{el}, \quad P^m = \int_{\mathcal{B}} \bar{\gamma} \cdot \dot{\mathbf{u}} dV + \int_{\partial\mathcal{B}_t} \bar{\mathbf{t}} \cdot \dot{\mathbf{u}} dA \quad \text{and} \quad P^{el} = \int_{\partial\mathcal{B}_q} q \dot{\phi} dA, \quad (3.21)$$

where q is the externally provided surface charge to the body and ϕ is the electric potential. With these definitions at hand [\(3.7\)](#) can be reformulated as

$$G = G^m + G^{el} = -\frac{d\Pi^m}{dA} - \frac{d\Pi^{el}}{dA} = 2\gamma. \quad (3.22)$$

Theoretical calculations of the mechanical G^m and electrical energy G^{el} release rates has been done in literature PARK & SUN [191], FANG ET AL. [70], McMEEKING [160] and SCHNEIDER [209]. It has been shown that the electrical energy release rate is negative and theoretically predicts an excessive increase in fracture toughness for applied electrical fields. Such a total energy release rate not only overestimates the fracture toughness but also fails to capture the asymmetry for positive and negative fields seen in experiments. A more detailed discussion regarding the same will be provided in [Chapter 6](#).

3.2.1. Crack Face Electrical Boundary Conditions

One of the important aspects of electromechanical fracture is to define the electrical nature of the crack opening itself. The behavior of electric field in the damage-zone is of critical importance and can starkly vary the fracture behavior. The different electrical crack conditions considered in literature are presented below.

Permeable crack boundary conditions. For small deformations, the crack can be modeled as an idealized slit, such that the deformed and undeformed configurations are the same. The crack faces are considered to be closed and the crack should not be able to perturb the electrical fields. This approach can be traced back to the work of PARTON [192]. Physically this means that the jumps in both the electric potential and normal component of the electric displacement across the crack are zero such that

$$\Delta\mathcal{D}_n = \mathcal{D}_n^+ - \mathcal{D}_n^- = 0, \quad \text{with} \quad \mathcal{D}_n^+ = \mathcal{D}_n^- \neq 0, \quad (3.23)$$

where, + and - are the upper and lower crack faces and index n represents the component normal to the crack face. This case of the boundary conditions is visualized in [Figure 3.4 a\)](#) and b) on the right most side. It can be mathematically realized by taking the permittivity of the crack same as the piezo material $\epsilon_s = \epsilon_c$ such that the crack gap has no influence on the electrical field.

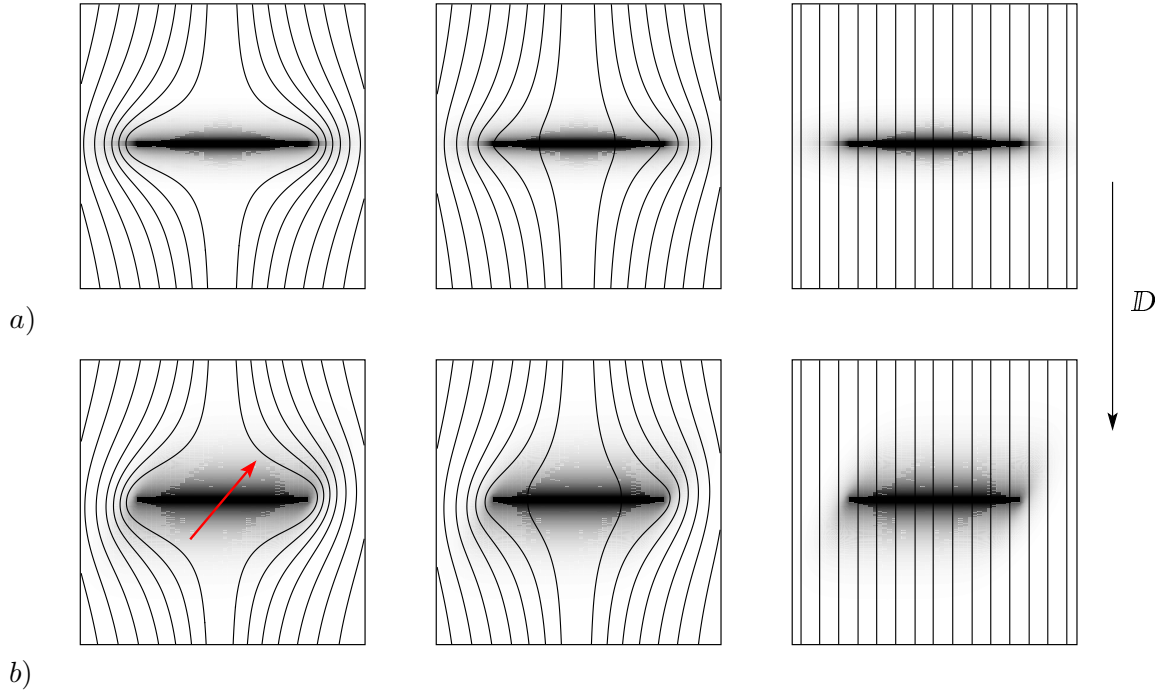


Figure 3.4: *Solutions of the electric field for various crack boundary conditions.* The behavior of the electric field around a diffuse crack is shown for an isotropic crack *a)* and an anisotropic crack *b)* (anisotropy direction indicated by red arrow). Different crack electrical conditions impermeable, semi-permeable and permeable are shown. For the impermeable case the electric field does not penetrate the crack and for the permeable case the crack is completely penetrated by the electric field with the semi-permeable case lying in-between these two extreme cases. The affect of fracture anisotropy on the field distribution is clearly visible.

Impermeable crack boundary conditions. The permeable crack model is limited in its description of electrical crack conditions as it has to be considered that if a crack propagation occurs in an electromechanical solid, the crack will actually be open and hence the medium inside the crack gap will be able to support electric fields and electric displacements. DEEG [51] and PAK [188], argued that electromechanical materials of interest have much higher permittivity than free space and in that case the permittivity of the crack gap can be approximated to zero. Such an approach was considered in SUO ET AL. [230], GAO ET AL. [77] and MIEHE ET AL. [172]. Physically this means that the normal component of the electric displacement on the crack faces must be zero,

$$\Delta \mathcal{D}_n = \mathcal{D}_n^+ - \mathcal{D}_n^- = 0, . \quad (3.24)$$

Figure 3.4 a) and b), left most plots show the field distribution for an impermeable notch where $\epsilon_s \gg \epsilon_c = 0$. The field lines circumvent the crack and also the crack anisotropy affects the field distribution.

Semi-permeable crack boundary conditions. The permeable and impermeable boundary conditions can be considered as extreme cases. In order to address the fact that cracks are actually open and that electrical fields can permeate inside the crack gap, TIAN-HU & ZI-YUAN [236]) introduced electrical boundary conditions that treat the crack faces as parallel plate capacitors. The idea is to consider that the crack gap behaves like a linear

dielectric material with a permittivity $\epsilon_s \neq \epsilon_c$. This can be written as,

$$\mathbb{D}_n^+ = \mathbb{D}_n^- = \mathbb{D}_c = \epsilon_c \mathbb{E}_c = -\epsilon_c \frac{\Delta\phi}{\Delta u_n}, \quad (3.25)$$

where \mathbb{D}_c and \mathbb{E}_c are the normal components of the electric displacement and field supported by the crack gap, $\Delta\phi$ is the potential drop across the crack faces and Δu_n is the crack opening displacement. The electric permittivity of the crack ϵ_c is of a material that fills the crack gap when it is opened, in most cases this can be identified by the permittivity of free space taken to be 8.854×10^{-12} C/Vm. A semi-permeable crack is visualized in Figure 3.4 a) and b), center plots. It has to be noted that the permeable, impermeable and semi-permeable crack conditions in addition also assume mechanical traction free conditions on the crack faces. However, it has been shown in recent works by MCMEEKING [161] and later by the work of LANDIS [144] that crack faces under the influence of electric fields develop mechanical traction force, which need to be accounted for. These tractions arise due to the Maxwell stresses developed inside the crack gap under influence of the electric field. It is trivial to point out the influence of Maxwell tractions developed in a static crack penetrated by electric field, which essentially behaves like a capacitor plate. However, while considering crack propagation in piezoelectric ceramics specifically, that undergo instantaneous *brittle fracture*, the influence of the Maxwell tractions in the post-critical regime might not have significant influence (SCHNEIDER [209]). The focus of this work is to set up the constitutive modeling framework for anisotropic crack propagation in the context of electromechanical crack propagation. In this context, a small strain formulation is set up neglecting the nonlinear Maxwell tractions inside the crack gap, which can be accounted for in later investigations.

— Part II —

**Variational Phase-Field Approach to
Micro-Magneto-Mechanics: Small
Strain Homogenization and Finite
Deformation Modeling**

Variational Homogenization of Micro-Magneto-Elasticity at Small Strains

Ferromagnetic materials are characterized by a heterogeneous microstructure that can be altered by external magnetic and/or mechanical stimuli. The macroscopic response of the ferromagnetic material results from complex magnetomechanical interactions that occur on microscopic length scales, which are mainly driven by magnetization reorientation and the associated domain wall motions. In this chapter the macroscopic response of these materials is directly based on the description of micromagnetic domain evolution. This is realized by the incorporation of ferromagnetic phase field formulation with the magnetization order parameter into a macroscopic Boltzmann type continuum through a computational homogenization framework. The micro-macro transition conditions are obtained through rate-type and incremental variational principles, which automatically incorporate an extended version of the classical Hill-Mandel macro-homogeneity condition. An efficient operator-split method is introduced to account for unity constraint on the magnetization order parameter. Two- and three-dimensional problems showcase the capability of the framework to capture nonlinear hysteresis response of such materials. Traditional ferromagnetic materials like iron, nickel, cobalt and even *giant magnetostrictive materials* like Terfenol-D, generally show only small deformations (a few per mille). Due to this the homogenization framework presented here is in *small strain setting*. This section is motivated and follows the work presented in SRIDHAR ET AL. [227].

4.1. Variational Formulation of Macroscopic Response

Consider $\bar{\mathcal{B}} \subset \bar{\mathcal{V}}$ as a macroscopic body embedded into a free space box $\bar{\mathcal{V}} \subset \mathcal{R}^d$ with dimension $d \in [2, 3]$ as depicted in Figure 4.1. The body is assumed to undergo quasistatic, magnetomechanical coupled external loading in the time interval $\bar{\mathcal{T}} \subset \mathcal{R}_+$. In this two-scale homogenization framework, macroscopic quantities are denoted by $(\bar{\cdot})$ with $\bar{\nabla}(\bar{\cdot}) := \partial_{\bar{\mathbf{x}}}(\bar{\cdot})$ and $(\dot{\bar{\cdot}}) := \partial_t(\bar{\cdot})$ denote the gradient and the time derivative of the macroscopic fields, respectively.

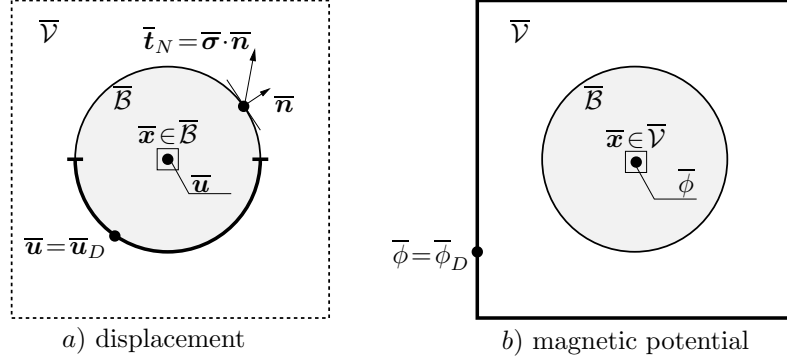


Figure 4.1: Macroscopic magnetomechanically coupled boundary value problem of a magnetic body embedded in a free space box. a) Mechanical displacement field $\bar{\mathbf{u}}$ defined in the solid $\bar{\mathcal{B}} \subset \bar{\mathcal{V}}$ and b) scalar magnetic potential $\bar{\phi}$ defined on the full free space box $\bar{\mathcal{V}} \subset \mathcal{R}^d$. The boundary of the body decomposes into Dirichlet and Neumann boundaries such that $\partial\bar{\mathcal{B}} = \partial\bar{\mathcal{B}}_{\bar{\mathbf{u}}} \cup \partial\bar{\mathcal{B}}_{\bar{\mathbf{t}}}$. The boundary $\partial\bar{\mathcal{V}}$ of the free space box is a pure Dirichlet boundary that allows the definition of applied magnetic fields.

4.1.1. Introduction of Macroscopic Fields

The primary variables of the coupled magnetomechanical boundary value problem are *displacement field* $\bar{\mathbf{u}}$ and *magnetic potential* $\bar{\phi}$ visualized in Figure 4.1 of the material point $\bar{\mathbf{x}} \in \bar{\mathcal{V}}$ at time $t \in \bar{\mathcal{T}}$ given by

$$\bar{\mathbf{u}} : \begin{cases} \bar{\mathcal{B}} \times \bar{\mathcal{T}} \rightarrow \mathcal{R}^d \\ (\bar{\mathbf{x}}, t) \mapsto \bar{\mathbf{u}}(\bar{\mathbf{x}}, t) \end{cases} \quad \text{and} \quad \bar{\phi} : \begin{cases} \bar{\mathcal{V}} \times \bar{\mathcal{T}} \rightarrow \mathcal{R} \\ (\bar{\mathbf{x}}, t) \mapsto \bar{\phi}(\bar{\mathbf{x}}, t) \end{cases}. \quad (4.1)$$

The primary fields $\bar{\mathbf{u}}$ and $\bar{\phi}$ define the macroscopic displacement gradient and the magnetic field through their first gradients as

$$\bar{\mathbf{f}} := \bar{\nabla} \bar{\mathbf{u}} \quad \text{and} \quad \bar{\mathbf{H}} = -\bar{\nabla} \bar{\phi}. \quad (4.2)$$

The definition of these primary fields automatically satisfy the *deformation compatibility* condition $\text{curl}[\bar{\mathbf{f}}] = \mathbf{0}$ in $\bar{\mathcal{B}}$ and the third Maxwell's equation, $\text{curl}[\bar{\mathbf{H}}] = \mathbf{0}$ in $\bar{\mathcal{V}}$. The symmetric part of the displacement gradient defines the small strain tensor

$$\bar{\boldsymbol{\varepsilon}} = \bar{\nabla}_s \bar{\mathbf{u}} = \frac{1}{2} (\bar{\nabla} \bar{\mathbf{u}} + \bar{\nabla}^T \bar{\mathbf{u}}). \quad (4.3)$$

As mentioned previously the strains are assumed to be small, i.e. $|\bar{\nabla} \bar{\mathbf{u}}| < \epsilon$ with $\epsilon \approx 0$. In contrast, the norm of the gradient of the magnetic potential $|\bar{\nabla} \bar{\phi}|$ is not bounded. Note that the magnetization field that governs the microscopic domain evolution is defined only on the micro level.

4.1.2. Rate-type Variational Formulation of Macroscopic Response

The evolution of macroscopic mechanical displacement and magnetic potential fields, defined in (6.21) can be formulated in terms of a *rate-type variational principle*

$$\{\dot{\bar{\mathbf{u}}}, \dot{\bar{\phi}}\} = \arg \left\{ \inf_{\dot{\bar{\mathbf{u}}} \in \bar{\mathbb{W}}_{\bar{\mathbf{u}}}} \sup_{\dot{\bar{\phi}} \in \bar{\mathbb{W}}_{\bar{\phi}}} \int_{\bar{\mathcal{V}}} \bar{w}(\dot{\bar{\boldsymbol{\varepsilon}}}, \dot{\bar{\mathbf{H}}}) dV - \bar{P}_{\text{mech}}(\dot{\bar{\mathbf{u}}}) \right\} \quad (4.4)$$

The variational principle is a saddle point principle due to the scalar magnetic potential chosen as the primary field. The *macroscopic potential density functional* \bar{w} defines the energy storage in the material and the external mechanical loading contribution \bar{P}_{mech} accounts for external loads. Together they govern the evolution of the macroscopic variables. Note that the *macroscopic potential density* \bar{w} is obtained by *homogenization* of the *microscopic potential density* considered in the subsequent [Section 4.3](#). The admissible space for the evolution of displacement and magnetic potential fields are defined as

$$\bar{\mathcal{W}}_{\dot{\mathbf{u}}} := \{\dot{\mathbf{u}} \in \mathcal{R}^d \mid \dot{\mathbf{u}} = \dot{\mathbf{u}}_D \text{ on } \partial\bar{\mathcal{B}}_{\dot{\mathbf{u}}}\} \quad \text{and} \quad \bar{\mathcal{W}}_{\dot{\phi}} := \{\dot{\phi} \in \mathcal{R} \mid \dot{\phi} = \dot{\phi}_D \text{ on } \partial\bar{\mathcal{V}}\}. \quad (4.5)$$

The Dirichlet condition for the magnetic potential on the surface $\partial\bar{\mathcal{V}}$ of a suitable free space box $\bar{\mathcal{V}}$, allows for definition of far field magnetic fields in an FE² context, see [Figure 4.1](#). The external mechanical loading contribution defined on the body \mathcal{B} is given as

$$\bar{P}_{mech}(\dot{\mathbf{u}}) = \int_{\bar{\mathcal{B}}} \bar{\boldsymbol{\gamma}} \cdot \dot{\mathbf{u}} dV + \int_{\partial\bar{\mathcal{B}}_{\dot{\mathbf{t}}}} \bar{\mathbf{t}}_N \cdot \dot{\mathbf{u}} dA, \quad (4.6)$$

where $\bar{\boldsymbol{\gamma}}$ is the macroscopic body force per unit volume and $\bar{\mathbf{t}}_N$ are the prescribed tractions. The first variation of the rate-type variational principle (4.4) gives,

$$- \int_{\bar{\mathcal{B}}} (\overline{\text{div}}[\partial_{\bar{\boldsymbol{\varepsilon}}}\bar{w}] + \bar{\boldsymbol{\gamma}}) \cdot \delta\dot{\mathbf{u}} dV + \int_{\partial\bar{\mathcal{B}}_{\dot{\mathbf{t}}}} (\partial_{\bar{\boldsymbol{\varepsilon}}}\bar{w} \cdot \bar{\mathbf{n}} - \bar{\mathbf{t}}_N) \cdot \delta\dot{\mathbf{u}} dA - \int_{\bar{\mathcal{V}}} \overline{\text{div}}[-\partial_{\bar{\mathbf{H}}}\bar{w}] \delta\dot{\phi} dV = 0, \quad (4.7)$$

where $\bar{\mathbf{n}}$ is the outward normal depicted in [Figure 4.1](#). This in turn results in the Euler-Lagrange equations on the macro-scale as

$$\overline{\text{div}}[\partial_{\bar{\boldsymbol{\varepsilon}}}\bar{w}] + \bar{\boldsymbol{\gamma}} = \mathbf{0} \text{ in } \bar{\mathcal{B}} \quad \text{and} \quad \overline{\text{div}}[-\partial_{\bar{\mathbf{H}}}\bar{w}] = 0 \text{ in } \bar{\mathcal{V}}, \quad (4.8)$$

along with the mechanical Neumann-type boundary conditions $\partial_{\bar{\boldsymbol{\varepsilon}}}\bar{w} \cdot \bar{\mathbf{n}} = \bar{\mathbf{t}}_N$ on $\partial\bar{\mathcal{B}}_{\dot{\mathbf{t}}}$ and $\partial_{\bar{\mathbf{H}}}\bar{w} \cdot \bar{\mathbf{n}} = 0$ on $\partial\bar{\mathcal{B}}_{\bar{\mathbf{H}}}$. With this the macroscopic mechanical stresses and the magnetic induction fields can be identified as

$$\bar{\boldsymbol{\sigma}} = \partial_{\bar{\boldsymbol{\varepsilon}}}\bar{w}(\bar{\boldsymbol{\varepsilon}}, \bar{\mathbf{H}}) \quad \text{and} \quad \bar{\mathbf{B}} = -\partial_{\bar{\mathbf{H}}}\bar{w}(\bar{\boldsymbol{\varepsilon}}, \bar{\mathbf{H}}), \quad (4.9)$$

governed by the macroscopic potential \bar{w} obtained by the homogenization of the microstructure as commented on in [Section 4.3](#).

4.1.3. Macroscopic Incremental Variational Formulation

In the numerical setting, a time discretization of the *rate-type* variational principle presented above has to be considered in a typical time step $[t_n, t_{n+1}]$ with step length $\tau = t_{n+1} - t_n > 0$. For conciseness, the subscript t_{n+1} is dropped for all variables evaluated at time t_{n+1} . With the fields known at time t_n , the update problem for the macro-fields at the current time t_{n+1} is defined by the *incremental variational principle* as

$$\{\bar{\mathbf{u}}, \bar{\phi}\} = \arg \left\{ \inf_{\bar{\mathbf{u}} \in \bar{\mathcal{W}}_{\bar{\mathbf{u}}}} \sup_{\bar{\phi} \in \bar{\mathcal{W}}_{\bar{\phi}}} \int_{\bar{\mathcal{V}}} \bar{w}^\tau(\bar{\boldsymbol{\varepsilon}}, \bar{\mathbf{H}}) dV - \bar{P}_{mech}(\bar{\mathbf{u}} - \bar{\mathbf{u}}_n) \right\}. \quad (4.10)$$

which is presented in terms of the time discrete *incremental macroscopic potential density* \bar{w}^τ obtained from the continuous potential \bar{w} by a time integration algorithm of the form

$$\bar{w}^\tau(\bar{\boldsymbol{\varepsilon}}, \bar{\mathbb{H}}) := ALGO \left\{ \int_{t_n}^t \bar{w}(\dot{\bar{\boldsymbol{\varepsilon}}}, \dot{\bar{\mathbb{H}}}) dt \right\}. \quad (4.11)$$

The admissible space for the mechanical displacement and magnetic potential fields follow directly from (4.5)

$$\bar{\mathcal{W}}_{\bar{\mathbf{u}}} := \{\bar{\mathbf{u}} \in \mathcal{R}^d \mid \bar{\mathbf{u}} = \bar{\mathbf{u}}_D \text{ on } \partial\bar{\mathcal{B}}_{\bar{\mathbf{u}}}\} \quad \text{and} \quad \bar{\mathcal{W}}_{\bar{\phi}} := \{\bar{\phi} \in \mathcal{R} \mid \bar{\phi} = \bar{\phi}_D \text{ on } \partial\bar{\mathcal{B}}_{\bar{\phi}}\}. \quad (4.12)$$

Variation of the incremental principle (4.10) in turn gives the time discrete Euler-Lagrange equations

$$\text{div}[\partial_{\bar{\boldsymbol{\varepsilon}}}\bar{w}^\tau] + \bar{\boldsymbol{\gamma}} = \mathbf{0} \text{ in } \bar{\mathcal{B}} \quad \text{and} \quad \text{div}[-\partial_{\bar{\mathbb{H}}}\bar{w}^\tau] = 0 \text{ in } \bar{\mathcal{B}}, \quad (4.13)$$

along with the Neumann-type boundary conditions $\bar{\boldsymbol{\sigma}} \cdot \bar{\mathbf{n}} = \bar{\mathbf{t}}_N$ on $\partial\bar{\mathcal{B}}_{\bar{\mathbf{t}}}$ and $\bar{\mathbb{B}} \cdot \mathbf{n} = 0$ on $\partial\bar{\mathcal{V}}_{\bar{\mathbb{B}}}$. The time discrete macroscopic stresses and magnetic induction fields obtained as

$$\bar{\boldsymbol{\sigma}} = \partial_{\bar{\boldsymbol{\varepsilon}}}\bar{w}^\tau(\bar{\boldsymbol{\varepsilon}}, \bar{\mathbb{H}}) \quad \text{and} \quad \bar{\mathbb{B}} = -\partial_{\bar{\mathbb{H}}}\bar{w}^\tau(\bar{\boldsymbol{\varepsilon}}, \bar{\mathbb{H}}) \quad (4.14)$$

from the derivative of the incremental potential \bar{w}^τ defined in (4.11).

4.1.4. Space-Time Discrete Incremental Variational Principle

The spatial discretization of the incremental principle by a finite element method is given in terms of a set of primary state variables, $\bar{\boldsymbol{\varepsilon}} := \{\bar{\nabla}_s \bar{\mathbf{u}}, -\bar{\nabla} \bar{\phi}\}$. For the space discretization a finite element interpolation $\bar{\boldsymbol{\varepsilon}}^h$ of the full free space region $\bar{\mathcal{V}}$ with \bar{N}^h global nodes has to be considered. The primary state vectors are approximated via the interpolations $\bar{\boldsymbol{\varepsilon}}^h$

$$\bar{\boldsymbol{\varepsilon}}^h = \bar{\boldsymbol{\mathfrak{B}}}(\bar{\boldsymbol{x}})\bar{\boldsymbol{\delta}} \quad \text{with} \quad \bar{\boldsymbol{\delta}} := \mathbf{A}_{\bar{I}=1}^{\bar{N}^h} [\bar{\mathbf{u}}_{\bar{I}}, -\bar{\phi}_{\bar{I}}]^T. \quad (4.15)$$

In terms of the macroscopic *nodal variable vector* $\bar{\boldsymbol{\delta}}$, which contains the displacement and magnetic potential at a typical nodal point of the finite element mesh. The *strain-displacement* vector $\bar{\boldsymbol{\mathfrak{B}}}$ approximates the first gradients of the primary fields. Considering a pure Dirichlet problem with $\bar{P}_{mech} = 0$, the discrete stationary principle can be written as

$$\bar{\boldsymbol{\delta}} = \arg \left\{ \text{stat}_{\bar{\boldsymbol{\delta}}} \int_{\bar{\mathcal{V}}} \bar{w}^\tau(\bar{\boldsymbol{\mathfrak{B}}}\bar{\boldsymbol{\delta}}) dV \right\}. \quad (4.16)$$

The space-time discrete variational principle determines the macroscopic nodal values at current time t_{n+1} governed by the macro-potential \bar{w}^τ . Considering the non linear nature of the coupled problem a Newton Raphson method with updates $\bar{\boldsymbol{\delta}} \leftarrow \bar{\boldsymbol{\delta}} - \bar{\boldsymbol{\mathfrak{K}}}^{-1}\bar{\boldsymbol{\mathfrak{R}}}$ based on the residual and tangent arrays is implemented as

$$\bar{\boldsymbol{\mathfrak{R}}} := \int_{\bar{\mathcal{V}}} \bar{\boldsymbol{\mathfrak{B}}}^T [\partial_{\bar{\boldsymbol{\varepsilon}}}\bar{w}^\tau] dV \quad \text{and} \quad \bar{\boldsymbol{\mathfrak{K}}} := \int_{\bar{\mathcal{V}}} \bar{\boldsymbol{\mathfrak{B}}}^T [\partial_{\bar{\boldsymbol{\varepsilon}}\bar{\boldsymbol{\varepsilon}}}\bar{w}^\tau] \bar{\boldsymbol{\mathfrak{B}}} dV \quad (4.17)$$

until convergence $|\bar{\boldsymbol{\mathfrak{R}}}| < tol$. The macro-array $\bar{\boldsymbol{\mathfrak{S}}} := \partial_{\bar{\boldsymbol{\varepsilon}}}\bar{w}^\tau$ contains the current homogenized stresses $\bar{\boldsymbol{\sigma}}$ and the homogenized field $\bar{\mathbb{B}}$ as introduced in (4.14) defined by the *volume averages* defined in (4.55). Similarly the macroscopic tangent moduli $\bar{\boldsymbol{\mathfrak{T}}} := \partial_{\bar{\boldsymbol{\varepsilon}}\bar{\boldsymbol{\varepsilon}}}\bar{w}^\tau$ for the

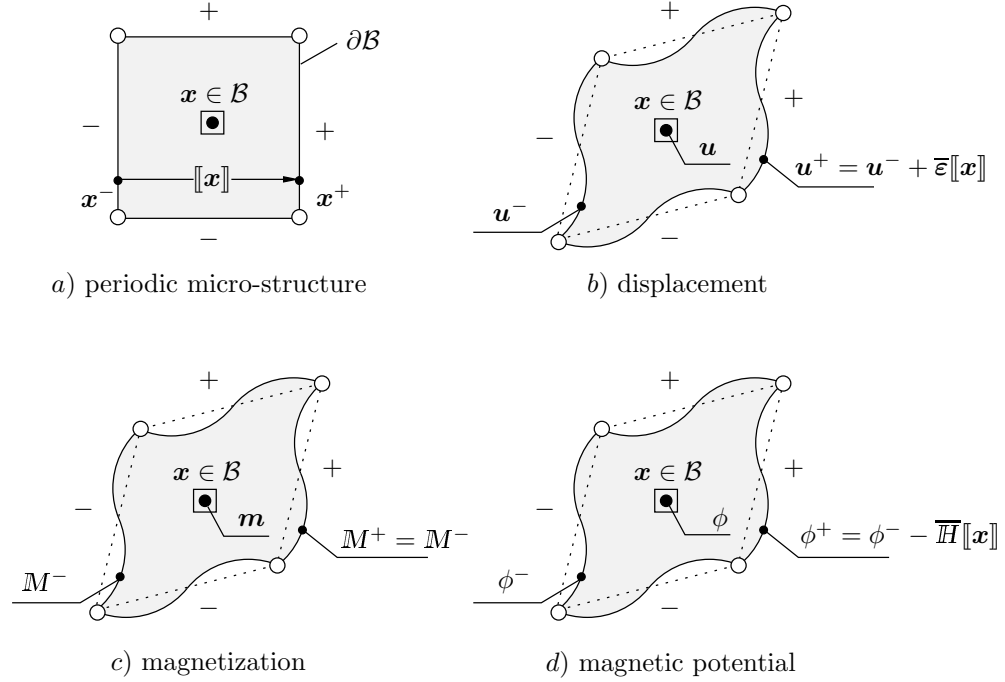


Figure 4.2: Deformation of a periodic micro-structure \mathcal{B} for a three field formulation of the microstructure. a) Points on the opposite faces '+' and '-' with $\mathbf{x}^+ \in \partial\mathcal{B}^+$ and $\mathbf{x}^- \in \partial\mathcal{B}^-$. Periodic boundary conditions for b) the displacement $\mathbf{u}^+ = \mathbf{u}^- + \bar{\boldsymbol{\varepsilon}}[[\mathbf{x}]]$, c) the magnetization $\mathbb{M}^+ = \mathbb{M}^-$ and d) the magnetic potential $\phi^+ = \phi^- - \bar{\mathbf{H}}[[\mathbf{x}]]$, driven by the macroscopic strain $\bar{\boldsymbol{\varepsilon}}$ and magnetic field $\bar{\mathbf{H}}$. Note that contrary to the mechanical displacement and the magnetic potential, the order parameter \mathbb{M} has no macroscopic conjugate.

coupled problem is specified by the volume average as (4.56). The above procedure provides a variational principle based FE² scenario in micro-magneto-mechanics, in line with that outlined in (MIEHE [164]) for dissipative problems in mechanics. The symmetry of the tangent matrix $\bar{\mathcal{K}}$ is induced by the proposed multi-scale variational principles. Note that in this work only a single material point is considered on the macroscale and not the whole continuum considering the computational cost. The focus of this work is on the material behavior of the coupled magnetomechanical coupled behavior.

4.2. Variational Homogenization of Micro-Magneto-Elasticity

On the microscale let $\mathcal{B} \subset \mathcal{R}^d$ denote a periodic microstructure with dimension $d \in [2, 3]$ as depicted in Figure 4.2. Similar to the macroscopic case $\nabla(\cdot) := \partial_{\mathbf{x}}(\cdot)$ and $\dot{(\cdot)} := \partial_t(\cdot)$ denote the gradient and the time derivative of the *microscopic fields* (\cdot) , respectively.

4.2.1. Introduction of Microscopic Fields

The microscopic material response is modeled by a dissipative continuum formulation with the magnetization acting as an order parameter similar to (MIEHE ET AL. [176], ZÄH & MIEHE [258]) in micro-electro-mechanics and (MIEHE & ETHIRAJ [168] and ETHIRAJ, SRIDHAR & MIEHE [69]) in micro-magneto-mechanics. Similar to these works a three field formulation incorporates the primary fields as displacement, magnetic potential and

magnetization unit director

$$\mathbf{u} : \begin{cases} \mathcal{B} \times \mathcal{T} \rightarrow \mathcal{R}^d \\ (\mathbf{x}, t) \mapsto \mathbf{u}(\mathbf{x}, t) \end{cases} \quad \phi : \begin{cases} \mathcal{B} \times \mathcal{T} \rightarrow \mathcal{R} \\ (\mathbf{x}, t) \mapsto \phi(\mathbf{x}, t) \end{cases} \quad \mathbf{M} : \begin{cases} \mathcal{B} \times \mathcal{T} \rightarrow \mathcal{S}^{d-1} \\ (\mathbf{x}, t) \mapsto \mathbf{M}(\mathbf{x}, t) \end{cases}. \quad (4.18)$$

Similar to the macroscopic response the gradients of the fields \mathbf{u} and ϕ define the displacement gradient and the magnetic field

$$\mathbf{f} := \nabla \mathbf{u} \quad \text{and} \quad \mathbb{H} := -\nabla \phi. \quad (4.19)$$

An objective constitutive state depends on the symmetric part of the displacement gradient

$$\boldsymbol{\varepsilon} = \nabla_s \mathbf{u} = \frac{1}{2} [\nabla \mathbf{u} + \nabla^T \mathbf{u}]. \quad (4.20)$$

Again the strains are assumed to be small, i.e. $|\nabla \mathbf{u}| < \epsilon$ is bounded by a small number ϵ . In contrast, the norm of the gradients of the magnetization vector $|\nabla \mathbf{M}|$ and the magnetic potential $|\nabla \phi|$ are not bounded. The magnetization director \mathbf{M} defines the magnetization as

$$\mathbf{M} = m_s \mathbf{M}, \quad (4.21)$$

where the material constant m_s is the spontaneous magnetization of the solid under consideration. Note that the magnetization director in the micromagnetic framework is constrained by the geometric condition

$$\|\mathbf{M}\| = 1, \quad (4.22)$$

which restricts the order parameter \mathbf{M} to the unit sphere \mathcal{S}^{d-1} . This property has to be considered consistently in the subsequent theoretical and computational formulation.

4.2.2. Microscopic Rate-Type Variational Principle of Homogenization

To determine the macroscopic potential density \bar{w} , a *rate-type variational principle of homogenization* is proposed. On the microscale the time evolution of the magnetization is a dissipative process which needs to be accounted for. In a rate dependent setting, the macroscopic potential density \bar{w} is defined by

$$\bar{w}(\dot{\boldsymbol{\varepsilon}}, \dot{\mathbb{H}}) = \inf_{\dot{\mathbf{u}} \in \mathcal{W}_{\dot{\mathbf{u}}}} \sup_{\dot{\phi} \in \mathcal{W}_{\dot{\phi}}} \inf_{\dot{\mathbf{M}} \in \mathcal{W}_{\dot{\mathbf{M}}}} \frac{1}{|\mathcal{B}|} \int_{\mathcal{B}} w(\dot{\boldsymbol{\varepsilon}}, \dot{\mathbb{H}}, \dot{\mathbf{M}}, \nabla \dot{\mathbf{M}}) dV. \quad (4.23)$$

The macroscopic rate-type variational potential is the volume average of a microscopic rate-type potential density w , that takes into account the *energy storage* and the *dissipative mechanisms* of the micro-material and is defined as

$$\underbrace{w(\dot{\boldsymbol{\varepsilon}}, \dot{\mathbb{H}}, \dot{\mathbf{M}}, \nabla \dot{\mathbf{M}})}_{\text{potential density}} = \underbrace{\frac{d}{dt} \Psi(\boldsymbol{\varepsilon}, \mathbb{H}, \mathbf{M}, \nabla \mathbf{M})}_{\text{rate of energy function}} + \underbrace{d(\dot{\mathbf{M}})}_{\text{dissipation potential}}. \quad (4.24)$$

The potential density is defined by the rate of the Gibbs energy function Ψ and the dissipation function d . Note that the microstructure is considered to be periodic such

that the material response is driven by the macroscopic strains $\bar{\boldsymbol{\varepsilon}}$ and the macroscopic magnetic field $\bar{\mathbf{H}}$. The admissible fields on the microstructure are then given by

$$\mathcal{W}_{\dot{\mathbf{u}}} := \{\dot{\mathbf{u}} \in \mathcal{R}^d \mid \llbracket \dot{\mathbf{u}} \rrbracket = \dot{\bar{\boldsymbol{\varepsilon}}}[\mathbf{x}] \text{ on } \partial\mathcal{B}\} \quad \text{and} \quad \mathcal{W}_{\dot{\phi}} := \{\dot{\phi} \in \mathcal{R} \mid \llbracket \dot{\phi} \rrbracket = -\dot{\bar{\mathbf{H}}}[\mathbf{x}] \text{ on } \partial\mathcal{B}\}. \quad (4.25)$$

where, $\llbracket (\cdot) \rrbracket := (\cdot)^+ - (\cdot)^-$ is the jump of the quantity (\cdot) with respect to opposite faces of the periodic microstructure as visualized in Figure 4.2. The focus in this work is exclusively on periodic microstructures. Alternative boundary conditions may be formulated and implemented in full analogy to the treatment in ZÄH & MIEHE [258] for micro-electro-mechanics. The magnetization order parameter is considered as a generalized internal variable with no macroscopic counterpart. For periodic microstructures under consideration, the admissible rates of the order parameter are

$$\mathcal{W}_{\dot{\mathbf{M}}} := \{\dot{\mathbf{M}} \in T_{\mathbf{M}}\mathcal{S}^{d-1} \mid \llbracket \dot{\mathbf{M}} \rrbracket = \mathbf{0} \text{ on } \partial\mathcal{B}\}. \quad (4.26)$$

As mentioned in Subsection 4.2.1 the variational principle (4.23) needs to account for the geometric structure of the magnetization director of the form $\mathbf{M} \in \mathcal{S}^{d-1}$ such that $\dot{\mathbf{M}} \in T_{\mathbf{M}}\mathcal{S}^{d-1}$, where $T_{\mathbf{M}}\mathcal{S}^{d-1}$ is the *tangent space* of \mathcal{S}^{d-1} at \mathbf{M} as depicted in Figure 4.3. Taking into account the definitions (4.9), the variation of the principle (4.23) at the solution point gives the generalized extended Hill-Mandel condition

$$\underbrace{\bar{\boldsymbol{\sigma}} : \delta \dot{\bar{\boldsymbol{\varepsilon}}} - \bar{\mathbf{B}} : \delta \dot{\bar{\mathbf{H}}}}_{\text{macro power}} = \frac{1}{|\mathcal{B}|} \int_{\mathcal{B}} \underbrace{\{\boldsymbol{\sigma} : \delta \dot{\boldsymbol{\varepsilon}} - \mathbf{B} \cdot \delta \dot{\mathbf{H}} + \mathbf{F} \cdot \delta \dot{\mathbf{M}} + \mathbf{G} : \nabla \delta \dot{\mathbf{M}}\}}_{\text{extended micro power}} dV, \quad (4.27)$$

for the dissipative magnetomechanical microstructure evolution. At the micro-level the mechanical stresses, the magnetic induction and the conjugate forces dual to the magnetization vector and its gradient can be identified as

$$\boldsymbol{\sigma} := \partial_{\boldsymbol{\varepsilon}} \Psi, \quad \mathbf{B} := -\partial_{\mathbf{H}} \Psi, \quad \mathbf{F} := \partial_{\mathbf{M}} \Psi + \partial_{\dot{\mathbf{M}}} d, \quad \mathbf{G} := \partial_{\nabla \mathbf{M}} \Psi \quad (4.28)$$

governed by the constitutive functions Ψ and d introduced in (4.24). In order to account for the geometric structure $\mathbf{M} \in \mathcal{S}^{d-1}$, the variation of the rate of the magnetization director can be given as

$$\delta \dot{\mathbf{M}} = \delta \boldsymbol{\Theta} \times \mathbf{M}, \quad (4.29)$$

where $\boldsymbol{\Theta} \in \mathcal{R}^d$ is the *spin of magnetization* which satisfies the condition $\dot{\mathbf{M}} \in T_{\mathbf{M}}\mathcal{S}^{d-1}$. With this definition, the variation of the principle (4.23) gives

$$\begin{aligned} 0 &= \frac{1}{|\mathcal{B}|} \int_{\mathcal{B}} (-\operatorname{div}[\partial_{\boldsymbol{\varepsilon}} \Psi]) \cdot \delta \dot{\mathbf{u}} dV + \frac{1}{|\mathcal{B}|} \int_{\partial\mathcal{B}} (\partial_{\boldsymbol{\varepsilon}} \Psi \cdot \mathbf{n}) \cdot \delta \dot{\mathbf{u}} dA \\ &\quad - \frac{1}{|\mathcal{B}|} \int_{\mathcal{B}} \operatorname{div}[-\partial_{\mathbf{H}} \Psi] \delta \dot{\phi} dV + \frac{1}{|\mathcal{B}|} \int_{\partial\mathcal{B}} (-\partial_{\mathbf{H}} \Psi \cdot \mathbf{n}) \delta \dot{\phi} dA \\ &\quad + \frac{1}{|\mathcal{B}|} \int_{\mathcal{B}} \mathbf{M} \times (\delta_{\mathbf{M}} \Psi + \partial_{\dot{\mathbf{M}}} d) \cdot \delta \boldsymbol{\Theta} dV + \frac{1}{|\mathcal{B}|} \int_{\partial\mathcal{B}} \mathbf{M} \times (\partial_{\nabla \mathbf{M}} \Psi \cdot \mathbf{n}) \cdot \delta \boldsymbol{\Theta} dA, \end{aligned} \quad (4.30)$$

with the variational derivative $\delta_{\mathbf{M}} \Psi := \partial_{\mathbf{M}} \Psi - \operatorname{div}[\partial_{\nabla \mathbf{M}} \Psi]$. The Euler-Lagrange equations for the stationarity condition of the variational principle (4.23) are,

$$\begin{aligned} \operatorname{div}[\partial_{\boldsymbol{\varepsilon}} \Psi] &= \mathbf{0} \quad \text{in } \mathcal{B} \\ \mathbf{M} \times [\delta_{\mathbf{M}} \Psi + \partial_{\dot{\mathbf{M}}} d] &= \mathbf{0} \quad \text{in } \mathcal{B} \\ \operatorname{div}[-\partial_{\mathbf{H}} \Psi] &= 0 \quad \text{in } \mathcal{B}. \end{aligned} \quad (4.31)$$

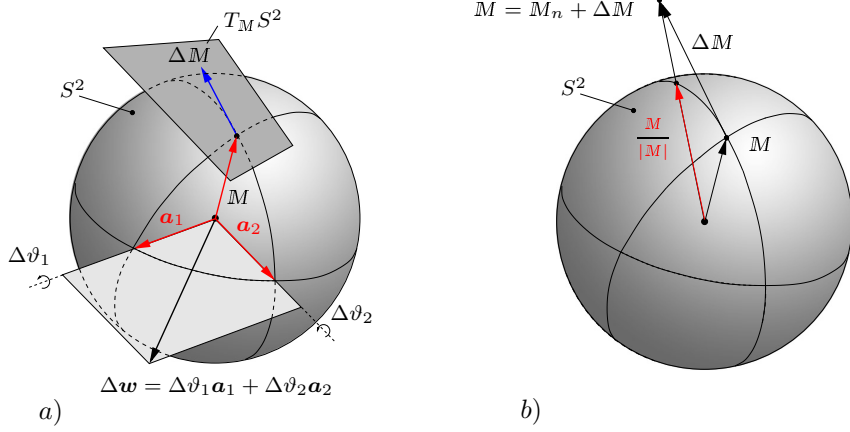


Figure 4.3: Illustration of the update methods for the magnetization director. a) The exponential update in MIEHE & ETHIRAJ [168] calculates an increment ΔM that lies in the tangent space defined by \mathbf{a}_1 and \mathbf{a}_2 . b) The projection method in the current work provides a substantially simplified alternative to maintain the unity constraint on the magnetization director by employing a post-processing normalization step.

Equation (4.31)₂ governs the evolution of the magnetization. Defining a quadratic constitutive dissipation potential as $d(\dot{M}) = \frac{\eta}{2} \|\dot{M}\|^2$ and taking the cross product of (4.31)₂ with the vector M the magnetization evolution can be reformulated as

$$\dot{M} = \frac{1}{\eta} M \times (M \times \delta_M \Psi) \quad \text{in } \mathcal{B}. \quad (4.32)$$

This is consistent with the Landau-Lifshitz equation, see (LANDAU & LIFSHITZ [142]), without the Gilbert damping term but contains the damping term of the Landau-Lifshitz equation for non-stationary micromagnetics, see (GILBERT [78]).

4.2.3. Microscopic Incremental Variational Principle of Homogenization

In the numerical setting, an incremental variational principle which governs the magneto-mechanical problem at discrete time t_{n+1} for finite time increments $\tau = t_{n+1} - t_n$ is needed. An *incremental variational principle of homogenization* is proposed of the form

$$\bar{w}^\tau(\bar{\boldsymbol{\varepsilon}}, \bar{\mathbb{H}}) = \inf_{\mathbf{u} \in \mathcal{W}_{\mathbf{u}}(\bar{\boldsymbol{\varepsilon}})} \sup_{\phi \in \mathcal{W}_\phi(\bar{\mathbb{H}})} \inf_{M \in \mathcal{W}_M} \frac{1}{|\mathcal{B}|} \int_{\mathcal{B}} w^\tau(\boldsymbol{\varepsilon}, \mathbb{H}, M, \nabla M) dV. \quad (4.33)$$

The macroscopic incremental potential density \bar{w}^τ is obtained by optimizing the volume average of the microscopic potential w^τ . Such a formulation is conceptually in line with formulations for nonlinear mechanical problems in MIEHE [164], PONTE CASTAÑEDA & SUQUET [196]. Similar to (4.11), the incremental potential density w^τ is related to the rate-type potential w by the time integration algorithm

$$w^\tau(\boldsymbol{\varepsilon}, \mathbb{H}, M, \nabla M) := \text{ALGO} \left\{ \int_{t_n}^t w(\dot{\boldsymbol{\varepsilon}}, \dot{\mathbb{H}}, \dot{M}, \nabla \dot{M}) dt \right\}. \quad (4.34)$$

The admissible spaces for the displacement and magnetic potential are defined by the jump conditions

$$\mathcal{W}_{\mathbf{u}} := \{\mathbf{u} \in \mathcal{R}^d \mid \llbracket \mathbf{u} \rrbracket = \bar{\boldsymbol{\varepsilon}} \llbracket \mathbf{x} \rrbracket \text{ on } \partial \mathcal{B}\} \quad \text{and} \quad \mathcal{W}_\phi := \{\phi \in \mathcal{R} \mid \llbracket \phi \rrbracket = -\bar{\mathbb{H}} \cdot \llbracket \mathbf{x} \rrbracket \text{ on } \partial \mathcal{B}\}, \quad (4.35)$$

driven by the macroscopic strain $\bar{\boldsymbol{\varepsilon}}$ and the magnetic field $\bar{\mathbf{H}}$. The admissible magnetization fields are

$$\mathcal{W}_M := \{M \in \mathcal{R}^d \mid \llbracket M \rrbracket = \mathbf{0} \text{ on } \partial\mathcal{B}\} . \quad (4.36)$$

Recall that the geometric structure of the magnetization such that $M \in \mathcal{S}^{d-1}$ needs to be accounted for.

4.2.4. A Staggered Solution Scheme of Micromagnetic Evolution Problem

To enforce the above constraint on the magnetization director M , a staggered solution scheme is proposed such that the overall solution algorithm is composed of two sub-algorithms

$$ALGO = ALGO_{u\phi} \circ ALGO_M . \quad (4.37)$$

Here, $ALGO_M$ is a *magnetization step* that updates the magnetization director, and is followed by the *magnetomechanical step* $ALGO_{u\phi}$ that determines the displacements and the magnetic potential. The magnetization step $ALGO_M$ is further decomposed according to

$$ALGO_M = ALGO_M^2 \circ ALGO_M^1 \quad (4.38)$$

into two sub-steps, which ensures the geometric constraint on M such that $M \in \mathcal{S}^{d-1}$. Here, $ALGO_M^1$ is an unconstrained predictor step and $ALGO_M^2$ is a corrector step that enforces the constraint on the magnetization. The overall solution procedure is described below.

Magnetic Predictor $ALGO_M^1$. A time-discrete potential for the first sub-problem is obtained by constraining the rates of the displacements $\dot{\mathbf{u}} = \mathbf{0}$ and magnetic potential $\dot{\phi} = 0$ in the original potential. Then the magnetization predictor potential is defined as

$$w_M^\tau(M, \nabla M) = ALGO_m^1 \left\{ \int_{t_n}^t w(\dot{\boldsymbol{\varepsilon}} = \mathbf{0}, \dot{\mathbf{H}} = \mathbf{0}, \dot{M}, \nabla \dot{M}) dt \right\} , \quad (4.39)$$

with the closed form algorithmic representation of the incremental potential as

$$w_M^\tau(M, \nabla M) = \Psi(\boldsymbol{\varepsilon}_n, \mathbf{H}_n, M, \nabla M) - \Psi_n + \tau d((M - M_n)/\tau) . \quad (4.40)$$

The *magnetic predictor* algorithm is represented by the variational statement

$$\{M\} = \arg \left\{ \inf_{M \in \mathcal{W}_M} \frac{1}{|\mathcal{B}|} \int_{\mathcal{B}} w_M^\tau(M, \nabla M) dV \right\} , \quad (4.41)$$

with the Euler equation that gives the fully implicit update equation for the magnetization director

$$\partial_M \Psi - \text{div}[\partial_{\nabla M} \Psi] + \tau \partial_M d((M - M_n)/\tau) = \mathbf{0} \text{ in } \mathcal{B} . \quad (4.42)$$

Magnetic Corrector $ALGO_M^2$. Clearly, (4.42) does not obey the constraint $M \in \mathcal{S}^{d-1}$. To satisfy this a post-processing corrector step is implemented that projects the magnetizations to the unit sphere \mathcal{S}^{d-1} i.e.,

$$M \leftarrow M/|M| . \quad (4.43)$$

This is an easy to implement algebraic scaling conceptually in line with proposals reviewed by KRUŽÍK & PROHL [136].

Magnetomechanical step $ALGO_{u\phi}$. In a similar formulation as before an incremental potential for the magnetomechanical step is proposed

$$w_{u\phi}^\tau(\boldsymbol{\varepsilon}, \mathbb{H}) = ALGO_{u\phi} \left\{ \int_{t_n}^t w(\dot{\boldsymbol{\varepsilon}}, \dot{\mathbb{H}}, \dot{\mathbb{M}} = \mathbf{0}, \nabla \dot{\mathbb{M}} = \mathbf{0}) dt \right\}, \quad (4.44)$$

with the potential density for the magnetomechanical corrector step defined by

$$w_{u\phi}^\tau(\boldsymbol{\varepsilon}, \mathbb{H}) = \Psi(\boldsymbol{\varepsilon}, \mathbb{H}, \mathbb{M}, \nabla \mathbb{M}) - \Psi_n. \quad (4.45)$$

Note that \mathbb{M} and $\nabla \mathbb{M}$ are *determined* from the predictor step in (4.43). As a consequence, the magnetomechanical algorithm for the update of the displacements and potential at frozen magnetization is governed by the variational statement

$$\{\mathbf{u}, \phi\} = \bar{w}^\tau(\bar{\boldsymbol{\varepsilon}}, \bar{\mathbb{H}}) = \inf_{\mathbf{u} \in \mathcal{W}_u(\bar{\boldsymbol{\varepsilon}})} \sup_{\phi \in \mathcal{W}_\phi(\bar{\mathbb{H}})} \frac{1}{|\mathcal{B}|} \int_{\mathcal{B}} w_{u\phi}^\tau(\boldsymbol{\varepsilon}, \mathbb{H}, \mathbb{M}, \nabla \mathbb{M}) dV. \quad (4.46)$$

Consequently the necessary condition for the stationarity of this equation yields the mechanical equilibrium and Gauss's law as Euler equations

$$\left. \begin{aligned} \operatorname{div}[\partial_{\boldsymbol{\varepsilon}} \Psi] &= \mathbf{0} \\ \operatorname{div}[-\nabla \phi + m_s \mathbb{M}] &= 0 \end{aligned} \right\} \text{ in } \mathcal{B}. \quad (4.47)$$

These Euler equations are the *time-discrete, algorithmic counterparts* of the corresponding rate-type, time-continuous equations (4.31).

4.2.5. Space-Time Discretization of Staggered Solution Scheme

The space discretization covers the two algorithmic steps $ALGO_M$ and $ALGO_{u\phi}$ covered in the above staggered scheme. For both subproblems, the same finite element interpolation \mathfrak{T}^h of the microstructure \mathcal{B} with N^h nodes is employed.

Magnetic Predictor $ALGO_M^1$. For the discretization of the problem (4.41), consider the set of constitutive state variables assembled in $\mathbf{c}_M := \{\mathbb{M}, \nabla \mathbb{M}\}$. The finite element interpolations can then be written in the form

$$\mathbf{c}_M^h = \mathfrak{B}_M(\mathbf{x}) \mathfrak{d}_m \quad \text{with} \quad \mathfrak{d}_M := \mathbf{A}_{I=1}^{N^h} [M_I]^T \quad (4.48)$$

in terms of nodal values \mathfrak{d}_m of the magnetization directors. Consequently the space-time discrete stationary principle for the magnetic predictor step is defined as

$$\mathfrak{d}_M = \arg \left\{ \inf_{\mathfrak{d}_M} \frac{1}{|\mathcal{B}|} \int_{\mathcal{B}} w_M^\tau(\mathfrak{B}_M \mathfrak{d}_M) dV \right\} \quad (4.49)$$

which determines the *unconstrained values* for the nodal magnetization directors at current time t_{n+1} . The problem is solved by a Newton-Raphson method with updates $\mathfrak{d}_M \leftarrow \mathfrak{d}_M - \mathfrak{K}_M^{-1} \mathfrak{R}_m$ based on the residual and tangent arrays

$$\mathfrak{R}_M := \frac{1}{|\mathcal{B}|} \int_{\mathcal{B}} \mathfrak{B}_M^T [\partial_{\mathbf{c}_M} w_M^\tau] dV \quad \text{and} \quad \mathfrak{K}_M := \frac{1}{|\mathcal{B}|} \int_{\mathcal{B}} \mathfrak{B}_M^T [\partial_{\mathbf{c}_M \mathbf{c}_M}^2 w_M^\tau] \mathfrak{B}_M dV \quad (4.50)$$

until convergence $|\mathfrak{R}_M| < tol_M$.

Magnetic Corrector $ALGO_M^2$. For the converged state obtained from the predictor step, $ALGO_M^2$ is performed according to (4.43), yielding the *constrained values*

$$\mathfrak{d}_M := \mathbf{A}_{I=1}^{N^h} [M_I / |M_I|]^T \quad (4.51)$$

of the magnetization directors at a nodal point of the finite element mesh.

Magnetomechanical step $ALGO_{u\phi}$. For the space discretization of the problem (4.46), consider the set of state variables assembled in $\mathbf{c}_{u\phi} := \{\nabla_s \mathbf{u}, -\nabla\phi\}$. The finite element interpolations takes the form

$$\mathbf{c}_{u\phi}^h = \mathfrak{B}_{u\phi}(\mathbf{x}) \mathfrak{d}_{u\phi} \quad \text{with} \quad \mathfrak{d}_{u\phi} := \mathbf{A}_{I=1}^{N^h} [\mathbf{u}_I, -\phi_I]^T \quad (4.52)$$

with the nodal values $\mathfrak{d}_{u\phi}$ containing the displacement and the magnetic potential. Then, the space-time discrete stationary principle

$$\bar{w}^\tau(\bar{\boldsymbol{\varepsilon}}, \bar{H}) = \text{stat}_{\mathfrak{d}_{u\phi}} \frac{1}{|\mathcal{B}|} \int_{\mathcal{B}} w_{u\phi}^\tau(\mathfrak{B}_{u\phi} \mathfrak{d}_{u\phi}) dV \quad (4.53)$$

determines the macroscopic potential at current time t_{n+1} . A Newton-Raphson method is employed with updates $\mathfrak{d}_{u\phi} \leftarrow \mathfrak{d}_{u\phi} - \mathfrak{K}_{u\phi}^{-1} \mathfrak{R}_{u\phi}$ based on the residual and tangent arrays

$$\mathfrak{R}_{u\phi} := \frac{1}{|\mathcal{B}|} \int_{\mathcal{B}} \mathfrak{B}_{u\phi}^T [\partial_{\mathbf{c}_{u\phi}} w_{u\phi}^\tau] dV \quad \text{and} \quad \mathfrak{K}_{u\phi} := \int_{\mathcal{B}} \mathfrak{B}_{u\phi}^T [\partial_{\mathbf{c}_{u\phi} \mathbf{c}_{u\phi}}^2 w_{u\phi}^\tau] \mathfrak{B}_{u\phi} dV \quad (4.54)$$

until convergence $|\mathbf{r}_{u\phi}| < \text{tol}_{u\phi}$.

4.2.6. Algorithmic Representation of Homogenized Quantities

The homogenized mechanical stresses and magnetic field $\bar{\mathfrak{s}} := \{\bar{\boldsymbol{\sigma}}, -\bar{B}\}$ are obtained by taking the variation of the functional \bar{w}^τ defined in (4.53) such that

$$\bar{\mathfrak{s}} := \partial_{\bar{\boldsymbol{\varepsilon}}} \bar{w}^\tau = \frac{1}{|\mathcal{B}|} \int_{\mathcal{B}} [\partial_{\mathbf{c}_{u\phi}} w_{u\phi}^\tau] dV, \quad (4.55)$$

which is the *volume average* of the associated microscopic quantities $\mathfrak{s} := \partial_{\mathbf{c}} w^\tau$. For a FE² implementation the tangent moduli related to the macroscopic finite element arrays (4.17) are obtained by a further derivation

$$\bar{\boldsymbol{\varepsilon}} := \partial_{\bar{\boldsymbol{\varepsilon}}}^2 \bar{w}^\tau = \frac{1}{|\mathcal{B}|} \int_{\mathcal{B}} [\partial_{\mathbf{c}_{u\phi} \mathbf{c}_{u\phi}}^2 w_{u\phi}^\tau] dV - \boldsymbol{\varepsilon}_{u\phi}^T \mathfrak{K}_{u\phi}^{-1} \boldsymbol{\varepsilon}_{u\phi}, \quad (4.56)$$

with the tangent matrix $\mathfrak{K}_{u\phi}$ defined in (4.54) and the additional finite element array

$$\boldsymbol{\varepsilon}_{u\phi} := \frac{1}{|\mathcal{B}|} \int_{\mathcal{B}} \mathfrak{B}_{u\phi}^T [\partial_{\mathbf{c}_{u\phi} \mathbf{c}_{u\phi}}^2 w_{u\phi}^\tau] dV. \quad (4.57)$$

Note that the macroscopic moduli contain the average of the microscopic moduli $\boldsymbol{\varepsilon} := \partial_{\mathbf{c}_{u\phi} \mathbf{c}_{u\phi}}^2 w_{u\phi}^\tau$ and a softening term due to the microstructure evolution. This is in full analogy to the variational FE² scenario in dissipative mechanics outlined in MIEHE [164]. Note that in this work only a single point on the macro continuum $\bar{\mathcal{B}}$ is considered. However, the theoretical formulation presented above can be embedded in a FE² formulation.

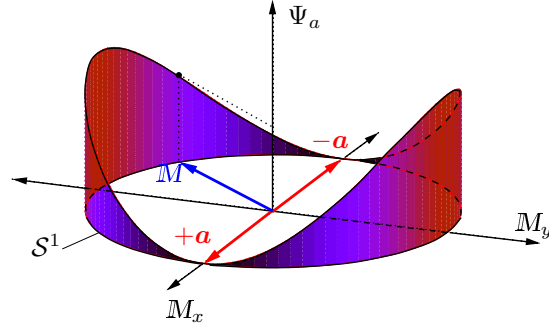


Figure 4.4: *Uniaxial anisotropy energy density function characterizing the magnetization easy axes. Two-well potential characterized by a unit vector \mathbf{a} for the uniaxial case. The magnetization director \mathbf{M} evolves on the unit circle \mathcal{S}^1 , MIEHE & ETHIRAJ [168].*

4.3. Functionals in Micro-Magneto-Elasticity

4.3.1. Energy Density and Dissipation Potential Functionals

In order to describe the energy storage in micromagnetics in terms of the constitutive energy and dissipation functions described in (4.24), a constitutive free-energy function is first introduced and later transformed by a Legendre transformation to a magnetic Gibbs energy function, suitable for the choice of primary variables introduced previously¹.

Contributions to the Energy Density. The energy contributions due to the presence of a magnetic field in the free space Ξ_{vac} and an additional contribution Ξ_{mat} due to the elastic deformation and the magnetization of the solid needs to be considered. Hence, the total free-energy density of the solid material embedded into the free space decomposes according to

$$\Xi(\boldsymbol{\varepsilon}, \mathbf{M}, \nabla \mathbf{M}, \mathcal{B}) = \Xi_{mat}(\boldsymbol{\varepsilon}, \mathbf{M}, \nabla \mathbf{M}) + \Xi_{vac}(\mathbf{M}, \mathcal{B}), \quad (4.58)$$

into contributions from the material and free space respectively. The material part of the free energy is a function of the strain $\boldsymbol{\varepsilon}$, the magnetization director \mathbf{M} and its gradient $\nabla \mathbf{M}$. It is assumed to consist of the three contributions

$$\Xi_{mat}(\boldsymbol{\varepsilon}, \mathbf{M}, \nabla \mathbf{M}) = \Xi_e(\boldsymbol{\varepsilon}, \mathbf{M}) + \Xi_a(\mathbf{M}) + \Xi_{ex}(\nabla \mathbf{M}), \quad (4.59)$$

where $\Xi_e(\boldsymbol{\varepsilon}, \mathbf{M})$ defines the elastic energy, $\Xi_a(\mathbf{M})$ the anisotropy energy and $\Xi_{ex}(\nabla \mathbf{M})$ the exchange energy.

Anisotropy Energy Density. Crystalline ferromagnetic materials show an inherent energy dependence on the magnetization orientation relative to the crystalline structural axis. These materials show preferred directions of magnetization, often denoted as the *easy directions*, i.e. the directions along which the material is magnetized most easily. This can be modeled by an anisotropy energy density Ξ_a with the minimum of the energy defining

¹The choice of naming the energy functions as “free-energy” $\Xi(\boldsymbol{\varepsilon}, \mathbf{M}, \nabla \mathbf{M}, \mathcal{B}; \theta)$ and “magnetic Gibbs energy” $\Psi(\boldsymbol{\varepsilon}, \mathbf{M}, \nabla \mathbf{M}, \mathcal{H}; \theta)$ is assuming an implicit dependence of the energy functions on the temperature field θ , even though temperature dependence is not explicitly considered in this work. On the other hand energy functions depending on the entropy field η are called “internal energy” or “enthalpy” functions which are not considered here.

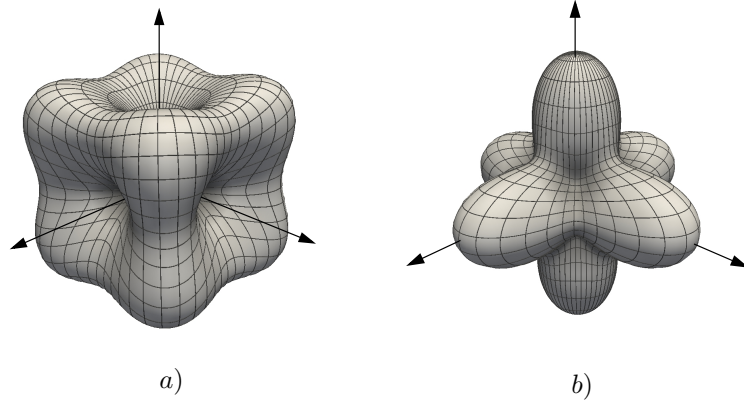


Figure 4.5: Cubic magnetocrystalline anisotropy energy density function. a) Energy landscape is shown in the case of $\langle 100 \rangle$ as easy direction, for the case of Galfenol and b) shows the energy landscape for $\langle 111 \rangle$ as easy direction, for Terfenol-D.

the easy directions. Specific representations of this non-convex energy contribution Ξ_a for different crystals are reported in CULLITY [45], KITTEL [131, 132] and HUBERT & SCHÄFER [103]. Uniaxial and cubic bulk magnetic anisotropies are considered here while surface magnetic anisotropy interactions are not considered in this work. The reader is referred to [103] for a more detailed overview in this topic. Hexagonal and tetragonal crystals show a uniaxial magnetocrystalline anisotropy, the anisotropy energy landscape for such materials is shown in Figure 4.4. The energy function is the well known *two well potential* with the minima in the direction of the easy axes. This uniaxial energy can be written as

$$\Xi_a(\mathbf{M}) = \frac{K_1}{2} \{1 - \text{tr}^2[\mathbf{M} \otimes \mathbf{A}]\} + \frac{K_2}{4} \{1 - \text{tr}^2[\mathbf{M} \otimes \mathbf{A}]\}^2, \quad (4.60)$$

where the vector $\|\mathbf{A}\| = 1$ defines the direction of the easy axis. For cubic magnetocrystalline anisotropy the energy landscape is shown in Figure 4.5. $\langle 100 \rangle$ or $\langle 111 \rangle$ are the anisotropy directions of the crystal. For such a cubic anisotropy the energy can be expressed as

$$\Xi_a(\mathbf{M}) = K[(\mathbf{M} \otimes \mathbf{M} : \mathbf{A}^{12})^2 + (\mathbf{M} \otimes \mathbf{M} : \mathbf{A}^{13})^2 + (\mathbf{M} \otimes \mathbf{M} : \mathbf{A}^{23})^2], \quad (4.61)$$

with the material parameter K as the anisotropy constant. $\langle 100 \rangle$ or $\langle 111 \rangle$ are the easy axis determines by the sign of the constant K . $\mathbf{A}^{ij} = \mathbf{A}^i \otimes \mathbf{A}^j_{\{i,j=1..3\}}$ is the set of structural tensor given in terms of three perpendicular cubic axes \mathbf{A}^1 , \mathbf{A}^2 and \mathbf{A}^3 of the crystal.

Elastic Energy Density. Energy stored in the crystal due to elastic lattice deformations are modeled by the elastic energy Ξ_e . The magnetization director evolution \mathbf{M} causes energy changes in the crystalline solid. Similar to DESIMONE & JAMES [54], ENGD AHL [63], HUBERT & SCHÄFER [103], ZHANG & CHEN [259] the magnetostrictive strain $\boldsymbol{\varepsilon}_0(\mathbf{M})$ is introduced, where $\boldsymbol{\varepsilon}_0(\mathbf{M})$ is the *stress-free strain* corresponding to the magnetization director \mathbf{M} . For uniaxial crystal assuming isotropic behavior this is given as

$$\boldsymbol{\varepsilon}_0(\mathbf{M}) = \frac{3}{2}E \mathbb{P} : [\mathbf{M} \otimes \mathbf{M}], \quad (4.62)$$

where \mathbb{P} is the fourth order projection tensor defined as $\mathbb{P}_{ijkl} = \mathbb{I}_{ijkl} - 1/3\delta_{ij}\delta_{kl}$ and E is the magnetostrictive constant. The elastic energy density can be formulated as a function

of the elastic, stress-producing strain $\boldsymbol{\varepsilon}_e := \boldsymbol{\varepsilon} - \boldsymbol{\varepsilon}_0$ as

$$\Xi_e(\boldsymbol{\varepsilon}, \mathbb{M}) = \frac{1}{2}[\boldsymbol{\varepsilon} - \boldsymbol{\varepsilon}_0(\mathbb{M})] : \mathbb{C}^{iso} : [\boldsymbol{\varepsilon} - \boldsymbol{\varepsilon}_0(\mathbb{M})], \quad (4.63)$$

with the positive definite fourth order elasticity tensor of the crystal \mathbb{C}^{iso} . The isotropic tensor \mathbb{C}^{iso} is given in terms of two constants λ and μ , for materials with *uniaxial* magneto-crystalline anisotropy. For giant magnetostrictive materials which show cubic anisotropy the energies are given in *lattice frame of the crystal*. The strain corresponding to the magnetization in this case can be given as

$$\boldsymbol{\varepsilon}_0(\mathbb{M}) = \frac{3}{2}[\boldsymbol{\mathcal{K}} : (\mathbb{M} \otimes \mathbb{M}) - \frac{E_{100}}{3} \mathbf{1}]|_{CF}, \quad (4.64)$$

where $\boldsymbol{\mathcal{K}}$ is the fourth order material modulus defined in terms of constants E_{111} and E_{100} , which define the material response in the $\langle 111 \rangle$ and $\langle 100 \rangle$ directions. The free energy function in this case is given as

$$\Xi_e(\boldsymbol{\varepsilon}, \mathbb{M}) = \frac{1}{2}[\boldsymbol{\varepsilon} - \boldsymbol{\varepsilon}_0(\mathbb{M})] : \mathbb{C}^{cub} : [\boldsymbol{\varepsilon} - \boldsymbol{\varepsilon}_0(\mathbb{M})]|_{CF}, \quad (4.65)$$

with the cubic elasticity tensor defined in terms of three constants C_{11}, C_{12} and C_{44} . The local axes are aligned with the local magnetic easy directions $\mathbf{A}^1, \mathbf{A}^2$ and \mathbf{A}^{32} .

Exchange Energy Density. Neighboring magnetization in ferromagnetic materials shows tendency to align parallel to each other. The exchange energy Ξ_{ex} models this behavior. Focusing on an isotropic response, the energy is given as

$$\Xi_{ex}(\nabla \mathbb{M}) = \frac{A}{2} \text{tr} [\nabla \mathbb{M} \cdot \nabla^T \mathbb{M}], \quad (4.66)$$

where material parameter $A > 0$ is the exchange energy coefficient. It is a material length scale parameter related to the width of the magnetic domain walls.

Energy Density of Free Space. The magnetic induction in free space (including the material) is defined in terms of the magnetization $m_s \mathbb{M}$ along with the magnetic field \mathbb{H} as

$$\mathbb{B} = \mu_0(\mathbb{H} + \hat{m}_s \mathbb{M}) \text{ in } \mathcal{B}, \quad (4.67)$$

²The magnetostrictive strain for a cubic response in (4.64) can be explicitly written as,

$$\boldsymbol{\varepsilon}_0 = \frac{3}{2} \begin{pmatrix} E_{100}(m_1^2 - 1/3) & E_{111}m_1m_2 & E_{111}m_1m_3 \\ E_{111}m_2m_1 & E_{100}(m_2^2 - 1/3) & E_{111}m_2m_3 \\ E_{111}m_3m_1 & E_{111}m_3m_2 & E_{100}(m_3^2 - 1/3) \end{pmatrix}_{CF}$$

The material modulus $\boldsymbol{\mathcal{K}}$ can be filled with the entries $\mathcal{K}_{1111} = E_{100}, \mathcal{K}_{2222} = E_{100}, \mathcal{K}_{3333} = E_{100}, \mathcal{K}_{1212} = \mathcal{K}_{1221} = E_{111}/2, \mathcal{K}_{2112} = \mathcal{K}_{2121} = E_{111}/2, \mathcal{K}_{1313} = \mathcal{K}_{1331} = E_{111}/2, \mathcal{K}_{3113} = \mathcal{K}_{3131} = E_{111}/2, \mathcal{K}_{2323} = \mathcal{K}_{2332} = E_{111}/2, \mathcal{K}_{3223} = \mathcal{K}_{3232} = E_{111}/2$. The fourth order cubic mechanical modulus \mathbb{C}^{cub} in (4.65) is given as

$$\mathbb{C}^{cub} = \begin{pmatrix} \mathbb{C}_{11} & \mathbb{C}_{12} & \mathbb{C}_{12} & & & \\ \mathbb{C}_{12} & \mathbb{C}_{11} & \mathbb{C}_{12} & & & \\ \mathbb{C}_{12} & \mathbb{C}_{12} & \mathbb{C}_{11} & & & \\ & & & \mathbb{C}_{44} & & \\ & & & & \mathbb{C}_{44} & \\ & & & & & \mathbb{C}_{44} \end{pmatrix}$$

The magnetic energy stored in the space occupied by the body and the space surrounding it is described by the vacuum energy Ξ_{vac} . Resolving (4.67) for the magnetic field $\mathbb{H} = \hat{\mathbb{H}}(\mathbb{M}, \mathbb{B})$ gives the quadratic form

$$\Xi_{vac}(\mathbb{M}, \mathbb{B}) = \frac{\mu_0}{2} \text{tr}[\mathbb{H} \otimes \mathbb{H}] = \frac{1}{2\mu_0} \text{tr}[(\mathbb{B} - \mu_0 \hat{m}_s \mathbb{M}) \otimes (\mathbb{B} - \mu_0 \hat{m}_s \mathbb{M})]. \quad (4.68)$$

It is defined in terms of the magnetic permeability of vacuum $\mu_0 = 4\pi \times 10^{-7}$ [N/A²].

4.3.2. Energy-Enthalpy Function of Micro-Magneto-Elasticity

The free energy functions presented above can be reformulated in terms of the primary fields introduced before by a partial Legendre transformation with respect to the magnetic slot

$$\Psi(\boldsymbol{\varepsilon}, \mathbb{M}, \nabla \mathbb{M}, \mathbb{H}) = \inf_{\mathbb{B}} [\Xi(\boldsymbol{\varepsilon}, \mathbb{M}, \nabla \mathbb{M}, \mathbb{B}) - \mathbb{H} \cdot \mathbb{B}], \quad (4.69)$$

given in terms of the magnetic Gibbs energy function $\Psi(\boldsymbol{\varepsilon}, \mathbb{M}, \nabla \mathbb{M}, \mathbb{H})$. This transformation affects only the free space part Ξ_{vac} of the free energy. The necessary condition of (4.69) gives the magnetic induction definition (4.67). Using this as an elimination equation for \mathbb{B} , we get from (4.69) the Gibbs energy function as

$$\Psi(\boldsymbol{\varepsilon}, \mathbb{M}, \nabla \mathbb{M}, \mathbb{H}) = \Xi_{mat}(\boldsymbol{\varepsilon}, \mathbb{M}, \nabla \mathbb{M}) - \frac{\mu_0}{2} \mathbb{H} \cdot \mathbb{H} - \mu_0 m_s \mathbb{M} \cdot \mathbb{H}, \quad (4.70)$$

in terms of the free energy density Ξ_{mat} of the solid material defined in (4.59).

4.3.3. Dissipation Potential for Magnetization Evolution

A kinetic dissipation potential functional is required to model the time dependent, dynamic evolution of the magnetization director \mathbb{M} . An isotropic dissipation potential functional in terms of the rates of the magnetization director is given as

$$d(\dot{\mathbb{M}}) = \frac{\eta}{2} \|\dot{\mathbb{M}}\|^2, \quad (4.71)$$

where the scalar parameter η is viscosity coefficient, which governs the kinetic rate of the magnetic domain wall evolution.

4.4. Numerical Examples: Homogenization and Macroscopic Response

In this section some numerical examples are presented to demonstrate the capability of the proposed framework. Magnetic domain wall motion on the microstructure of the ferromagnetic material driven by macroscopic magnetic field and mechanical load are presented. The simulations are performed on a converged equilibrium state obtained starting from a random distribution of the magnetization in the microstructure. The computational homogenization framework enables the determination of *macroscopic hysteresis curves*. The homogenization framework presented above is employed for the analysis of microscopic domain evolution driven by macroscopic loading and the associated overall response of the material.

Table 4.1: Material parameters for Galfenol $\text{Fe}_{81.3}\text{Ga}_{18.7}$ [259].

No.	Parameter	Name	Unit	Value
1.	C_{11}	Mechanical parameter	N/m^2	1.96×10^{11}
2.	C_{12}	Mechanical parameter	N/m^2	1.56×10^{11}
3.	C_{44}	Mechanical parameter	N/m^2	1.23×10^{11}
4.	E_{100}	Magnetostrictive coefficient	-	2.64×10^{-4}
5.	E_{111}	Magnetostrictive coefficient	-	-
6.	A	Exchange energy coefficient	N	6×10^{-11}
7.	κ_0	Magnetic permeability	N/A^2	1.3×10^{-6}
8.	K	Anisotropy energy coefficient	N/m^2	1×10^5
9.	m_s	Saturation magnetization	A/m	1.43×10^4
10.	η	Damping coefficient	Ns^2/m^2	2×10^{-1}

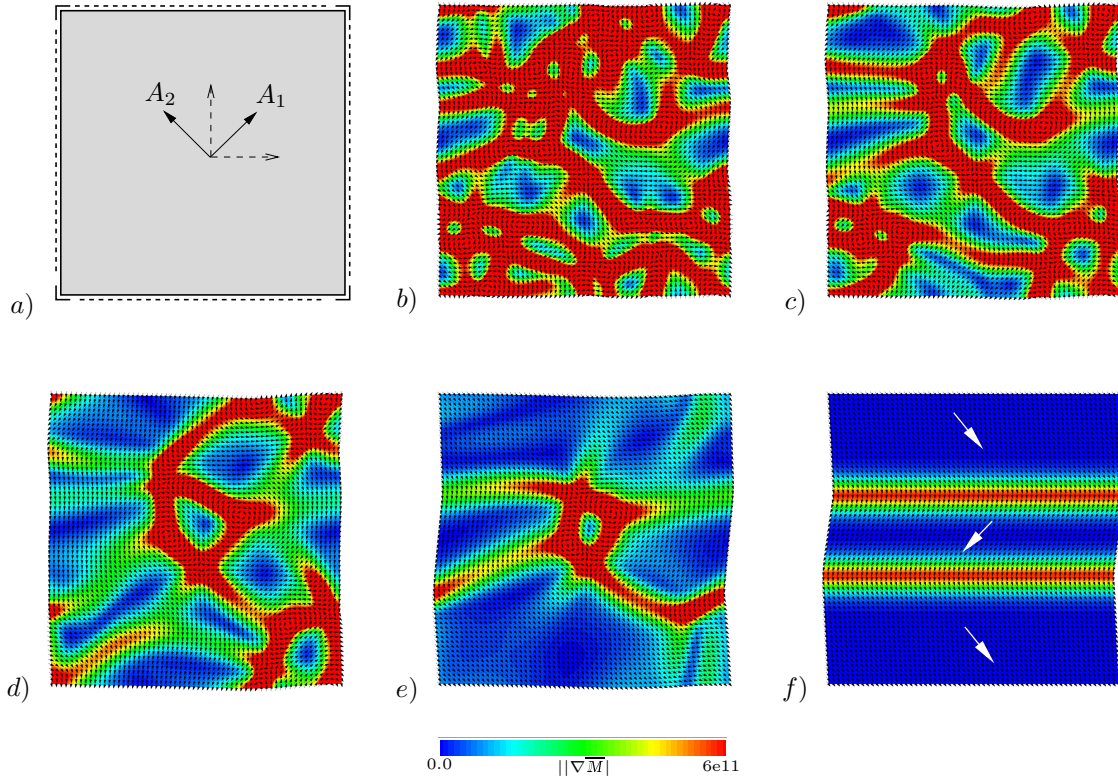


Figure 4.6: Representative volume element with periodic boundary conditions. Initialization of magnetization order parameter and evolution to equilibrium state. a) Single-crystal volume element with the easy axes oriented at 45° as shown. The edge length is taken as $l = 240$ [nm]. b) – f) Micro-magnetic domain evolution starting from a random distribution of the magnetization. The microstructure evolves and finally converges to a stable state. Vectors represent the magnetization and the general poling direction is indicated by white arrows. The contour represents the gradient of the magnetization.

4.4.1. Problem 1: Homogenization of a Galfenol Single Crystal

Single crystal Galfenol $\text{Fe}_{81.3}\text{Ga}_{18.7}$ is considered first below the Curie-Weiss transition temperature. Galfenol is a “giant magnetostrictive” material with cubic magnetocrys-

talline anisotropy and its magnetic easy axes aligned along the $\langle 100 \rangle$ direction. A two dimensional simulation can be performed with the magnetic easy axes oriented in the plane of the sample. Here the magnetic easy axes are oriented at 45° from the global axes as shown in Figure 4.7 a). The material parameters are taken from ZHANG & CHEN [259] and presented in Table 4.1. The boundary value problem is shown in Figure 4.7 a). As described previously periodic boundary conditions are applied on the edges of the microstructure for all degrees of freedom. The mechanical displacement and the magnetic potential at the corner nodes are fixed to constrain the rigid body modes. Four node quad elements with 60×60 elements are used to discretize the boundary value problem.

Starting from a random distribution of the magnetization order parameter a relaxation process is performed to achieve a stable equilibrium state, shown in Figure 4.7 b) – f). Mechanical fluctuations are magnified, in order to visualize the periodicity of the microstructure. Magnetization vector distribution along with the contour of its gradient are plotted. Relaxation causes the magnetization to align in some regions known as magnetic domains while each individual region is separated by domain walls. General poling directions in a domain are indicated with white arrows. The magnetocrystalline anisotropy is clearly visible in the equilibrium state, with the magnetization pointing in the magnetic easy directions.

A saw-tooth type magnetic loading is applied starting from the equilibrium state, with the magnetic field oriented in the horizontal direction. The magnetization reorients in the field direction as can be seen from Figure 4.8 b) – c). Accordingly this causes domain wall motions with the magnetic domains parallel to the field getting larger while others shrink. Figure 4.8 c) – d) shows that near the coercive field the domain walls start to disappear and the magnetization finally points in the direction of the applied field resulting in saturation of the magnetization. A further increase in the magnetic field does not affect the magnetization. Upon removal of the field the material still shows a remanent magnetization. The reversal of the magnetic field causes the magnetizations to follow the applied field direction Figure 4.8 e). It can be clearly seen that all the magnetization rotate together and no domain walls evolve. The single crystal chosen along with no nucleation sites maybe the cause for this. Hysteresis behavior associated with this domain evolution are shown in Figure 4.9. The first plot shows the variation of the magnetization \overline{M}_1/m_s with the applied magnetic field \overline{H}_1 . The magnetization increases upto the saturation and then remains constant on further application of magnetic field. The plot of

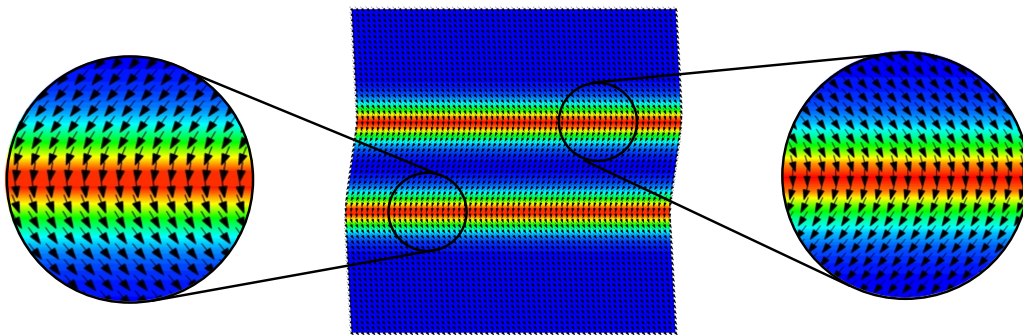


Figure 4.7: The zoomed out view of the magnetization vectors at the domain walls. The 90° transition of the magnetization can be clearly seen. This smooth transition of the magnetization vectors is captured by the discretization used.

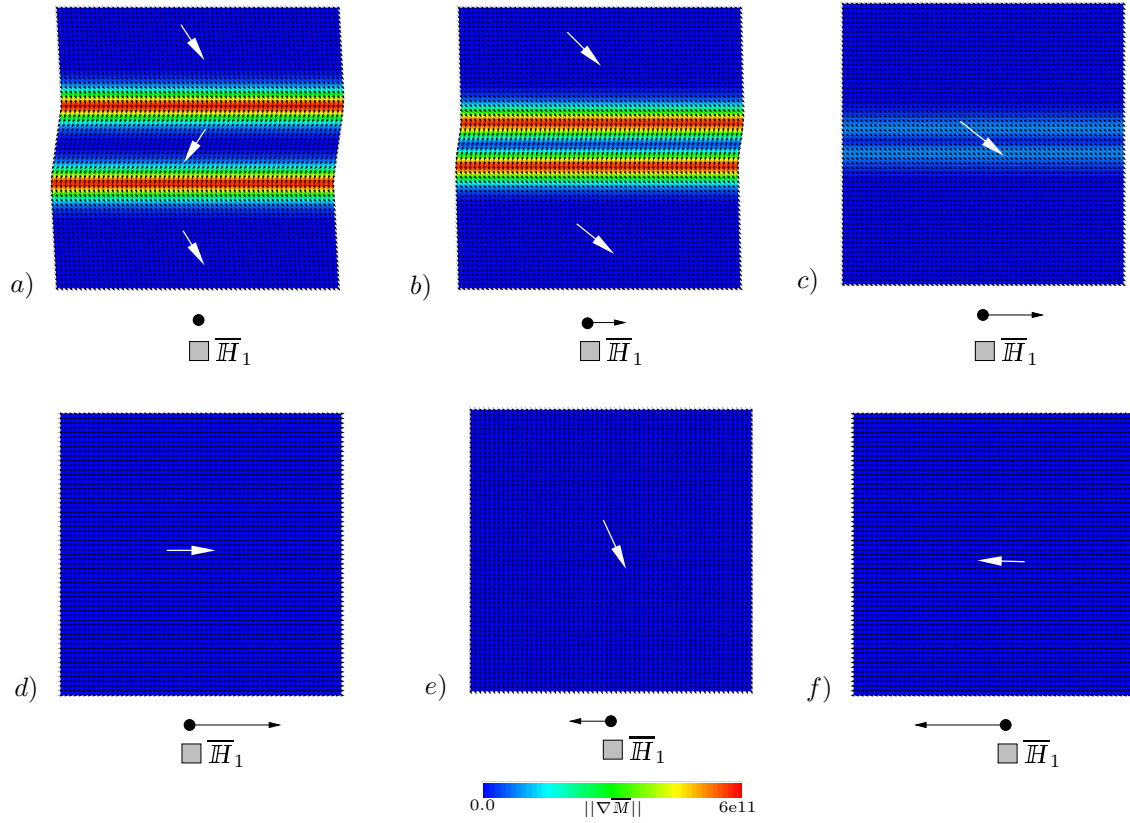


Figure 4.8: Magnetic field driven loading on a converged equilibrium state with magnetic loading applied in the horizontal direction. a) – f) shows the domain wall evolution for a cyclic magnetic field loading applied in the horizontal direction. Black arrow indicates the applied macroscopic field. As a consequence of the applied field a single domain is formed and remains even under the reversal of the applied field. Once the domain walls vanish field reversal does not nucleate new domains.

magnetostrictive strain $\bar{\varepsilon}_{11}^0$ and the applied magnetic field \bar{H}_1 is also shown. The strain is maximum when all the magnetizations point in the direction of the magnetic field and the value of this strain is equal to the magnetostrictive coefficient E_{100} . The two wells

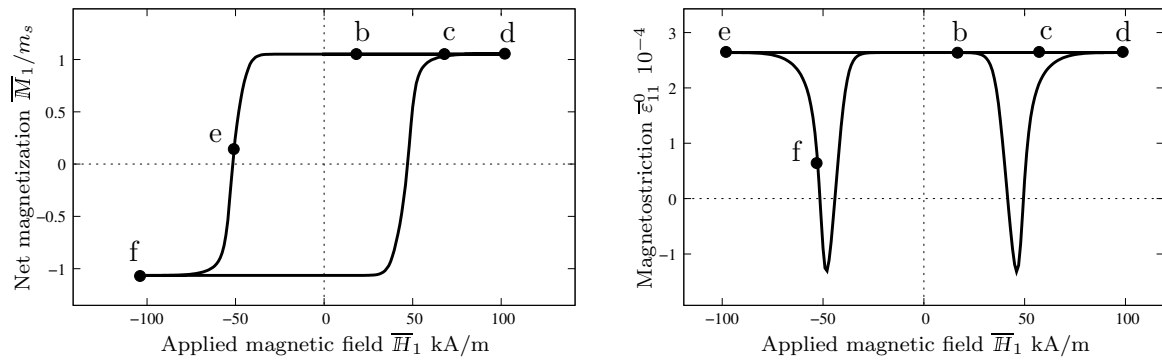


Figure 4.9: Macroscopic hysteresis curves for a cyclic magnetic field loading. The magnetostrictive strain $\bar{\varepsilon}_{11}^0$ and the net magnetization \bar{M}_1/m_s in the horizontal direction vs. the applied magnetic field \bar{H}_1 . Note that point a), is omitted to showcase symmetry.

Table 4.2: Material parameters for Nd₂Fe₁₄B permanent magnet [80].

No.	Parameter	Name	Unit	Value
1.	λ	Lamé parameter	N/m ²	2×10^{11}
2.	μ	Lamé parameter	N/m ²	8×10^{10}
3.	E	Magnetostrictive coefficient	-	12×10^{-6}
4.	A	Exchange energy coefficient	N	1×10^{-12}
5.	κ_0	Magnetic permeability	N/A ²	1.3×10^{-6}
6.	K_1	Anisotropy energy coefficient	N/m ²	4×10^6
7.	K_2	Anisotropy energy coefficient	N/m ²	6×10^5
8.	m_s	Saturation magnetization	A/m	8×10^5
9.	η	Damping coefficient	Ns ² /m ²	2×10^1

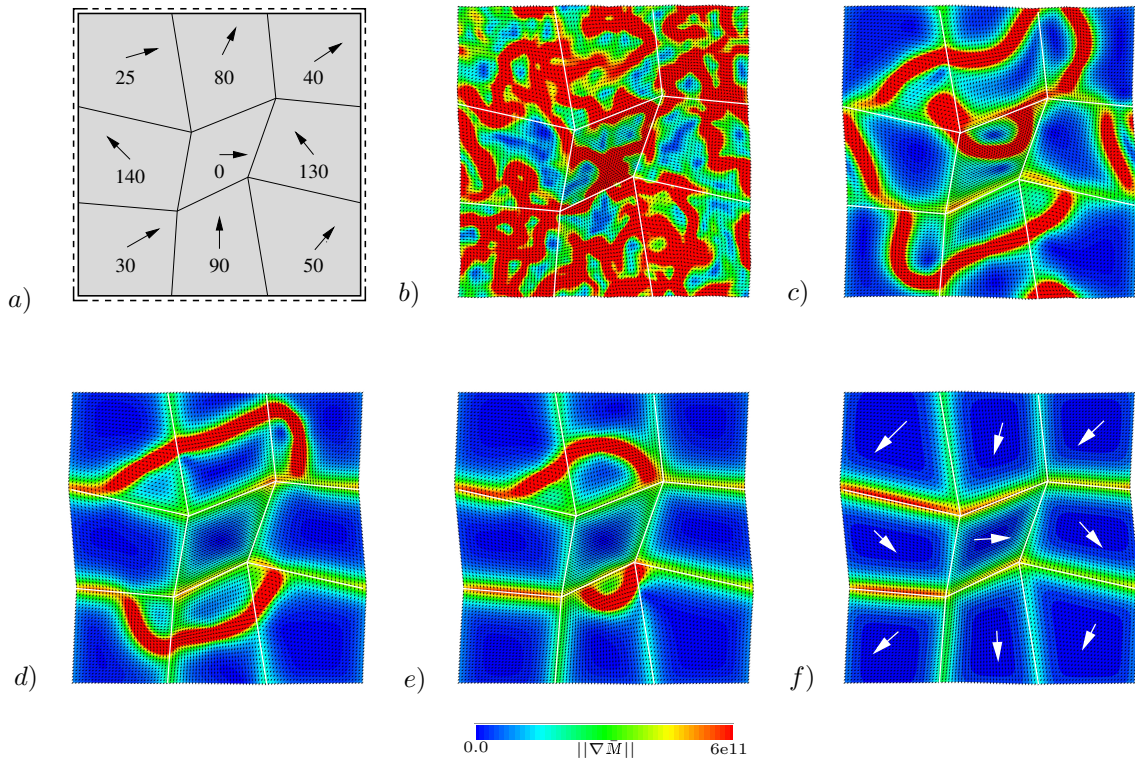


Figure 4.10: Representative volume of polycrystal permanent magnet. Evolution of magnetization from random distribution to equilibrium state. a) Representative volume element of a polycrystal with random distribution of the easy axes. The edge length is taken as $l=20$ [nm]. b) – f) micro-magnetic domain evolution starting from a random distribution of the magnetization. The micro-structure evolves and finally converges to a stable state. Vectors represent the magnetization and the general poling direction is indicated by white arrows. The contour represents the gradient of the magnetization.

of minima in the plot correspond to the point when the magnetization rotates in the direction of the magnetic field and its component in the horizontal direction is zero.

4.4.2. Problem 2: Homogenization of NdFeB Permanent Magnet

The second example analyzes a periodic polycrystal of Neodymium permanent magnet $\text{Nd}_2\text{Fe}_{14}\text{B}$ as shown in Figure 4.10 a). Each grain has different preferred directions characterized by the lattice orientations $\{\vartheta_i\}_{i=1,9}$, however the material parameters are identical in each grain. The boundary value problem is discretized with four-node quad elements with 90×90 elements (30×30 elements per grain). The relaxation process from random to equilibrium state is shown in Figure 4.10 b) – f). Grain boundaries are highlighted with white lines for better visualization. The equilibrium state showcases the high anisotropy of the permanent magnets with the magnetization in each grain pointing in the easy direction. The maximum domain wall thickness is seen between the grains where the difference in the easy directions is the largest. No transgranular domain walls are formed in the equilibrium state which can be attributed to the high anisotropy of the material. In the regions separated by domain walls the magnetizations are almost aligned.

Domain wall motions due to application of a magnetic field in the horizontal direction are shown in Figure 4.11 a) – h). The magnetizations rotate in the field direction and saturate when the coercive field is reached. Reversal of the applied field causes the magnetization in each grain to rotate in the direction of their respective easy direction. A remanent magnetization is seen upon removal of the magnetic field, with the domain walls appearing along the grain boundaries. Further application of the magnetic field in the opposite direction causes the magnetization to rotate in the opposite direction and finally yields saturation. This is also clearly seen in the characteristic hysteretic plot Figure 4.12. The first plot again shows the variation of the magnetization \overline{M}_1/m_s with the applied magnetic field \overline{H}_1 . The magnetization increases upto the saturation and then remains constant on further application of magnetic field. Upon removal of the magnetic field we can see a remanent magnetization in the aggregate. The value of this remanent magnetization however is seen to be lower than the saturation magnetization. The second plot shows the plot of the magnetostrictive strain $\overline{\varepsilon}_{11}^0$ with the applied field. We can see the characteristic butterfly hysteresis here, with the maximum strain observed at the saturation magnetization.

Table 4.3: Material parameters for Iron α -Fe [80].

No.	Parameter	Name	Unit	Value
1.	λ	Lamé parameter	N/m^2	2×10^{11}
2.	μ	Lamé parameter	N/m^2	8×10^{10}
3.	E	Magnetostrictive coefficient	-	12×10^{-6}
4.	A	Exchange energy coefficient	N	1×10^{-12}
5.	κ_0	Magnetic permeability	N/A^2	1.3×10^{-6}
6.	K_1	Anisotropy energy coefficient	N/m^2	4×10^4
7.	K_2	Anisotropy energy coefficient	N/m^2	6×10^3
8.	m_s	Saturation magnetization	A/m	5×10^6
9.	η	Damping coefficient	Ns^2/m^2	2×10^1

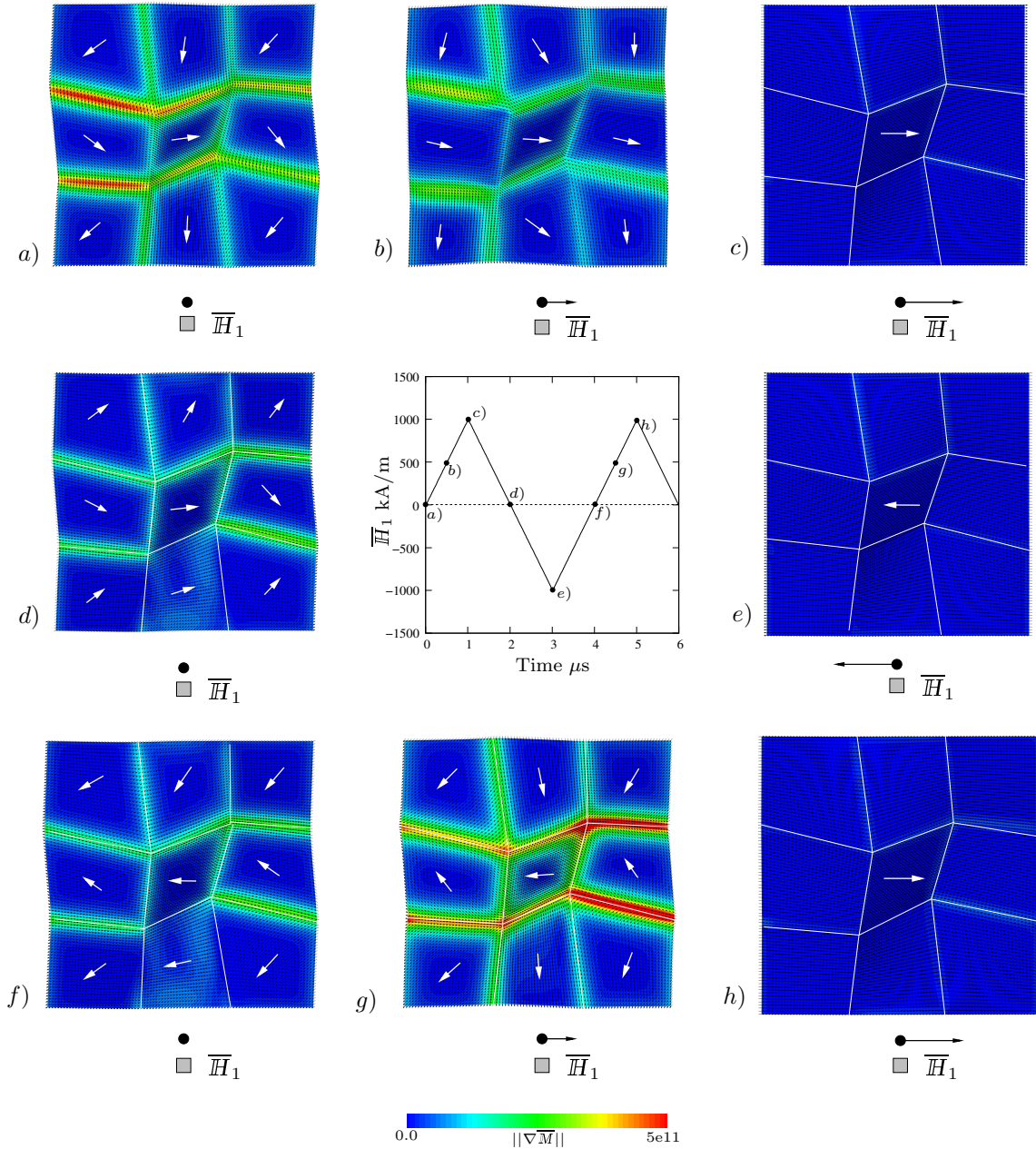


Figure 4.11: Domain wall motion for an applied cyclic loading of the magnetic field \overline{H}_1 . Loading curve is plotted in the middle. a) – h) show the domain wall motion for the applied cyclic loading. Complex domain wall evolution concentrated along the grain boundaries are observed. Black arrows indicate the direction of the applied magnetic field.

4.4.3. Problem 3: Homogenization of a Two Phase Magnet

A three dimensional homogenization is shown in order to showcase the capability of the proposed homogenization framework. A representative grain structure is created using a periodic Voronoi tessellation, such that a three dimensional grain growth is created with the average grain diameter taken as 1000 [nm]. A two-phase permanent magnet, consisting of a soft magnetic material α -Fe and a hard magnetic material $\text{Nd}_2\text{Fe}_{14}\text{B}$ is considered. The material parameters are shown in Table 4.2 and Table 4.3 for $\text{Nd}_2\text{Fe}_{14}\text{B}$ and α -Fe

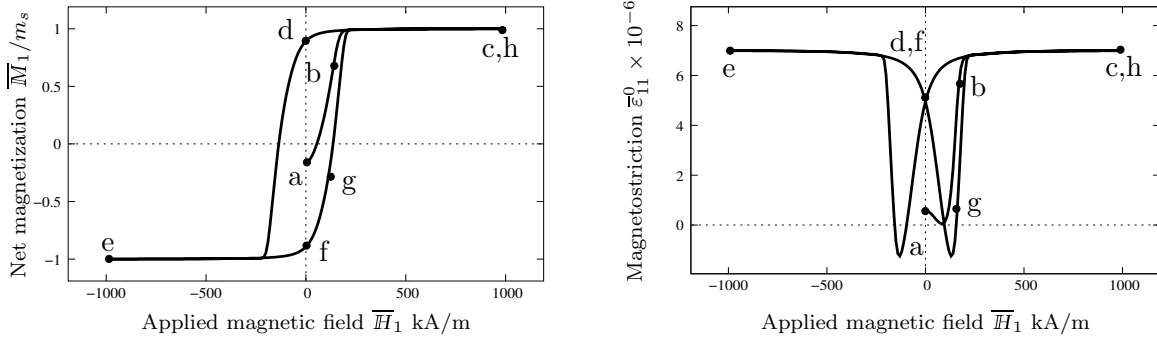


Figure 4.12: Macroscopic hysteresis curves of poly-crystalline permanent magnet. Aggregate showing the average magnetization \bar{M}_1/m_s versus the applied magnetic field \bar{H}_1 and butterfly hysteresis of the average magnetostrictive strain $\bar{\epsilon}_{11}^0$ versus the applied magnetic field.

respectively. Soft magnetic materials are used to enhance the magnetic properties of hard magnets (GOLL & KRONMÜLLER [80]). The grain structure is shown in Figure 4.13 for a Nd-rich microstructure. Different compositions of these materials can be simulated and the consequent effect on the microscopic domain formation and macroscopic properties can be studied. This example is used to showcase the capability of the model to simulate complex micromagnetic domain evolution. The problem is discretized using around 39,000 four node triangular elements. Periodic boundary conditions are applied on the surface of the microstructure. The domain evolution and the equilibrium state are shown in Figure 4.14. It can be seen that transgranular domains are formed. Such transgranular domains were not observed in the previous example where we considered a single-phase hard magnetic material. It may be inferred that the inclusion of the soft magnetic phase is the reason for the formation of these transgranular domains, however further investigations need to be done to investigate the influence of the soft magnetic phase. Due to high computational cost the magnetic loading processes are not considered here.

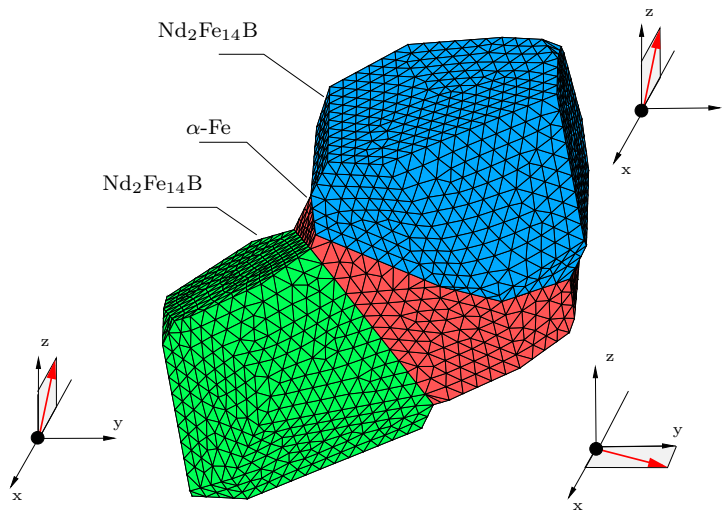


Figure 4.13: Three-dimensional periodic representative volume element of two-phase permanent magnet. Periodic Voronoi tessellation of a two-phase permanent magnet with grains of α -Fe and $\text{Nd}_2\text{Fe}_{14}\text{B}$. Periodic boundary conditions are applied on the surface of the microstructure. The easy axis of the magnetisation is shown for each grain, by the red arrows.

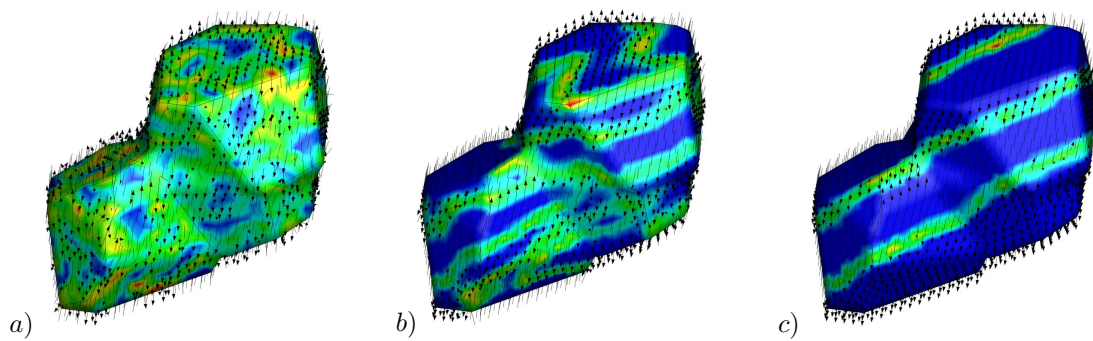


Figure 4.14: *Domain evolution of magnetization order parameter starting from a random distribution.* Vectors represent the magnetization and contour represents the gradient of the magnetization. Trans-granular domain patterns can be observed due to the interaction of soft and hard magnetic phases.

Variational Phase-Field Approach to Micro-Magneto-Mechanics at Finite Strains

Ferromagnetic particles suspended in an elastomeric substrate show realignment under the influence of an external applied field, in turn causing large deformations of the substrate material. The magnetomechanical coupling in these materials is governed by the magnetic properties of the inclusion and mechanical properties of the matrix. The magnetic phenomenon in ferromagnetic materials is governed by the formation and evolution of domains on the micro-scale as was presented in the previous chapter. The large deformations observed in these materials under applied fields due to nonlinear Maxwell interactions, provides the motivation to extend the microscopic micromagnetic framework presented in the last chapter to the finite strain scenario. Objectivity restrictions and variational principles are thoroughly investigated to derive an appropriate framework that can capture and predict this behavior. Numerical examples showcase the capability of the presented framework to accurately capture and predict the behavior of these materials without any a priori assumptions. Note that the variational structure and the fields are quite similar to the previous chapter however they are reintroduced here to clearly emphasize the subtle changes required for an extension to the finite strain setting. The theory and examples presented in this chapter follow the work presented in KEIP & SRIDHAR [124].

5.1. Functionals in Finite Deformation Micromagnetics

5.1.1. Deformation, Magnetization and Magnetic Potential

The coupled magnetomechanical problem is depicted in [Figure 5.1](#). Similar to the last chapter $\Omega \subset \mathcal{R}^3$ is a general non-magnetic region and $\mathcal{B} \subset \Omega$ a ferromagnetic body that is embedded in this region¹. This work focuses on evolution of the magnetization order parameter as well as the corresponding domain evolution and mechanical deformations that occur under quasistatic coupled magnetomechanical loading in the time interval $\mathcal{T} \subset$

¹The non-magnetic region can be in general vacuum or an elastomer as in the case of magnetorheological elastomers.

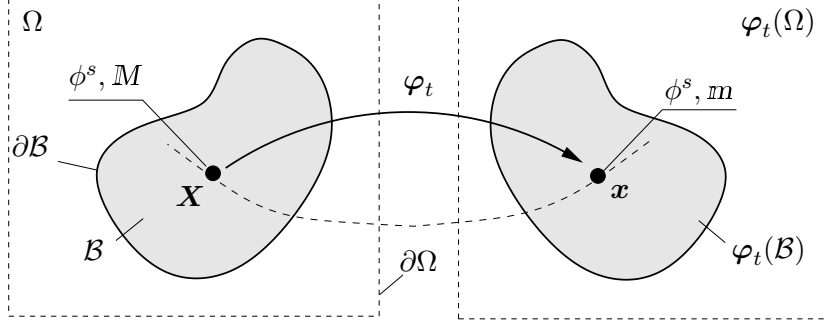


Figure 5.1: Deformation of a ferromagnetic material embedded in vacuum (non-magnetic substrate), from Lagrangian to the Eulerian configuration. An undeformed magnetic body \mathcal{B} is considered to be embedded in a generic free space box Ω in the Lagrangian frame, in terms of the material coordinates \mathbf{X} . The deformation of such a body is then parametrized with the coordinates $\mathbf{x} = \varphi_t(\mathbf{X})$. In this configuration the magnetic body occupies the space $\varphi_t(\mathcal{B})$ in the non magnetic region $\varphi_t(\Omega)$. The primary fields associated with the micro-magneto-elastic process are the deformation map φ , the magnetic self potential ϕ^s and the reference magnetization director M .

\mathcal{R}_+ . The primary fields required to describe this multi field problem of micromagnetics are

$$\varphi : \begin{cases} \Omega \times \mathcal{T} \rightarrow \mathcal{R}^3 \\ (\mathbf{X}, t) \mapsto \mathbf{x} = \varphi(\mathbf{X}, t) \end{cases} \quad \text{and} \quad M : \begin{cases} \mathcal{B} \times \mathcal{T} \rightarrow \mathcal{S}^{d-1} \\ (\mathbf{X}, t) \mapsto M(\mathbf{X}, t) \end{cases}. \quad (5.1)$$

Here the large strain *deformation map* φ describes the mechanical deformation of the body (and the space surrounding the body) while the *referential magnetization director* M , characterizes the magnetic state of the ferromagnet at $\mathbf{X} \in \mathcal{B}$ and $t \in \mathcal{T}$. Note that similar to the previous introduction of the magnetization director (4.18) the magnetization director $M \in \mathcal{S}^{d-1}$ has the property such that $\|M\| = 1$. Magnetization in the ferromagnetic body induces a magnetic field in and around the body known as the magnetic *self field*. This is described by a scalar valued magnetic self potential ϕ^s such that

$$\phi^s : \begin{cases} \Omega \times \mathcal{T} \rightarrow \mathcal{R} \\ (\mathbf{X}, t) \mapsto \phi^s(\mathbf{X}, t) \end{cases}. \quad (5.2)$$

This potential field is assumed to be continuous across the interface $\partial\mathcal{B}$ between the domain \mathcal{B} and the surrounding space $\Omega \setminus \mathcal{B}$, that is

$$[[\phi^s]] = 0 \quad \text{on} \quad \partial\mathcal{B}. \quad (5.3)$$

Where $[[\cdot]] := (\cdot)_+ - (\cdot)_-$ denotes the jump across the sides $\partial\mathcal{B}_+$ and $\partial\mathcal{B}_-$ of the interface between the magnetic and the non magnetic region. In addition to the field generated by the magnetic body magnetic fields can be generated by external sources. A continuous and continuously differentiable scalar magnetic potential ϕ^a is introduced so that the total magnetic potential at $\mathbf{X} \in \Omega$ is given by

$$\phi := \phi^s + \phi^a \quad \text{in} \quad \Omega. \quad (5.4)$$

The deformation map φ and the magnetic self potential ϕ^s are defined in the whole region Ω , whereas the *magnetization field per unit mass* \mathcal{M} is non-zero only in the (magnetic) region \mathcal{B} . Formally this can be written as

$$\hat{\mathcal{M}}(\mathbf{X}) := \begin{cases} m_s M & \text{for } \mathbf{X} \in \mathcal{B} \\ \mathbf{0} & \text{otherwise,} \end{cases} \quad (5.5)$$

where the magnetization $\mathcal{M} = m_s \mathbb{M}$ is defined in terms of the *magnetization director* \mathbb{M} and the saturation magnetization per unit mass m_s . Note that in the previous chapter the magnetic self field was treated as a microscopic quantity while applied fields were governed by macroscopic quantities.

5.1.2. Gradients of the Primary Fields

The gradients of the primary fields defined in (5.1) and (5.2) define the *deformation gradient* and *reference magnetic self field*

$$\mathbf{F} := \nabla \boldsymbol{\varphi}(\mathbf{X}, t) \quad \text{and} \quad \mathbb{H}^s := -\nabla \phi^s(\mathbf{X}, t). \quad (5.6)$$

Here, $\nabla(\cdot) := \partial_{\mathbf{X}}(\cdot)$ denotes the gradient of (\cdot) with respect to the reference coordinates \mathbf{X} . As a consequence of (5.4) the total magnetic field in $\mathbf{X} \in \Omega$ is given as

$$\mathbb{H} := \mathbb{H}^a + \mathbb{H}^s \quad \text{in} \quad \Omega. \quad (5.7)$$

Here \mathbb{H}^a defines the applied magnetic field generated by external sources unaffected by the presence of the magnetic body. The applied magnetic field \mathbb{H}^a is considered to be known and predefined similar to the interpretations considered in STEIGMANN [228], KANKANALA & TRIANTAFYLIDIS [118] and KEIP & RAMBAUSEK [122]. The magnetic mappings can be identified as

$$\mathbb{H}^s = \mathbf{F}^T \cdot \mathbb{h}^s, \quad \mathbb{M} = \mathbf{F}^{-1} \cdot \mathbb{m} \quad \text{and} \quad \mathbb{B}^s = J \mathbf{F}^{-1} \cdot \mathbb{b}^s, \quad (5.8)$$

similar to the interpretation presented in Subsection 2.3.4. Here \mathbb{h}^s and \mathbb{m} are the magnetic self field and the magnetization director associated with the current configuration, respectively. Note that contrary to the self field the applied magnetic field is unaffected by the deformation such that $\mathbb{H}^a = \mathbb{h}^a$. The *magnetic self induction field* \mathbb{b}^s is defined in the Eulerian configuration as

$$\mathbb{b}^s = \mu_0(\mathbf{g}^{-1} \cdot \mathbb{h}^s + \rho m_s \mathbb{m}) \quad \text{in} \quad \boldsymbol{\varphi}_t(\Omega), \quad (5.9)$$

where μ_0 is the magnetic permeability of vacuum and ρ is the current mass density of the deformed solid. The latter is related to the density ρ_0 of the reference configuration via the balance of mass $\rho = \rho_0/J$. Based on the mappings defined in (5.8) we can define the Lagrangian counterpart of (5.9) via a pull-back operation

$$\mathbb{B}^s = \mu_0(J \mathbf{C}^{-1} \cdot \mathbb{H}^s + \rho_0 m_s \mathbb{M}) \quad \text{in} \quad \Omega. \quad (5.10)$$

5.1.3. Objective State Variables and Material Symmetry Conditions

For a ferromagnetic body \mathcal{B} embedded in a non magnetic region Ω a constitutive theory of grade one is formulated. The constitutive functions defined later are assumed to depend on the primary variables and their first gradients. For a generic scalar constitutive function \mathfrak{F} a functional dependence can be formulated such that

$$\mathfrak{F} = \hat{\mathfrak{F}}(\mathbf{c}_0) \quad \text{with} \quad \mathbf{c}_0 := \{\boldsymbol{\varphi}, \nabla \boldsymbol{\varphi}, \mathbb{m}, \nabla \mathbb{m}, \phi^s, -\nabla \phi^s\}. \quad (5.11)$$

The function \mathfrak{F} needs to satisfy the invariance conditions under special deformations such that

$$\hat{\mathfrak{F}}(\mathbf{c}_0^+) = \hat{\mathfrak{F}}(\mathbf{c}_0) \quad \forall \mathbf{Q} \in \mathcal{SO}(3), \quad (5.12)$$

\mathbf{c}_0^+ denotes set of primary fields subjected to superimposed rigid body modes $\boldsymbol{\varphi}^+ = \mathbf{Q}(t) \cdot \boldsymbol{\varphi} + \mathbf{c}(t)$, $m^+ = \mathbf{Q}(t) \cdot m$ and $\phi^{s+} = \phi^s + c(t)$. The orthogonal tensor \mathbf{Q} denotes a proper rotation while \mathbf{c} denotes a rigid body translation and c denotes a scalar. Keeping the invariance condition (5.12) in mind the constitutive state function is reformulated as

$$\mathfrak{F} := \hat{\mathfrak{F}}(\mathbf{c}) \quad \text{with} \quad \mathbf{c} := \{\nabla^T \boldsymbol{\varphi} \cdot \nabla \boldsymbol{\varphi}, M, \nabla M, -\nabla \phi^s\}. \quad (5.13)$$

Depending on the set of *objective state variables* \mathbf{c} that satisfy a priori the constraint (5.12). $\nabla^T \boldsymbol{\varphi} \cdot \nabla \boldsymbol{\varphi} =: \mathbf{C}$ is the right Cauchy–Green tensor and ∇M is the referential gradient of the magnetization director. In addition the principle of *material symmetry* states that locally $\hat{\mathfrak{F}}$ has to be invariant with respect to rotations \mathbf{Q} superimposed onto $\mathcal{N}_{\mathbf{X}} \subset \Omega$ of a material point \mathbf{X} , in case these rotations are elements of the appropriate *material symmetry group* $\mathcal{G} \subset \mathcal{SO}(3)$. This implies that²

$$\hat{\mathfrak{F}}(\mathbf{Q} \star \mathbf{C}, \mathbf{Q} \star M, \mathbf{Q} \star \nabla M, \mathbf{Q} \star H^s) := \hat{\mathfrak{F}}(\mathbf{C}, M, \nabla M, H^s) \quad \forall \mathbf{Q} \in \mathcal{G} \subset \mathcal{SO}(3). \quad (5.15)$$

Inherent anisotropies of the material are accounted for via a referential structural tensor of the form $A_i := \mathbf{A}_i \otimes \mathbf{A}_i$, where \mathbf{A}_i represent referential preferred directions. An isotropic tensor function can be formulated such that

$$\hat{\mathfrak{F}}(\mathbf{Q} \star \mathbf{C}, \mathbf{Q} \star M, \mathbf{Q} \star \nabla M, \mathbf{Q} \star H^s; \mathbf{Q} \star A_i) := \hat{\mathfrak{F}}(\mathbf{C}, M, \nabla M, H^s; A_i) \quad \forall \mathbf{Q} \in \mathcal{SO}(3). \quad (5.16)$$

Following the works of BOEHLER [22], SPENCER [225] and SCHRÖDER & NEFF [217]), an invariant representation of the scalar function \mathfrak{F} can be formulated as

$$\hat{\mathfrak{F}}(\mathbf{C}, M, \nabla M, H^s; A_i) := \hat{\mathfrak{F}}(I_1, \dots, I_n), \quad (5.17)$$

where I_1, \dots, I_n are the invariants of the extended set $\{\mathbf{C}, M, \nabla M, H^s; A_i\}$.

5.2. Magnetic energy, Loading and Dissipation Potential Functional

A constitutive function considering objectivity, material symmetry and implicit anisotropy of the material will be defined in this section in an *invariant Lagrangian setting* (5.16). A *purely energetic formulation* in terms of a free-energy function is first formulated and later transformed into a *magnetic Gibbs functional* suitable for the aforementioned choice of primary variables by a partial Legendre transformation. The reader is referred to [Section 4.3](#) for the naming convention of the energy functions.

²In what follows, the action of the proper orthogonal tensor $\mathbf{Q} \in \mathcal{SO}(3)$ on vectors \mathbf{v} and tensors \mathbf{T} of order $r > 1$ is denoted by the Rayleigh product

$$\mathbf{Q} \star \mathbf{v} := [v]_i \mathbf{Q} \cdot \mathbf{e}_i \quad \text{and} \quad \mathbf{Q} \star \mathbf{T} := [T]_{i_1 \dots i_r} \mathbf{Q} \cdot \mathbf{e}_{i_1} \otimes \dots \otimes \mathbf{Q} \cdot \mathbf{e}_{i_r}. \quad (5.14)$$

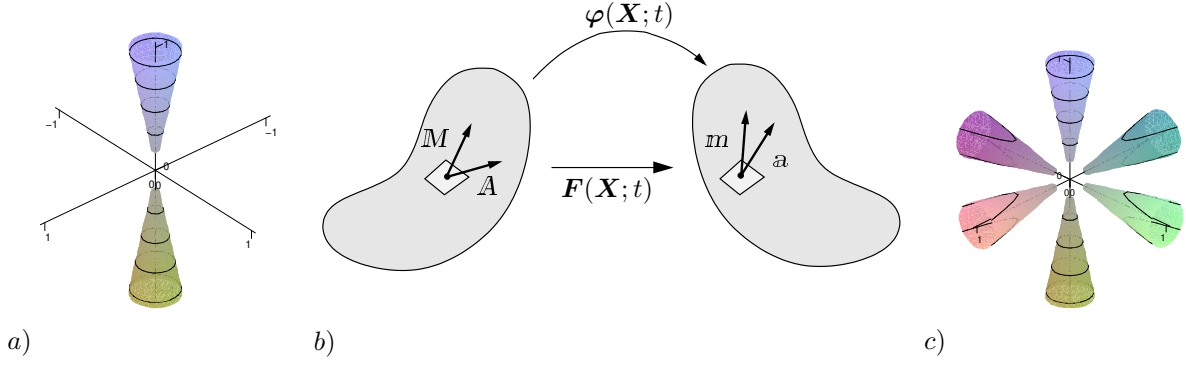


Figure 5.2: Energy functions for magnetocrystalline anisotropy in ferromagnetic solids. *a)* Sketch of magnetic anisotropy energy of a ferromagnet with uniaxial symmetry characterized by a single easy axis. *b)* Mapping of the magnetization director $m = \mathbf{F}M$ and the anisotropy vector $a = \mathbf{F}A$ from reference to the actual setting. *c)* Sketch of magnetic anisotropy energy of a ferromagnet with cubic symmetry characterized by three perpendicular easy axes. The anisotropy energies are finite strain extensions of the energies presented in Section 4.3.

5.2.1. Contributions to Energy Density Function

The coupled material response is described by means of a free-energy function that is composed of a contribution $\Xi_{vac}(\mathbf{C}, M, B)$ due to the presence of a magnetic field and a contribution $\Xi_{mat}(\mathbf{C}, M, \nabla M; A_i)$ that accounts for the behavior of the material. Hence, the free-energy function $\Xi(\mathbf{C}, M, \nabla M, B; A_i)$ can be written as

$$\Xi(\mathbf{C}, M, \nabla M, B; A_i) := \Xi_{mat}(\mathbf{C}, M, \nabla M; A_i) + \Xi_{vac}(\mathbf{C}, M, B) \quad \text{for } \mathbf{X} \in \Omega. \quad (5.18)$$

The material part of the energy is assumed to consist of three contributions

$$\Xi_{mat}(\mathbf{C}, M, \nabla M; A_i) = \Xi_{elas}(\mathbf{C}) + \Xi_{aniso}(\mathbf{C}, M; A_i) + \Xi_{ex}(\nabla M), \quad (5.19)$$

where Ξ_{elas} is the elastic energy, Ξ_{aniso} is the magnetic anisotropy energy, and Ξ_{ex} is the exchange energy. The set of structural tensors A_i accounts for referential *magnetic easy axes* that characterize the magnetocrystalline anisotropy of the material. Please note that $M = \mathbf{0}$ and $\nabla M = \mathbf{0}$ in $\Omega \setminus \mathcal{B}$, see (5.5). The energy contributions are the large deformation counterpart of the energies presented in Section 4.3.

Elastic Energy Density. The energy due to deformations in the material are accounted for by the elastic energy density Ξ_{elas} in the whole domain Ω . A simple Neo-Hookean model is proposed of the form

$$\Xi_{elas}(\mathbf{C}) = \frac{\mu}{2}(\text{tr}[\mathbf{C}] - 3) + \frac{\mu}{\beta}(J^{-\beta} - 1), \quad (5.20)$$

where μ is the shear modulus and $\beta = \frac{\lambda}{\nu} = \frac{2\nu}{1-2\nu}$ is given in terms of Poisson's ratio ν . Note that the elastic contribution does not account for the magnetostriction of the ferromagnetic material itself as was done previously in Section 4.3. In magnetorheological elastomers the deformations of the composite as a whole far exceeds the magnetostriction of the ferromagnetic inclusions. Considering this the magnetostriction of the inclusions has been neglected in this work. This can however be included in the formulation by considering a *multiplicative split* similar to the one proposed in ETHIRAJ & MIEHE [68].

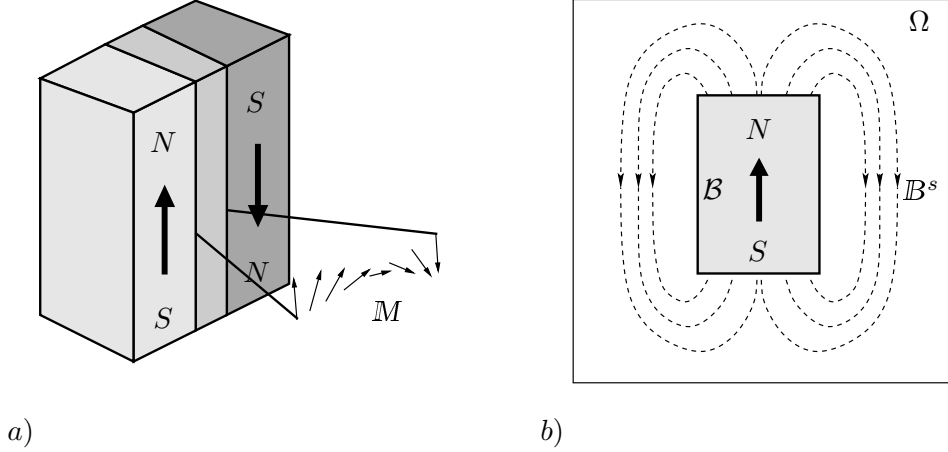


Figure 5.3: *Magnetic domain walls and energy in free space occupied by the body.* a) Two adjacent domains with different orientation of magnetization are separated by domain walls which act as a smooth transition between these homogeneously magnetized regions. In the exchange energy (5.23) accounts for this by penalizing the gradients of the order parameter. b) Any magnetized body creates a self field in its surrounding explicitly the functional (5.30) accounts for this energy in the complete region Ω .

Magnetocrystalline Anisotropy Energy Density. The inherent crystalline structure of the material is characterized by the magnetization relative to the easy axes of the material. In the large deformation context the uniaxial anisotropy depicted in Figure 5.2 a) can be given by

$$\Xi_{aniso}(\mathbf{C}, \mathbf{M}; \mathbf{A}) = \frac{K}{2} \{1 - [\mathbf{C} : (\mathbf{M} \otimes \mathbf{A})]^2\}, \quad (5.21)$$

where K is a material parameter. This referential energy can be interpreted as the pull back of the anisotropy energy from the current configuration Figure 5.2 b). For cubic magnetocrystalline anisotropy the energy landscape is shown in Figure 5.2 c) and the easy axes lie along the $\langle 100 \rangle$ or $\langle 111 \rangle$ directions of the crystal. The energy function takes the form

$$\Xi_{aniso}(\mathbf{C}, \mathbf{M}; \mathbf{A}_{i=1,2,3}) = \frac{K}{2} [(m_1 m_2)^2 + (m_2 m_3)^2 + (m_1 m_3)^2], \quad (5.22)$$

where $m_i := \mathbf{C} : (\mathbf{M} \otimes \mathbf{A}_i) = \text{tr}[\mathbf{C} \cdot (\mathbf{M} \otimes \mathbf{A}_i)]$ with $i = 1, 2, 3$ are the components of the current magnetization along the set of the three perpendicular cubic axes \mathbf{a}_1 , \mathbf{a}_2 and \mathbf{a}_3 in the current configuration.

Exchange Energy Density. The exchange energy Ψ_{ex} models the tendency of neighboring magnetizations to align. Focusing on isotropic response and considering that the deformation of the ferromagnetic material is negligible the energy is formulated as

$$\Xi_{ex}(\nabla \mathbf{M}) = \frac{A}{2} \nabla^T \mathbf{M} : \nabla \mathbf{M} = \frac{A}{2} \|\nabla \mathbf{M}\|^2, \quad (5.23)$$

where the length-scale parameter $A > 0$ is the exchange energy coefficient.

Energy density due to the magnetic field. The energy Ξ_{vac} defines the energy storage due to the presence of a magnetic field in the full space Ω . By resolving (5.10) for

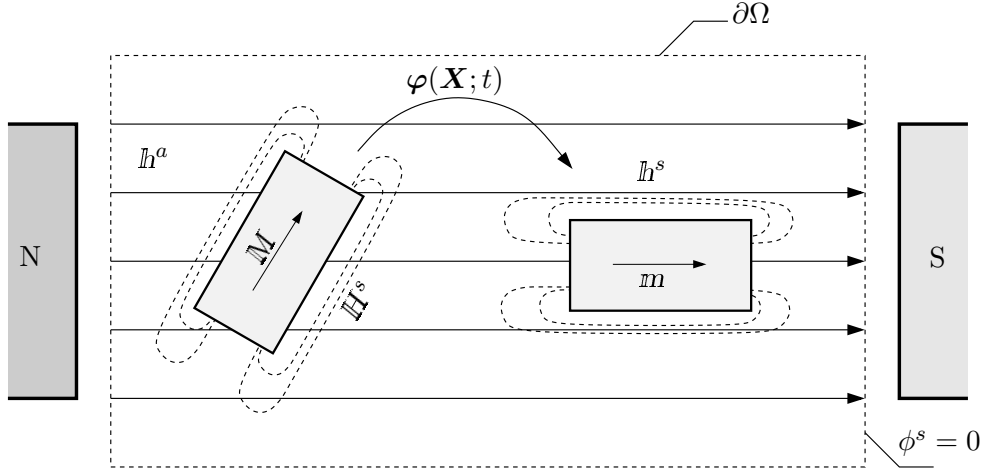


Figure 5.4: Motion of a magnetized body with strong magnetic anisotropy under the action of an externally applied magnetic field h^a . In the reference configuration, the magnetic state of the body is characterized by the magnetization \mathbf{M} . The magnetization creates a magnetic self-field \mathbb{H}^s . Under action of an applied magnetic field h^a causes the magnetization to rotate until it finally aligns along with the applied field. Due to the assumed strong anisotropy, this realignment causes a rotation of the body. In this deformed configuration, the Eulerian fields h^s and m can be identified. The mappings between the two configurations are given by $\mathbb{H}^s = \mathbf{F}^T \cdot h^s$ and $\mathbf{M} = \mathbf{F}^{-1} \cdot m$. Note, however, that the applied field is unaffected by the deformation, i.e. $h^a \equiv \mathbb{H}^a$.

the magnetic field $\mathbb{H} = \hat{\mathbb{H}}(\mathbf{C}, \mathbf{M}, \mathbb{B})$ one obtains

$$\Xi_{vac}(\mathbf{C}, \mathbf{M}, \mathbb{B}) = \frac{\mu_0 J}{2} \|\hat{\mathbb{H}}(\mathbf{C}, \mathbf{M}, \mathbb{B})\|_{\mathbf{C}^{-1}}^2 = \frac{1}{2\mu_0 J} \|\mathbb{B} - \rho_0 \mu_0 m_s \mathbf{M}\|_{\mathbf{C}}^2, \quad (5.24)$$

where the notation $\|*\|_{\mathbb{X}} := \sqrt{* \cdot \mathbb{X} \cdot *}$ is the norm with respect to the second-order tensor \mathbb{X} and $*$ denotes a first-order tensor.

5.2.2. Coupled Magnetomechanical Loading Functional

External magnetomechanical coupled loading in the region Ω are accounted via an Eulerian loading functional formulated as

$$L(\dot{\varphi}, \dot{m}; t) = \int_{\varphi_t(\Omega)} \rho(\bar{\gamma} \cdot \dot{\varphi} + \mu_0 h^a \cdot \mathcal{L}_v m) dv + \int_{\partial\varphi_t(\Omega)} \bar{\mathbf{t}} \cdot \dot{\varphi} da, \quad (5.25)$$

given in terms of the mechanical body forces $\bar{\gamma}$ per unit mass, the mechanical tractions $\bar{\mathbf{t}} = \bar{\boldsymbol{\sigma}} \cdot \mathbf{n}$ and the applied magnetic field h^a . The rate functional depends on the rates of the deformation map $\dot{\varphi}$ and the objective Lie rate $\mathcal{L}_v m$ of the current magnetization director m . This can be reformulated in the Lagrangian setting via a pull back operation as

$$L(\dot{\varphi}, \dot{\mathbf{M}}; t) = \int_{\Omega} \rho_0(\bar{\gamma} \cdot \dot{\varphi} + \mu_0 m_s h^a \cdot \mathbf{F} \cdot \dot{\mathbf{M}}) dV + \int_{\partial\Omega} \bar{\mathbf{t}} \cdot \dot{\varphi} dA, \quad (5.26)$$

where $\bar{\mathbf{t}} = \bar{\mathbf{P}} \cdot \mathbf{N}$ is the mechanical traction field in the Lagrangian setting with $\bar{\mathbf{P}}$ being the two-point Piola-Kirchhoff stress. Recall that the applied magnetic field is not affected by the deformation of the solid such that numerically $h^a \equiv \mathbb{H}^a$.

5.2.3. Magnetic energy Functional of Micro-Magneto-Elasticity

With the definition of the free-energy functions a coupled magnetomechanical functional E can be formulated in the full space Ω as

$$E(\mathbf{C}, \mathbb{M}, \mathbb{B}) = \int_{\Omega} \Xi_{mat}(\mathbf{C}, \mathbb{M}, \nabla \mathbb{M}; \mathbb{A}) + \frac{\mu_0 J}{2} \|\hat{\mathbb{H}}(\mathbb{M}, \mathbb{B})\|_{\mathcal{C}^{-1}}^2 dV. \quad (5.27)$$

It should be pointed out here that the magnetic field \mathbb{H} decomposes according to (5.7) into $\mathbb{H} = \mathbb{H}^a + \mathbb{H}^s$. Then, following KANKANALA & TRIANTAFYLIDIS [118] all terms containing \mathbb{H}^a can be dropped from the functional and reformulated in terms of only the self fields as

$$E(\mathbf{C}, \mathbb{M}, \mathbb{B}^s) = \int_{\Omega} \Xi_{mat}(\mathbf{C}, \mathbb{M}, \nabla \mathbb{M}; \mathbb{A}) + \frac{\mu_0 J}{2} \|\hat{\mathbb{H}}^s(\mathbb{M}, \mathbb{B}^s)\|_{\mathcal{C}^{-1}}^2 dV. \quad (5.28)$$

The reader is referred to KANKANALA & TRIANTAFYLIDIS [118] for a detailed discussion regarding the same. A partial Legendre transformation with respect to the magnetic slot that replaces the magnetic induction \mathbb{B}^s by the magnetic field \mathbb{H}^s gives

$$E^*(\mathbf{C}, \mathbb{M}, \mathbb{H}^s) = \inf_{\mathbb{B}^s} \left[E(\mathbf{C}, \mathbb{M}, \mathbb{B}^s) - \mathbb{H}^s \cdot \mathbb{B}^s \right]. \quad (5.29)$$

This transformation affects only the free-space contribution of the free-energy function. The necessary condition for the Legendre transformation results in (5.10). Using this as an elimination equation for \mathbb{B}^s one can obtain from (5.29) the *magnetic Gibbs energy functional*

$$E^*(\mathbf{C}, \mathbb{M}, \mathbb{H}^s) = \int_{\Omega} \Xi dV = \int_{\Omega} \Xi_{mat}(\mathbf{C}, \mathbb{M}, \nabla \mathbb{M}; \mathbb{A}) - \rho_0 \mu_0 m_s \mathbb{M} \cdot \mathbb{H}^s - \frac{\mu_0 J}{2} \|\mathbb{H}^s\|_{\mathcal{C}^{-1}}^2 dV \quad (5.30)$$

governed by the objective state \mathbf{c} which was defined in (5.13). The reduced Gibbs energy functional (5.30) will be used in the variational structure that follows. However to keep the notation compact $(\cdot)^*$ is dropped in the following.

5.2.4. Objective Dissipation Potential Functional

A kinetic law is required to model the time dependent, dynamic evolution of the magnetization order parameter \mathbb{M} . An objective formulation in terms of the Lie rate of the magnetization is given as

$$d(\dot{\mathbb{m}}; t) = \frac{\eta}{2} \text{tr}(\mathcal{L}_{\mathbf{v}} \mathbb{m} \otimes \mathcal{L}_{\mathbf{v}} \mathbb{m}). \quad (5.31)$$

The scalar parameter η is a viscosity coefficient that governs the rate of the magnetization evolution. A pull back operation gives the Lagrangian description as

$$d(\dot{\mathbb{M}}; \mathbf{C}, t) = \frac{\eta}{2} \|\mathbf{F} \cdot \dot{\mathbb{M}}\|^2 = \frac{\eta}{2} \|\dot{\mathbb{M}}\|_{\mathcal{C}}^2. \quad (5.32)$$

The dissipation potential functional over the whole domain is defined in terms of the magnetization director as

$$D(\dot{\mathbb{M}}; \boldsymbol{\varphi}, t) = \frac{\eta}{2} \int_{\mathcal{B}} \|\dot{\mathbb{M}}\|_{\mathcal{C}}^2 dV. \quad (5.33)$$

5.3. Variational Formulation of Finite Strain Micromagnetics

The rates of the primary fields $\{\dot{\boldsymbol{\varphi}}, \dot{\mathbb{M}}, \dot{\phi}^s\}$ at a given state $\{\boldsymbol{\varphi}, \mathbb{M}, \phi^s\}$ are governed by a dynamic variational functional of the form

$$W(\dot{\boldsymbol{\varphi}}, \dot{\mathbb{M}}, \dot{\phi}^s) := \frac{d}{dt} E(\boldsymbol{\varphi}, \mathbb{M}, \phi^s) + D(\dot{\mathbb{M}}; \boldsymbol{\varphi}, t) - L(\dot{\boldsymbol{\varphi}}, \dot{\mathbb{M}}; t). \quad (5.34)$$

In terms of the Gibbs energy functional E (5.30), the dissipation potential D (5.33) and the magnetomechanical loading functional L (5.26). Expanding the respective terms the energy functional can be given as

$$\begin{aligned} W(\dot{\boldsymbol{\varphi}}, \dot{\mathbb{M}}, \dot{\phi}^s) := & \frac{d}{dt} \int_{\Omega} \underbrace{\Xi_{mat}(\mathbf{C}, \mathbb{M}, \nabla \mathbb{M}; \mathbb{A})}_{\text{magneto-elastic}} - \underbrace{\rho_0 \mu_0 m_s \mathbb{H}^s \cdot \mathbb{M}}_{\text{self field}} - \underbrace{\frac{\mu_0 J}{2} \|\mathbb{H}^s\|_{\mathbf{C}^{-1}}}_{\text{vacuum}} dV \\ & + \int_{\Omega} \underbrace{\frac{\eta}{2} \|\dot{\mathbb{M}}\|_{\mathbf{C}}^2}_{\text{dissipation}} dV - \int_{\Omega} \underbrace{\rho_0 \mu_0 m_s \mathbb{h}^a \cdot \mathbf{F} \cdot \dot{\mathbb{M}}}_{\text{Zeeman}} dV - \int_{\Omega} \underbrace{\rho_0 \bar{\boldsymbol{\gamma}} \cdot \dot{\boldsymbol{\varphi}}}_{\text{body forces}} dV \\ & - \int_{\partial\Omega} \underbrace{\bar{\mathbf{t}} \cdot \dot{\boldsymbol{\varphi}}}_{\text{tractions}} dA. \end{aligned} \quad (5.35)$$

Individual contributions to the variational functional are highlighted. Applying the divergence theorem this functional can be reformulated as

$$\begin{aligned} W(\dot{\boldsymbol{\varphi}}, \dot{\mathbb{M}}, \dot{\phi}^s) = & - \int_{\Omega} \text{Div}[\partial_{\mathbf{F}} \Xi + \rho_0 \bar{\boldsymbol{\gamma}}] \cdot \dot{\boldsymbol{\varphi}} dV + \int_{\partial\Omega} (\partial_{\mathbf{F}} \Xi \cdot \mathbf{N} - \bar{\mathbf{t}}) \cdot \dot{\boldsymbol{\varphi}} dA \\ & + \int_{\mathcal{B}} (\partial_{\mathbb{M}} \Xi - \text{Div}[\partial_{\nabla \mathbb{M}} \Xi] + \eta \mathbf{C} \cdot \dot{\mathbb{M}} - \rho_0 \mu_0 m_s \mathbf{F}^T \cdot \mathbb{h}^a) \cdot \dot{\mathbb{M}} dV \\ & + \int_{\partial\mathcal{B}} (\partial_{\nabla \mathbb{M}} \Xi \cdot \mathbf{N}) \cdot \dot{\mathbb{M}} dA - \int_{\Omega} \text{Div}[-\partial_{\mathbb{H}^s} \Xi] \dot{\phi}^s dV \\ & - \int_{\partial\Omega} \partial_{\mathbb{H}^s} \Xi \cdot \mathbf{N} \dot{\phi}^s dA. \end{aligned} \quad (5.36)$$

The rates of the deformation map, the magnetization director and the self magnetic potential at a given state are governed by the *rate type saddle point variational principle*

$$\{\dot{\boldsymbol{\varphi}}, \dot{\mathbb{M}}, \dot{\phi}^s\} = \arg \left\{ \inf_{\dot{\boldsymbol{\varphi}} \in \mathcal{W}_{\dot{\boldsymbol{\varphi}}}} \sup_{\dot{\phi}^s \in \mathcal{W}_{\dot{\phi}^s}} \inf_{\dot{\mathbb{M}} \in \mathcal{W}_{\dot{\mathbb{M}}}} W(\dot{\boldsymbol{\varphi}}, \dot{\mathbb{M}}, \dot{\phi}^s; t) \right\}. \quad (5.37)$$

The admissible fields for the deformation gradient and self potential on the complete space Ω are given by Dirichlet conditions

$$\mathcal{W}_{\dot{\boldsymbol{\varphi}}} := \{\dot{\boldsymbol{\varphi}} \in \mathcal{R}^d \mid \dot{\boldsymbol{\varphi}} = \dot{\bar{\boldsymbol{\varphi}}} \text{ on } \partial\Omega_D^{\boldsymbol{\varphi}}\} \quad \text{and} \quad \mathcal{W}_{\dot{\phi}^s} := \{\dot{\phi}^s \in \mathcal{R} \mid \dot{\phi}^s = \dot{\bar{\phi}^s} \text{ on } \partial\Omega_D^{\phi^s}\}, \quad (5.38)$$

while for the magnetization director which is a priori defined only in the ferromagnetic body \mathcal{B} the admissible space is

$$\mathcal{W}_{\dot{\mathbb{M}}} := \{\dot{\mathbb{M}} \in T_{\mathbb{M}} \mathcal{S}^{d-1} \mid \nabla \mathbb{M} \cdot \mathbf{n} = \mathbf{0} \text{ on } \partial\mathcal{B}\}, \quad (5.39)$$

where $T_M \mathcal{S}^{d-1}$ is the *tangent space* of \mathcal{S}^{d-1} at M . Similar to the last chapter, see (4.29) the variation of the rate of the magnetization director appears as

$$\delta \dot{M} = \delta \dot{\Theta} \times M, \quad (5.40)$$

where $\dot{\Theta} \in \mathcal{R}^d$ is the spin of the magnetization. Then the necessary condition of the above variational principle is provided by the first variation of the rate type functional (5.36) with the exact update of the magnetization director (5.40)

$$\begin{aligned} \delta W(\dot{\varphi}, \dot{M}, \dot{\phi}^s) = & - \int_{\Omega} \text{Div}[\partial_{\mathbf{F}} \Xi + \rho_0 \bar{\gamma}] \cdot \delta \dot{\varphi} \, dV - \int_{\Omega} \text{Div}[-\partial_{\mathbb{H}^s} \Xi] \delta \dot{\phi}^s \, dV \\ & + \int_{\mathcal{B}} [M \times (-H_{eff} + \eta \mathbf{C} \cdot \dot{M})] \cdot \delta \dot{\Theta} \, dV \\ & + \int_{\partial\Omega} [M \times (\partial_{\nabla M} \Xi \cdot \mathbf{N})] \cdot \delta \dot{\Theta} \, dA - \int_{\partial\Omega} \partial_{\mathbb{H}^s} \Xi \cdot \mathbf{N} \delta \dot{\phi}^s \, dA \\ & + \int_{\partial\Omega} (\partial_{\mathbf{F}} \Xi \cdot \mathbf{N} - \bar{\mathbf{t}}) \cdot \delta \dot{\varphi} \, dA \end{aligned} \quad (5.41)$$

for the virtual fields $\{\delta \dot{\varphi}, \delta \dot{\Theta}, \delta \dot{\phi}^s\}$. The Euler-Lagrange equations for the necessary condition of the variational principle are

$$\begin{aligned} \text{Div}[\partial_{\mathbf{F}} \Xi + \rho_0 \bar{\gamma}] &= \mathbf{0} \quad \text{in } \Omega, \\ \text{Div}[-\partial_{\mathbb{H}^s} \Xi] &= 0 \quad \text{in } \Omega, \\ M \times (-H_{eff} + \eta \mathbf{C} \cdot \dot{M}) &= \mathbf{0} \quad \text{in } \mathcal{B}, \end{aligned} \quad (5.42)$$

with the boundary conditions $\partial_{\mathbf{F}} \Xi \cdot \mathbf{N} = \bar{\mathbf{t}}$ on $\partial\Omega$, $\partial_{\mathbb{H}^s} \Xi \cdot \mathbf{N} = \bar{\mathbb{B}}$ on $\partial\Omega$ and $M \times (\partial_{\nabla M} \Xi \cdot \mathbf{N}) = \mathbf{0}$ on $\partial\mathcal{B}$. Above the *effective magnetic field* H_{eff} is introduced as the force acting on the magnetization

$$H_{eff} := \text{Div}[\partial_{\nabla M} \Xi] - \partial_M \Xi + \rho_0 \mu_0 m_s \mathbf{F}^T \cdot \mathbf{h}^a. \quad (5.43)$$

If the rate of the magnetization director \dot{M} vanishes, (5.42)₃ yields the stationary equilibrium equation given by BROWN [32],

$$M \times H_{eff} = \mathbf{0} \quad \text{in } \mathcal{B}. \quad (5.44)$$

which states that the torque exerted on the magnetization by the effective magnetic field must be at equilibrium. Now, by taking the cross product of the Euler equation involving the magnetization director (5.42)₃ with the vector M gives the evolution equation for the magnetization director

$$\mathbf{C} \cdot \dot{M} = -\frac{1}{\eta} M \times M \times H_{eff}, \quad (5.45)$$

which constitutes the large deformation counterpart of the Landau-Lifshitz equation of micromagnetics derived in (4.32). Considering high mechanical stiffness and no magnetostriction in the inclusions, the right Cauchy Green tensor is given as $\mathbf{C} \rightarrow \mathbf{1} \in \mathcal{B}$.

Table 5.1: Material parameters for permalloy (MIEHE & ETHIRAJ [168]).

No.	Parameter	Name	Value	Units
1.	β	Mechanical parameter 1	1.5	–
2.	μ	Mechanical parameter 2	8.32×10^7	N/m ²
3.	K	Anisotropy coefficient	5×10^2	N/m ²
4.	A	Exchange coefficient	1.3×10^{-11}	N
5.	$\rho_0 m_s$	Saturation magnetization	8×10^5	A/m
6.	η	Viscosity parameter	1×10^{-1}	Ns ² /m ²
7.	μ_0	Magnetic vacuum permeability	$4\pi \times 10^{-7}$	N/A ²

5.3.1. Space-Time Discrete Formulation of Finite Micromagnetics

For the considered constitutive state variable $\mathbf{c} := \{\nabla \boldsymbol{\varphi}, \mathbb{M}, \nabla \mathbb{M}, -\nabla \phi^s\}$ the finite element interpolation in the incremental setting is given by

$$\mathbf{c}^h = \mathfrak{B}(\mathbf{X})\mathfrak{d} \quad \text{with} \quad \mathfrak{d} := \mathbf{A}_{I=1}^{N^h} [\boldsymbol{\varphi}_I, \mathbb{M}_I, \phi_I^s]^T. \quad (5.46)$$

In terms of the nodal variable vectors \mathfrak{d} at a typical nodal point of the finite element mesh and the *strain-displacement* vector in the referential setting $\mathfrak{B}(\mathbf{X})$. The space-time discrete variational principle appears as

$$\mathfrak{d} = \arg \left\{ \text{stat}_a \int_{\Omega} W^\tau(\mathfrak{B} \mathfrak{d}) dV \right\}, \quad (5.47)$$

in terms of the incremental potential W^τ conjugate to the rate type potential defined in (5.34). The problem is implemented by a Newton-Raphson method with updates $\mathfrak{d} \leftarrow \mathfrak{d} - \mathfrak{K}^{-1} \mathfrak{R}$ based on the residual and tangent arrays

$$\mathfrak{R} := \int_{\Omega} \mathfrak{B}^T [\partial_{\mathbf{c}} W^\tau] dV \quad \text{and} \quad \mathfrak{K} := \int_{\Omega} \mathfrak{B}^T [\partial_{\mathbf{c}\mathbf{c}}^2 W^\tau] \mathfrak{B} dV. \quad (5.48)$$

Note that the implementation follows the same procedure as discussed in Subsection 4.2.4 and Subsection 4.2.5. This entails the split of the constitutive variables into $\mathbf{c} = \mathbf{c}_M \cup \mathbf{c}_{\varphi\phi^s}$ and the consistent split of the space-time discrete potential along with the tangent and residual arrays. For brevity a detailed explanation regarding the same has been skipped here. The reader is referred to the previous chapter for more details.

5.4. Numerical Examples: Domain Evolution, Objectivity and Large Strains

Numerical simulations that showcase the capability of the proposed framework to capture domain evolution, to satisfy objectivity restrictions and predict magnetomechanical interactions at large deformations are shown. Representative examples are selected to highlight the specific features of the model. Normalization of the material parameters is carried out for numerical stability, a short comment is provided regarding the same.

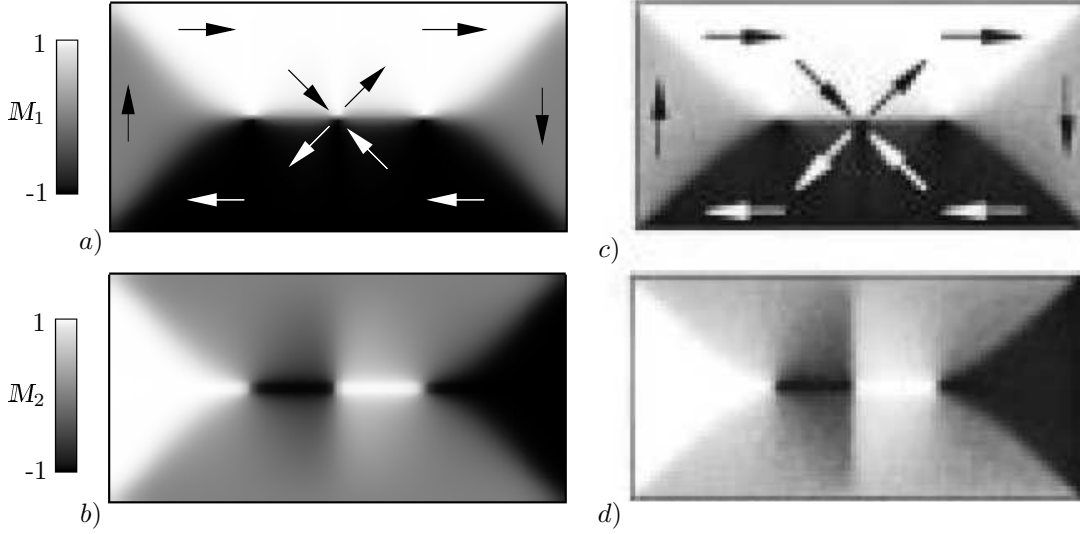


Figure 5.5: *Theoretical equilibrium states of the magnetization director \mathbb{M} for a thin film of soft magnetic permalloy material. The boundary value problem is allowed to evolve over time from a random distribution of the order parameter. The observed equilibrium states predicted by the present formulation, a) and b), agree well with the *single-crostate* equilibrium states, c) and d), found by RAVE & HUBERT [199].*

5.4.1. Normalization of the material parameters

Numerically a large variation in material parameters causes problems in the solution procedure, especially in simulations that are highly non-linear due to large deformations. In this case a variation of 10^{18} is seen between the exchange parameter and the mechanical stiffness, see table. 5.1, which leads to numerical instabilities. To overcome such difficulties a normalization of material parameters is done with respect to four physical parameters, mechanical stiffness μ [N/m²], saturation magnetization per unit volume $\rho_0 m_s$ [A/m], magnetic exchange coefficient A [N] and viscosity η [Ns²/m²]. The normalized primary variables represented by $(\cdot)'$, in terms of their counterparts (\cdot) are related via

$$\varphi' = \varphi \sqrt{\mu/A}, \quad \phi^{s'} = \phi^s \sqrt{\mu/A(\rho_0 m_s)^2}, \quad M' = M \quad \text{and} \quad t' = t \sqrt{\mu/\tilde{\eta}}. \quad (5.49)$$

The modified equations, in terms of the normalized variables, remain the same as presented in the previous section. All simulations presented in the following section are performed with normalized constants, however the corresponding material parameters and sample dimensions are presented in physical units for ease of reading and interpretation.

5.4.2. Problem 1: Standard Micromagnetic Problem

Ferromagnetic materials show spontaneous magnetic domains under the Curie temperature. Experimentally, magnetic domains in demagnetized samples have been observed with the help of polarization optics, Kerr microscopy and other techniques, by BITTER [20], KHAIYER & O'DELL [126], DEFOUG ET AL. [52] and RAVE [199]) among many others. From a theoretical perspective, the formation of magnetic domains can be viewed as the stationary solution of the coupled magnetomechanical functional (5.34). As a benchmark problem to evaluate the capability of the present formulation to capture domain

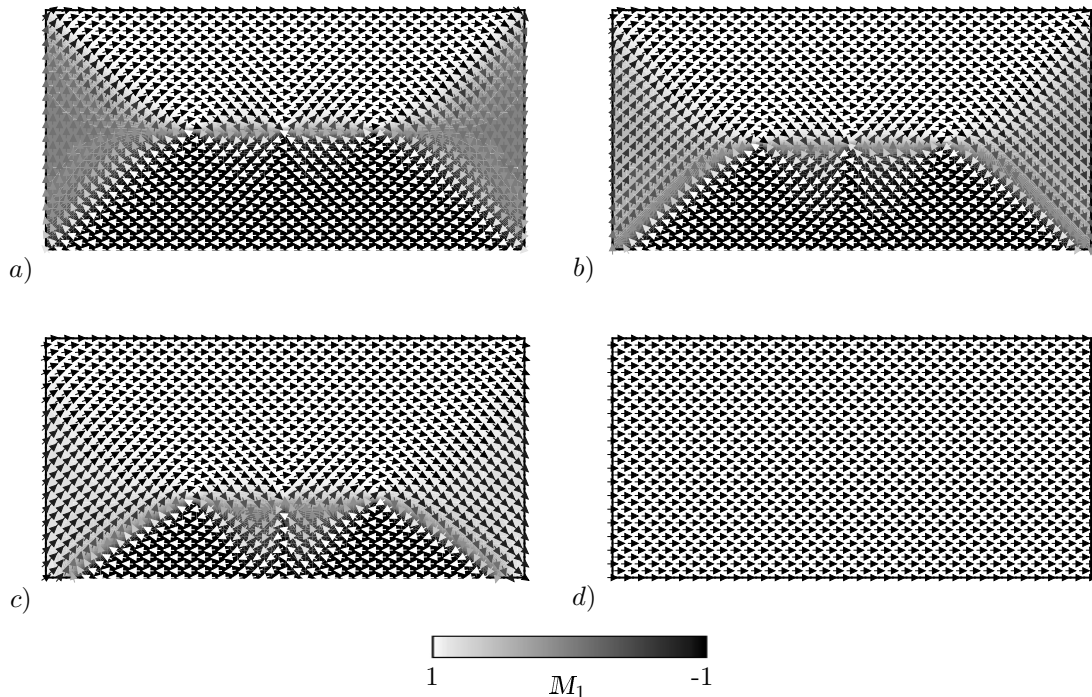


Figure 5.6: *Reorientation of magnetization under externally applied magnetic field loading in horizontal direction.* Starting from the equilibrium structure obtained previously *a)*, an external magnetic field is applied in the horizontal direction. This causes a reorientation of the directors in the field direction *b)* and *c)*. Upon reaching coercive field the sample is completely magnetized in field direction *d)*.

evolution, consider the standard problem 1 from the μ Mag group [56], see Figure 5.5. The problem consists of a thin film of the magnetically soft material, known as permalloy, that is initialized with a random distribution of the order parameter and appropriate boundary conditions are prescribed to suppress rigid body motions. The dimensions of the sample are $1 \times 2 \mu\text{m}^2$ and the material parameters are listed in table 5.1. The simulation is run until an equilibrium structure for the magnetization is obtained. The results of the simulation are depicted in Figure 5.5 *a)*, *b)*. As shown, the simulation results are in perfect agreement with the results presented by RAVE & HUBERT [199], see Figure 5.5 *c)*, *d)*. The reader is referred to the same for further explanation on the reasoning for formation of such domains. Note that other equilibrium structures shown in [199] can be obtained depending on the initial distribution of the magnetization.

The motion of magnetization under application of an external magnetic field in the horizontal direction is presented in Figure 5.6 *a)*–*d)*. The magnetization directors reorient in direction of the applied field such that the domains with magnetization parallel to the external field grows. Upon reaching coercive field, magnetization in the sample is completely reoriented in field direction. Further application of external field does not influence the magnetization.

5.4.3. Problem 2: Behavior Under Superimposed Rigid body Motions

The second example underlines the necessity of objectivity considerations and ability of the model to accurately capture this phenomenon. A ferromagnetic sample of permalloy material, which is homogeneously magnetized along its easy axis is chosen. A rigid body

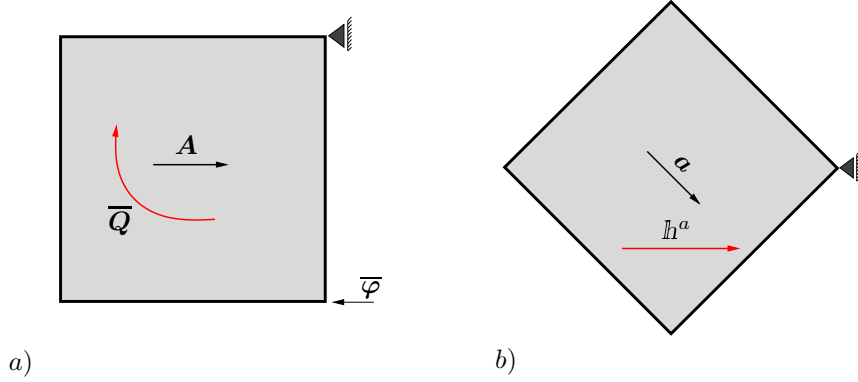


Figure 5.7: *Boundary value problem to ensure objectivity constraints are fulfilled. a) For a homogeneous premagnetized sample, the easy axis A and the magnetization M (not shown), point in horizontal direction in the reference configuration. b) A rigid-body rotation causes the easy axis and the magnetization to rotate with the sample. An external field H^a is applied to the sample in the horizontal direction.*

motion is superimposed onto the body such that the sample undergoes a rotation of 45° in clockwise direction. Then, an external magnetic field is applied in the horizontal direction. After full saturation of the magnetization, the magnetic field is removed from the sample so that the magnetizations rotate back into the easy directions. Finally, the sample is rotated back into the initial configuration. The boundary value problem is illustrated in Figure 5.7. The behavior of the sample under the applied rigid body motion and external field is shown in Figure 5.8, in which the current magnetization directors m are plotted for understanding. White arrows indicate average poling in the sample for clarity. The magnetic dissipation is plotted against time in the center of the figure. Various states of the sample are marked from Figure 5.8 a)–d). Figure 5.8 a) shows the sample with magnetization pointing in the horizontal direction (along easy axis). A superimposed rigid body motion causes the sample to rotate 45° in the clockwise direction, as depicted in Figure 5.8 b). The magnetization also rotates with the sample. Note that such a rotation must not entail magnetization dissipation. As a natural outcome of the formulation, this is fulfilled, which can be seen in the dissipation plot between points a) to b). Upon application of an external magnetic field, in the horizontal direction, magnetization vectors rotate in the direction of the applied field as shown in Figure 5.8 c). The rotation of magnetization (relative to the material) goes along with magnetic dissipation as shown in the dissipation plot from Figure 5.8 b)–c). Now upon removal of the external field magnetization vectors rotates back into the direction of the (rotated) easy axis. This rotation again goes along with magnetic dissipation, see Figure 5.8 c)–d). Finally, the sample is rotated back to its initial configuration, which is clearly not a dissipative process, see Figure 5.8 d)–a).

5.4.4. Problem 3: Circular inclusions Embedded in Elastomeric Matrix

The following example analyses the behavior of two ferromagnetic inclusions embedded in a non-magnetic elastomeric matrix under the application of an external field. The inclusions are assumed to be made of soft ferromagnetic material permalloy with material parameters given in table. 5.1. Material parameters of the elastomer are given in table. 5.2. Note that the easy axis of the ferromagnetic particles are assumed to point in

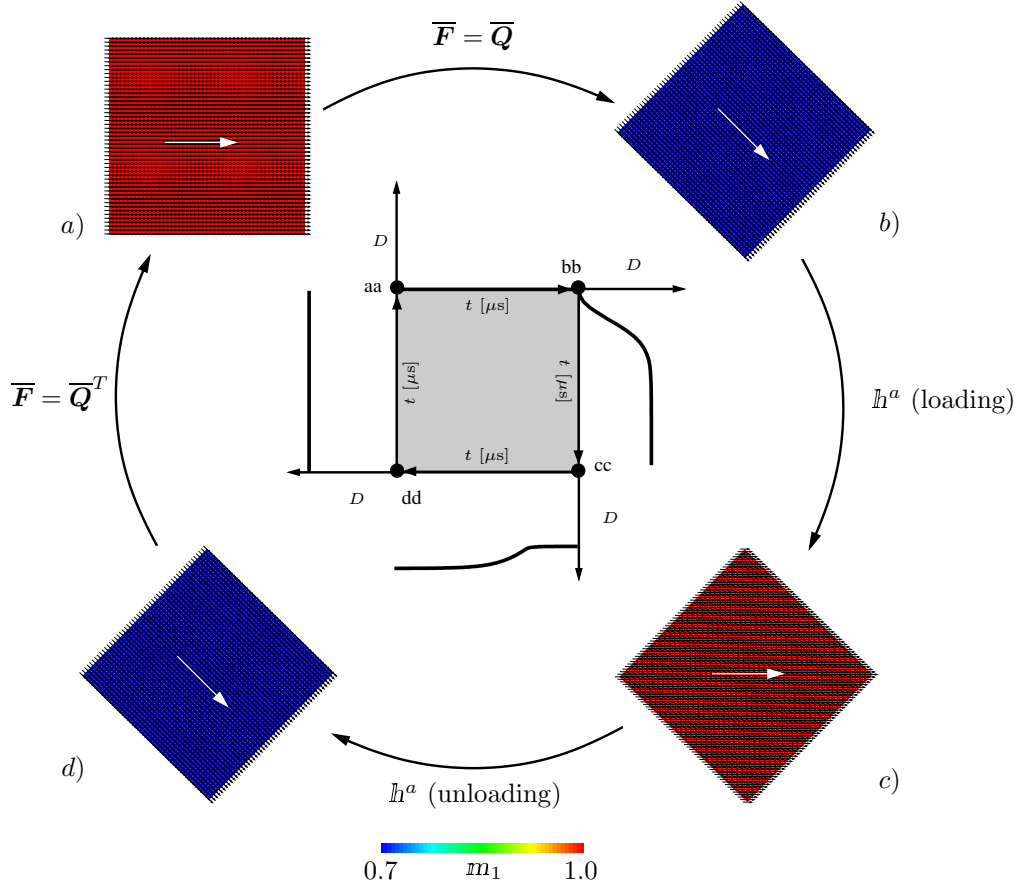


Figure 5.8: Investigation of objective dissipative response of proposed framework under superimposed rigid-body motion. *a) \rightarrow b)* a rigid-body rotation $\overline{\mathbf{F}} = \overline{\mathbf{Q}}$ is applied on the body. Magnetization directors rotate with the sample. This rotation of the directors is not a dissipative process as is indicated in the central plot of the dissipation potential D . *b) \rightarrow c)* Upon application of a magnetic field h^a in horizontal direction, the rotated magnetization directors align with it. This rotation is a dissipative process as indicated by the central plot. Saturation of the magnetization, also saturates the dissipation potential. *c) \rightarrow d)* When the magnetic loading is removed, the magnetization directors rotate back into the easy direction. This process is accompanied by another increase of dissipation. *d) \rightarrow a)* when the sample is finally rotated back into its initial configuration, the magnetizations follow this rotation. However as this rotation is associated with a rigid-body motion, no dissipation is expected. This is again reconfirmed by the central plot of the dissipation potential.

Table 5.2: Material parameters for the soft matrix material (MIEHE ET AL. [177]).

No.	Parameter	Name	Value	Units
1.	β	Mechanical parameter 1	10	–
2.	μ	Mechanical parameter 2	5×10^3	N/m ²
3.	μ_0	Magnetic vacuum permeability	$4\pi \times 10^{-7}$	N/A ²

the vertical direction. The boundary value problem and mesh discretization is shown in [Figure 5.9 a\)](#). The mechanical deformation and magnetic potential at the outer edges of the elastomer are constrained. The finite element mesh is refined within the inclusions to properly resolve the phase field. A random distribution of the magnetization, similar to the previous example, is prescribed in both circular inclusions as shown in [Figure 5.9 b\)](#). The magnetization directors are allowed to freely evolve from a random state in order to

eventually converge to some stable equilibrium structure, as shown in the evolution snapshots in Figure 5.9 b). The temporal evolution of magnetization results finally in a vortex structure, which is an energy minimum considering the boundary conditions and sample dimensions. Similar domain observations has been experimentally shown in SCHNEIDER ET AL. [210]. Following this the behavior of the sample under application of an external field h^a throughout the whole domain, is analyzed. Figure 5.10 a) shows the interaction of the particles under application of an external field in the horizontal direction. Similarly, Figure 5.10 b) shows the interaction of the particles when the applied field points in vertical direction. In both cases, the applied field causes the magnetizations to align in the direction of the applied field. The self field H^s evolves along with the magnetization in the inclusions. This in turn induces Maxwell interactions between the inclusions. The equipotential contour lines of the self field in the whole domain are shown along with contour plots of the magnetic potential field inside the inclusions. The potential in the inclusions clearly shows the formation of magnetically 'north' and 'south' poles.

The varied magnetic field application in turn evokes a varied mechanical response. When field is applied in the horizontal direction both particles magnetize in horizontal direction. Such configuration, which involves strong interactions in the sense north–north/south–south (observe equipotential lines) clearly induces repulsion of the particles. In the case of vertical loading, where we have strongest magnetic interaction in the sense of north–south, the particles attract. Both simulation results are in perfect agreement with physical expectations. The elastomeric matrix undergoes immense mechanical deformations Figure 5.11. The plot of displacement (of the upper inclusion) for both cases is plotted in Figure 5.12. Snapshots of the horizontal and vertical component of the

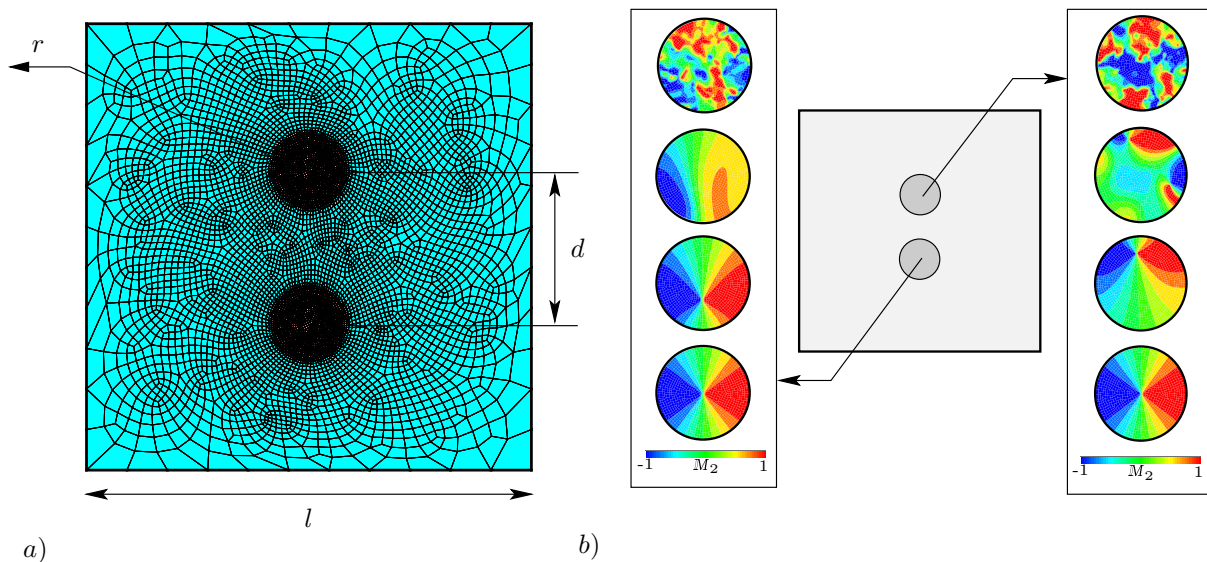


Figure 5.9: *Boundary value problem analyzing two ferromagnetic inclusions embedded in elastomer (non-magnetic) matrix. a)* The elastomeric matrix with square geometry is mechanically clamped along its outer boundaries of side length $l = 1.2 \mu\text{m}$. Two ferromagnetic particles with radius of $r = 0.1 \mu\text{m}$ are separated by distance $d = 0.4 \mu\text{m}$. The finite element discretization is performed with four node quad elements. Finer mesh discretization is employed within the particles to allow for the resolution of magnetic domains. *b)* Evolution of equilibrium domain pattern within the two particles starting from a random distribution of magnetization order parameter (from top to bottom). At equilibrium, the domain configuration is characterized by a vortex structure.

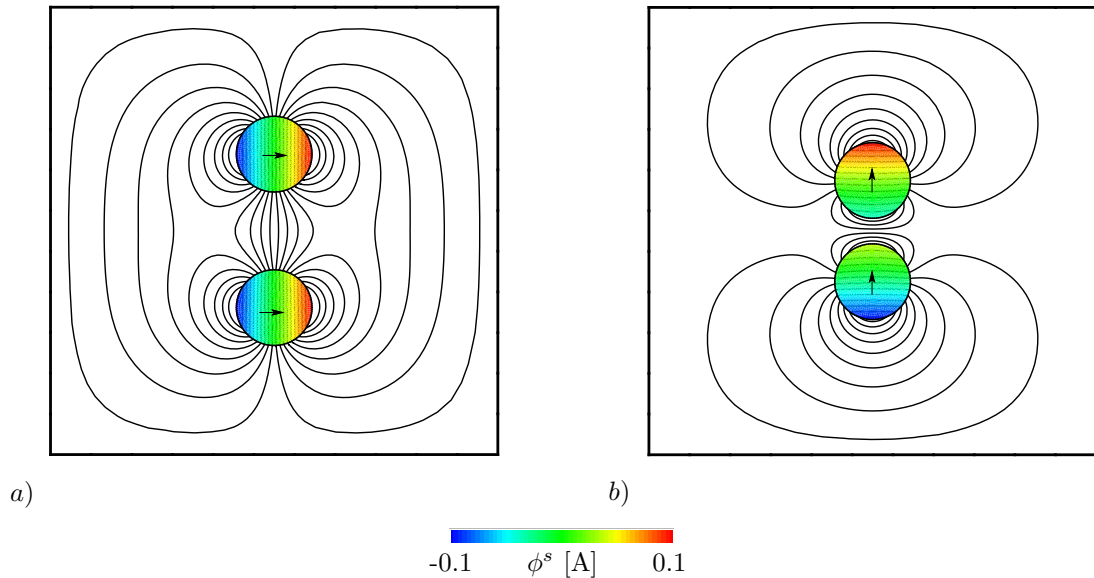


Figure 5.10: Ferromagnetic particles interacting with applied magnetic fields in the horizontal and vertical direction. *a)* Under horizontal magnetic field h^a , the particles fully magnetize in horizontal direction, indicated by black arrows. The resulting magnetic state and the following mechanical interaction between the particles causes repulsion of the particles. *b)* On the other hand application of a vertical field h^a , the particles fully magnetize in vertical direction, indicated again by black arrows. The magnetic state and mechanical interactions in this case causes attraction between the particles. In both pictures, the contour plot shows the magnetic self potential ϕ^s and the line plot shows the associated equipotential lines.

magnetization for both cases are shown in [Figure 5.12 a\), b\) c\)](#) and [Figure 5.12 a\), d\), e\)](#) respectively. Observe that the mechanical deformation saturates with the saturation of the magnetization.

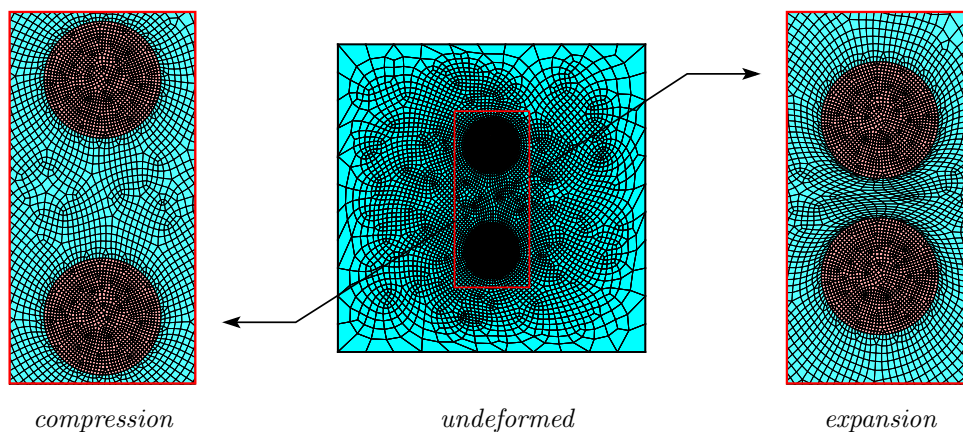


Figure 5.11: Mesh distortions of the system under the application of horizontal and vertical magnetic field, due to particle interactions. The FE mesh deformations in the undeformed, compression (vertical applied field h^a) and expansion (horizontal applied field h^a) state of the system are shown in the fully saturated states. Minimum mesh distortions are seen within the inclusion due to high stiffness and no magnetostriction. Maximum mesh distortion is seen under vertical field loading, when particles attract and come close to each other.

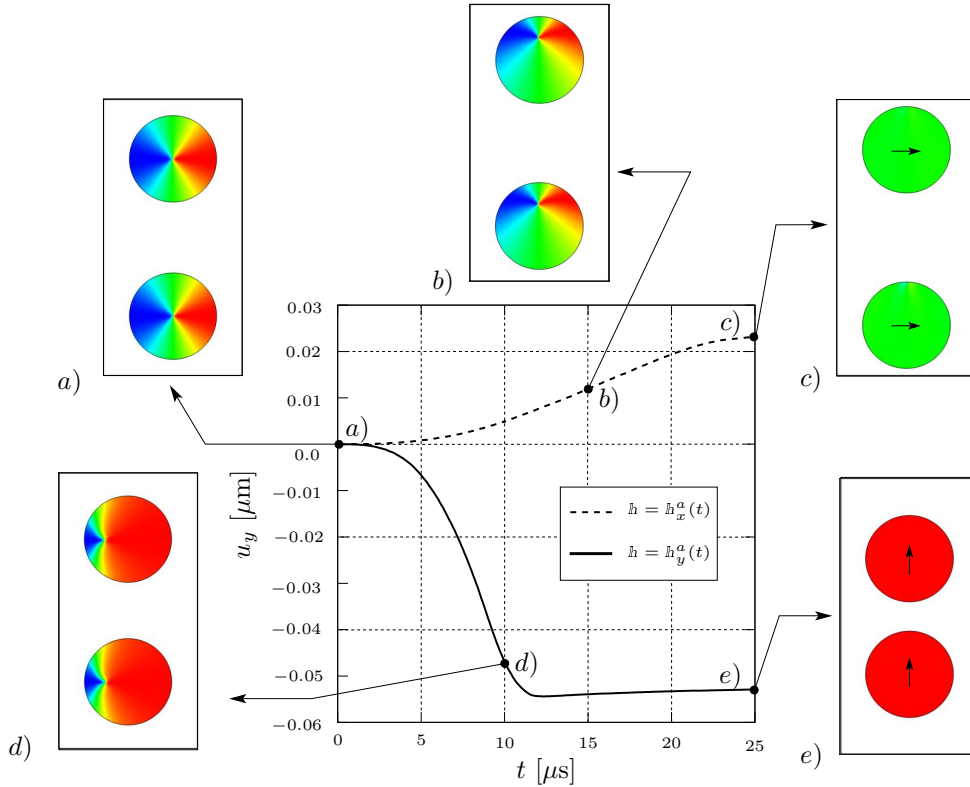


Figure 5.12: Contour of magnetization and plot of displacement under applied magnetic field \mathbf{h}^α . Under application of an external field in the vertical direction, the upper particle moves upwards (shown with dashed line). This motion goes along with magnetization reorientation of the inclusions shown in pictures a), d) and e). When applied field points in horizontal direction, the particle moves downwards (shown with solid line) along with magnetization reorientation a), b) and c). Saturation of magnetization under large fields in turn saturates the mechanical deformation.

5.4.5. Problem 4: Circular inclusions in a chain formation

As presented in Section 1.1, magnetorheological elastomers (MREs) are materials with micron sized ferromagnetic inclusions embedded in an elastomeric (non magnetic) matrix. The effective response of such materials can be tuned by microstructure design. Experiments have shown that the distribution of particles in MREs drives the overall behavior of the composite under the influence of an externally applied magnetic field DANAS ET AL. [47]. This has also been verified by numerical studies based on multiscale

Table 5.3: Material parameters for Iron [227].

No.	Parameter	Name	Value	Units
1.	β	Mechanical parameter 1	2.5	[-]
2.	μ	Mechanical parameter 2	8×10^8	N/m ²
3.	K	Anisotropy coefficient	4×10^4	N/m ²
4.	A	Exchange coefficient	1×10^{-12}	N
5.	$\rho_0 m_s$	Saturation magnetization	5×10^6	A/m
6.	η	Viscosity parameter	5×10^{-2}	Ns ² /m ²
7.	μ_0	Magnetic vacuum permeability	$4\pi \times 10^{-7}$	N/A ²

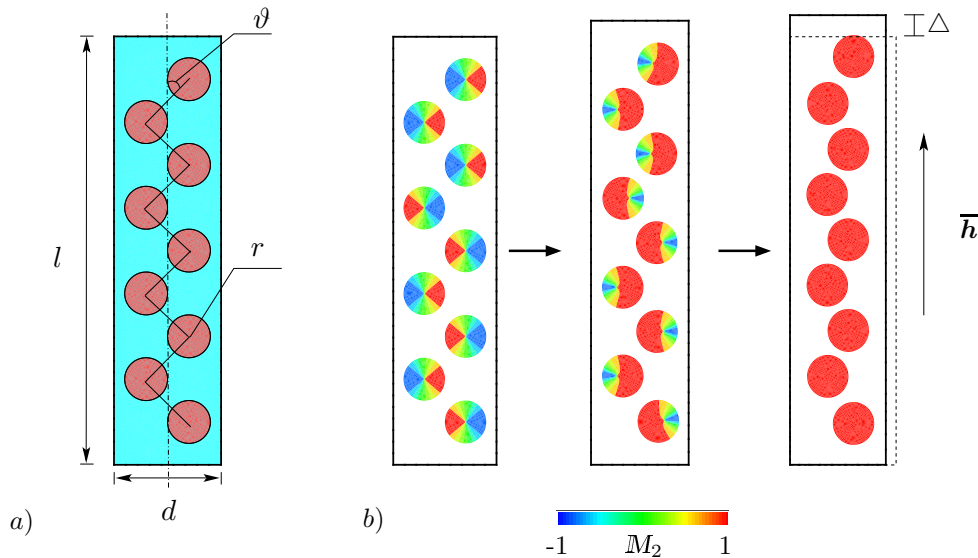


Figure 5.13: Behavior of a sample of magnetic inclusions embedded in a matrix, in chain arrangement at an angle of $\vartheta = 45^\circ$ under applied magnetic field. a) The boundary value problem consists of a rectangular elastomer specimen with side lengths of $l = 0.2 \mu\text{m}$ and $d = 0.05 \mu\text{m}$. Its meso-structure is characterized by a chain arrangement of ferromagnetic particles with radius $r = 0.01 \mu\text{m}$. b) Under the action of an external magnetic field \bar{h}^a , the body experiences an expansion in field direction. This deformation is due to the motion of ferromagnetic domains within the particles and the resulting particle–particle and particle–matrix interactions. The evolution of domains is visualized through a contour plot of the vertical component of the magnetization directors.

simulations by [122, 123]. To analyze the behavior of the current formulation to predict the influence of microstructure on the macro response two numerical examples are presented. Figure 5.13 a) and Figure 5.14 a) showcase two typical (chain) formations seen in such materials with different distributions of ferromagnetic particles characterized by the internal angle between the particles ϑ . In both examples, the embedded iron particles possess cubic magnetocrystalline anisotropy with their easy axes oriented in horizontal and vertical direction. The material parameters of the inclusions are given in table 5.3. The material parameters of the elastomer are again taken from table 5.2. Appropriate mechanical and magnetic boundary conditions are applied at the outer edges of the elastomer such that the body deforms homogeneously. Similar to the previous example the inclusions are initialized by a random distribution of magnetization and allowed to converge to an equilibrium state that is a vortex structure. An external magnetic field \bar{h}^a is applied in the vertical direction on both the samples, see Figure 5.13 b) and Figure 5.14 b). Snapshots at three different instances of magnetic loading are shown with the contour of the vertical magnetization plotted inside the inclusions. The applied magnetic field reorients the magnetization in the inclusions. In both examples the particles have the tendency to form chain structures, which can be seen in the corresponding deformation plots of the composite at saturation. However, depending on the initial distribution of particles, the sample either undergoes expansion (Figure 5.13 b)) or compression (Figure 5.14 b)). This behavior is in agreement with physical expectations. The overall deformations of the two samples are compared in Figure 5.15. The varied deformation modes for both examples along with the initial and final configurations of particles are shown.

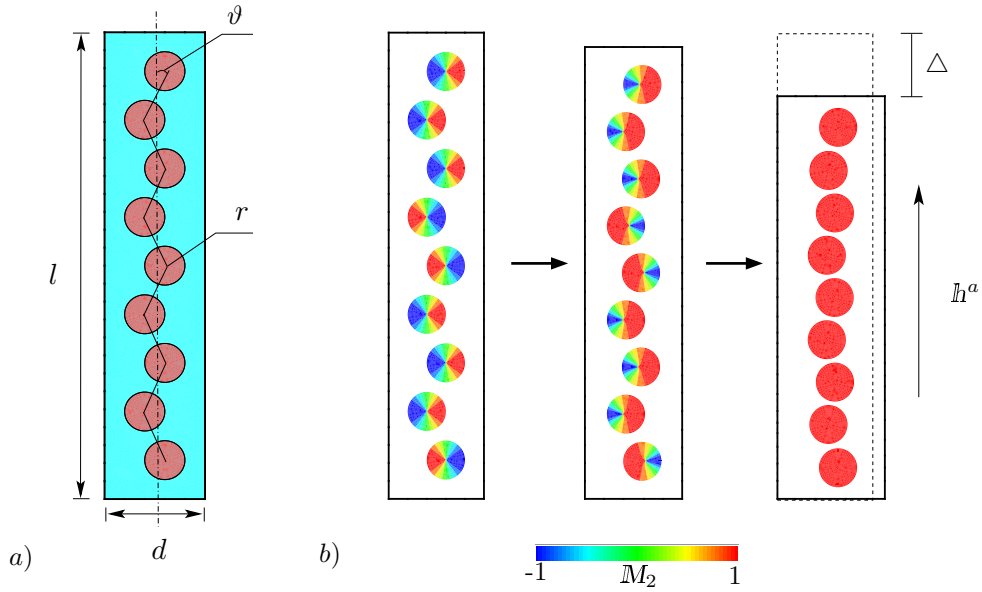


Figure 5.14: Behavior of a sample of magnetic inclusions embedded in a matrix, in chain arrangement at an angle of $\vartheta = 22^\circ$ under applied magnetic field. a) The boundary value problem consists of a rectangular elastomer specimen with side lengths of $l = 0.24 \mu\text{m}$ and $d = 0.045 \mu\text{m}$. Its meso-structure is characterized by a chain arrangement of ferromagnetic particles with radius $r = 0.01 \mu\text{m}$. b) Under the action of an external magnetic field h^a the body experiences a compression in field direction. This deformation is due to the motion of ferromagnetic domains within the particles and the resulting particle–particle and particle–matrix interactions. The evolution of domains is visualized through a contour plot of the vertical component of the magnetization directors.

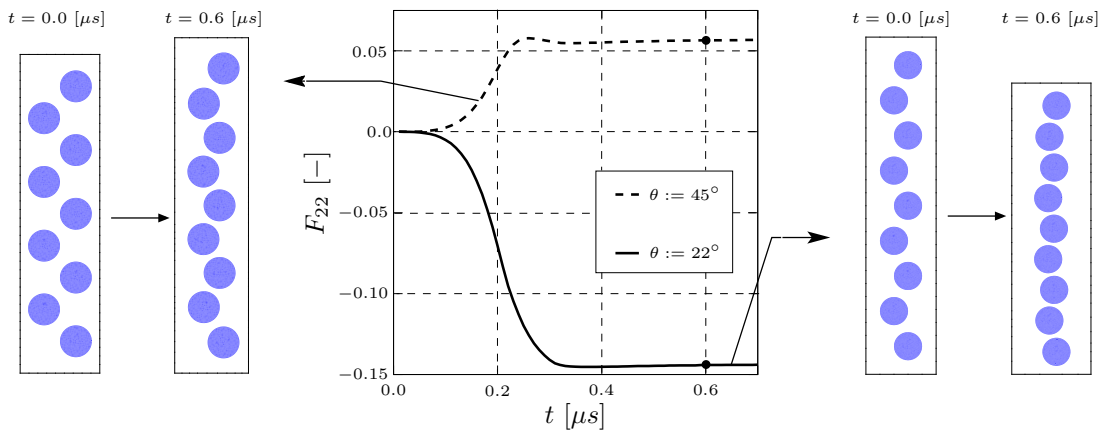


Figure 5.15: Deformation of the two samples containing different types of particle chains under the applied magnetic field \bar{h} . The central plot shows the effective deformations of the samples. In case of an inter-particle angle of $\theta = 45^\circ$ the composite experiences expansion (dashed line). The associated initial and final state of the sample are depicted on the left. In case of an inter-particle angle of $\theta = 22^\circ$ the composite experiences compression (solid line). In both cases the deformation saturates with the magnetization.

— Part III —

**Variational Phase-Field Approach to
Anisotropic Fracture in Coupled
Electromechanics: Piezoelectrics and
Ferroelectrics**

Variational Phase-Field Approach to Anisotropic Fracture in Piezoelectrics

Piezoelectric ceramics are electromechanically coupled materials that show brittle fracturing under applied external electric field or mechanical stress stimuli. In the recent years piezoelectric materials have garnered significant attention due to their established applications as sensors and actuators in manufacturing and automotive industry, and new niche applications being developed in the field of medicine and telecommunications. The reliability analysis of such materials under fracturing loads is of utmost importance. This chapter presents a *phase-field approach* to model anisotropic crack propagation in a coupled electromechanical setting. A three-field problem that couples the displacement and the electric potential along with the fracture phase-field is proposed. The current framework accounts for *anisotropic crack propagation* by employing appropriate structural tensors that influence the crack path. Appropriate choice of degradation functions allows for the accommodation of varied electrical crack boundary conditions. Experimental evidence available in literature and theoretical considerations motivate a non-associative dissipative framework where the fracture phase-field is driven by only mechanical part of the coupled electromechanical driving force.

6.1. Local damage model and electrical degradation functions

The fracture phase field $\alpha \in [0, 1)$ is considered to be geometric in nature, describing at a local point of the continuum the crack opening in a diffusive format. Subsequently, the electrical influence of the crack opening are considered by different electrical boundary conditions as introduced in, see [Section 3.1](#). This section outlines, the choice of crack driving force and the constitutive formulation of electromechanical fracture through a one-dimensional damage model. In this case the fracture phase-field can also be interpreted as a local damage variable. In order to better understand and motivate the electromechanical fracture model developed later, the local constitutive behavior is presented here. For a piezoelectric material undergoing fracture an *electromechanical energy function* $\Psi(\varepsilon, \mathbb{E}, \alpha)$ can be defined, depending on the strain ε , the electric field \mathbb{E} and the damage variable

α . The second axiom of thermodynamics in this case takes the form

$$\mathcal{D} = \sigma \dot{\varepsilon} - \mathcal{D} \dot{\mathbb{E}} - \dot{\Psi} \geq 0, \quad (6.1)$$

in terms of the local dissipation \mathcal{D} and conjugate energy variables, mechanical stress σ and electric displacement field \mathcal{D} . Exploitation of dissipation inequality taking into account the time rate of the energy yields appropriate constitutive equations,

$$\sigma = \partial_{\varepsilon} \Psi \quad \text{and} \quad \mathcal{D} = -\partial_{\mathbb{E}} \Psi. \quad (6.2)$$

Following this the local dissipation can be written as a product of thermodynamic driving force f and evolution of the local damage variable $\dot{\alpha}$

$$\mathcal{D} = f \dot{\alpha} \geq 0 \quad \text{with} \quad f = -\partial_{\alpha} \Psi. \quad (6.3)$$

Traditionally a positive and convex (possibly non-smooth) *dissipation function* Φ^* , of the thermodynamic forces is presented such that evolution of the internal damage variable is determined by,

$$\dot{\alpha} \in \partial_f \Phi^*(f). \quad (6.4)$$

Here, $\partial_f(\cdot)$ denotes the sub-differential of (\cdot) . With this structure of the evolution equation, the dissipation inequality (6.3) is automatically satisfied. However irreversible destruction of the material, such that healing processes are prevented, entails a growth of the damage variable α . This in turn induces constraints on damage growth and driving force as,

$$\dot{\alpha} \geq 0 \quad \rightarrow \quad f \geq 0. \quad (6.5)$$

This constraint on the driving force $f = -\partial_{\alpha} \Psi \geq 0$, needs to be satisfied for $\alpha \in [0, 1)$. In the purely mechanical framework this is always satisfied, however in the electromechanical setting there might be violation of this constraint (especially in cases where $\mathbb{E} \gg \varepsilon$). To heal this inconsistency, an additional contribution to the Gibbs energy $\hat{\kappa}(\alpha)$ has to be prescribed such that $\partial_{\alpha} \kappa(\alpha) < 0$, see MIEHE ET AL. [172] for more details. Note that this contribution does not influence the constitutive behavior of the model but is presented here for completeness. Such a formulation allows for arbitrary choice of evolution for the damage variable with the only restriction being $\dot{\alpha} \geq 0$.

6.1.1. Electromechanical Energy and Degradation Functions

Various formulations of the energy function $\Psi(\varepsilon, \mathbb{E}, \alpha)$, depending on the strain ε , the electric field \mathbb{E} and the damage variable α , have been proposed in literature. A general additive energy function can be postulated as

$$\Psi(\varepsilon, \mathbb{E}, \alpha) = g_m(\alpha) \Psi_m(\varepsilon) + g_{em}(\alpha) \Psi_{em}(\varepsilon, \mathbb{E}) + g_e(\alpha; \xi) \Psi_e(\mathbb{E}), \quad (6.6)$$

in terms of the mechanical degradation function $g_m(\alpha)$, coupled electromechanical degradation function $g_{em}(\alpha)$ and the electric degradation function $g_e(\alpha; \xi)$. Here $\xi = \varepsilon_c / \varepsilon_s \in [0, 1]$ is the ratio of the electric permittivity of the material ε_s and crack ε_c ¹. $\Psi_m(\varepsilon)$,

¹This ratio can also be defined as $\xi := \frac{1 + \chi_c}{1 + \chi_s}$, in terms of the susceptibility of the crack and solid χ_c and χ_s , respectively. It is a constant that characterizes electric degradation in the semi-permeable case.

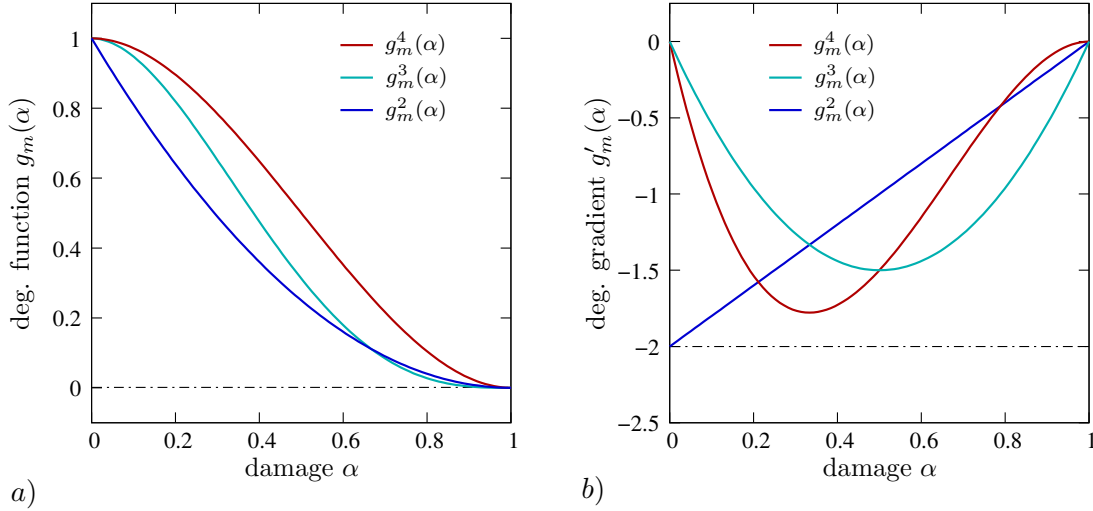


Figure 6.1: Different mechanical degradation functions (6.8) and their gradients, plotted against the damage parameter $\alpha \in [0, 1)$. a) Shows the plot of the quadratic $g_m^2(\alpha)$, cubic $g_m^3(\alpha)$ and fourth order $g_m^4(\alpha)$ degradation functions and b) shows the plot of the gradients for the same. The degradation functions satisfy the conditions proposed in [137], with no degradation in case of undamaged material and complete degradation for a damaged material.

$\Psi_{em}(\varepsilon, \mathbb{E})$ and $\Psi_e(\mathbb{E})$ are the pure mechanical, coupled and electric energy functions respectively. In this case they assume the simple form

$$\Psi_m(\varepsilon) = \frac{1}{2}E_s\varepsilon^2, \quad \Psi_{em}(\varepsilon, \mathbb{E}) = -\varepsilon H_s \mathbb{E}, \quad \text{and} \quad \Psi_e(\mathbb{E}) = -\frac{1}{2}\epsilon_s \mathbb{E}^2, \quad (6.7)$$

in terms of the mechanical stiffness E_s , the piezoelectric coupling modulus H_s and the electric permittivity of the material ϵ_s .

Mechanical and coupled energy degradation functions. There are many forms of degradation functions proposed for the purely mechanical case. However, the mechanical degradation function $g_m(\alpha)$ has to satisfy some conditions that are related to physically observed phenomena, see KUHN ET AL. [137], for an overview in this topic. This essentially entails that:

- degradation function must be monotonically decreasing and continuously differentiable.
- no degradation for intact material $g_m(0) = 1$ and full degradation for completely damaged material $g_m(1) = 0$.
- The crack driving force in case of complete damage must be zero, $g'_m(1) = 0$.

Some degradation functions proposed in literature that satisfy these conditions are

$$g_m^2(\alpha) = (1 - \alpha)^2, \quad g_m^3(\alpha) = 3(1 - \alpha)^2 - 2(1 - \alpha)^3 \quad \text{and} \quad g_m^4(\alpha) = 4(1 - \alpha)^3 - 3(1 - \alpha)^4, \quad (6.8)$$

proposed by KUHN ET AL. [137], BOURDIN ET AL. [28] and KARMA ET AL. [119]) respectively. These functions and their gradients are plotted in Figure 6.1. The above conditions are also directly applicable for the coupled degradation function $g_{em}(\alpha)$. For the current formulation the quadratic form $g_m(\alpha) = g_{em}(\alpha) = (1 - \alpha)^2$ for the mechanical and coupled degradation functions are chosen.

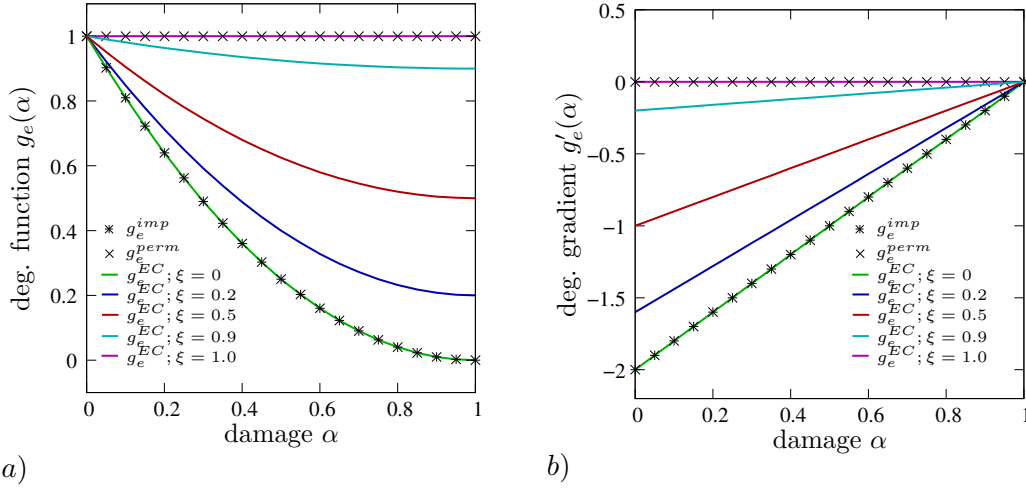


Figure 6.2: Plot of the electric degradation functions and their gradients, against the damage parameter $\alpha \in [0,1)$. a) Shows the plot of the electric degradation function for the permeable (6.9)₁, impermeable (6.9)₂ and the proposed semi-permeable degradation function (6.10). The semi-permeable function approximates smoothly between the extreme case of permeable $\xi = 1$ and impermeable $\xi = 0$. b) Shows the plot of the gradient for the three degradation functions. The degradation functions satisfy the physical restrictions.

Electrical energy degradation function. The electric degradation function models the electric behavior of crack in a piezoelectric solid. Refer Section 3.2 for details regarding various electric crack conditions. In the most general case considering that the crack can sustain some electric field, the function $g_e(\alpha; \xi)$ needs to have information regarding the electric properties of the crack. In order to account for this, the degradation function is proposed to depend on $\xi = \epsilon_c/\epsilon_s$ in addition to the damage field α . The material constant ξ accounts for the semi-permeable crack face boundary conditions with $\xi = 1$ for complete field penetration and $\xi = 0$ for impermeable crack boundary conditions, as the extreme cases. Similar to the mechanical and coupled degradation functions the electric degradation function $g_e(\alpha; \xi)$ also needs to satisfy some physical conditions. These restrictions follow the mechanical restrictions with the exception that $g_e(1; \xi) = \xi$. This condition ensures that in the case of a semi-permeable crack a certain electric field is still sustained by the crack. Initial models for piezoelectric fracture focused on the permeable (PARTON [192]) and impermeable fracture (MIEHE ET AL. [172]) which can be modeled by the degradation functions

$$g_e^{perm}(\alpha; \xi = 1) = 1 \quad \text{and} \quad g_e^{imp}(\alpha; \xi = 0) = (1 - \alpha)^2. \quad (6.9)$$

Here the permeable case assumes no degradation of the electric energy while the impermeable case assumes complete degradation. Intuitively the extension of these formulations to include semi-permeable crack boundary conditions can be formulated by extending these electric degradation function to include an additional part such that the crack is capable of sustaining a partial electric field

$$g_e^{semi}(\alpha; \xi) = 1 + 2(\xi - 1)\alpha + (1 - \xi)\alpha^2. \quad (6.10)$$

These degradation functions and their gradients are plotted in Figure 6.2 a) and b). The semi-permeable degradation function is plotted for different ξ values. It has to be noted that this degradation function is consistent with the energetically consistent (EC) bound-

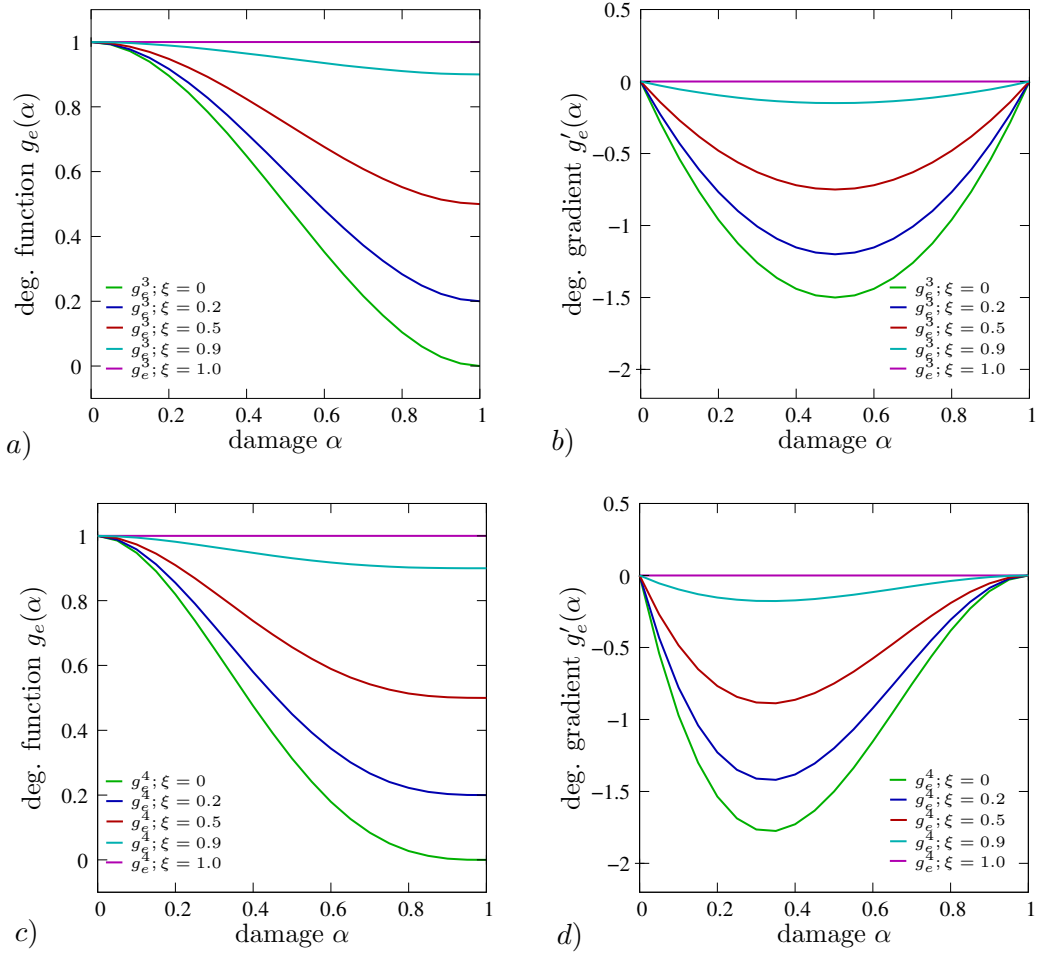


Figure 6.3: Proposed higher order electric degradation functions plotted against the damage parameter $\alpha \in [0, 1)$. a) and b) shows the third-order degradation function (6.11)₁ and its gradient for different values of ξ . c) and d) are the same plots for the fourth-order degradation function (6.11)₂. Such higher order degradation functions could be employed to capture additional physical phenomena. It is interesting to note that contrary to the quadratic degradation function, higher order functions show $g'_e(\alpha = 0, \xi) = 0$, that is no crack driving in undamaged state.

ary conditions proposed by LANDIS [144]². It can be seen that such a degradation function automatically satisfies the physical constraints that are proposed above and shows a smooth approximation for the semi-permeable electric boundary conditions between the two extreme cases. This degradation function (6.10) is a second-order degradation function. Similar to the mechanical degradation functions, higher order degradation functions to model the electric degradation can be proposed. Third- and fourth-order degradation function take the form

$$g_e^3(\alpha; \xi) = 1 + 3(\xi - 1)\alpha^2 + 2(1 - \xi)\alpha^3 \quad \text{and} \quad g_e^4(\alpha; \xi) = 1 + 6(\xi - 1)\alpha^2 + 8(1 - \xi)\alpha^3 + 3(\xi - 1)\alpha^4. \quad (6.11)$$

The third- and fourth-order degradation function and its gradient are plotted in Figure 6.3 a) and b). Such a formulation in terms of degradation functions gives more flexibility to model coupled electromechanical fracture. For further investigation of the crack driving force quadratic degradation functions and impermeable electric conditions are assumed.

²No additional nonlinear Maxwell contribution is assumed in the crack gap, as the crack opening is considered to be small and crack propagation instantaneous for the case of brittle fracture considered.

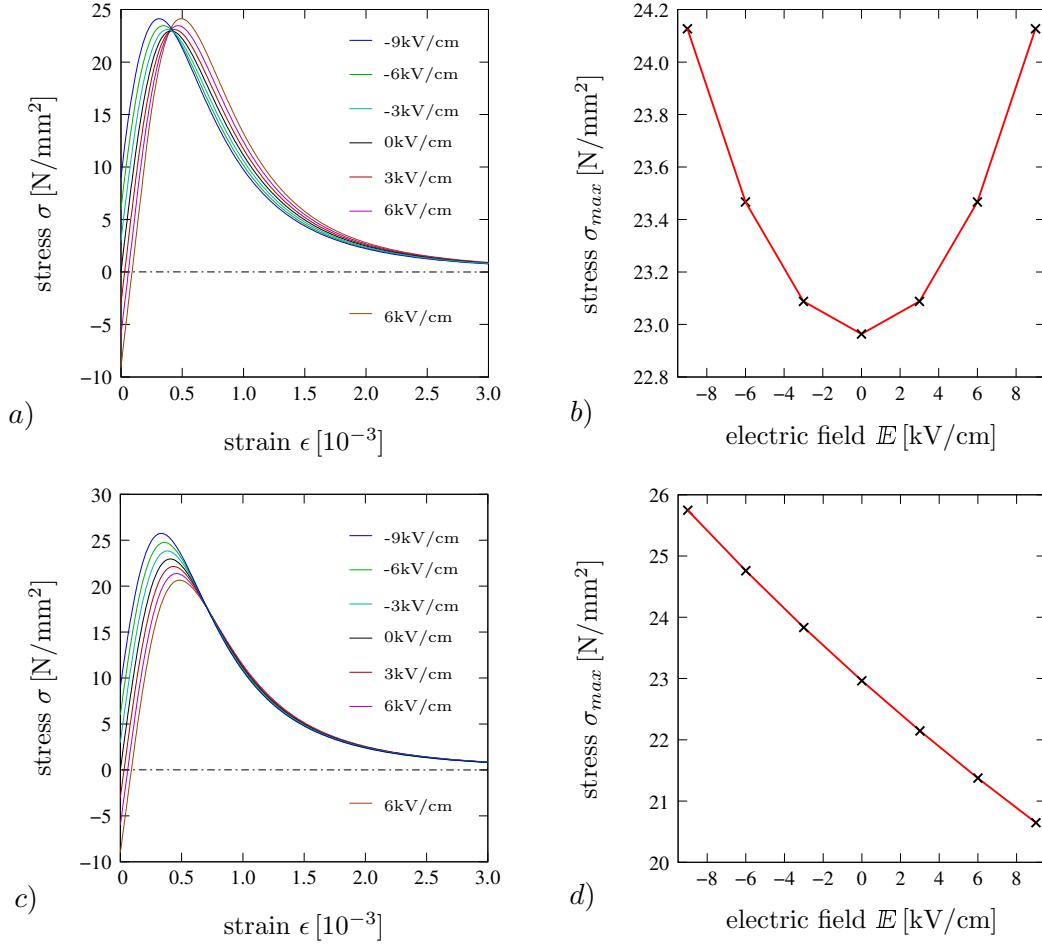


Figure 6.4: Comparison of a local electromechanical damage model for damage accumulation driven by mechanical and full driving force. a) and c) show the stress-strain response for both the models for positive (in poling direction) and negative (opposite to poling) applied electric fields \mathbb{E} . b) and d) shows the maximum stress (fracture load) for various applied electrical fields. For damage accumulation driven by complete driving force the fracture load increases for positive or negative fields, whereas for mechanical driving force there is a decrease in fracture load for positive fields.

6.1.2. Electromechanical Driving Force and Damage Evolution

With the degradation functions at hand, (6.6) and (6.2) gives the relations

$$\sigma = (1 - \alpha)^2 (E_s \epsilon - H_s \mathbb{E}) \quad \text{and} \quad \mathcal{D} = (1 - \alpha)^2 (H_s \epsilon + \epsilon_s \mathbb{E}), \quad (6.12)$$

assuming quadratic degradation functions and impermeable crack conditions. The thermodynamic damage driving force from (6.3)₂ takes the form

$$f = -\partial_\alpha \Psi = (1 - \alpha) [E_s \epsilon^2 - 2\epsilon H_s \mathbb{E} - \epsilon_s \mathbb{E}^2]. \quad (6.13)$$

Considering a rate-independent, discontinuous evolution of the local damage variable α , an evolution criteria can be postulated of the form

$$t(f; \alpha) = f - c\alpha. \quad (6.14)$$

Here the constant c , models resistance of the material to damage and has the unit of an energy per unit volume. With this function at hand, a rate-independent evolution of

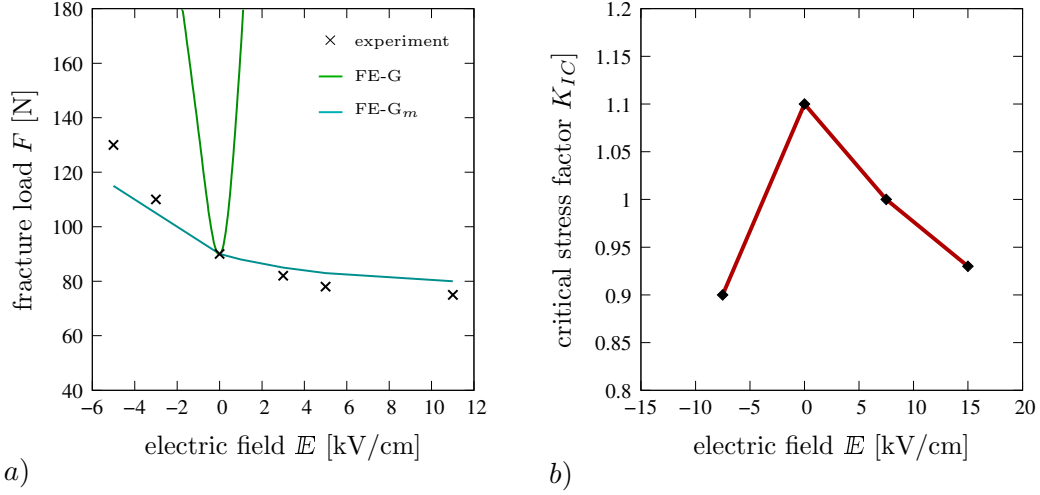


Figure 6.5: *Experimental results for comparison with the constitutive response predicted by the damage model.* a) Mode-1 fracture test results from PARK AND SUN [191] for commercial PZT-4 sample. Experimental results (dotted) and FEM results (full lines) for full driving force FE-G and mechanical driving force FE-G_m are plotted. The authors propose the use of mechanical driving force as fracture criteria. b) Experimental results from FU AND ZHANG [74], for PZT-841 sample for different applied electric field loading. The results vary from [191] only for negative fields.

damage is defined by the KKT conditions equations

$$\dot{\alpha} \geq 0, \quad t(f; \alpha) \leq 0, \quad \dot{\alpha} t(f; \alpha) = 0. \quad (6.15)$$

Note that due to $\dot{\alpha} \geq 0$ and the initial condition $\alpha(t = 0) = 0$ the above loading condition selects in the case of damage loading, only positive driving forces. Ensuring positive dissipation the current damage variable α can be computed from the condition $t(f; \alpha) = 0$ in (6.15)₂ as

$$\alpha = \frac{\mathfrak{h}(\varepsilon, \mathbb{E})}{c + \mathfrak{h}(\varepsilon, \mathbb{E})} \quad \text{for } \dot{\alpha} \geq 0. \quad (6.16)$$

Here, it is obvious that the function $\mathfrak{h}(\varepsilon, \mathbb{E}) := E_s \varepsilon^2 - 2\varepsilon H_s \mathbb{E} - \varepsilon_s \mathbb{E}^2$ drives the damage variable α however damage accumulation $\dot{\alpha} > 0$ occurs only if the function \mathfrak{h} grows. Defining $\mathcal{H}(t)$, as the maximum value of \mathfrak{h} obtained in time history to prevent healing, evolution of damage variable is given as

$$\alpha(t) = \frac{\mathcal{H}(t)}{c + \mathcal{H}(t)} \in [0, 1) \quad \text{with} \quad \mathcal{H}(t) := \max_{s \in [0, t]} [\mathfrak{h}(\varepsilon(s), \mathbb{E}(s))] \in [0, \infty). \quad (6.17)$$

This evolution, (6.17)₁, provides the desired property $\alpha \rightarrow 1$ for $\mathcal{H} \rightarrow \infty$. The equations (6.12) and (6.17) then govern exclusively the degradation of the stresses and electric displacements of a piezoelectric solid. With the damage variable at hand the stress and the electric displacement can be defined from (6.12) as

$$\sigma = \left(\frac{c}{c + \mathcal{H}(t)} \right)^2 (E_s \varepsilon - H_s \mathbb{E}) \quad \text{and} \quad D = \left(\frac{c}{c + \mathcal{H}(t)} \right)^2 (H_s \varepsilon + \varepsilon_s \mathbb{E}). \quad (6.18)$$

The behavior of the model is shown in Figure 6.4 a) and b). It can be seen that the stress shows degradation after reaching maximum value with increasing strain. The model predicts an increase in fracture load under the influence of a positive (in poling direction)

or negative (opposite to poling) applied fields [Figure 6.4 b](#)). Now, following the work of MIEHE ET AL. [172] and PARK & SUN [191], the electromechanical fracture is assumed to be purely mechanically driven. To this end (6.13) can be split into a purely mechanical and electric driving force such that

$$f_m = (1 - \alpha)(\varepsilon E_s \varepsilon - \varepsilon H_s \mathbb{E}) \quad \text{and} \quad f_e = -(1 - \alpha)(\varepsilon H_s \mathbb{E} + \varepsilon_s \mathbb{E}^2). \quad (6.19)$$

Note that the sum of the driving forces is the total driving force $f_m + f_e = f$. Then taking only the mechanical driving force (6.19)₁ in (6.14), the closed form solution for the damage variable is

$$\alpha(t) = \frac{\mathcal{H}_m(t)}{c + \mathcal{H}_m(t)} \in [0, 1) \quad \text{with} \quad \mathcal{H}_m(t) := \max_{s \in [0, t]} [\mathfrak{h}_m(\varepsilon(s), \mathbb{E}(s))] \in [0, \infty), \quad (6.20)$$

where $\mathfrak{h}_m := \varepsilon E_s \varepsilon - \varepsilon H_s \mathbb{E}$. Note that such an assumption only affects the damage evolution while mechanical stress and electric displacement remains the same as in (6.18). The thermodynamic consistency (6.3) is still fulfilled as $f \geq 0$ and $\dot{\alpha} \geq 0$. The behavior of such a model is shown in [Figure 6.4 c](#)) and [d](#)). This model shows an increase in fracture load for negative fields however, for positive electric fields the fracture load decreases. As a comparison, experimental observations for fracture in piezoelectric PZT samples by (PARK AND SUN [191] and FU AND ZHANG [74]) are shown in [Figure 6.5 a](#)) and [b](#)). The results from PARK AND SUN agrees with the prediction made by a purely mechanically driven damage accumulation. Similar observation led them also to choose the mechanical driving force as the fracture criterion. FEM results for the same are shown in [Figure 6.5 a](#)), which quantitatively concur with the results in [Figure 6.4 b](#)) and [d](#)). The results from FU AND ZHANG predict decrease in fracture load for positive or negative fields. Both the experimental results differ only when the field is opposite to poling direction, however an increase in fracture toughness for positive fields is not predicted by both. With the experimental results at hand, a purely mechanical driven damage accumulation seems the correct choice. Note that this is a *constitutive assumption*, keeping in mind experimental data. The framework presented allows for choice of any driving force that fulfills the consistency condition $\dot{\alpha} \geq 0$.

6.2. Variational Principle for Evolution of Phase Field Fracture in Piezoelectrics

Taking the above outlined damage model as a guideline, in this section a framework of diffuse fracture in poled anisotropic piezoelectric solids is developed. This is based on the introduction of a crack phase-field that governs a crack surface density function as presented in [Section 3.1](#). A degrading electromechanical energy functional based on particular kinematic assumptions is constructed taking into account electrical crack conditions.

6.2.1. Primary Fields for Fracture in Piezoelectrics

In a small-strain context, the coupled electromechanical response of fracture in piezoelectric solid \mathcal{B} , is described by introduction of displacement and electric potential fields

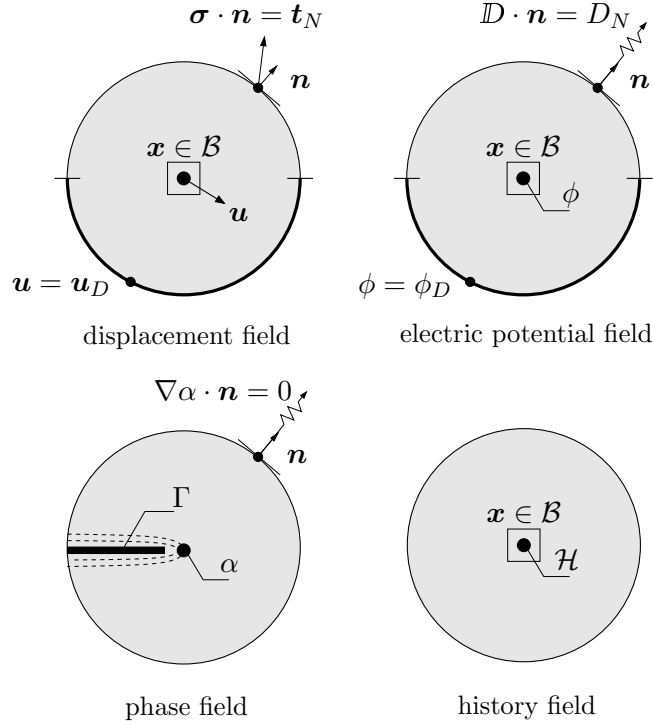


Figure 6.6: Three-field approach for phase-field fracture in coupled electromechanical piezoelectric ceramics. The displacement field \mathbf{u} , the electric potential field ϕ , the fracture phase field α and the history field \mathcal{H} are defined on the solid domain \mathcal{B} .

as

$$\mathbf{u} : \begin{cases} \mathcal{B} \times \mathcal{T} \rightarrow \mathcal{R}^d \\ (\mathbf{x}, t) \mapsto \mathbf{u}(\mathbf{x}, t) \end{cases} \quad \text{and} \quad \phi : \begin{cases} \mathcal{B} \times \mathcal{T} \rightarrow \mathcal{R} \\ (\mathbf{x}, t) \mapsto \phi(\mathbf{x}, t) \end{cases}. \quad (6.21)$$

Here, $\mathbf{u} \in \mathcal{R}^d$ is the displacement and $\phi \in \mathcal{R}$ the electric potential of the material point $\mathbf{x} \in \mathcal{B}$ at time $t \in \mathcal{T}$. The strains are assumed to be small. The gradients of the above fields define the small-strain tensor and the electric-field vector

$$\boldsymbol{\varepsilon}(\mathbf{u}) = \nabla_s \mathbf{u} \quad \text{and} \quad \mathbb{E}(\phi) = -\nabla \phi, \quad (6.22)$$

of the geometrically linear theory with $\nabla_s \mathbf{u} = \frac{1}{2}[\nabla \mathbf{u} + \nabla^T \mathbf{u}]$. These definitions automatically satisfy the *deformation compatibility condition* $\text{curl}[\boldsymbol{\varepsilon}] = \mathbf{0}$ and *Faraday's law* $\text{curl}[\mathbb{E}] = \mathbf{0}$. In addition the fracture phase-field describes in a diffuse manner the fracture in a piezoelectric solid \mathcal{B} as

$$\alpha : \begin{cases} \mathcal{B} \times \mathcal{T} \rightarrow [0, 1] \\ (\mathbf{x}, t) \mapsto \alpha(\mathbf{x}, t) \end{cases}. \quad (6.23)$$

6.2.2. Variational Principle and Euler-Lagrange Equations

The coupled electromechanical total energy functional is described in terms of above introduced primary fields as

$$W(\mathbf{u}, \phi, \alpha) := E(\mathbf{u}, \phi, \alpha) + \Gamma_l(\alpha) := \int_{\mathcal{B}} w(\nabla_s \mathbf{u}, -\nabla \phi, \alpha, \nabla \alpha) dV, \quad (6.24)$$

where $E(\mathbf{u}, \phi, \alpha)$ is the stored energy functional of the bulk and $\Gamma_l(\alpha)$ is the regularized crack surface functional (3.14). The constitutive total energy function w depends on the

first gradient of the phase-field and the gradient fields introduced in (6.22). This energy density function can be split such that,

$$w(\nabla_s \mathbf{u}, -\nabla \phi, \alpha, \nabla \alpha) = \Psi(\nabla_s \mathbf{u}, -\nabla \phi, \alpha) + g_c \gamma_l(\alpha, \nabla \alpha; \mathbf{A}), \quad (6.25)$$

where Ψ is the bulk electromechanical energy of the piezoelectric material, γ_l is the anisotropic crack surface density function introduced in (3.16) and g_c is a material parameter. Furthermore a dissipation potential functional of the form

$$D(\dot{\alpha}) = \int_{\mathcal{B}} d(\dot{\alpha}) dV, \quad (6.26)$$

is considered, that depends on a convex and non-smooth dissipation potential density function $d(\dot{\alpha})$. The two functionals W and D define the rate potential functional

$$\Pi(\dot{\mathbf{u}}, \dot{\phi}, \dot{\alpha}) = \frac{d}{dt} W + D. \quad (6.27)$$

The potential $\Pi(\dot{\mathbf{u}}, \dot{\phi}, \dot{\alpha})$ governs the variational principle for coupled three-field evolution problem for electromechanical fracture as

$$\{\dot{\mathbf{u}}, \dot{\phi}, \dot{\alpha}\} = \arg \left\{ \inf_{\dot{\mathbf{u}} \in \mathcal{W}_{\dot{\mathbf{u}}}} \sup_{\dot{\phi} \in \mathcal{W}_{\dot{\phi}}} \inf_{\dot{\alpha} \in \mathcal{W}_{\dot{\alpha}}} \Pi \right\}. \quad (6.28)$$

The admissible spaces for rates of displacement, electric potential and the fracture phase-field are given by the Dirichlet conditions

$$\begin{aligned} \mathcal{W}_{\dot{\mathbf{u}}} &:= \{\dot{\mathbf{u}} \in \mathcal{R}^d \mid \dot{\mathbf{u}} = \dot{\bar{\mathbf{u}}} \text{ on } \partial \mathcal{B}_D^u\}, \\ \mathcal{W}_{\dot{\phi}} &:= \{\dot{\phi} \in \mathcal{R} \mid \dot{\phi} = \dot{\bar{\phi}} \text{ on } \partial \mathcal{B}_D^\phi\} \quad \text{and} \\ \mathcal{W}_{\dot{\alpha}} &:= \{\dot{\alpha} \in \mathcal{R} \mid \dot{\alpha} = \dot{\bar{\alpha}} \text{ on } \partial \mathcal{B}_D^\alpha\}. \end{aligned} \quad (6.29)$$

The Euler equations of the variational principle (6.28) are

$$\operatorname{div}[\boldsymbol{\sigma}] = \mathbf{0}, \quad \operatorname{div}[\mathbb{D}] = 0 \quad \text{and} \quad 0 \in \delta_\alpha w + \partial_{\dot{\alpha}} d, \quad (6.30)$$

in the domain \mathcal{B} . The mechanical stress tensor $\boldsymbol{\sigma}$ and the electric displacement field \mathbb{D} are introduced as work conjugates of the strain $\boldsymbol{\varepsilon}$ and electric field \mathbb{E} , respectively. In the above equation (6.30), $\delta_\alpha w$ denotes the variational derivative of the function w with respect to α , defined as $\delta_\alpha w = \partial_\alpha w - \operatorname{div}[\partial_{\nabla \alpha} w]$. Furthermore, $\partial_{\dot{\alpha}} d$ denotes the sub-gradient of the non-smooth function d . Clearly (6.30)₁ is the quasistatic balance of momentum and (6.30)₂ is the Gauss law of electrostatics.

6.2.3. Irreversible Evolution of Fracture

To account for the irreversibility of the fracture phase field a non-smooth dissipation potential function is proposed of the form

$$d(\dot{\alpha}) = I(\dot{\alpha}) + \frac{\eta}{2} \dot{\alpha}^2. \quad (6.31)$$

The dissipation potential consists of a quadratic part that could be employed to control the rate of damage evolution. The parameter η is a mobility parameter for the phase-field

evolution, which provides for $\eta \rightarrow 0$ the rate-independent limit. A non-smooth indicator function ensures positive damage evolution as

$$I(\dot{\alpha}) = \begin{cases} 0 & \text{for } \dot{\alpha} \geq 0 \\ \infty & \text{otherwise,} \end{cases} \quad \text{with} \quad \partial_{\dot{\alpha}} I(\dot{\alpha}) = \begin{cases} 0 & \text{for } \dot{\alpha} > 0 \\ \mathcal{R}_- & \text{for } \dot{\alpha} = 0. \end{cases} \quad (6.32)$$

With the specific form (6.31), the evolution equation for the damage field (6.30)₃ can be written in the form

$$\dot{\alpha} = \left\langle -\frac{1}{\eta} \delta_{\alpha} w \right\rangle_+. \quad (6.33)$$

The Macaulay bracket $\langle (\cdot) \rangle_+ := [(\cdot) + |(\cdot)|]/2$ chooses positive driving force for damage growth. (6.33) is a generalized Ginzburg-Landau type evolution equation for fracture evolution as considered in MIEHE ET AL. [172, 173]. The above equation reduces to the rate-independent limit $\eta \rightarrow 0$ to the evolutionary system

$$\dot{\alpha} \geq 0, \quad -\delta_{\alpha} w \leq 0, \quad \text{and} \quad \dot{\alpha}[-\delta_{\alpha} w] = 0, \quad (6.34)$$

in Karush-Kuhn-Tucker form. Eqs. (6.33) and (6.34) provide the basis for the phase-field modeling of brittle fracture proposed by MIEHE ET AL. [172]. They represent evolution equations for rate-dependent and rate-independent gradient damage, respectively. The fracture evolution equation can then be recast for quadratic degradation function as

$$\eta \dot{\alpha} = (1 - \alpha) \mathcal{H} - \frac{g_c}{l} \alpha + g_c l \operatorname{div}[\mathbf{A} \cdot \nabla \alpha]. \quad (6.35)$$

Here similar to the discussion in Section 6.1, $\mathcal{H}(\mathbf{x}, t)$ denotes a positive crack driving force which is expressed as

$$\mathcal{H}(\mathbf{x}, t) := \max_{s \in [0, t]} \mathfrak{H}(\mathbf{x}, s). \quad (6.36)$$

In terms of the crack driving state function $\mathfrak{H}(\mathbf{x}, s)$ depending on the state array. The function $\mathfrak{H}(\mathbf{x}, s)$ is specific to the choice of the energy density used to model the electromechanical behavior described in Subsection 6.3.3.

6.3. Degrading Gibbs Energy Functional Due to Fracture

6.3.1. Stored Electromechanical Energy Functional

The focus here is on the linear theory of piezoelectricity considered through an electromechanical energy functional of the form

$$E(\mathbf{u}, \phi, \dot{\alpha}) = \int_B \Psi(\boldsymbol{\varepsilon}, \mathbb{E}, \alpha; \mathbf{p}) dV, \quad (6.37)$$

depending on the displacement field \mathbf{u} , the electric potential ϕ and the fracture phase-field α . The function Ψ describes the energy density per unit volume of the solid, which also depends on the constant structural vector \mathbf{p} with $|\mathbf{p}| = 1$. The structural vector \mathbf{p} , describes the *electric poling direction* of the material. Note that this structural tensor is in general independent of the fracture anisotropy tensor \mathbf{a} . Due to the electric poling Ψ is a transversely isotropic function with the symmetry group \mathcal{G}_{trans} , i.e.

$$\Psi(\mathbf{Q}\boldsymbol{\varepsilon}\mathbf{Q}^T, \mathbf{Q}\mathbb{E}, \alpha; \mathbf{p}) = \Psi(\boldsymbol{\varepsilon}, \mathbb{E}, \alpha; \mathbf{p}) \quad \text{for} \quad \mathbf{Q} \in \mathcal{G}_{trans} := \{\mathbf{Q} \in \mathcal{O}(3) | \mathbf{Q}\mathbf{p} = \mathbf{p}\}. \quad (6.38)$$

Standard representation theorems of isotropic tensor functions, gives the dependence of the energy on invariants of the form (SCHRÖDER & ROMANOWSKI [218] and MIEHE ET AL. [172]),

$$\begin{aligned} \Psi(\boldsymbol{\varepsilon}, \mathbb{E}, \alpha; \mathbf{p}) := & \Psi(\text{tr } \boldsymbol{\varepsilon}, \text{tr } \boldsymbol{\varepsilon}^2, \text{tr } \boldsymbol{\varepsilon}^3, \text{tr}[\mathbb{E} \otimes \mathbb{E}], \text{tr}[\boldsymbol{\varepsilon}(\mathbb{E} \otimes \mathbb{E})], \text{tr}[\boldsymbol{\varepsilon}^2(\mathbb{E} \otimes \mathbb{E})], \text{tr}[\boldsymbol{\varepsilon}(\mathbf{p} \otimes \mathbf{p})], \\ & \text{tr}[\boldsymbol{\varepsilon}^2(\mathbf{p} \otimes \mathbf{p})], \text{tr}[\boldsymbol{\varepsilon}(\mathbb{E} \otimes \mathbf{p})], \text{tr}[\boldsymbol{\varepsilon}^2(\mathbb{E} \otimes \mathbf{p})], \text{tr}[\mathbb{E} \otimes \mathbf{p}, \alpha]), \end{aligned} \quad (6.39)$$

in terms of the base and coupled invariants of the symmetric tensor $\boldsymbol{\varepsilon}$ and the vectors \mathbb{E} and \mathbf{p} . A simple quadratic function has the representation similar to (6.6),

$$\begin{aligned} \Psi(\boldsymbol{\varepsilon}, \mathbb{E}, \alpha; \mathbf{p}) := & g_m(\alpha)\psi_m(\boldsymbol{\varepsilon}) + g_{em}(\alpha)\psi_{em}(\boldsymbol{\varepsilon}, \mathbb{E}) + g_e(\alpha, \xi)\psi_e(\mathbb{E}) \quad \text{with} \\ \psi_m := & \mu \text{tr } \boldsymbol{\varepsilon}^2 + \lambda \text{tr}^2 \boldsymbol{\varepsilon} / 2, \quad \psi_e := -\epsilon_s \text{tr}(\mathbb{E} \otimes \mathbb{E}) / 2 \quad \text{and} \\ \psi_{em} = & (H_{\parallel} - H_{\perp} - H_{-}) \text{tr}[\boldsymbol{\varepsilon}(\mathbf{p} \otimes \mathbf{p})] \text{tr}[\mathbf{p} \otimes \mathbb{E}] - H_{\perp} \text{tr } \boldsymbol{\varepsilon} \text{tr}[\mathbf{p} \otimes \mathbb{E}] - H_{-} \text{tr}[\boldsymbol{\varepsilon}(\mathbf{p} \otimes \mathbb{E})], \end{aligned} \quad (6.40)$$

in terms of the mechanical, coupled and electric degradation functions $g_m(\alpha)$, $g_{em}(\alpha)$ and $g_e(\alpha)$. In this formulation, quadratic degradation functions introduced in Section 6.1 are employed. The total energy is defined in terms of the mechanical ψ_m , coupled ψ_{em} and electric ψ_e energy contributions of the undamaged solid. These energies in turn are given in terms of the Lamé parameters $\lambda := E\nu/[(1+\nu)(1-2\nu)]$ and $\mu := E/[2(1+\nu)]$ of isotropic elasticity, the isotropic electric permittivity of the solid ϵ_s , the ratio $\xi := \epsilon_s/\epsilon_c$ of the solid and the crack permittivity and finally the electromechanical coupling coefficients H_{\parallel} , H_{\perp} and H_{-} . For simplicity, the purely mechanical and electrical contributions are assumed to be isotropic. Note that for an undamaged material with $\alpha = 0$ the above expression (6.40) returns the energy of a linear piezoelectric material

$$\psi(\boldsymbol{\varepsilon}, \mathbb{E}; \mathbf{p}) = \frac{1}{2} \boldsymbol{\varepsilon} : \bar{\mathbb{C}} : \boldsymbol{\varepsilon} - \mathbb{E} \cdot \bar{\boldsymbol{e}} : \boldsymbol{\varepsilon} + \frac{1}{2} \mathbb{E} \cdot \bar{\mathbb{H}} \cdot \mathbb{E}, \quad (6.41)$$

with the standard quadratic mechanical and electric contributions along with a bi-linear coupled electromechanical energetic term. The material matrices $\bar{\mathbb{C}}$, $\bar{\boldsymbol{e}}$ and $\bar{\mathbb{H}}^3$ define the mechanical, electrical and coupled material response and manifest in this case as,

$$\bar{\mathbb{C}} := \lambda \mathbf{I} \otimes \mathbf{I} + 2\mu \mathbb{I}, \quad \bar{\boldsymbol{e}} = (H_{\parallel} - H_{\perp} - H_{-}) \mathbf{p} \otimes \mathbf{p} \otimes \mathbf{p} + H_{\perp} \bar{\boldsymbol{e}} + H_{-} \mathbf{I} \otimes \mathbf{p} \quad \text{and} \quad \bar{\mathbb{H}} = -\epsilon_s. \quad (6.42)$$

Given in terms of the second-, third- and fourth-order tensors $[\mathbf{I}]_{ij} = \delta_{ij}$, $[\mathbb{I}]_{ijkl} = \frac{1}{2}(\delta_{ik}\delta_{jl} + \delta_{il}\delta_{jk})$ and $[\bar{\boldsymbol{e}}]_{ijk} = \frac{1}{2}(p_j\delta_{ik} + p_k\delta_{ij})$.

6.3.2. Tension-Compression Split of Energy

In the above principle, the stress degradation affects the full stress tensor. Thus, energy is released due to fracture in both tension and compression. This is physically unrealistic and limits the framework, as the electromechanical coupling might give rise to local compressive stress even in pure *Mode-1* problems. To account for this consider the split of the strain

$$\boldsymbol{\varepsilon} = \boldsymbol{\varepsilon}^+ + \boldsymbol{\varepsilon}^- \quad \text{with} \quad \boldsymbol{\varepsilon}^{\pm} := \sum_{a=1}^3 \langle \boldsymbol{\varepsilon} \rangle_{\pm} \mathbf{n}_a \otimes \mathbf{n}_a. \quad (6.43)$$

³note that the symbol \mathbb{H} has also been used in this work for the magnetic field. However, the symbol is used here to denote the electrical material matrix and not the magnetic field.

With the ramp functions $\langle x \rangle_+ := (x + |x|)/2$ and $\langle x \rangle_- := (x - |x|)/2$ for $x \in \mathcal{R}$. This allows an additive decomposition of the undamaged energy of the solid (6.41) as

$$\begin{aligned} \psi(\boldsymbol{\varepsilon}^+, \boldsymbol{\varepsilon}^-, \mathbb{E}; \mathbf{p}) &= \frac{1}{2} \boldsymbol{\varepsilon}^+ : \bar{\mathbb{C}} : \boldsymbol{\varepsilon}^+ + \frac{1}{2} \boldsymbol{\varepsilon}^- : \bar{\mathbb{C}} : \boldsymbol{\varepsilon}^- + \boldsymbol{\varepsilon}^- : \bar{\mathbb{C}} : \boldsymbol{\varepsilon}^+ \\ &\quad - \frac{1}{2} \mathbb{E} \cdot \bar{\boldsymbol{\varepsilon}} : \boldsymbol{\varepsilon}^+ - \frac{1}{2} \mathbb{E} \cdot \bar{\boldsymbol{\varepsilon}} : \boldsymbol{\varepsilon}^- - \frac{1}{2} \mathbb{E} \cdot \bar{\boldsymbol{\varepsilon}} : \boldsymbol{\varepsilon}^+ - \frac{1}{2} \mathbb{E} \cdot \bar{\boldsymbol{\varepsilon}} : \boldsymbol{\varepsilon}^- \\ &\quad - \frac{1}{2} \mathbb{E} \cdot \bar{\mathbb{H}} \cdot \mathbb{E}. \end{aligned} \quad (6.44)$$

Note that some terms in the above equation are intentionally separated in order to degrade the energies in full consistence with the motivation presented previously. Then degrading only the tensile part of the energies the energy of a piezoelectric solid undergoing damage can be presented in the form

$$\begin{aligned} \Psi(\boldsymbol{\varepsilon}^+, \boldsymbol{\varepsilon}^-, \mathbb{E}, \alpha; \mathbf{p}) &= g_m(\alpha) \frac{1}{2} \boldsymbol{\varepsilon}^+ : \bar{\mathbb{C}} : \boldsymbol{\varepsilon}^+ + \frac{1}{2} \boldsymbol{\varepsilon}^- : \bar{\mathbb{C}} : \boldsymbol{\varepsilon}^- + \boldsymbol{\varepsilon}^- : \bar{\mathbb{C}} : \boldsymbol{\varepsilon}^+ \\ &\quad - g_{em}(\alpha) \frac{1}{2} \mathbb{E} \cdot \bar{\boldsymbol{\varepsilon}} : \boldsymbol{\varepsilon}^+ - \frac{1}{2} \mathbb{E} \cdot \bar{\boldsymbol{\varepsilon}} : \boldsymbol{\varepsilon}^- - \frac{1}{2} \mathbb{E} \cdot \bar{\boldsymbol{\varepsilon}} : \boldsymbol{\varepsilon}^+ - \frac{1}{2} \mathbb{E} \cdot \bar{\boldsymbol{\varepsilon}} : \boldsymbol{\varepsilon}^- \\ &\quad - g_e(\alpha; \xi) \frac{1}{2} \mathbb{E} \cdot \bar{\mathbb{H}} \cdot \mathbb{E}. \end{aligned} \quad (6.45)$$

Note that the degradation function in such a case acts only on the tension part of the stored energy. This models *crack closing* for different loading paths in case the strains enter the fully compressive range.

6.3.3. Rate of Electromechanical Energy Functional and Crack Driving Force

The time derivative of the functional (6.37) yields the electromechanical rate functional

$$\dot{E}(\dot{\mathbf{u}}, \dot{\phi}, \dot{\alpha}) = \frac{d}{dt} \int_{\mathcal{B}} \Psi(\boldsymbol{\varepsilon}, \mathbb{E}, \alpha; \mathbf{p}) dV, \quad (6.46)$$

that depends on the rates $\{\dot{\mathbf{u}}, \dot{\phi}, \dot{\alpha}\}$ of the displacement, the electric potential and the phase-field α at a given state $\{\mathbf{u}, \phi, \alpha\}$. The energy can be decomposed according to

$$\dot{E}(\dot{\mathbf{u}}, \dot{\phi}, \dot{\alpha}) = \int_{\mathcal{B}} [\partial_{\boldsymbol{\varepsilon}} \Psi : \dot{\boldsymbol{\varepsilon}} + \partial_{\mathbb{E}} \Psi \cdot \dot{\mathbb{E}} + \partial_{\alpha} \Psi \dot{\alpha}] dV. \quad (6.47)$$

Where the mechanical stress and the electric displacement field are identified as,

$$\boldsymbol{\sigma} := \partial_{\boldsymbol{\varepsilon}} \Psi(\boldsymbol{\varepsilon}, \mathbb{E}, \alpha; \mathbf{p}) \quad \text{and} \quad \mathbb{D} := -\partial_{\mathbb{E}} \Psi(\boldsymbol{\varepsilon}, \mathbb{E}, \alpha; \mathbf{p}). \quad (6.48)$$

With the total crack driving force governing the dissipation per unit volume of the electromechanical problem given in the form

$$f := -\partial_{\alpha} \Psi(\boldsymbol{\varepsilon}, \mathbb{E}, \alpha; \mathbf{p}) \quad \text{with} \quad \mathcal{D} := f \dot{\alpha} \geq 0. \quad (6.49)$$

The fracture driving force f , characterizes the electromechanical fracture model as a generalized standard dissipative material. However, as discussed in [Subsection 6.1.2](#), the driving force of the fracture process in piezoelectrics seems to be governed by the release of the *mechanical energy*. Then similar to (6.19) the driving force can be split according to

$$f := f_m + f_e \quad \text{with} \quad f_m := -\partial_{\alpha} \boldsymbol{\sigma} : \boldsymbol{\varepsilon} \quad \text{and} \quad f_e := \partial_{\alpha} \mathbb{D} : \mathbb{E}. \quad (6.50)$$

Table 6.1: Material parameters for PZT-4 [173, 191].

No.	Parameter	Name	Value	Units
1.	λ	mechanical parameter	77.8×10^3	N/mm ²
2.	μ	mechanical parameter	30.6×10^3	N/mm ²
3.	g_c	critical energy parameter	7×10^{-3}	N/mm
4.	l_s	length scale parameter	0.09	mm
5.	β	fracture anisotropy parameter	10	-
6.	H_{\parallel}	axial piezo-electric parameter	-6.98×10^{-3}	N/(Vmm)
7.	H_{\perp}	lateral piezo-electric parameter	-6.06×10^{-3}	N/(Vmm)
8.	$H_{=}$	shear piezo-electric parameter	16×10^{-3}	N/(Vmm)
9.	ϵ_s	electric permittivity	6.0×10^{-3}	mC/(kVmm)
10.	ϵ_0	vacuum permittivity	8.85×10^{-6}	mC/(kVmm)

As mentioned previously, this work uses the mechanical driving force f_m as the only driving force, following the works of MIEHE ET AL. [172] and PARK & SUN [191]. Note that due to the introduction of the *mechanical driving force*, which is different from the stored total energy functional, the variational principle is not consistent. The thermodynamic consistency is however, *always* fulfilled for $\dot{\alpha} \geq 0$ for appropriate choice of the contribution $\kappa(\alpha)$ introduced in Section 6.1. The choice of the quadratic degradation functions in the formulation will then give the evolution equation of the fracture phase field as given in (6.35) with the crack driving state function \mathfrak{H} defined as,

$$\mathfrak{H} := [\boldsymbol{\epsilon}^+ : \bar{\mathbb{C}} : \boldsymbol{\epsilon}^+ - \boldsymbol{\epsilon}^+ : \bar{\boldsymbol{e}} \cdot \boldsymbol{E}]. \quad (6.51)$$

In line with the MIEHE ET AL. [173], the electromechanical fracture problem is solved in this case also in a staggered solution scheme. This means that the electromechanical problem is solved first with frozen values of the damage variable, and as a second step the damage phase-field is resolved with the electromechanical degrees being frozen. This process is iteratively repeated until convergence is achieved.

6.4. Numerical examples

This section presents some benchmark numerical examples that showcase the behavior of the proposed model. *Mode-1* fracture behavior of the proposed framework is evaluated first under assumption of isotropic crack propagation. Effect of applied electric field, choice of crack driving force and crack boundary conditions are investigated. The following examples showcase the capability of the model to capture anisotropic fracture in a coupled electromechanical setting.

6.4.1. Problem 1: Isotropic Electromechanical Crack Propagation

The first boundary value problem describes a notched PZT-4 specimen under mechanical tensile and electric field loading, which results in a mode one fracture pattern. The material parameters chosen for PZT-4 are presented in table 6.1. The boundary value problem is shown in Figure 6.7 a). A pre-notched specimen, poled in the vertical direction is subjected to varied electrical fields in the direction of poling (positive) or opposite (negative)

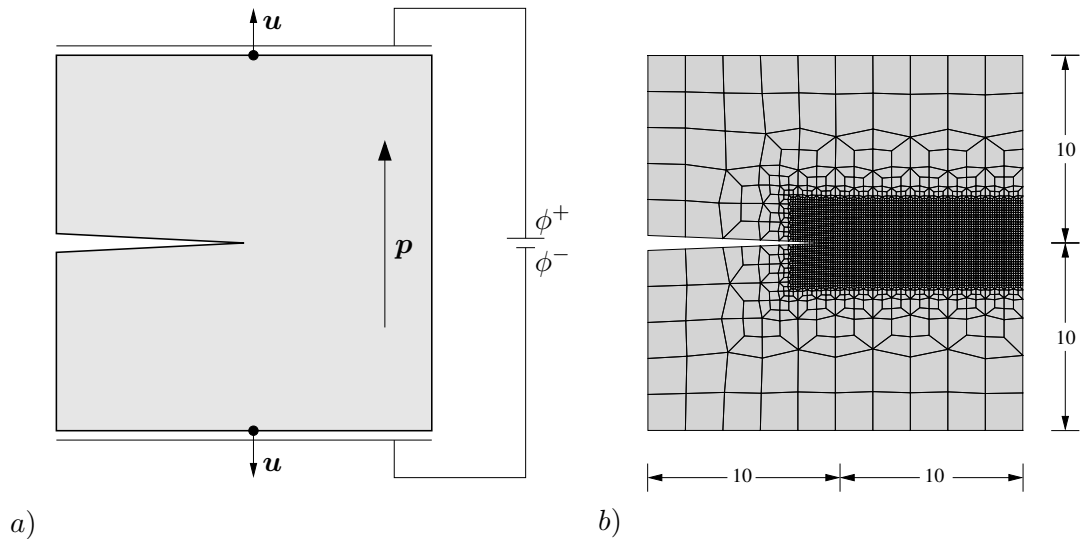


Figure 6.7: Boundary value problem for mode-1 compact tension test with a predefined notch. *a)* The electrical and mechanical boundary conditions are shown. The specimen is poled in the vertical direction and it is subjected to electrical fields in the vertical direction. Mechanical displacements are applied on top and bottom edges as shown. *b)* Mesh discretization of the boundary value problem, with mesh refinement in the area where the crack is expected to propagate. The dimensions of the sample are given in *mm* units.

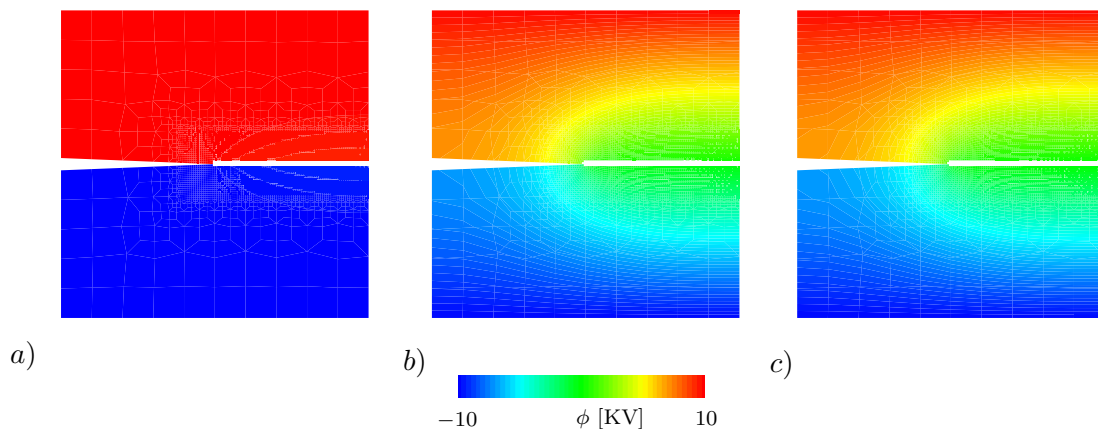


Figure 6.8: Electric potential contour plots of fractured specimen. The cells with damage parameter $\alpha > 0.97$, are blanked to showcase the crack topology. *a)* Impermeable crack conditions $\xi = 0$, with the electric potential jump across the crack topology. *b)* Semi-permeable crack conditions $\xi = 0.5$ with partial penetration of electric field in the crack and *c)* permeable crack conditions $\xi = 1$ with complete penetration of crack topology.

directions. The computations are performed in a monotonic displacement driven scenario in combination with a ramped loading for the electric potential which reaches it's maximum at a mechanical displacement of 0.0001 [mm]. The dimensions of the sample and the mesh discretization is shown in Figure 6.7 b). For isotropic crack propagation the mesh is refined in the areas where crack propagation is expected to occur. Standard quadratic degradation functions are chosen for the mechanical, piezoelectric and electric contributions. The contour plots of the electric potential for various crack boundary conditions, post fracture are plotted in Figure 6.8. Note that FE-cells with the damage parameter $\alpha > 0.99$ are blanked to showcase the crack topology. The contour plots showcase the varied distribution of the electric potential for impermeable $\xi = 0$, semi-permeable $\xi = 0.5$

and permeable $\xi = 1$, crack conditions. The load versus displacement and maximum fracture loads for various applied fields are plotted in Figure 6.9, for impermeable crack conditions. The characteristic behavior of electromechanical fracture presented in experiments in Subsection 6.1.2, with higher fracture loads for negative fields and lower for positive fields. This behavior is due to the choice of the crack driving force, on the other hand Figure 6.10 presents the results for the complete driving force, which predicts higher fracture loads for positive or negative fields. The load–displacement plot for impermeable, semi-permeable and permeable conditions for -5 [KV/cm] and 5 [KV/cm] applied fields alongwith maximum fracture load is plotted against various applied fields in Figure 6.11. The general behavior remains the same for all crack conditions with increase in fracture load for negative fields and decrease for positive fields. The permeable crack conditions shows the maximum increase and decrease in fracture loads across the spectrum, with the impermeable showing the least influence and semi-permeable lying in between these extremes.

6.4.2. Problem 2: Anisotropic Electromechanical Crack Propagation

The behavior of the model under anisotropic crack propagation is now showcased. The boundary value problem is the same as the isotropic case, as shown in Figure 6.7 and the material is poled in the vertical direction. However, mesh refinement is done where crack is expected to propagate according to the chosen fracture anisotropy angle. The fracture is assumed to propagate along the poling direction, indicated by black arrows. Figure 6.12 showcases anisotropic crack propagation for various crack conditions. The anisotropy angle is chosen to be 30° from the horizontal in this case. As it can be seen the fracture tends to follow the anisotropy direction at 21.8° , for the chosen anisotropic parameter of $\beta = 10$. The anisotropy parameter can be increased such that the fracture follows the fracture anisotropy, see for reference ([235]), for the choice of the anisotropic

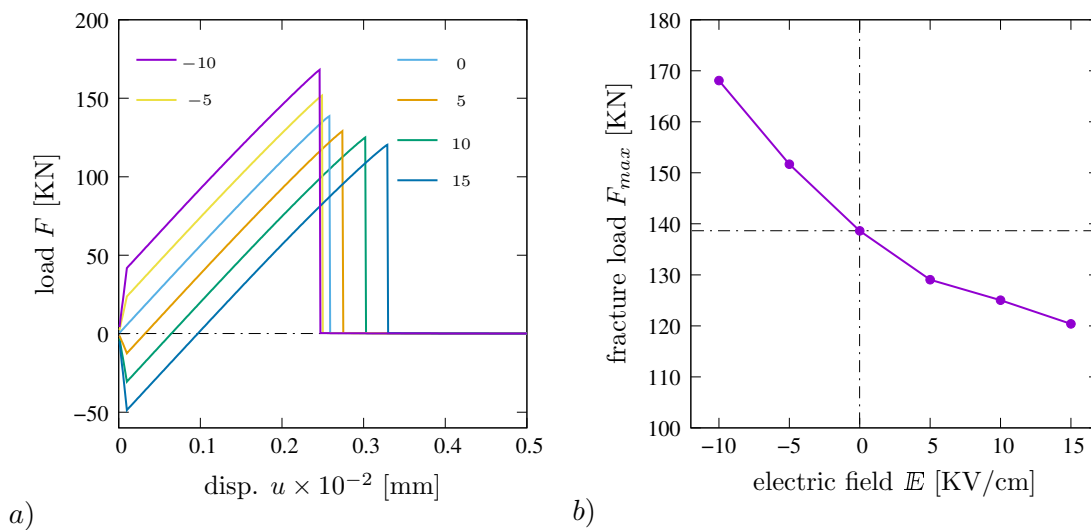


Figure 6.9: Load displacement and fracture load plots. The fracture behavior of the model is presented for various applied electrical fields ranging from -10 [KV/cm] to 15 [KV/cm]. *a)* Load displacement plot for various applied electrical fields and *b)* maximum fracture load for positive and negative applied fields. Increased fracture load is predicted for negative fields and decrease in fracture load for positive fields.

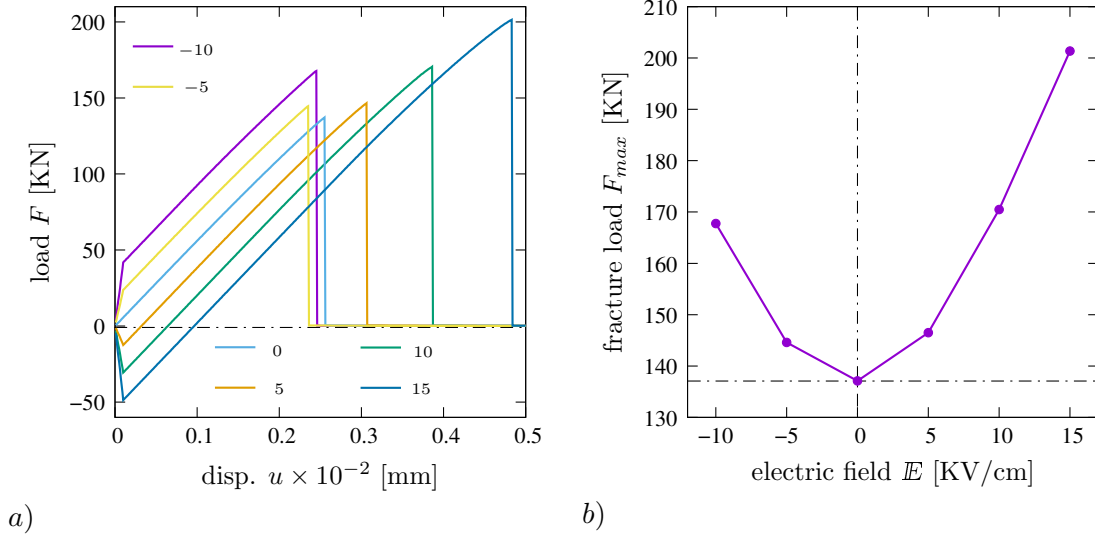


Figure 6.10: Load displacement and fracture load plots with full driving force for comparison with presented model. The fracture behavior of the model is presented for various applied electrical fields. a) Load displacement plot for various applied electric fields and b) maximum fracture load for positive and negative applied fields. Increased fracture load is predicted for negative fields and positive fields.

parameter. As it can be seen the discontinuity in the electric potential follows the crack path for all the chosen cases of impermeable Figure 6.12 a), semi-permeable Figure 6.12 b) and the permeable case Figure 6.12 c). The fracture plots for this example are plotted in Figure 6.13, for an applied electric field of 10 [KV/cm]. The load–displacement plot shows the same behavior as the isotropic case with the maximum increase in fracture load seen for the impermeable case, for the case of positive applied fields. The maximum fracture load plots also follows the same characteristics, however it is noted that the

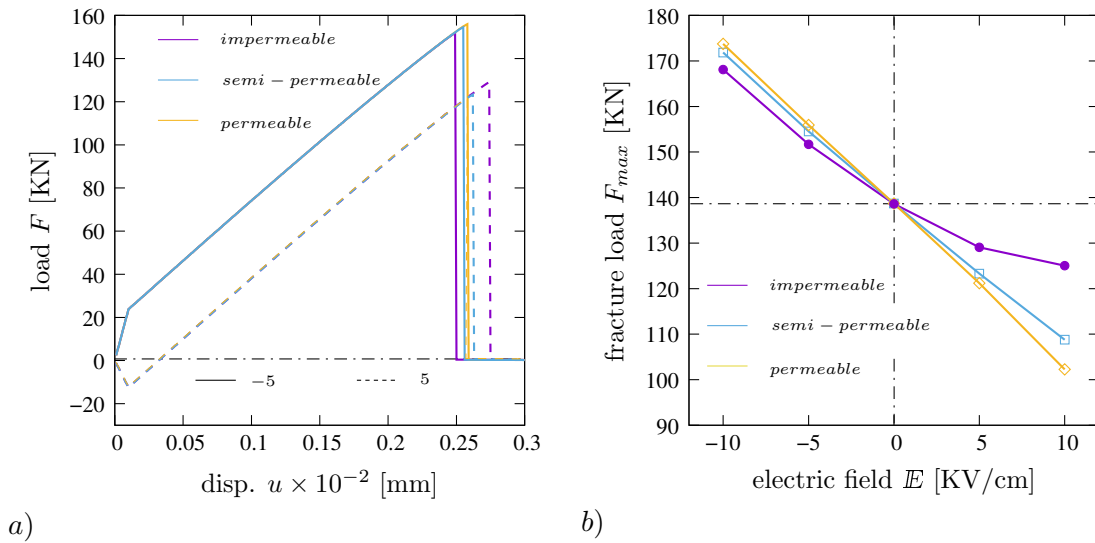


Figure 6.11: Load displacement and fracture load plots for various crack conditions. a) Load displacement plot for impermeable $\xi = 0$, semi-permeable $\xi = 0.5$ and permeable $\xi = 0$, for -5 [KV/cm] and 5 [KV/cm] and b) maximum fracture load for the different electric fields, maximum variation in fracture loads seen for permeable case and least for impermeable with semi-permeable inbetween the two extremes.

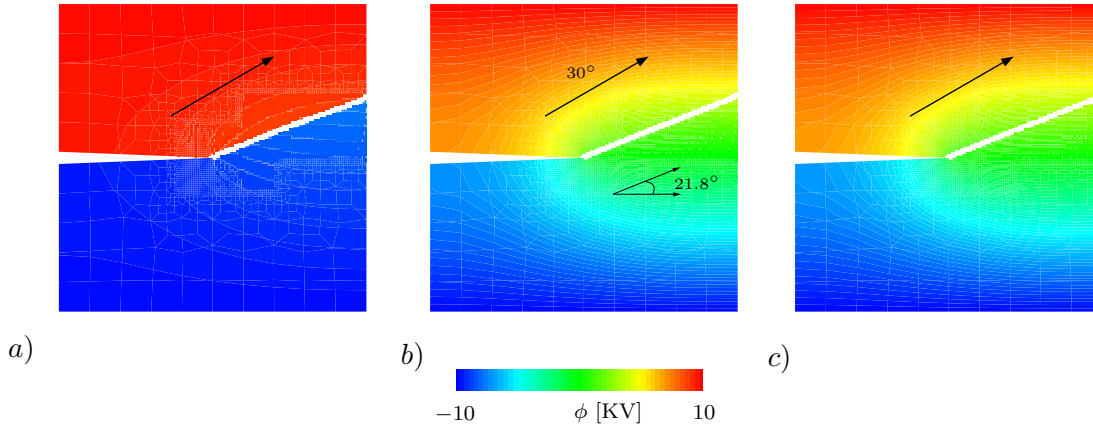


Figure 6.12: Electric potential contour plots of anisotropic fractured specimen. The cells with damage parameter $\alpha > 0.99$, are blanked to showcase the crack topology. Fracture anisotropy angle is 30° from horizontal, indicated by black arrows. a) Impermeable crack conditions $\xi = 0$, b) Semi-permeable crack conditions $\xi = 0.5$ and c) permeable crack conditions $\xi = 1$ are shown. Fracture path approximately follows the anisotropy angle at 21.8° .

influence of the crack conditions seems to have negligible effect, especially in the case of negative applied fields. The behavior of the model for anisotropy angles of 0° , 30° and 45° are shown in Figure 6.14. Similar to the previous example it is seen that the crack propagation approximately follows the anisotropy angle, with the electrical jump conditions following the crack path. The load–displacement and fracture loads for various anisotropy angles and applied fields are plotted in Figure 6.15. The load–displacement plot for applied fields of -5 [KV/cm] and 5 [KV/cm] show similar behavior. There is a consistent increase in the fracture load with increasing anisotropy, which can also be seen in the fracture load plots, where the electrical influence on the fracture load remains almost consistent for all anisotropic angles.

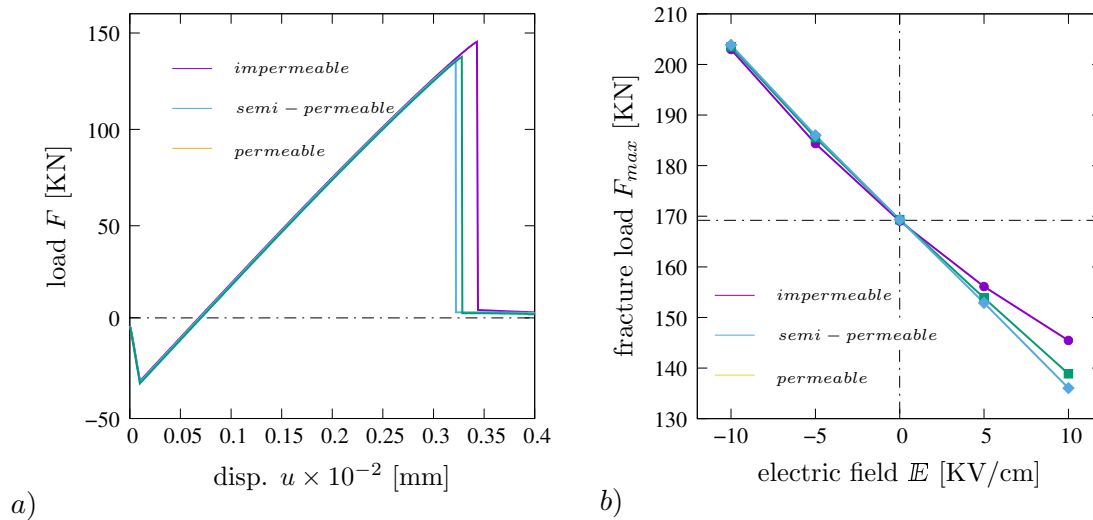


Figure 6.13: Load displacement and fracture load plots for anisotropic fracture under varied electrical crack conditions. The anisotropic fracture behavior of the model is presented for applied electrical field. Anisotropic fracture angle is 30° with anisotropic parameter of $\beta = 10$. a) Load displacement plot for various crack conditions with applied field of 10 [KV/cm] and b) maximum fracture load for positive and negative applied fields. Increased fracture load is predicted for negative fields and decrease in fracture load for positive fields.

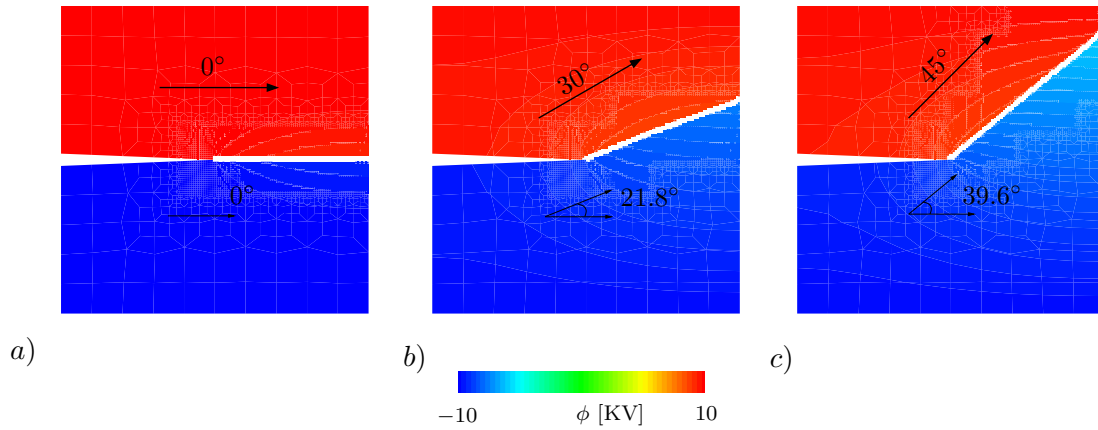


Figure 6.14: Electric potential contour plots of anisotropic fractured specimen. The cells with damage parameter $\alpha > 0.99$, are blanked to showcase the crack topology. Fracture anisotropy angle is a) 0° , b) 30° and c) 45° from horizontal, indicated by black arrows. Fracture path approximately follows the anisotropy angle at 0° , 21.8° and 39.6° .

6.4.3. Problem 3: Three-dimensional electromechanical crack propagation

The last example analyses the anisotropic crack propagation for *mode-1* fracture test in a three-dimensional setting. The rectangular specimen is discretized using approximately 12,000 brick elements, with five degrees of freedom. The boundary value problem is shown in Figure 6.16 a) and the dimensions shown in Figure 6.16 b). The mesh is refined along the predicted path of fracture growth. The specimen is poled in the vertical direction along which the electric field and mechanical displacement is applied. The fracture propagation and electric potential contour are shown in Figure 6.17 a)–i), for various anisotropy crack directions. The fracture path for 0° , 30° and 45° are shown in Figure 6.17 a)–c), Figure 6.17 d)–f) and Figure 6.17 g)–i) respectively. The fracture path tends to follow the anisotropy angle and the electric potential jump follows the crack path.

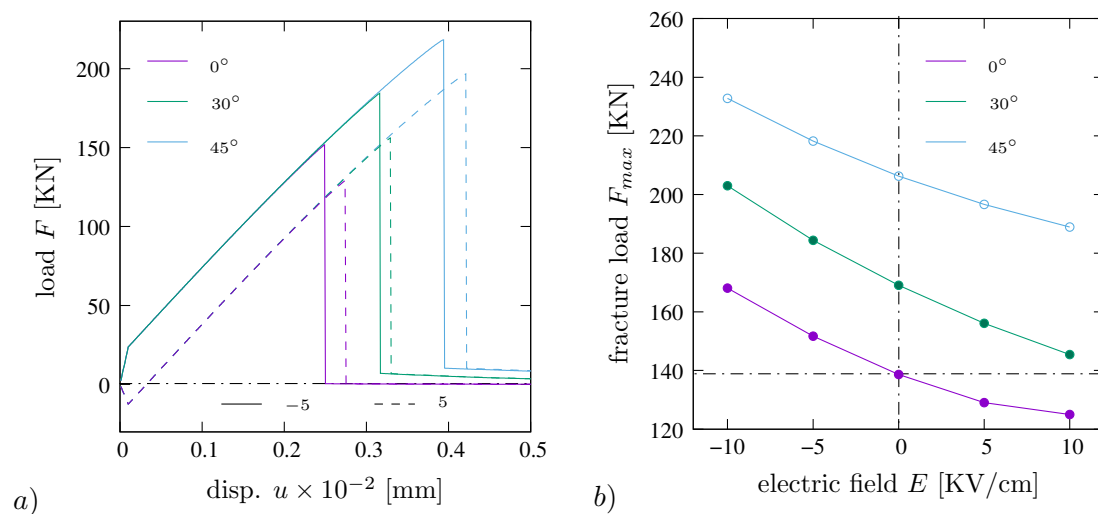


Figure 6.15: Load displacement and fracture load plots. The anisotropic fracture behavior of the model is presented for applied electrical field. Anisotropic fracture angle is chosen to be 0° , 30° and 45° , with anisotropic parameter of $\beta = 10$. a) Load displacement plot for various crack anisotropy angles and applied fields of -5 [KV/cm] and 5 [KV/cm] b) maximum fracture load for positive and negative applied fields.

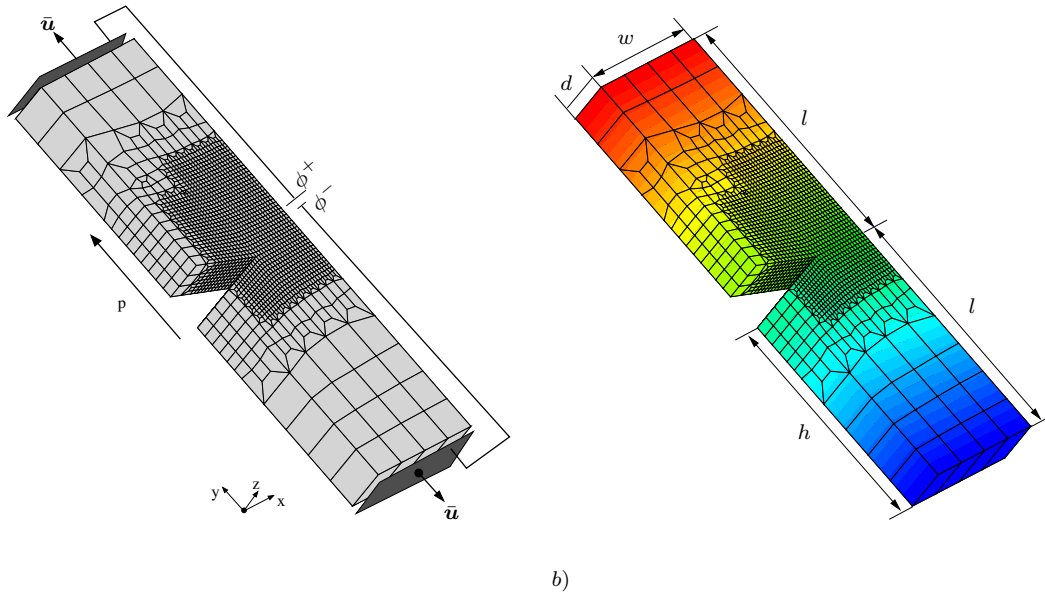


Figure 6.16: *Three-dimensional boundary value problem for mode one fracture investigation of a rectangular notch specimen. a) The boundary conditions for a rectangular notch specimen, with poling along the y -direction the electric field and mechanical displacement applied along the same direction. b) The dimensions of the sample are shown with $d=1$ [mm], $l=5$ [mm], $w=3$ [mm] and $h=4.6$ [mm].*

The fracture behavior and crack propagation is similar to the two-dimensional examples presented previously. The example showcases the capability of the presented framework to capture the characteristic behavior of coupled electro-mechanical fracture propagation in a three-dimensional setting.

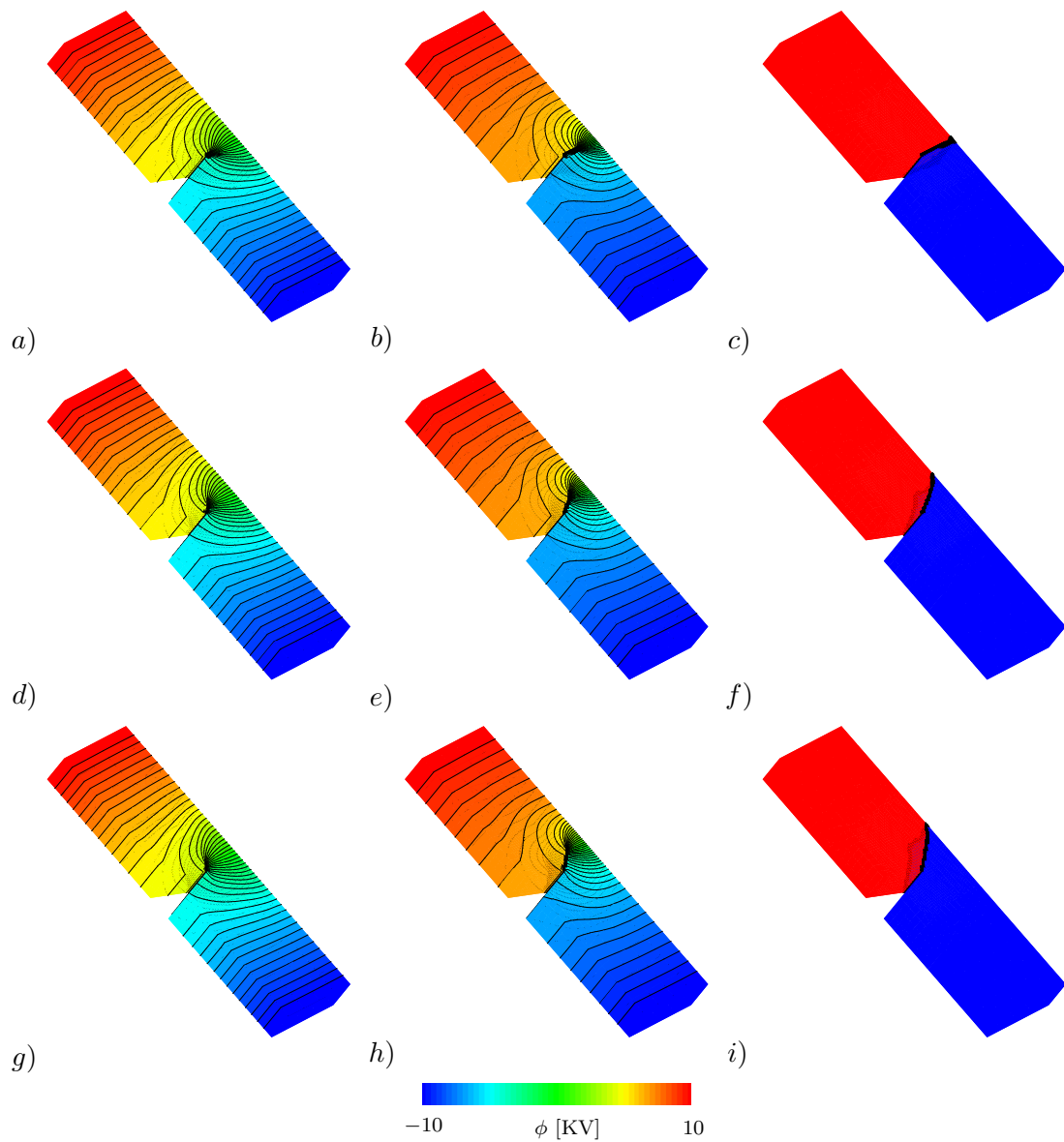


Figure 6.17: *Electric potential contour plots of anisotropic fracture in three dimensional tension test.* A three dimensional piezo-electric specimen subjected to mode-1 fracture under the influence of external electric field. Contour plot show case the electric potential distribution and the equipotential lines. Fracture anisotropy angle chosen as 0° in *a, b, c*), 30° in *d, e, f*) and 45° in *g, h, i*). Crack path tends to follow the anisotropy in each case.

Variational Phase-Field Approach to Anisotropic Fracture in Ferroelectrics

This chapter deals with the extension of the electromechanical fracture theory presented in [Chapter 6](#), to crack propagation in ferroelectric materials. Ferroelectric materials are a special class of piezoelectric ceramics, that show spontaneous polarization under the Curie temperature. To account for this an additional phase-field, that is the polarization, is introduced as an order parameter. The first section details constitutive behavior of the proposed model by analyzing the one-dimensional local response. Following this, the variational framework for the theory is presented in a rate-dependent setting. This results in an additional Euler equation for the time-dependent, non-local response of the polarization field. A brief description of the energy contributions is given. Finally, numerical examples are presented that showcase polarization evolution, crack propagation and interaction between both the processes.

7.1. Local Ferroelectric Damage Model

In the subsequent sections the electromechanical fracture with a polarization phase-field $\mathbb{P} \in \mathcal{R}^{d=1,2,3}$ is presented. The sharp crack topology is considered in a diffuse manner by the damage field $\alpha \in [0, 1)$. Similar, to our previous interpretation, in this section α is considered as a local damage variable to analyze the constitutive response of the model. The polarization is also considered as a local, time independent variable dependent on the electric field and mechanical strains.

7.1.1. Thermodynamic Formulation of Local Damage

For a ferroelectric material undergoing fracture an energy function $\Psi(\varepsilon, \mathbb{E}, \mathbb{P}, \alpha)$ depending on the strain ε , the electric field \mathbb{E} , the polarization \mathbb{P} and the damage variable α can be defined to model the material response. For such an electromechanical energy the second axiom of thermodynamics may be written in the form of the local dissipation \mathcal{D}

as,

$$\mathcal{D} = \sigma \dot{\varepsilon} - \mathcal{D} \dot{\mathbb{E}} + \mathcal{G} \dot{\mathbb{P}} - \dot{\Psi} \geq 0, \quad (7.1)$$

in terms of the energy conjugate variables, the mechanical stress σ , dielectric displacement \mathcal{D} and the polarization conjugate \mathcal{G} . Exploitation of the dissipation inequality by standard arguments yields the constitutive equations,

$$\sigma = \partial_{\varepsilon} \Psi, \quad \mathcal{D} = -\partial_{\mathbb{E}} \Psi \quad \text{and} \quad \mathcal{G} = \partial_{\mathbb{P}} \Psi. \quad (7.2)$$

The reduced dissipation equation then appears as the product of a thermodynamic driving force f and the evolution of the the damage variable $\dot{\alpha}$

$$\mathcal{D} = f \dot{\alpha} \geq 0 \quad \text{with} \quad f = -\partial_{\alpha} \Psi. \quad (7.3)$$

Note that polarization evolution is also a dissipative process. However, for this analysis no time evolution of the polarization field is considered. Then, for a growth of the damage variable α , that is considered to describe irreversible destruction of the material microstructure to prevent healing processes, the damage field evolve such that

$$\dot{\alpha} \geq 0 \rightarrow f \geq 0. \quad (7.4)$$

Assuming a *dissipation function* Φ^* of thermodynamic forces, the evolution of the internal damage variable is determined by,

$$\dot{\alpha} \in \partial_f \Phi^*(f). \quad (7.5)$$

Here, $\partial_f(\cdot)$ denotes the sub-differential of (\cdot) . With this structure of the evolution equation, the dissipation inequality (7.3) is automatically satisfied. Note that, similar to [Subsection 6.1.1](#), an additional contribution to the driving force of the form $\partial_{\alpha} \kappa(\alpha) < 0$ is required to ensure $f \geq 0$, MIEHE ET AL. [173]. As this contribution does not influence the constitutive behavior of the model, it has not been discussed in detail here.

7.1.2. Electromechanical Energy Function for Ferroelectric Damage

The energy function $\Psi(\varepsilon, \mathbb{E}, \mathbb{P}, \alpha)$, depending on the the strain ε , the electric field \mathbb{E} , the polarization \mathbb{P} and the damage variable α describes local damage mechanism in a ferroelectric material, has the contributions

$$\Psi(\varepsilon, \mathbb{E}, \mathbb{P}, \alpha) = g_m(\alpha) \Psi_m(\varepsilon, \mathbb{P}) + g_{lan}(\alpha) \Psi_{lan}(\mathbb{P}) + g_{ele}(\alpha) \Psi_{ele}(\mathbb{P}, \mathbb{E}). \quad (7.6)$$

In terms of the mechanical $g_m(\alpha)$, polarization $g_{lan}(\alpha)$ and electric $g_{ele}(\alpha)$ degradation functions. In addition $\Psi_m(\varepsilon, \mathbb{P})$, $\Psi_{lan}(\mathbb{P})$ and $\Psi_{ele}(\mathbb{P}, \mathbb{E})$ are the mechanical, polarization and electric energy functions respectively. For this one dimensional analysis they assume the simple form

$$\Psi_m(\varepsilon) = \frac{1}{2} E_s \varepsilon^2 - \frac{a_0}{2} \varepsilon^2 \mathbb{P}^2, \quad \Psi_{lan}(\mathbb{P}) = \frac{a_1}{2} \mathbb{P}^2 + \frac{a_2}{4} \mathbb{P}^4 \quad \text{and} \quad \Psi_{ele}(\mathbb{P}, \mathbb{E}) = -\mathbb{P} \mathbb{E} - \frac{1}{2} \epsilon_0 \mathbb{E}^2, \quad (7.7)$$

in terms of the mechanical stiffness E_s , the electrostrictive constant a_0 , the Landau potential constants a_1 and a_2 and the electric permittivity of vacuum ϵ_0 . The mechanical part of the energy accounts for material deformation and electrostriction. The coupled energy contains a reduced form of the Landau-Devonshire energy to model the energy minima of the polarization. Finally, the electric contribution is the vacuum energy due to the electric field and polarization. In this work only impermeable electrical boundary conditions and quadratic degradation functions are considered such that, $g_m = g_{lan} = g_{ele} = (1 - \alpha^2)$.

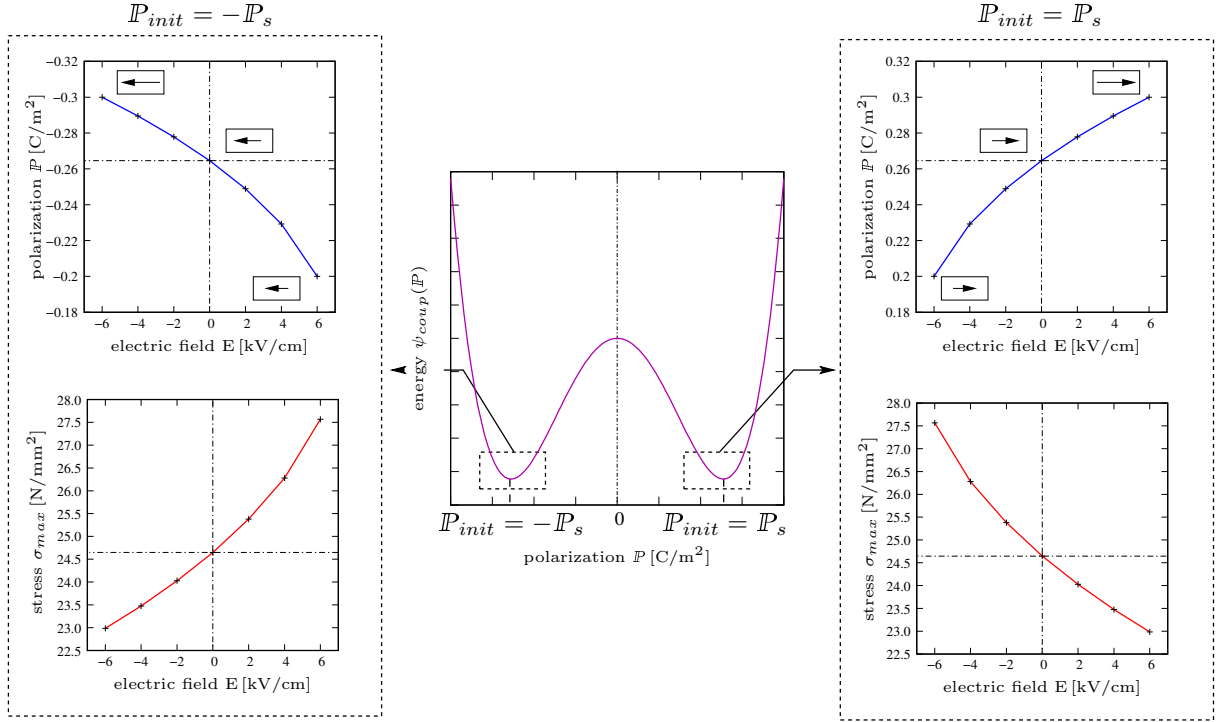


Figure 7.1: Fracture load dependence for 'low' applied electric fields, due to polarization fluctuations. The reduced Landau-Devonshire energy presented in (7.7) is plotted for various polarization values. The energy minima lies at $P_s = \pm 0.26$ as seen from the plot. The polarization is initialized at $P = \pm P_s$ and the plot of the polarization and fracture loads for varied electric fields are plotted. For low electric fields applied in this case, no polarization switching is noted and a decrease in fracture load is seen for fields in the direction of polarization while fields opposite to polarization increases the fracture load. This can be attributed to the assumed mechanical driving force such that fracture load varies with the polarization magnitude, (7.8). The fracture behavior is similar to the piezoelectric case.

7.1.3. Electromechanical Driving Force and Damage Evolution

With the definitions of the conjugate variables (7.2) and the energy (7.7), the conjugate energy variables can be explicitly written as

$$\begin{aligned} \sigma &= (1 - \alpha)^2 (E_s \varepsilon - a_0 \varepsilon P^2), & G &= (1 - \alpha)^2 (-a_0 \varepsilon^2 P + a_1 P + a_2 P^3 - \mathbb{E}) \\ D &= (1 - \alpha)^2 (\epsilon_0 \mathbb{E} + P) & \text{and} & \quad f^m = (1 - \alpha) \left(\frac{1}{2} E_s \varepsilon^2 - \frac{a_0}{2} \varepsilon^2 P^2 \right). \end{aligned} \quad (7.8)$$

Note that similar to the piezoelectric case only the mechanical part of the driving force is considered to drive the damage evolution. These assumptions are made following the arguments presented in Chapter 6. The complete driving force can be split according to

$$f = -\partial_\alpha \Psi = f^m + f^P + f^{\mathbb{E}} \quad \text{with} \quad f^m = -\partial_\alpha \Psi_m, \quad f^P = -\partial_\alpha \Psi_{lan} \quad \text{and} \quad f^{\mathbb{E}} = -\partial_\alpha \Psi_{ele}. \quad (7.9)$$

A detailed analysis of various driving forces and their influence on crack propagation is required to understand the coupled phenomenon. This is however beyond the scope of this work and not considered here. For a rate-independent, discontinuous evolution of the internal variables α and polarization P an evolution function can be given as

$$t(f^m; \alpha) = f^m - c\alpha \quad \text{and} \quad G(P; \varepsilon, \mathbb{E}) = 0. \quad (7.10)$$

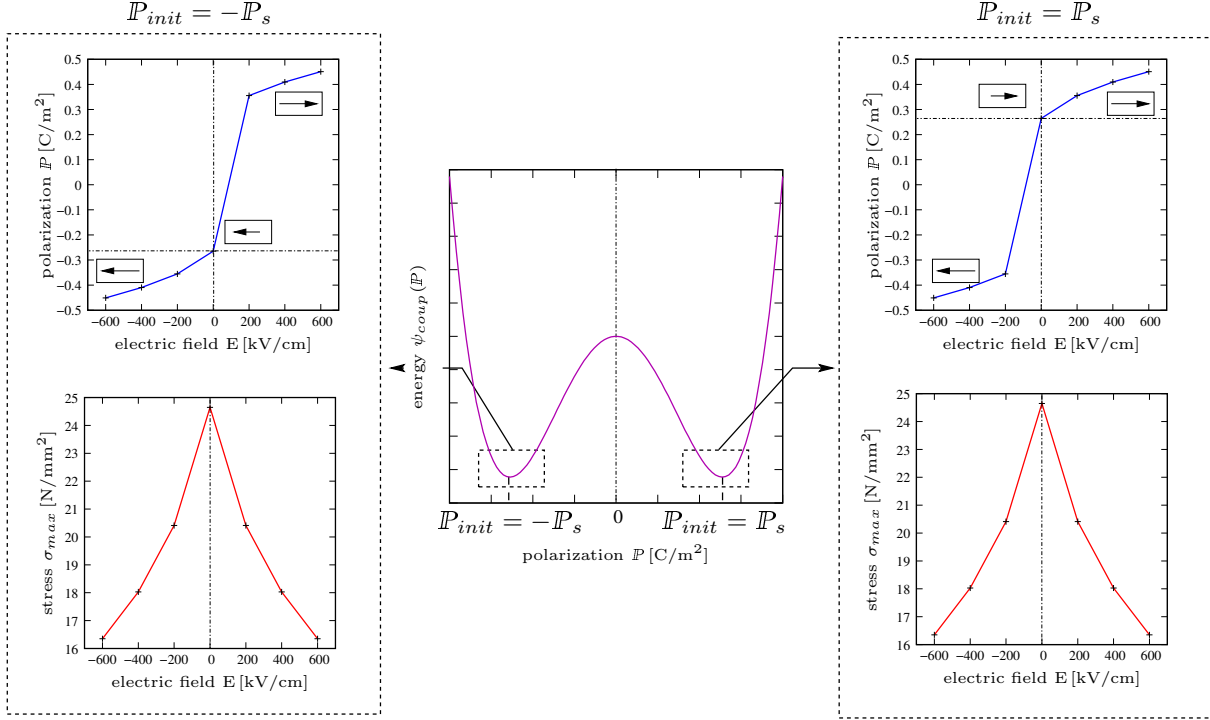


Figure 7.2: Fracture load dependence for 'high' applied electric fields, due to polarization switching. The reduced Landau-Devonshire energy presented in (7.7) is plotted for various polarization values. The energy minima lies at $P_s = \pm 0.26$ as seen from the plot. The polarization is initialized at $P = \pm P_s$ and the plot of the polarization and fracture loads for varied electric fields are plotted. For high electric fields applied in this case, polarization switching occurs and a decrease in fracture load is seen for fields in the direction and opposite to the polarization. This can be attributed to the assumed mechanical driving force such that fracture load varies with the polarization magnitude (7.8).

For given strain ε and electric field \mathbb{E} , the polarization P can be computed from (7.10)₂. Note that due to the non-linear nature of this equation the computation of the polarization will require a Newton iteration to solve. The damage variable can be computed with the condition $t(f; \alpha) = 0$ from (7.10)₁ giving the closed form solution

$$\alpha = \frac{\mathfrak{h}(\varepsilon, P)}{c + \mathfrak{h}(\varepsilon, P)} \quad \text{for } \dot{\alpha} \geq 0, \quad (7.11)$$

with $\mathfrak{h}(\varepsilon, P) = \frac{1}{2}E_s\varepsilon^2 - \frac{a_0}{2}\varepsilon^2P^2$. The function \mathfrak{h} drives the evolution of the damage variable α . To ensure the growth of the damage variable $\dot{\alpha} \geq 0$ let $\mathcal{H}(t)$ denote the maximum value of \mathfrak{h} over time such that

$$\alpha(t) = \frac{\mathcal{H}(t)}{c + \mathcal{H}(t)} \in [0, 1) \quad \text{with } \mathcal{H}(t) := \max_{s \in [0, t]} [\mathfrak{h}(\varepsilon(s), P(s))] \in [0, \infty). \quad (7.12)$$

It is important to note that contrary to the piezoelectric case (6.17) where \mathfrak{h} depends on the electric field \mathbb{E} , for the ferroelectric case \mathfrak{h} depends on the polarization field P . The polarization is coupled with the strain and the electric field through (7.8)₂. The equations (7.8)₁, (7.8)₂ and (7.8)₃ then govern exclusively the degradation of the mechanical stress, polarization conjugate and electric displacements of a ferroelectric solid. Behavior of the model for electric fields applied in the direction (positive) or opposite (negative) to poling are shown in Figure 7.1 and Figure 7.2. Polarization is initialized

with $\mathbb{P}_{init} = \pm p_s$, where p_s is the saturation value of the polarization for no applied electric or mechanical loading ($p_s = 0.26 [\text{C}/\text{m}^2]$ for Barium Titanate at room temperature). The reduced Landau-Devonshire potential depending on the polarization is plotted in the middle. [Figure 7.1](#) shows the dependence of the polarization and fracture loads for relatively low applied fields. In such a case polarization switching is not observed and only the magnitude of the polarization changes. This in turn influences damage evolution such that negative fields increase fracture load while positive fields decrease fracture load. The results quantitatively agree with those for the piezoelectric case [PARK & SUN \[191\]](#). On the other hand high electric fields cause switching of the polarization direction as is seen in [Figure 7.2](#). This results in a rather symmetric behavior of the fracture load which predicts a decrease for positive or negative fields. Quantitatively this agrees with the results of [FU & ZHANG \[74\]](#). The results clearly indicate a strong dependency of the fracture load on the polarization orientation and in turn the applied field. As noted previously this analysis assumes: 1) impermeable crack conditions and 2) only the mechanical part of the energy drives damage evolution. These assumptions are also carried on in the general fracture formulation in the next sections. Further analysis on various choices of the driving forces and their influence along with varied electrical conditions are required. As an initial step towards this a simplified theory is considered in this work.

7.2. Variational Principle for Evolution of Phase-Field Fracture in Ferroelectrics

7.2.1. Primary Fields of Ferroelectric Fracture

In the small-strain context, the coupled electromechanical response in a ferroelectric solid $\mathcal{B} \in \mathcal{R}^d$ at time $\mathcal{T} \in \mathcal{R}_+$, can be described via the mechanical displacement, electric potential and polarization order parameter defined as

$$\mathbf{u} : \begin{cases} \mathcal{B} \times \mathcal{T} \rightarrow \mathcal{R}^d \\ (\mathbf{x}, t) \mapsto \mathbf{u}(\mathbf{x}, t), \end{cases} \quad \phi : \begin{cases} \mathcal{B} \times \mathcal{T} \rightarrow \mathcal{R} \\ (\mathbf{x}, t) \mapsto \phi(\mathbf{x}, t), \end{cases} \quad \mathbb{P} : \begin{cases} \mathcal{B} \times \mathcal{T} \rightarrow \mathcal{R}^d \\ (\mathbf{x}, t) \mapsto \mathbb{P}(\mathbf{x}, t). \end{cases}$$

The mechanical strains are assumed to be small and the gradients of the above fields define the small-strain tensor, the electric-field vector and the gradient of the polarization

$$\boldsymbol{\varepsilon}(\mathbf{u}) = \nabla_s \mathbf{u}, \quad \mathbb{E}(\phi) = -\nabla \phi \quad \text{and} \quad \mathbb{P} = \nabla \mathbb{P}. \quad (7.13)$$

Moreover, to capture the fracture mechanics in ferroelectrics in addition to the above mentioned fields the fracture phase-field α is introduced

$$\alpha : \begin{cases} \mathcal{B} \times \mathcal{T} \rightarrow [0, 1] \\ (\mathbf{x}, t) \mapsto \alpha(\mathbf{x}, t). \end{cases} \quad (7.14)$$

The crack phase-field α describes the crack propagation in terms of the crack surface density function as introduced in [Chapter 3](#).

7.2.2. Variational Principle and Euler-Lagrange Equations

The coupled electromechanical total energy functional for a ferroelectric ceramic undergoing fracture can be given as

$$W(\mathbf{u}, \phi, \mathbb{P}, \nabla \mathbb{P}, \alpha) := E(\mathbf{u}, \phi, \mathbb{P}, \nabla \mathbb{P}, \alpha) + \Gamma_l(\alpha) := \int_{\mathcal{B}} w(\nabla_s \mathbf{u}, -\nabla \phi, \alpha, \mathbb{P}, \nabla \mathbb{P}, \nabla \alpha) dV, \quad (7.15)$$

where $E(\mathbf{u}, \phi, \mathbb{P}, \nabla \mathbb{P}, \alpha)$ is the stored energy functional of the bulk and $\Gamma_l(\alpha)$ is the regularized crack surface functional (3.14). The constitutive total energy density function w depends on the first gradient of the phase-fields, damage variable and polarization, along with the gradient fields introduced in (7.13). This energy density function can be split such that,

$$w(\nabla_s \mathbf{u}, -\nabla \phi, \mathbb{P}, \nabla \mathbb{P}, \alpha, \nabla \alpha) = \Psi(\nabla_s \mathbf{u}, -\nabla \phi, \mathbb{P}, \nabla \mathbb{P}, \alpha) + g_c \gamma_l(\alpha, \nabla \alpha; \mathbf{A}), \quad (7.16)$$

where Ψ is a specific representation of the bulk electromechanical energy of the ferroelectric material, γ_l is the anisotropic crack surface density function introduced in (3.16) and g_c is a material parameter. Furthermore consider a dissipation potential functional governing the evolution of fracture phase field and polarization as

$$D(\dot{\alpha}, \dot{\mathbb{P}}) = \int_{\mathcal{B}} [d_{frac}(\dot{\alpha}) + d_{pol}(\dot{\mathbb{P}})] dV, \quad (7.17)$$

that depends on a convex and non-smooth dissipation potential density function $d_{frac}(\dot{\alpha})$ for the fracture phase field and a smooth, convex and quadratic function $d_{pol}(\dot{\mathbb{P}})$ for the polarization phase field. The two functionals W and D define the rate-potential functional

$$\Pi(\dot{\mathbf{u}}, \dot{\phi}, \dot{\mathbb{P}}, \dot{\alpha}) = \frac{d}{dt} W + D. \quad (7.18)$$

The rate-potential governs the variational principle for the coupled four-field evolution problem as

$$\{\dot{\mathbf{u}}, \dot{\phi}, \dot{\mathbb{P}}, \dot{\alpha}\} = \arg \left\{ \inf_{\dot{\mathbf{u}} \in \mathcal{W}_{\dot{\mathbf{u}}}} \sup_{\dot{\phi} \in \mathcal{W}_{\dot{\phi}}} \inf_{\dot{\mathbb{P}} \in \mathcal{W}_{\dot{\mathbb{P}}}} \inf_{\dot{\alpha} \in \mathcal{W}_{\dot{\alpha}}} \Pi \right\}. \quad (7.19)$$

The admissible spaces for the rates of the displacement, electric potential and the order parameters are,

$$\begin{aligned} \mathcal{W}_{\dot{\mathbf{u}}} &:= \{\dot{\mathbf{u}} \in \mathcal{R}^d \mid \dot{\mathbf{u}} = \dot{\hat{\mathbf{u}}} \text{ on } \partial \mathcal{B}_D^u\}, \\ \mathcal{W}_{\dot{\phi}} &:= \{\dot{\phi} \in \mathcal{R} \mid \dot{\phi} = \dot{\hat{\phi}} \text{ on } \partial \mathcal{B}_D^\phi\}, \\ \mathcal{W}_{\dot{\alpha}} &:= \{\dot{\alpha} \in \mathcal{R} \mid \dot{\alpha} = \dot{\hat{\alpha}} \text{ on } \partial \mathcal{B}_D^\alpha\} \quad \text{and} \\ \mathcal{W}_{\dot{\mathbb{P}}} &:= \{\dot{\mathbb{P}} \in \mathcal{R}^d \mid \dot{\mathbb{P}} = \dot{\hat{\mathbb{P}}} \text{ on } \partial \mathcal{B}_D^{\mathbb{P}}\}. \end{aligned} \quad (7.20)$$

The Euler equations of the variational principle (7.19) are

$$\operatorname{div}[\boldsymbol{\sigma}] = \mathbf{0}, \quad \operatorname{div}[\mathbb{D}] = 0, \quad 0 = \delta_{\mathbb{P}} w + \partial_{\dot{\mathbb{P}}} d_{pol} \quad \text{and} \quad 0 \in \delta_{\alpha} w + \partial_{\dot{\alpha}} d_{frac}, \quad (7.21)$$

where the mechanical stress tensor $\boldsymbol{\sigma}$ and electric displacement field \mathbb{D} are identified as the work conjugate of the strain and electric field, respectively. In the above equation (7.21), $\delta_{\alpha} w$ denotes the variational derivative of the function with α , defined as $\delta_{\alpha} w = \partial_{\alpha} w - \operatorname{div}[\partial_{\nabla \alpha} w]$ and $\delta_{\mathbb{P}} w$ denotes the variational derivative of the function with \mathbb{P} , defined

as $\delta_{\mathbb{P}} w = \partial_{\mathbb{P}} w - \operatorname{div}[\partial_{\nabla \mathbb{P}} w]$. Taking into account the irreversibility of the fracture phase field by the non-smooth dissipation potential functional of the form

$$d_{\text{frac}}(\dot{\alpha}) = I(\dot{\alpha}) + \frac{\eta}{2} \dot{\alpha}^2, \quad (7.22)$$

and following the framework presented in the case of piezoelectric fracture [Subsection 6.2.3](#) the fracture evolution can be reformulated in the form

$$\eta \dot{\alpha} = (1 - \alpha) \mathcal{H} - \frac{g_c}{l} \alpha + g_c l \operatorname{div}[\mathbf{A} \cdot \nabla \alpha], \quad (7.23)$$

where, \mathcal{H} denotes the positive crack driving force which is expressed as the maximum over time of a crack driving state function \mathfrak{H}

$$\mathcal{H}(\mathbf{x}, t) := \max_{s \in [0, t]} \mathfrak{H}(\mathbf{x}, s). \quad (7.24)$$

For the evolution of polarization order parameter an isotropic, quadratic dissipation potential is assumed of the form

$$d_{\text{pol}}(\dot{\mathbb{P}}) = \frac{\eta^*}{2} \operatorname{tr}[\dot{\mathbb{P}} \otimes \dot{\mathbb{P}}]. \quad (7.25)$$

7.3. Degrading Energy Functional Due to Fracture Evolution

7.3.1. Stored Ferroelectric Energy Functional

The energy functional considered for fracture propagation in a ferroelectric ceramic can be defined as

$$E(\mathbf{u}, \phi, \mathbb{P}, \nabla \mathbb{P}, \alpha) = \int_{\mathcal{B}} \Psi(\boldsymbol{\varepsilon}, \mathbb{E}, \mathbb{P}, \nabla \mathbb{P}, \alpha) \, dV. \quad (7.26)$$

The function Ψ describes the energy density per unit volume of the solid. For impermeable crack conditions along with quadratic degradation functions considered in this work, the energy can be split according to

$$\Psi(\boldsymbol{\varepsilon}, \mathbb{E}, \mathbb{P}, \nabla \mathbb{P}, \alpha) = (1 - \alpha)^2 [\psi_e(\boldsymbol{\varepsilon}, \mathbb{P}) + \psi_a(\mathbb{P}) + \psi_{ex}(\nabla \mathbb{P}) + \psi_{vac}(\mathbb{P}, \mathbb{E})], \quad (7.27)$$

in terms of the elastic contribution due to lattice distortions $\psi_e(\boldsymbol{\varepsilon}, \mathbb{P})$, the non-convex Landau-Devonshire anisotropy energy $\psi_a(\mathbb{P})$ that models easy directions of the crystal and the exchange energy $\psi_{ex}(\nabla \mathbb{P})$ that models tendency of neighboring polarizations to align. The vacuum contribution $\psi_{vac}(\mathbb{P}, \mathbb{E})$ captures the electric energy storage in the space occupied by the ferroelectric \mathcal{B} . The modeling of microelectric energy contributions are similar to those presented in ZHANG & BHATTACHARYA [263, 264], MIEHE ET AL.

[176] and ZÄH & MIEHE [258]. These contributions can be explicitly written in the form,

$$\begin{aligned}
\psi_e(\mathbb{P}, \mathbb{E}) &= \frac{\lambda}{2} \operatorname{tr}^2[\boldsymbol{\varepsilon}] + \mu \operatorname{tr}[\boldsymbol{\varepsilon}^2] - \frac{\alpha}{2} \operatorname{tr}[\boldsymbol{\varepsilon}] \operatorname{tr}[\mathbb{P} \otimes \mathbb{P}] - \beta \operatorname{tr}[\boldsymbol{\varepsilon} \cdot (\mathbb{P} \otimes \mathbb{P})], \\
\psi_a(\mathbb{P}) &= \frac{a_1}{2} [\tilde{\mathbb{P}}_1^2 + \tilde{\mathbb{P}}_2^2 + \tilde{\mathbb{P}}_3^2] + \frac{a_2}{4} [\tilde{\mathbb{P}}_1^4 + \tilde{\mathbb{P}}_2^4 + \tilde{\mathbb{P}}_3^4] + \frac{a_3}{2} [\tilde{\mathbb{P}}_1^2 \tilde{\mathbb{P}}_2^2 + \tilde{\mathbb{P}}_2^2 \tilde{\mathbb{P}}_3^2 + \tilde{\mathbb{P}}_1^2 \tilde{\mathbb{P}}_3^2] \\
&\quad + \frac{a_4}{6} [\tilde{\mathbb{P}}_1^6 + \tilde{\mathbb{P}}_2^6 + \tilde{\mathbb{P}}_3^6] + \frac{a_5}{4} [\tilde{\mathbb{P}}_1^4 \tilde{\mathbb{P}}_2^4 + \tilde{\mathbb{P}}_2^4 \tilde{\mathbb{P}}_3^4 + \tilde{\mathbb{P}}_1^4 \tilde{\mathbb{P}}_3^4], \\
\psi_{ex}(\nabla \mathbb{P}) &= \frac{A}{2} \operatorname{tr}[\nabla \mathbb{P} \cdot \nabla^T \mathbb{P}], \\
\psi_{vac}(\mathbb{E}, \mathbb{P}) &= -\frac{\epsilon_0}{2} \mathbb{E} \cdot \mathbb{E} - \mathbb{E} \cdot \mathbb{P}.
\end{aligned} \tag{7.28}$$

Note, that in this formulation the split of electric field into the “self-field” and “applied-field” similar to Section 5.2 is not considered. This is due to the fact that in the boundary value problems considered later, this distinction is not required. This can however be incorporated by considering appropriate electric load potential functionals similar to the representations given in MIEHE ET AL. [176], ZÄH & MIEHE [258]. In the anisotropy energy, $\tilde{\mathbb{P}}_i = \mathbb{A}_i \cdot \mathbb{P}$ are the polarization components along the easy directions of the crystal represented by the structural vectors $\{\mathbb{A}_i\}_{i=d=1,2,3}$. A detailed explanation regarding the energies is given in MIEHE ET AL. [176].

7.3.2. Tension-Compression Split of Energy

Following the arguments presented in Subsection 6.3.2, a tension-compression split of the energy is proposed of the form

$$\boldsymbol{\varepsilon} = \boldsymbol{\varepsilon}^+ + \boldsymbol{\varepsilon}^- \quad \text{with} \quad \boldsymbol{\varepsilon}^\pm := \sum_{a=1}^3 \langle \boldsymbol{\varepsilon} \rangle_\pm \mathbf{n}_a \otimes \mathbf{n}_a, \tag{7.29}$$

with the ramp functions $\langle x \rangle_+ := (x + |x|)/2$ and $\langle x \rangle_- := (x - |x|)/2$ for $x \in \mathcal{R}$. This allows an additive decomposition of the energy as,

$$\Psi(\boldsymbol{\varepsilon}, \mathbb{E}, \mathbb{P}, \nabla \mathbb{P}, \alpha) := (1 - \alpha)^2 [\psi_e^+(\boldsymbol{\varepsilon}^+, \mathbb{P}) + \psi_a(\mathbb{P}) + \psi_{ex}(\nabla \mathbb{P}) + \psi_{vac}(\mathbb{E}, \mathbb{P})] + \psi_e^-(\boldsymbol{\varepsilon}^-, \mathbb{P}) \tag{7.30}$$

into a positive part of the energy ψ^+ due to tension and a negative part ψ^- due to compression, depending on the strain. Note that the degradation function in such a case acts only on the tension part of the stored energy.

7.3.3. Rate of Energy Functional and Crack Driving Force

The time derivative of the functional (7.26) yields the electromechanical rate functional

$$\dot{E}(\mathbf{u}, \phi, \mathbb{P}, \nabla \mathbb{P}, \alpha) = \frac{d}{dt} \int_{\mathcal{B}} \Psi(\boldsymbol{\varepsilon}, \mathbb{E}, \mathbb{P}, \nabla \mathbb{P}, \alpha) dV, \tag{7.31}$$

that depends on the rates $\{\dot{\mathbf{u}}, \dot{\phi}, \dot{\alpha}, \dot{\mathbb{P}}, \nabla \dot{\mathbb{P}}\}$ at a given state $\{\mathbf{u}, \phi, \alpha, \mathbb{P}, \nabla \mathbb{P}\}$. The time rate of the energy functional can be explicitly written as

$$\dot{E}(\dot{\mathbf{u}}, \dot{\phi}, \dot{\mathbb{P}}, \nabla \dot{\mathbb{P}}, \dot{\alpha}) = \int_{\mathcal{B}} [\partial_{\boldsymbol{\varepsilon}} \Psi : \dot{\boldsymbol{\varepsilon}} + \partial_{\mathbb{E}} \Psi \cdot \dot{\mathbb{E}} + \partial_{\alpha} \Psi \dot{\alpha} + \partial_{\mathbb{P}} \Psi \dot{\mathbb{P}} + \partial_{\nabla \mathbb{P}} \Psi \nabla \dot{\mathbb{P}}] dV. \tag{7.32}$$

Table 7.1: Material parameters for barium titanate BaTiO₃ [176].

No.	Parameter	Name	Value	Units
1.	λ	mechanical parameter 1	111×10^9	N/m ²
2.	μ	mechanical parameter 2	37×10^9	N/m ²
3.	α	electrostrictive coefficient 1	-2.7×10^9	Nm ² /C ²
4.	β	electrostrictive coefficient 2	11.93×10^9	Nm ² /C ²
5.	a_1	anisotropy energy coefficient 1	-10.35×10^7	Nm ² /C ²
6.	a_2	anisotropy energy coefficient 2	-19.60×10^8	Nm ⁶ /C ⁴
7.	a_3	anisotropy energy coefficient 3	39.38×10^8	Nm ⁶ /C ⁴
8.	a_4	anisotropy energy coefficient 4	84.48×10^9	Nm ¹⁰ /C ⁶
9.	a_5	anisotropy energy coefficient 5	23.90×10^{13}	Nm ¹⁴ /C ⁸
10.	ϵ_0	vacuum electric permittivity	8.85×10^{-12}	C ² /(Nm ²)
11.	p_s	saturation polarization	0.26	C/m ²
12.	A	electric length-scale parameter	1×10^{-10}	m
13.	η^*	electric viscosity parameter	0.25	Nsm ² /C ²
14.	g_c	critical energy parameter	0.5	N/m
15.	l	damage length-scale parameter	5×10^{-10}	m
16.	β	fracture anisotropy parameter	10	-

Where the mechanical stress, the electric displacement field and the conjugate to polarization and its gradient are identified as

$$\boldsymbol{\sigma} := \partial_{\boldsymbol{\varepsilon}} \Psi, \quad \mathbb{D} := -\partial_{\mathbb{E}} \Psi, \quad G := \partial_{\mathbb{P}} \Psi \quad \text{and} \quad K := \partial_{\nabla \mathbb{P}} \Psi. \quad (7.33)$$

With the total crack driving force of the electromechanical problem that governs the dissipation per unit volume of the model

$$f := -\partial_{\alpha} \Psi(\boldsymbol{\varepsilon}, \mathbb{E}, \mathbb{P}, \nabla \mathbb{P}, \alpha) \quad \text{with} \quad \mathcal{D} := f \dot{\alpha} \geq 0. \quad (7.34)$$

The fracture driving force f , characterizes the ferroelectric fracture model as a generalized standard dissipative material. However crack propagation is assumed to be governed by the release of the *mechanical energy*, similar to the piezoelectric response. In this context the mechanical driving force $f_m := -\partial_{\alpha} \boldsymbol{\sigma} : \boldsymbol{\varepsilon}$ is assumed to solely govern the fracture propagation in ferroelectric ceramics. Note that the other work conjugate variables i.e. the dielectric displacement \mathbb{D} and the polarization contributions $\{G, K\}$ also contribute to the total crack driving force. However, these are not considered in this work. With the above introduced choice of energy, the crack driving state function \mathfrak{H} appears as,

$$\mathfrak{H} := \lambda \operatorname{tr}^2[\boldsymbol{\varepsilon}^+] + 2\mu \operatorname{tr}[\boldsymbol{\varepsilon}^+ \boldsymbol{\varepsilon}^+] - \alpha \operatorname{tr}[\boldsymbol{\varepsilon}^+] \operatorname{tr}[\mathbb{P} \otimes \mathbb{P}] - 2\beta \operatorname{tr}[\boldsymbol{\varepsilon}^+ \cdot (\mathbb{P} \otimes \mathbb{P})]. \quad (7.35)$$

7.4. Numerical examples

This section presents some representative numerical examples that showcase the behavior of the proposed model to predict ferroelectric domain evolution and anisotropic fracture evolution. As for the piezoelectric case isotropic crack propagation is investigated initially under no applied fields and in turn under applied electrical fields. The next examples showcase anisotropic crack propagation in ferroelectric ceramics. The material parameters

of ferroelectric single crystal barium titanate below the Curie-Weiss temperature $\vartheta = 120^\circ \text{C}$ are given in table. 7.1.

7.4.1. Problem 1: Isotropic Crack Propagation in Ferroelectrics

The first example analyses isotropic crack propagation in a single crystal barium titanate. The boundary value problem considered in this example is shown in Figure 7.3. A pre-notched specimen is subjected to varied electrical and mechanical loading. The polarization easy axes $\{A_i\}$ and the boundary conditions are indicated in the Figure 7.3 a). The computations are performed in a monotonic displacement driven scenario in combination with a ramped loading of the electric potential. The dimensions of the sample and the mesh discretization is shown in Figure 7.3 b). The mesh is refined in the areas where crack propagation is expected to occur. Note that for no applied electric fields, the top and bottom surfaces are not clamped for electric potential. The polarization P is initialized to a random distribution and allowed to evolve to an equilibrium configuration. For no electric field loading the electric potential is free on the top and bottom surfaces. For such a scenario the polarization forms Landau-type structure on the top and bottom half of the specimen Figure 7.4 a), b), c), see also MIEHE ET AL. [176]. The domain evolution is different if electric potential is clamped as can be seen in Figure 7.4 d), e), f).

After equilibrium state is reached, a ramped electric potential field loading is applied, along with mechanical displacements. The fracture plots are shown in Figure 7.5. Figure 7.5 a), b), c) shows the fracture propagation for applied electric field of -100 [KV/cm] ,

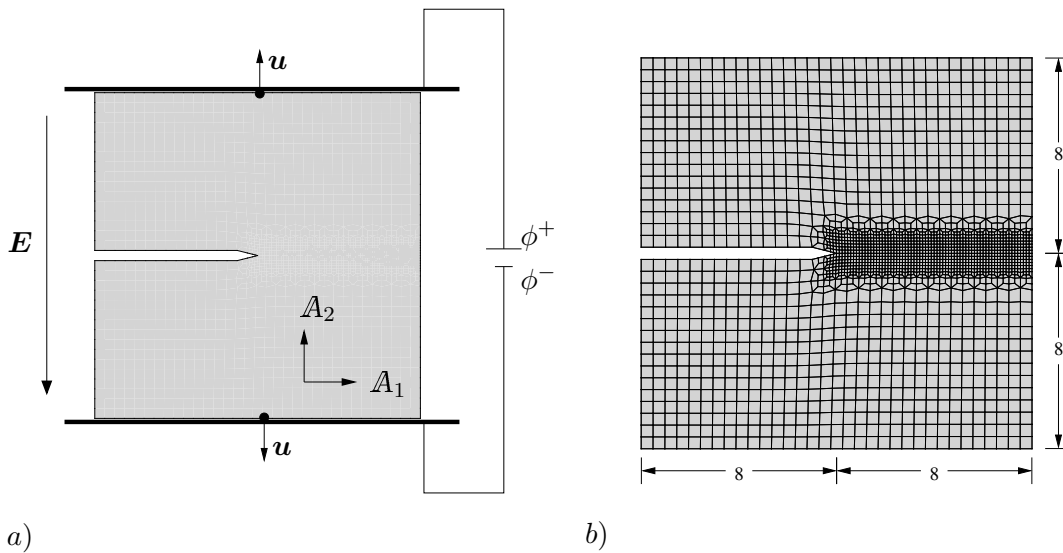


Figure 7.3: Mode-I fracture boundary value problem for ferroelectric specimen under combined electro-mechanical loading. a) A pre-notched specimen is initialized with a random distribution of the polarization order parameter. The top and bottom edges are constrained such that electric potential and displacement loads can be applied. The polarization is allowed to evolve initially, then electric potential and mechanical loads are applied simultaneously. The electric potential is applied until desired electric field is attained while mechanical displacement is applied until fracture. Polarization anisotropy axis $\{A_i\}_{i=1,2}$ are indicated in the figure. b) Dimensions of the specimen in $[nm]$ are shown. Appropriate mesh discretization is employed along the predicted crack path. Note that for anisotropic fracture tests shown later the mesh discretization varies from the one presented here.

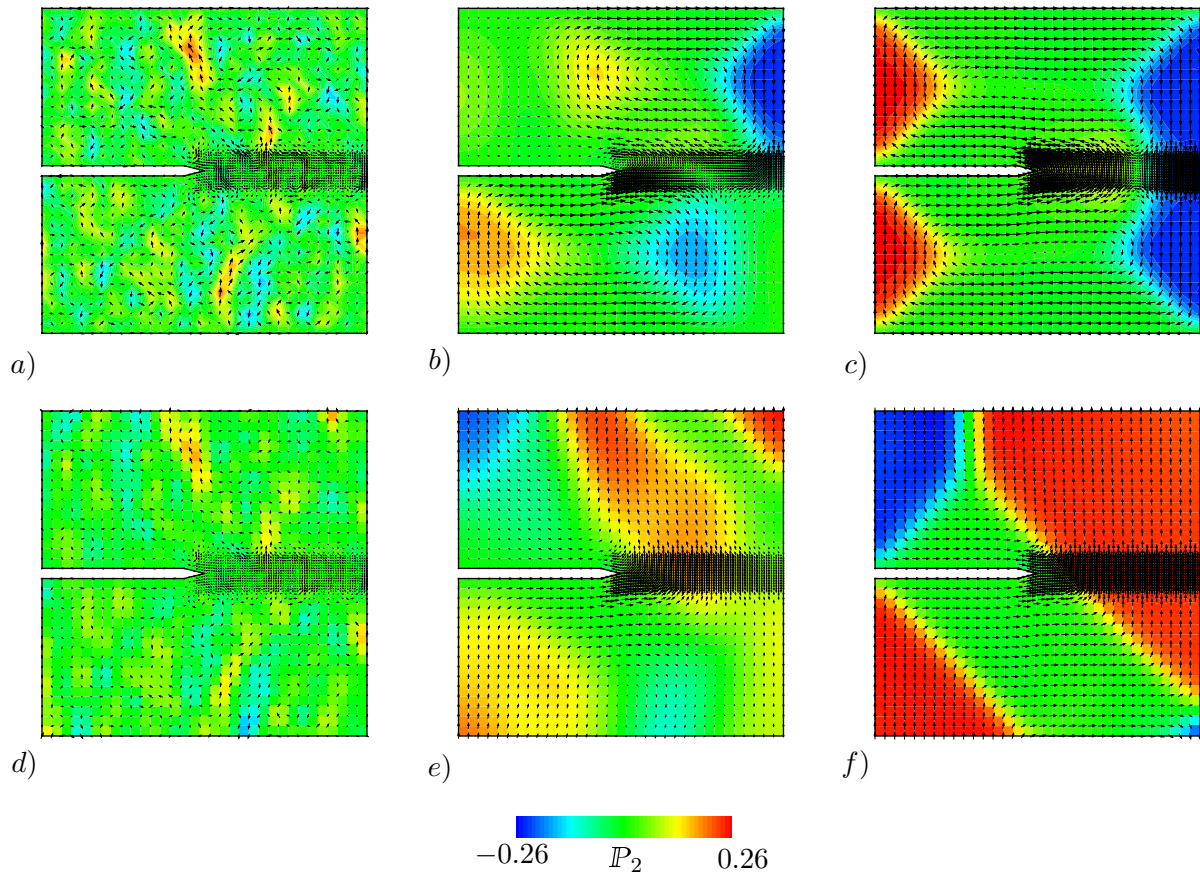


Figure 7.4: Evolution of polarization order parameter starting from random distribution for potential free and clamped surfaces. The polarization order parameter is initialized to a random distribution. Under no applied electric or mechanical loading the polarization evolves to an equilibrium state as shown in a), b), c). Final configuration similar to the Landau distribution seen in ferroelectric materials, in the top and bottom half of the specimen. For electric loading the electric potential on the top and bottom surfaces are clamped. The polarization evolution for such a boundary value problem is shown in d), e), f).

starting from the equilibrium state. The electric potential contour is plotted in each figure. Similarly, Figure 7.5 d), e) shows fracture for no applied field and Figure 7.5 f), g), h) for applied field of 100 [KV/cm]. Polarization reorients in the applied field direction as can be seen from Figure 7.5 b), c). The plot of fracture load for various applied fields is plotted in the center. As it can be seen the model predicts reduction in fracture toughness for applied positive or negative fields. The fracture behavior is almost symmetric for positive and negative fields due to symmetry of the boundary value problem itself. Post fracture the top and bottom half are electrically disconnected due to chosen impermeable electrical crack conditions. For no applied fields clearly the polarization orients in the Landau structure while for applied electric potential equipotential surfaces are created on the top and bottom half.

7.4.2. Problem 2: Anisotropic Crack Propagation in Ferroelectrics

Fracture propagation in ferroelectrics taking into account anisotropy is considered in this example. The boundary value problem is similar to Figure 7.3, however mesh refinement is done in areas where fracture is expected to occur. The simulation results are plotted

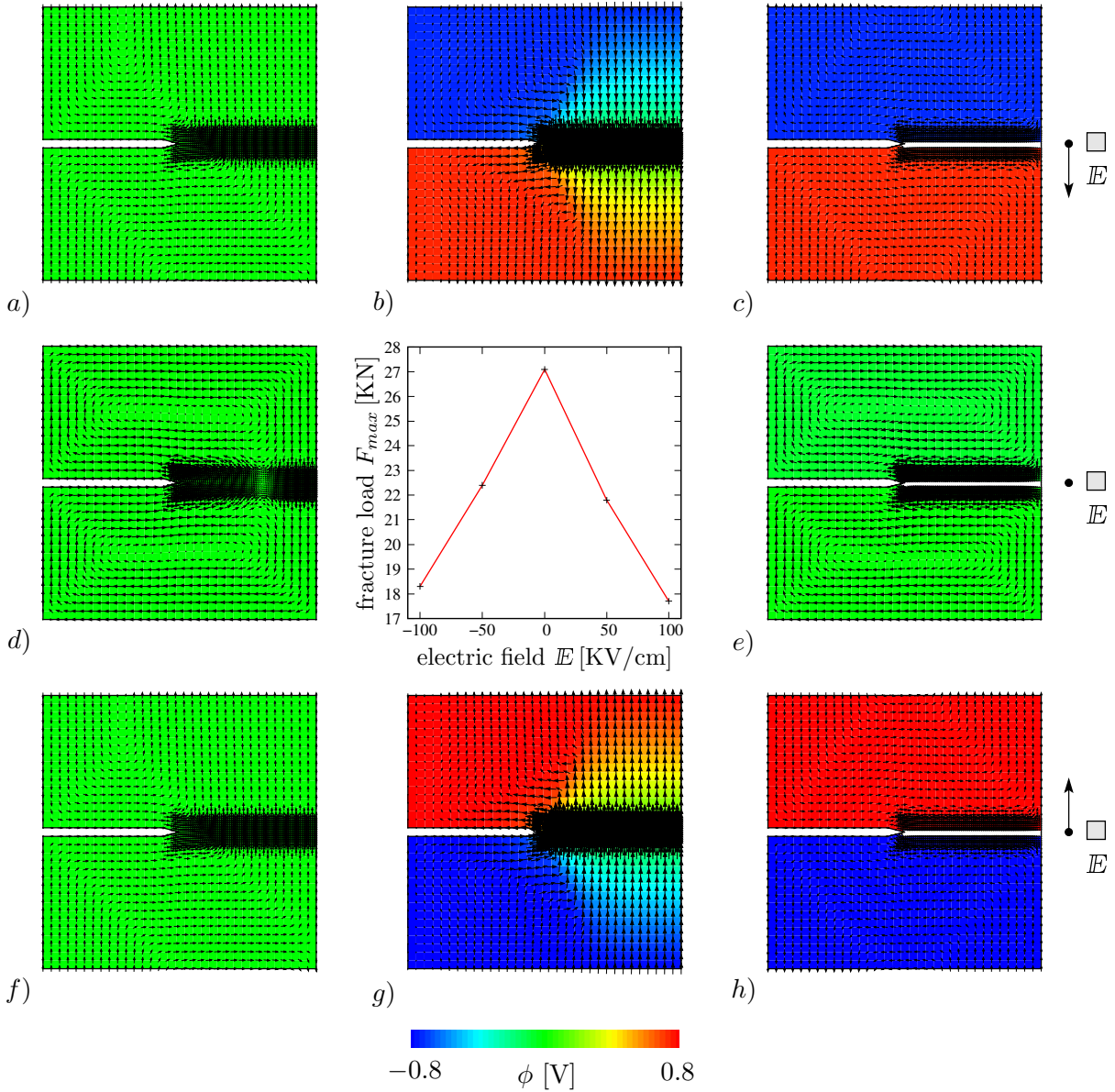


Figure 7.5: *Isotropic fracture propagation for mode-1 compact tension test with a predefined notch for applied electric fields.* Isotropic crack propagation is visualized in a single crystal barium titanate sample with a predefined notch. The polarization vectors are indicated by black arrows and contour of the potential is plotted. *a), b), c)* shows the crack propagation for applied electric field of -100 [KV/cm], *d), e)* for no applied electric field and *f), g), h)* for 100 [KV/cm]. The plot of fracture load f_{max} versus the applied electric field E is plotted in the center. For no applied electric fields the top and bottom surface are potential free, while for applied electric fields the electric potential on these surfaces are fixed. This is evident from the equilibrium plot *a), d)* and *f)*. The fracture load tends to reduce for applied positive or negative fields. The electric potential contour plots resemble those for the piezoelectric case, see [Figure 6.8](#).

in [Figure 7.6](#), with polarization vectors plotted as black arrows and contour of P_2 also shown. Results for various fracture anisotropy angles $\vartheta = 0^\circ, 30^\circ, 45^\circ$ at various simulation times t' are shown for no applied electric fields. The equilibrium state before mechanical loading at $t' = 200$ is plotted for various anisotropy angles. Note that there is a variation in the equilibrium structures due to the different initial distribution of polarizations (due to mesh refinement at expected fracture paths). The polarization state just before fracture $t' = 350$, shows similarities with slight variations due to the influence of crack

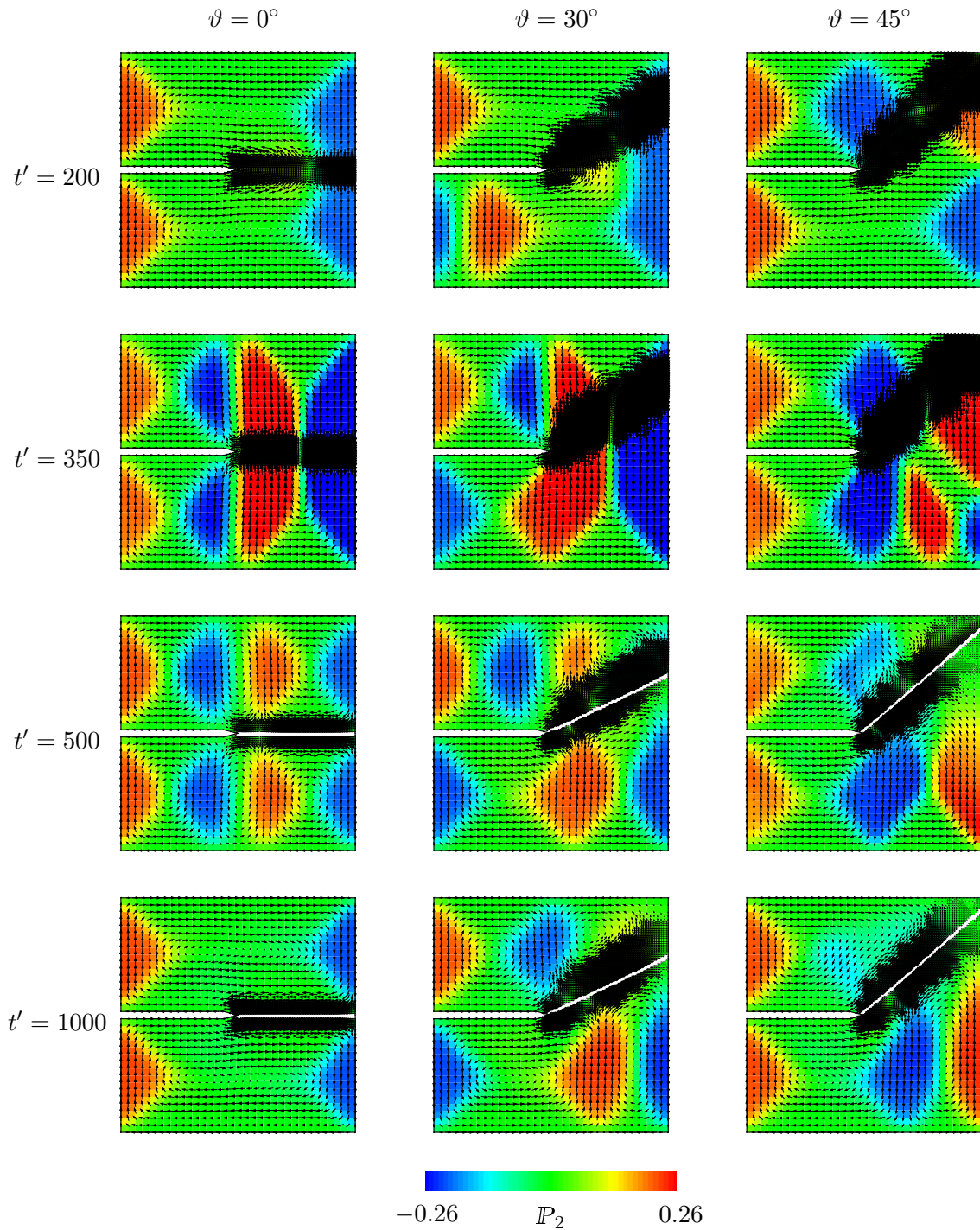


Figure 7.6: Anisotropic fracture propagation for mode-1 compact tension test with a predefined notch in ferroelectric ceramics. Anisotropic crack propagation is visualized in a single crystal barium titanate sample with a predefined notch. The polarization vectors are indicated by black arrows and contour of the polarization in y-direction is plotted at various simulation times t' . Crack propagation is plotted for various fracture anisotropy angle $\vartheta = 0^\circ, 30^\circ, 45^\circ$.

anisotropy. Fracture occurs later with increasing anisotropy angle, that is an increase in fracture load for increasing anisotropy angle is observed as expected. Post fracture, polarization reorients to new crack electrical conditions and forms new equilibrium states. The evolution of polarization post fracture can be seen from plots at time $t' = 500$ to $t' = 1000$.

Conclusion and Outlook

Various implementations of phase-field methods in the context of multi-functional materials have been explored in this work. The key focus is on electro and magnetomechanically coupled material responses. Each formulation is presented from a variational perspective, ensuring consistency and ease of implementation. A brief introduction into magnetomechanical coupling, electromechanical coupling and phase-field methods along with the state of the art is presented in the introduction. The rest of the manuscript is divided into three main parts. **Part I** presents the basics of continuum mechanics along with an introduction to electromagnetism and fracture mechanics. **Part II** focuses on phase-field methods in magnetomechanically coupled materials. This includes a computational homogenization framework to determine the aggregate behavior of ferromagnetic materials and an extension of the micromagnetic framework to large deformations to capture the behavior of magnetorheological elastomers. **Part III** focuses on phase-field methods for fracture propagation in electromechanically coupled materials. Crack propagation for linear piezoelectric is explored first and later an extension to the ferroelectric response is also presented.

Micromagnetics is essentially a *continuum theory of magnetically ordered materials*, which employs the magnetization as an order parameter to describe domain evolution and in turn the non-linear response of ferromagnetic materials. The evolution of magnetization is described by the *Landau-Lifshitz-Gilbert* equation. A unique property of this equation is the unity constraint on the magnetization which has to be satisfied in a time dependent setting. A numerical operator split method is presented which satisfies this constraint. A variational rate-type homogenization method is presented to predict the macroscopic response of soft and hard ferromagnetic materials. Further, extension of the micromagnetic framework to large deformations is proposed that is employed to capture the behavior of magnetorheological elastomers. Since this extension employs a vectorial order parameter, due consideration of objectivity constraints are presented and as a consequence objective Lie-rate is employed for the time evolution. Such a formulation helps predict the nonlinear magnetostrictive response in these composite materials without any prior assumptions. The framework presents unique aspects which could be employed for extension of other phase-field models to large deformations. Scale transition via integration of this framework into a homogenization framework enables a micro-macro transition

as has been done recently by VALLICOTTI ET AL. [242, 243]. The present framework is quite promising as it predicts physically observable phenomenon quite accurately.

Fracture in piezoelectric ceramics is discussed in the context of coupled electromechanical phase-field anisotropic fracture propagation. Extension of traditional fracture mechanics, with the damage variable as the phase-field is presented. A detailed discussion of the local constitutive response considering various electrical crack properties and fracture driving force is presented in a thermodynamic setting. In consideration of experimental results a mechanically driven crack propagation framework is proposed. Benchmark numerical examples for *mode-1* fracture propagation with applied electromechanical loading is presented that analyzes effect of crack anisotropy and crack electrical conditions. The framework can further be extended to include energetically consistent crack conditions. An extension of this framework to ferroelectrics is presented which includes an additional phase-field in terms of the polarization order parameter. In this work only impermeable crack conditions and mechanical crack driving force are considered. Further detailed analysis of polarization, polarization gradient and electric driving forces needs to be considered along with various electrical crack conditions.

Overall, the dissertation presents and explores fundamental theories in phase-field modeling of coupled electro-magneto-mechanical response. The variational approaches presented are robust and predict the material behavior quite accurately. However, the high computational cost and the limitation of phase-field models to small length scales remains a strong deterrent for large scale adoption in the industry. The future for such methods can be envisioned in two broad perspectives. With the rise of new functional and meta materials such methods can be extended to incorporate new physics such as to understand and thereby enhance the microstructure of these new materials. On the other hand, with machine learning, such phase-field methods can be readily employed as data points to feed the predictive models. Phase-field methods in conjunction with advanced machine learning techniques might be the way forward to predict the macroscopic behavior more and more accurately.

Bibliography

- [1] ABBUNDI, R.; CLARK, A. [1977]: *Anomalous thermal expansion and magnetostriction of single crystal $Tb_{27}Dy_{73}Fe_2$* . Magnetics, IEEE Transactions on, 13(5): 1519–1520.
- [2] ABDOLLAHI, A.; ARIAS, I. [2011]: *Phase-field simulation of anisotropic crack propagation in ferroelectric single crystals: effect of microstructure on the fracture process*. Modelling and Simulation in Materials Science and Engineering, 19: 074010.
- [3] ABDOLLAHI, A.; ARIAS, I. [2011]: *Phase-field modeling of the coupled microstructure and fracture evolution in ferroelectric single crystals*. Acta Materialia, 59: 4733–4746.
- [4] ABDOLLAHI, A.; ARIAS, I. [2012]: *Crack initiation patterns at electrode edges in multilayer ferroelectric actuators*. Smart Materials and Structures, 21: 094011.
- [5] ABDOLLAHI, A.; ARIAS, I. [2012]: *Phase-field modeling of crack propagation in piezoelectric and ferroelectric materials with different electromechanical crack conditions*. Journal of the Mechanics and Physics of Solids, 60: 2100–2126.
- [6] ABDOLLAHI, A.; ARIAS, I. [2012]: *Numerical simulation of intergranular and transgranular crack propagation in ferroelectric polycrystals*. International Journal of Fracture, 174: 3–15.
- [7] ALBANESE, A.; CUNEFARE, K. [2007]: *Performance of mre-based vibration absorbers*. Journal of Intelligent Material Systems and Structures, 19: 551–563.
- [8] AMBROSIO, L.; TORTORELLI, V. [1992]: *On the approximation of free discontinuity problems*. Bollettino della Unione Matematica Italiana, B 6: 105–123.
- [9] AMBROSIO, L.; FUSCO, N.; PALLARA, D. [2000]: *Functions of bounded variation and free discontinuity problems*. Clarendon Press, Oxford.
- [10] ARIAS, I.; SEREBRINSKY, S.; ORTIZ, M. [2006]: *A phenomenological cohesive model of ferroelectric fatigue*. Acta Materialia, 54: 975–984.
- [11] ARTEMEV, A.; JIN, Y.; KHACHATURYAN, A. [2001]: *Three-dimensional phase field model of proper martensitic transformation*. Acta materialia, pp. 1165–1177.
- [12] BAŞAR, Y.; WEICHERT, D. [2000]: *Nonlinear Continuum Mechanics of Solids*. Springer.
- [13] BARENBLATT, G. I. [1962]: *The mathematical theory of equilibrium cracks in brittle fracture*. Advances in Applied Mechanics, 7: 55–129.
- [14] BARTEL, T.; KIEFER, B.; BUCKMANN, K.; MENZEL, A. [2014]: *A kinematically-enhanced relaxation scheme for the modeling of displacive phase transformations*. Journal of Intelligent Material Systems and Structures, 26(6): 701–717.
- [15] BASSIOUNY, E.; GHALEB, A.; MAUGIN, G. [1988]: *Thermodynamical formulation for coupled electromechanical hysteresis effects. I. Basic equations*. International

- Journal of Engineering Science, 26(12): 1279–1295.
- [16] BASSIOUNY, E.; GHALEB, A.; MAUGIN, G. [1988]: *Thermodynamical formulation for coupled electromechanical hysteresis effects. II. Poling of ceramics*. International Journal of Engineering Science, 26(12): 1297–1306.
- [17] BEDNAREK, S. [1999]: *The giant magnetostriction in ferromagnetic composites within an elastomer matrix*. Applied Physics A, 68(1): 63–67.
- [18] BERTRAM, H. N. [1994]: *Theory of Magnetic Recording*. Cambridge University Press, Cambridge, UK.
- [19] BHATTACHARYA, K.; RAVICHANDRAN, G. [2003]: *Ferroelectric perovskites for electromechanical actuation*. Acta Materialia, 51: 5941–5960.
- [20] BITTER, F. [1932]: *Experiments on the nature of ferromagnetism*. Physical Review, 41(4): 507–515.
- [21] BLOM, P.; KARI, L. [2008]: *Smart audio frequency energy flow control by magneto-sensitive rubber isolators*. Smart Materials and Structures, 17: 2099–2110.
- [22] BOEHLER, J. P. [1987]: *Applications of Tensor Functions in Solid Mechanics*, Vol. 292 of *CISM Courses and Lectures*. Springer-Verlag, - Edition.
- [23] BONET, J.; WOOD, R. [1997-2008]: *Nonlinear Continuum Mechanics for Finite Element Analysis*. Cambridge University Press.
- [24] BORCEA, L.; BRUNO, O. [2001]: *On the magneto-elastic properties of elastomer-ferromagnet composites*. Journal of the Mechanics and Physics of Solids, 49: 2877–2919.
- [25] BORDEN, M. J.; VERHOESEL, C. V.; SCOTT, M. A.; HUGHES, T. J. R.; LANDIS, C. M. [2012]: *A phase-field description of dynamic brittle fracture*. Computer Methods in Applied Mechanics and Engineering, 217-220: 77–95.
- [26] BÖSE, H.; RABINDRANATH, R.; EHRlich, J. [2012]: *Soft magnetorheological elastomers as new actuators for valves*. Journal of Intelligent Material Systems and Structures, 14: 743–765.
- [27] BOURDIN, B.; FRANCFORT, G. A.; MARIGO, J. J. [2000]: *Numerical experiments in revisited brittle fracture*. Journal of the Mechanics and Physics of Solids, 48: 797–826.
- [28] BOURDIN, B.; FRANCFORT, G.; MARIGO, J.-J. [2000]: *Numerical experiments in revisited brittle fracture*. Journal of the Mechanics and Physics of Solids, 48(4): 797–826.
- [29] BOURDIN, B.; FRANCFORT, G. A.; MARIGO, J.-J. [2008]: *Special invited exposition: The variational approach to fracture*. Journal of Elasticity, 91: 5–148.
- [30] BRASSART, L.; STAINIER, L.; DOGHRI, I.; DELANNAY, L. [2011]: *A variational formulation for the incremental homogenization of elasto-plastic composites*. Journal of the Mechanics and Physics of Solids, 59(12): 2455–2475.
- [31] BRIGADNOV, A.; DORFMANN, A. [2003]: *Mathematical modeling of magneto-sensitive elastomers*. International Journal of Solids and Structures, 40: 4659–4674.
- [32] BROWN, JR., W. F. [1963]: *Micromagnetics*. Interscience Publishers.
- [33] BROWN, JR., W. F. [1966]: *Magnetoelastic Interactions*, Vol. 9 of *Tracts in Natural Philosophy*. Springer-Verlag.
- [34] BRUN, M.; LOPEZ-PAMIES, O.; PONTE CASTAÑEDA, P. [2007]: *Homogenization estimates for fiber-reinforced elastomers with periodic microstructures*. International Journal of Solids and Structures, 44: 5953–5979.
- [35] BUSTAMANTE, R.; DORFMANN, A.; OGDEN, R. W. [2006]: *Universal relations in*

- isotropic nonlinear magnetoelasticity*. Quarterly Journal of Mechanics and Applied Mathematics, 59 (3): 435–450.
- [36] CAHN, J. W.; ALLEN, S. M. [1977]: *A microscopic theory for domain wall motion and its experimental verification in Fe-Al alloy domain growth kinetics*. Le Journal de Physique Colloques, 38(27): 27–51.
- [37] CAHN, J.; HILLIARD, J. [1958]: *Free energy of a nonuniform system. I. Interfacial free energy*. The Journal of Chemical Physics, 28(2): 258–267.
- [38] CAO, W.; CROSS, L. [1991]: *Theory of tetragonal twin structures in ferroelectric perovskites with a first-order phase transition*. Physical Review B, 44(1): 5–12.
- [39] CHEN, L. Q. [2002]: *Phase-field models for microstructure evolution*. Annual review of materials research, 32(1): 113–140.
- [40] CHEN, W.; LYNCH, C. [1998]: *A micro-electro-mechanical model for polarization switching of ferroelectric materials*. Acta Materialia, 46(15): 5303–5311.
- [41] CHOUDHURY, S.; LI, Y.; KRILL III, C.; CHEN, L. [2007]: *Effect of grain orientation and grain size on ferroelectric domain switching and evolution: Phase field simulations*. Acta Materialia, 55: 1415–1426.
- [42] CLAEYSSSEN, F.; LHERMET, N.; LETTY, R. L.; BOUCHILLOUX, P. [1997]: *Actuators, transducers and motors based on giant magnetostrictive materials*. Journal of Alloys and Compounds, 258(1–2): 61–73.
- [43] CLARK, A. E.; RESTORFF, J. B.; WUN-FOGLE, M.; HATHAWAY, K. B.; LOGRASSO, T. A.; HUANG, M.; SUMMERS, E. [2007]: *Magnetostriction of ternary fe-ga-x(x=c,v,cr,mn,co,rh) alloys*. Journal of Applied Physics, 101(9): 09C507.
- [44] CLAYTON, J. D.; KNAP, J. [2015]: *Phase field modeling of directional fracture in anisotropic polycrystals*. Computational Material Science, 98: 158–169.
- [45] CULLITY, B. D. [1972]: *Introduction to Magnetic Materials*. Addison-Wesley, Reading, MA.
- [46] DANAS, K. [2017]: *Effective response of classical, auxetic and chiral magnetoelastic materials by use of a new variational principle*. Journal of the Mechanics and Physics of Solids, 105: 25–53.
- [47] DANAS, K.; KANKANALA, S. V.; TRIANTAFYLIDIS, N. [2012]: *Experiments and modeling of iron-particle-filled magnetorheological elastomers*. Journal of the Mechanics and Physics of Solids, 60: 120–138.
- [48] DANIEL, L.; HUBERT, O.; BILLARDON, R. [2004]: *Homogenisation of magneto-elastic behaviour: from the grain to the macro scale*. Computational & Applied Mathematics, 23: 285–308.
- [49] DANIEL, L.; HUBERT, O.; BUIRON, N.; BILLARDON, R. [2008]: *Reversible magneto-elastic behavior: A multiscale approach*. Journal of the Mechanics and Physics of Solids, 56(3): 1018 – 1042.
- [50] DEBLOIS, R. W.; GRAHAM, C. D. [1958]: *Domain observations on iron whiskers*. Journal of Applied Physics, 29(6): 931–939.
- [51] DEEG, W. [1980]: *The analysis of dislocation, crack, and inclusion problems in piezoelectric solids*. Ph.D. Thesis, Stanford University.
- [52] DEFOUG, S.; KACZMAREK, R.; RAVE, W. [1996]: *Measurements of local magnetization by Kerr effect on Si-Fe nonoriented sheets*. Journal of Applied Physics, 79(8): 6036–6038.
- [53] DESIMONE, A. [1993]: *Energy minimizers for large ferromagnetic bodies*. Archive for Rational Mechanics and Analysis, 125: 99–143.

- [54] DESIMONE, A.; JAMES, R. [2002]: *A constrained theory of magnetoelasticity*. Journal of the Mechanics and Physics of Solids, 50: 283–320.
- [55] DESIMONE, A.; KOHN, R. V.; MÜLLER, S.; OTTO, F. [2004]: *Recent analytical developments in micromagnetics*. Technical report, Max-Planck-Institut für Mathematik in den Naturwissenschaften, Leipzig.
- [56] DONAHUE, M. J.: *μ mag – micromagnetic modeling activity group*.
- [57] DORFMANN, A.; OGDEN, R. W. [2003]: *Magnetoelastic modelling of elastomers*. European Journal of Mechanics A/Solids, 22: 497–507.
- [58] DORNISCH, W.; SCHRADER, D.; XU, B.-X.; KEIP, M.-A.; MÜLLER, R. [2018]: *Coupled phase field simulations of ferroelectric and ferromagnetic layers in multiferroic heterostructures*. Archive of Applied Mechanics. Submitted for publication.
- [59] LUCATO, S. DOS SANTOS E ; BAHR, H.-A.; PHAM, V.-B.; LUPASCU, D.; BALKE, H.; BAHR, U. [2002]: *Electrically driven cracks in piezoelectric ceramics: experiments and fracture mechanics analysis*. Journal of Mechanics and Physics of Solids, 50: 2333–2353.
- [60] DYKE, S. J.; SPENCER JR, B. F.; SAIN, M. K.; CARLSON, J. D. [1996]: *Modeling and control of magnetorheological dampers for seismic response reduction*. Smart Materials and Structures, 5(5): 565.
- [61] EGGLESTON, J. J.; MCFADDEN, G. B.; VOORHEES, P. W. [2001]: *A phase-field model for highly anisotropic interfacial energy*. Physica D, 150: 91–103.
- [62] EINSTEIN, A.; HAAS, W, J. DE [1915]: *Experimental proof of the existence of ampère’s molecular currents*. KNAW, Proceedings, 18: 696–711.
- [63] ENGDahl, G. [2000]: *Handbook of Giant Magnetostrictive Materials*. Academic Press, San Diego.
- [64] ERINGEN, A. [1963]: *On the foundations of electroelastostatics*. International Journal of Engineering Science, 1(1): 127–153.
- [65] ESHELBY, J. D. [1951]: *The force on an elastic singularity*. Philosophical Transactions of the Royal Society London A, 244: 87–112.
- [66] ESHELBY, J. D. [1970]: *Energy relations and the energy-momentum tensor in continuum mechanics*. Inelastic Behavior of Solids, -: 77–115.
- [67] ESHELBY, J. D. [1975]: *The elastic energy-momentum tensor*. Journal of Elasticity, 5: 321–335.
- [68] ETHIRAJ, G.; MIEHE, C. [2016]: *Multiplicative magneto-elasticity of magnetosensitive polymers incorporating micromechanically-based network kernels*. International Journal of Engineering Science, 102: 93–119.
- [69] ETHIRAJ, G.; SRIDHAR, A.; MIEHE, C. [2015]: *Variational modeling and homogenization in dissipative magneto-mechanics*. GAMM-Mitteilungen, 38(1): 75–101.
- [70] FANG, D.; LIU, B.; HWANG, K. [1999]: *Energy analysis on fracture of ferroelectric ceramics*. International journal of fracture, 100: 401–408.
- [71] FEYNMAN, R.; LEIGHTON, R.; SANDS, M. [1963-1965]: *The Feynman Lectures on Physics*. Reading, Mass. : Addison-Wesley Pub. Co.
- [72] FRANÇOIS, A.; PASCAL, J. [2006]: *Convergence of a finite element discretization for the landau-lifshitz equations in micromagnetism*. Mathematical Models and Methods in Applied Sciences, 16(2): 299–316.
- [73] FRANCFORT, G. A.; MARIGO, J. J. [1998]: *Revisiting brittle fracture as an energy minimization problem*. Journal of the Mechanics and Physics of Solids, 46: 1319–1342.

- [74] FU, R.; ZHANG, T. [2000]: *Effects of an electric field on the fracture toughness of poled lead zirconate titanate ceramics*. Journal of the American Ceramic Society, 83(5): 1215–1218.
- [75] GALIPEAU, E.; PONTE CASTAÑEDA, P. [2012]: *The effect of particle shape and distribution on the macroscopic behavior of magnetoelastic composites*. International Journal of Solids and Structures, 49: 1–17.
- [76] GALIPEAU, E.; PONTE CASTAÑEDA, P. [2013]: *Giant field-induced strains in magnetoactive elastomer composites*. Proceedings of the Royal Society of London A, 469.
- [77] GAO, H.; ZHANG, T.; TONG, P. [1997]: *Local and global energy release rates for an electrically yielded crack in a piezoelectric ceramic*. Journal of the Mechanics and Physics of Solids, 45: 491–510.
- [78] GILBERT, T. L. [1956]: *Formulation, foundations, and applications of the phenomenological theory of ferromagnetism*. Ph.D. Thesis, Illinois Institute of Technology.
- [79] GILBERT, T. L. [2004]: *A phenomenological theory of damping in ferromagnetic materials*. IEEE Trans. Magn., 40: 3443–3449.
- [80] GOLL, D.; KRONMÜLLER, H. [2000]: *High-performance permanent magnets*. Naturwissenschaften, 87(10): 423–438.
- [81] GREAVES, S. [2008]: *Micromagnetic simulations of magnetic recording media*. In *High Performance Computing on Vector Systems 2007*. Springer Berlin Heidelberg.
- [82] GRIFFITH, A. A. [1920]: *The phenomena of rupture and flow in solids*. Philosophical Transactions of the Royal Society London A, 221: 163–198.
- [83] GRIFFITH, A. A. [1924]: *The theory of rupture*. In Biezeno, C. B.; Burgers, J. M. (Editors), *Proceedings of the First International Congress for Applied Mechanics, Delft*, pp. 55–63.
- [84] GRIFFITH, A. A. [1921]: *The phenomena of rupture and flow in solids*. Philosophical transactions of the royal society of london. Series A, containing papers of a mathematical or physical character, pp. 163–198.
- [85] GROHS, P.; HARDER, H.; SANDER, O.; SPRECHER, M. [2018]: *Projection-based finite elements for nonlinear function spaces*. arXiv preprint arXiv:1803.06576.
- [86] GÜRSES, E.; MIEHE, C. [2009]: *A computational framework of three-dimensional configurational-force-driven brittle crack propagation*. Computer Methods in Applied Mechanics and Engineering, 198: 1413–1428.
- [87] GURTIN, M. E. [1981]: *An Introduction to Continuum Mechanics*, Vol. 158 of *Mathematics in Science and Engineering*. Academic Press.
- [88] GURTIN, M. E.; FRIED, E.; ANAND, L. [2010]: *The Mechanics and Thermodynamics of Continua*. Cambridge University Press.
- [89] HAKIM, V.; KARMA, A. [2005]: *Crack path prediction in anisotropic brittle materials*. Physical Review Letters, 95: 235501–1–4.
- [90] HAKIM, V.; KARMA, A. [2009]: *Laws of crack motion and phase-field models of fracture*. Journal of the Mechanics and Physics of Solids, 57: 342–368.
- [91] HAUPT, P. [2002]: *Continuum Mechanics and Theory of Materials*. Springer.
- [92] HIRSINGER, L.; BARBIER, G.; GOURDIN, G.; BILLARDON, R. [2000]: *Application of the internal variable formalism to the modelling of magneto-elasticity*. Mechanics of Electromagnetic Materials and Structures, pp. 54–67.
- [93] HOFACKER, M. [2014]: *A Thermodynamically Consistent Phase Field Approach to*

- Fracture*. Ph.D. Thesis.
- [94] HOFACKER, M.; MIEHE, C. [2012]: *A phase field model of dynamic fracture: Robust field updates for the analysis of complex crack patterns*. International Journal for Numerical Methods in Engineering.
- [95] HOFACKER, M.; MIEHE, C. [2012]: *Continuum phase field modeling of dynamic fracture: Variational principles and staggered fe implementation*. International Journal of Fracture, pp. 1–17.
- [96] HOLZAPFEL, G. A. [2000]: *Nonlinear solid mechanics*. John Wiley & Sons.
- [97] HORI, M.; NEMAT-NASSER, S. [1998]: *Universal bounds for effective piezoelectric moduli*. Mechanics of Materials, 30: 1–19.
- [98] HU, H.-L.; CHEN, L.-Q. [1998]: *Three-dimensional computer simulation of ferroelectric domain formation*. Journal of the American Ceramic Society, 81(3): 492–500.
- [99] HU, R.; SOH, A.-K.; ZHENG, G.-P.; NI, Y. [2006]: *Micromagnetic modeling studies on the effects of stress on magnetization reversal and dynamic hysteresis*. J. Magn. Magn. Mater., 301(2): 458 – 468.
- [100] HUBER, J. [2005]: *Micromechanical modeling of ferroelectrics*. Current opinion in Solid State and Materials Science, 9: 100–106.
- [101] HUBER, J.; FLECK, N. [2001]: *Multi-axial electrical switching of a ferroelectric: theory versus experiment*. Journal of Mechanics and Physics of Solids, 49: 785–811.
- [102] HUBER, J.; FLECK, N.; LANDIS, C.; MCMEECKING, R. [1999]: *A constitutive model for ferroelectric polycrystals*. Journal of the Mechanics and Physics of Solids, 47: 1663–1697.
- [103] HUBERT, A.; SCHÄFER, R. [2001]: *Magnetic Domains*. Springer-Verlag, New York.
- [104] IRWIN, G. R. [1957]: *Analysis of stresses and strains near the end of a crack traversing a plate*. Journal of Applied Mechanics, 24: 361–364.
- [105] IRWIN, G. R. [1958]: *Fracture*. In Flü $\frac{1}{2}$ gge, S. (Editor), *Encyclopedia of Physics*, Vol. 6, Elasticity and Plasticity, pp. 551–590. Springer.
- [106] IRWIN, G. R. [1962]: *Crack-extension force for a part-through crack in a plate*. Journal of Applied Mechanics, 29: 651–654.
- [107] JAFFE, B.; COOK, W.; JAFFE, H. [1971]: *Piezoelectric Ceramics*. Academic Press, London, New York.
- [108] JAMES, R.; KINDERLEHRER, D. [1990]: *Frustration in ferromagnetic materials*. Continuum Mechanics and Thermodynamics, 2: 215–239.
- [109] JAVILI, A.; CHATZIGEORGIOU, G.; STEINMANN, P. [2013]: *Computational homogenization in magneto-mechanics*. Int. J. Solids. Struct., 50(25–26): 4197–4216.
- [110] JOLLY, M.; CARLSON, J.; MUNOZ, B. [1996]: *A model of the behaviour of magnetorheological materials*. Smart Materials Structures, 5: 607–614.
- [111] KALINA, K. A.; METSCH, P.; KÄSTNER, M. [2016]: *Microscale modeling and simulation of magnetorheological elastomers at finite strains: A study on the influence of mechanical preloads*. International Journal of Solids and Structures, 102: 286–296.
- [112] KALLIO, M. [2005]: *The Elastic and Damping Properties of Magnetorheological Elastomers*. Ph.D. Thesis, Tampere University of Technology.
- [113] KALTHOFF, J. [2000]: *Modes of dynamic shear failure in solids*. International Journal of Fracture, 101: 1–31.
- [114] KALTHOFF, J.; WINKLER, S. [1987]: *Impact Loading and Dynamic Behavior of*

- Materials*, chapter Failure mode transition at high rates of shear loading, pp. 185–195. DGM Informationsgesellschaft.
- [115] KAMLAH, M. [2001]: *Ferroelectric and ferroelastic piezoceramics – modelling of electromechanical hysteresis phenomena*. *Continuum Mechanics and Thermodynamics*, 13: 219–268.
- [116] KAMLAH, M.; BÖHLE, U. [2001]: *Finite element analysis of piezoceramic components taking into account ferroelectric hysteresis behavior*. *International Journal of Solids and Structures*, 38: 605–633.
- [117] KAMLAH, M.; TSAKMAKIS, C. [1999]: *Phenomenological modeling of the non-linear electro-mechanical coupling in ferroelectrics*. *International Journal of Solids and Structures*, 36: 669–695.
- [118] KANKANALA, S.; TRIANTAFYLIDIS, N. [2004]: *On finitely strained magnetorheological elastomers*. *Journal of the Mechanics and Physics of Solids*, 52: 2869–2908.
- [119] KARMA, A.; KESSLER, D.; LEVINE, H. [2001]: *Phase-field model of mode iii dynamic fracture*. *Physical Review Letters*, 87(4): 1–4.
- [120] KAZARYAN, A.; WANG, Y.; DREGIA, S.; PATTON, B. [2001]: *Grain growth in systems with anisotropic boundary mobility: Analytical model and computer simulation*. *Physical review B*, 63: 184102.
- [121] KEIP, M, A.; STEINMANN, P.; SCHRÖDER, J. [2014]: *Two-scale computational homogenization of electro-elasticity at finite strains*. *Computer Methods in Applied Mechanics and Engineering*, 278: 62–79.
- [122] KEIP, M.-A.; RAMBAUSEK, M. [2016]: *A multiscale approach to the computational characterization of magnetorheological elastomers*. *International Journal for Numerical Methods in Engineering*, 107(4): 338–360.
- [123] KEIP, M.-A.; RAMBAUSEK, M. [2017]: *Computational and analytical investigations of shape effects in the experimental characterization of magnetorheological elastomers*. *International Journal of Solids and Structures*, 121: 1–20.
- [124] KEIP, M.-A.; SRIDHAR, A. [2019]: *A variationally consistent phase-field approach for micro-magnetic domain evolution at finite deformations*. *Journal of the Mechanics and Physics of Solids*, 125: 805–824.
- [125] KEIP, M.-A.; SCHRADER, D.; THAI, H.; SCHRÖDER, J.; SVENDSEN, B.; MÜLLER, R.; GROSS, D. [2015]: *Coordinate-invariant phase field modeling of ferroelectrics, part II: Application to composites and polycrystals*. *GAMM-Mitteilungen*, 38(1): 115–131.
- [126] KHAIYER, I.; O'DELL, T. [1976]: *Domain wall observation of permalloy overlay bars by interference contrast technique*. *AIP Conference Proceedings*, 29(1): 37–38.
- [127] KHALAQUZZAMAN, M.; XU, B.-X.; RICKER, S.; MÜLLER, R. [2012]: *Computational homogenization of piezoelectric materials using fe^2 to determine configurational forces*. *Technische Mechanik*, 32(1): 21–37.
- [128] KIEFER, B.; LAGOUDAS, D. C. [2005]: *Magnetic field-induced martensitic variant reorientation in magnetic shape memory alloys*. *Philosophical Magazine, Special Issue: Recent Advances in Theoretical Mechanics*, 85(33–35): 4289–4329.
- [129] KIEFER, B.; LAGOUDAS, D. C. [2009]: *Modeling the coupled strain and magnetization response of magnetic shape memory alloys under magnetomechanical loading*. *Journal of Intelligent Material Systems and Structures*, 20(2): 143–170.
- [130] KIEFER, B.; KARACA, H. E.; LAGOUDAS, D. C.; KARAMAN, I. [2007]: *Characterization and modeling of the magnetic field-induced strain and work output in*

- Ni₂MnGa *shape memory alloys*. *Journal of Magnetism and Magnetic Materials*, 312(1): 164–175.
- [131] KITTEL, C. [1949]: *Physical theory of ferromagnetic domains*. *Reviews of Modern Physics*, 21(4): 541–583.
- [132] KITTEL, C. [1956]: *Introduction to Solid State Physics*. John Wiley & Sons, New York, 2nd Edition.
- [133] KLINKEL, S. [2006]: *A phenomenological constitutive model for ferroelastic and ferroelectric hysteresis effects in ferroelectric ceramics*. *International Journal of Solids and Structures*, 43: 7197–7222.
- [134] KOVETZ, A. [2000]: *Electromagnetic Theory*. Oxford University Press.
- [135] KRISHNAPRASAD, P. S.; TAN, X. [2001]: *Cayley transforms in micromagnetics*. *Physica B: Condensed Matter*, 306(1-4): 195–99.
- [136] KRUŽÍK, M.; PROHL, A. [2006]: *Recent developments in the modeling, analysis, and numerics of ferromagnetism*. *SIAM Review*, 48: 439–483.
- [137] KUHN, C.; SCHLÜTER, A.; MÜLLER, R. [2015]: *On degradation functions in phase field fracture models*. *Computational Materials Science*, 108: 374–384.
- [138] KUHN, C.; MÜLLER, R. [2011]: *A new finite element technique for a phase field model of brittle fracture*. *Journal of Theoretical and Applied Mechanics*, 49(4): 1115–1133.
- [139] KUNA, M. [2010]: *Fracture mechanics of piezoelectric materials - where are we right now?* *Engineering fracture mechanics*, 77: 309–326.
- [140] KUZNETSOV, S.; FISH, J. [2012]: *Mathematical homogenization theory for electroactive continuum*. *International Journal for Numerical Methods in Engineering*, 91(11): 1199–1226.
- [141] LAHELLEC, N.; SUQUET, P. [2007]: *On the effective behavior of nonlinear inelastic composites: I. Incremental variational principles*. *Journal of the Mechanics and Physics of Solids*, 55(9): 1932–1963.
- [142] LANDAU, L. D.; LIFSHITZ, E. M. [1935]: *On the theory of the dispersion of magnetic permeability in ferromagnetic bodies*. *Physikalische Zeitschrift der Sowjetunion*, 8: 153–169.
- [143] LANDIS, C. M. [2008]: *A continuum thermodynamics formulation for micro-magneto-mechanics with applications to ferromagnetic shape memory alloys*. *Journal of the Mechanics and Physics of Solids*, 56(10): 3059–3076.
- [144] LANDIS, C. [2004]: *Energetically consistent boundary conditions for electromechanical fracture*. *International Journal of Solids and Structures*, 4: 6291–6315.
- [145] LANDIS, M. [2002]: *Fully coupled, multi-axial, symmetric constitutive laws for polycrystalline ferroelectric ceramics*. *Journal of Mechanics and Physics of Solids*, 50: 127–152.
- [146] LANDIS, M. [2002]: *A new finite-element formulation for electromechanical boundary value problems*. *International Journal for Numerical Methods in Engineering*, 55: 613–628.
- [147] LANGER, J. S. [1983]: *MODELS OF PATTERN FORMATION IN FIRST-ORDER PHASE TRANSITIONS*, pp. 165–186.
- [148] LEFÈVRE, V.; DANAS, K.; LOPEZ-PAMIES, O. [2017]: *A general result for the magnetoelastic response of isotropic suspensions of iron and ferrofluid particles in rubber, with applications to spherical and cylindrical specimens*. *Journal of the Mechanics and Physics of Solids*, 107: 343–364.

- [149] LI, W.; McMEEKING, R.; LANDIS, C. [2008]: *On the crack face boundary conditions in electromechanical fracture and an experimental protocol for determining energy release rates*. European Journal of Mechanics A/Solids, 27: 285–301.
- [150] LIANG, C.-Y.; KELLER, S. M.; SEPULVEDA, A. E.; BUR, A.; SUN, W.-Y.; WETZLAR, K.; CARMAN, G. P. [2014]: *Modeling of magnetoelastic nanostructures with a fully coupled mechanical-micromagnetic model*. Nanotechnology, 25(43): 435701.
- [151] LINES, M.; GLASS, A. [1977]: *Principles and Applications of Ferroelectrics and Related Materials*. Clarendon Press, London.
- [152] LINNEMANN, K.; KLINKEL, S.; WAGNER, W. [2009]: *A constitutive model for magnetostrictive and piezoelectric materials*. International Journal of Solids and Structures, 46: 1149–1166.
- [153] MARSDEN, J.; HUGHES, T. [1983]: *Mathematical foundations of elasticity*. Prentice-Hall, Englewood Cliffs, New Jersey.
- [154] MAUGIN, G. A.; TRIMARCO, C. [1992]: *Pseudomomentum and material forces in nonlinear elasticity: Variational formulations and application to brittle fracture*. Acta Mechanica, 94: 1–28.
- [155] MAUGIN, G. [1988]: *Continuum Mechanics of Electromagnetic Solids*. Elsevier.
- [156] MAXWELL, J. C. [1873]: *A Treatise on Electricity and Magnetism*, Vol. 537:538. Oxford : Clarendon Press.
- [157] MCKEEHAN, L. [1926]: *Magnetostriction*. Journal of the Franklin Institute, 202(6): 737 – 773.
- [158] McMEEKING, M.; LANDIS, M. [2002]: *A phenomenological multi-axial constitutive law for switching in polycrystalline ferroelectric ceramics*. International Journal of Engineering Science, 40: 1553–1577.
- [159] McMEEKING, R. [1999]: *Crack tip energy release rate for a piezoelectric compact tension specimen*. Engineering Fracture Mechanics, 64: 217–244.
- [160] McMEEKING, R. [2003]: *The energy release rate for a griffith crack in a piezoelectric material*. Engineering Fracture Mechanics, 71: 1149–1163.
- [161] McMEEKING, R. [2004]: *The energy release rate for a griffith crack in a piezoelectric material*. Engineering Fracture Mechanics, 71: 1149–1163.
- [162] McMEEKING, R.; LANDIS, C.; JIMENEZ, S. [2007]: *A principle of virtualwork for combined electrostatic and mechanical loading of materials*. International Journal of Non-Linear Mechanics, 42: 831–838.
- [163] METSCH, P.; KALINA, K. A.; SPIELER, C.; KÄSTNER, M. [2016]: *A numerical study on magnetostrictive phenomena in magnetorheological elastomers*. Computational Materials Science, 124: 364–374.
- [164] MIEHE, C. [2002]: *Strain-driven homogenization of inelastic microstructures and composites based on an incremental variational formulation*. International Journal for numerical methods in engineering, 55: 1285–1322.
- [165] MIEHE, C. [2003]: *Computational micro-to-macro transitions of discretized microstructures of heterogeneous materials at finite strains based on the minimization of averaged incremental energy*. Computer Methods in Applied Mechanics and Engineering, 192: 559–591.
- [166] MIEHE, C. [2013]: *Geometrical methods of nonlinear continuum mechanics and continuum thermodynamics*. Lecture Notes.
- [167] MIEHE, C. [2014]: *Theoretical and computer-oriented material theory*. Lecture

Notes.

- [168] MIEHE, C.; ETHIRAJ, G. [2012]: *A geometrically consistent incremental variational formulation for phase field models in micromagnetics*. Computer Methods in Applied Mechanics and Engineering, 245–246: 331–347.
- [169] MIEHE, C.; GÜRSES, E. [2007]: *A robust algorithm for configurational-force-driven brittle crack propagation with r-adaptive mesh alignment*. International Journal for Numerical Methods in Engineering, 72: 127–155.
- [170] MIEHE, C.; ROSATO, D. [2011]: *A rate-dependent incremental variational formulation of ferroelectricity*. International Journal of Engineering Science, 49: 466–496.
- [171] MIEHE, C.; GÜRSES, E.; BIRKLE, M. [2007]: *A computational framework of configurational-force-driven brittle fracture based on incremental energy minimization*. International Journal of Fracture, 145: 245–259.
- [172] MIEHE, C.; WELSCHINGER, F.; HOFACKER, M. [2010]: *A phase field model of electromechanical fracture*. Journal of the Mechanics and Physics of Solids, 58(10): 1716–1740.
- [173] MIEHE, C.; WELSCHINGER, F.; HOFACKER, M. [2010]: *Thermodynamically consistent phase-field models of fracture*. International Journal for Numerical Methods in Engineering, 83(10): 1273–1311.
- [174] MIEHE, C.; KIEFER, B.; ROSATO, D. [2011]: *An incremental variational formulation of dissipative magnetostriction at the macroscopic continuum level*. International Journal of Solids and Structures, 48: 1846–1866.
- [175] MIEHE, C.; ROSATO, D.; KIEFER, B. [2011]: *Variational principles in dissipative electro-magneto-mechanics: A framework for the macro-modeling of functional materials*. International Journal for Numerical Methods in Engineering, 86: 1225–1276.
- [176] MIEHE, C.; ZÄH, D.; ROSATO, D. [2012]: *Variational-based modeling of micro-electro-elasticity with electric field- and stress-driven domain evolution*. International Journal for Numerical Methods in Engineering, 91(2): 115–141.
- [177] MIEHE, C.; VALLICOTTI, D.; TEICHTMEISTER, S. [2016]: *Homogenization and multiscale stability analysis in finite magneto-electro-elasticity. application to soft matter EE, ME and MEE composites*. Computer Methods in Applied Mechanics and Engineering, 300: 294 – 346.
- [178] MOULSON, A.; HERBERT, J. [2003]: *Electroceramics: Materilas, Properties, Applications*. John Wiley & Sons, Ltd., 2nd Edition.
- [179] MÜLLER, R.; GROSS, D.; SCHRADER, D.; XU, B. [2007]: *Phase field simulation of domain structures in ferroelectric materials within the context of inhomogeneity evolution*. International Journal of Fracture, 147: 173–180.
- [180] MÜLLER, R.; XU, B. X.; GROSS, D.; LYSCHIK, M.; SCHRADER, D.; KLINKEL, S. [2010]: *Deformable dielectrics – optimization of heterogeneities*. International Journal of Engineering Science, 48: 647–657.
- [181] MUMFORD, D.; SHAH, J. [1989]: *Optimal approximations by piecewise smooth functions and associated variational problems*. Communications on Pure and Applied Mathematics, 42: 577–685.
- [182] NASSERI, M. H. B.; MOHANTY, B. [2008]: *Fracture toughness anisotropy in granitic rocks*. International Journal of Rock Mechanics and Mining Sciences, 45: 167–193.
- [183] NEMAT-NASSER, S.; HORI, M. [1999]: *Micromechanics: overall properties of heterogeneous materials*. North-Holland series in applied mathematics and mechanics,

- Vol. 36. Elsevier Science Publisher B.V., 2. Edition.
- [184] NGUYEN, T.-T.; RÉTHORÉ, J.; YVONNET, J.; BAIETTO, M.-C. [2017]: *Multi-phase-field modeling of anisotropic crack propagation for polycrystalline materials*. Computational Mechanics, in press.
- [185] NIANDOU, H.; SHAO, J. F.; HENRY, J. P. [1997]: *Laboratory investigation of the mechanical behaviour of tournemire shale*. International Journal of Rock Mechanics and Mining Sciences, 34: 3–16.
- [186] OGDEN, R. [1984]: *Nonlinear Elastic Deformations*. John Wiley & Sons, LTD, Chichester.
- [187] OLABI, A.; GRUNWALD, A. [2008]: *Design and application of magnetostrictive materials*. Materials & Design, 29(2): 469–483.
- [188] PAK, Y. [1990]: *Crack extension force in a piezoelectric material*. Journal of Applied Mechanics, 57: 647–653.
- [189] PAK, Y.; TOBIN, A. [1993]: *On the electric field effects in fracture of piezoelectric materials*. Mechanics of electromagnetic materials and structures, 78.
- [190] PAO, Y.-H. [1978]: *Electromagnetic forces in deformable continua*. In Nemat-Nasser, S. (Editor), *Mechanics today*, Vol. 4, chapter 4, pp. 209–305. Pergamon Press, New York.
- [191] PARK, S.; SUN, C.-T. [1995]: *Fracture criteria for piezoelectric ceramics*. Journal of the American Ceramic Society, 78: 1475–1480.
- [192] PARTON, V. [1976]: *Fracture mechanics of piezoelectric materials*. Acta Astronautica, 3(9): 671–683.
- [193] PISANTE, G. [2004]: *Homogenization of micromagnetics large bodies*. ESAIM: Control, Optimisation and Calculus of Variations.
- [194] PONTE CASTAÑEDA, P.; GALIPEAU, E. [2011]: *Homogenization-based constitutive models for magnetorheological elastomers at finite strain*. Journal of the Mechanics and Physics of Solids, 59: 194–215.
- [195] PONTE CASTAÑEDA, P.; SIBONI, M. [2012]: *A finite-strain constitutive theory for electro-active polymer composites via homogenization*. International Journal of Non-Linear Mechanics, 47(2): 293–306. Nonlinear Continuum Theories.
- [196] PONTE CASTAÑEDA, P.; SUQUET, P. [1997]: *Nonlinear composites*. Vol. 34 of *Advances in Applied Mechanics*, pp. 171–302. Elsevier.
- [197] QIAO, Y.; ARGON, A. S. [2003]: *Cleavage crack-growth-resistance of grain boundaries in polycrystalline Fe-2%Si alloy: experiments and modeling*. Mechanics of Materials, 35: 129–154.
- [198] RAMULU, M.; KOBAYASHI, A. [1985]: *Mechanic of crack curving and branching - a dynamic fracture analysis*. International Journal of Fracture Mechanics, 27: 187–201.
- [199] RAVE, W.; HUBERT, A. [2000]: *Magnetic ground state of a thin-film element*. IEEE Transactions on Magnetics, 36: 3886–3899.
- [200] RAVI-CHANDAR, K.; KNAUSS, W. [1984]: *An experimental investigation into dynamic fracture: I. crack initiation and arrest*. International Journal of Fracture, 25: 247–262.
- [201] RAVI-CHANDAR, K.; KNAUSS, W. [1984]: *An experimental investigation into dynamic fracture: Ii. microstructural aspects*. International Journal of Fracture, 26: 65–80.
- [202] RAVI-CHANDAR, K.; KNAUSS, W. [1984]: *An experimental investigation into dy-*

- namic fracture: Iii. on steady-state crack propagation and crack branching.* International Journal of Fracture, 26: 141–154.
- [203] RAVI-CHANDAR, K.; KNAUSS, W. [1984]: *An experimental investigation into dynamic fracture: Iv. on the interaction of stress waves with propagation cracks.* International Journal of Fracture, 26: 189–200.
- [204] RICE, J. R. [1968]: *A path independent integral and the approximate analysis of strain concentration by notches and cracks.* Journal of Applied Mechanics, 35: 379–386.
- [205] RIEDLE, J.; GUMBSCH, P. [1996]: *Cleavage anisotropy in tungsten single crystals.* Physical Review Letters, 76: 3594–3597.
- [206] SABLİK, M. J.; JILES, D. C. [1993]: *Coupled magnetoelastic theory of magnetic and magnetostrictive hysteresis.* IEEE Transactions on Magnetics, 29(3): 2113–2123.
- [207] SANDLUND, L.; FAHLANDER, M.; CEDELL, T.; CLARK, A. E.; RESTORFF, J. B.; WUN-FOGLE, M. [1994]: *Magnetostriction, elastic moduli, and coupling factors of composite terfenol-d.* Journal of Applied Physics, 75(10): 5656–5658.
- [208] SCHÄNZEL, L. [2014]: *Phase Field Modeling of Fracture in Rubbery and Glassy Polymers at Finite Thermo-Viscoelastic Deformations.* Ph.D. Thesis.
- [209] SCHNEIDER, G. [2007]: *Influence of electric field and mechanical stresses on the fracture of ferroelectrics.* Annual Review of Materials Research, 37: 491–538.
- [210] SCHNEIDER, M.; HOFFMANN, H.; ZEWCK, J. [2001]: *Magnetic switching of single vortex permalloy elements.* Applied Physics Letters, 79: 3113–3115.
- [211] SCHRADER, D.; MÜLLER, R.; GROSS, D.; UTSCHIG, T.; SHUR, V.; LUPASCU, D. [2007]: *Interaction of domain walls with defects in ferroelectric materials.* Mechanics of Materials, 39: 161–174.
- [212] SCHRADER, D.; MÜLLER, R.; XU, B. X.; GROSS, D. [2007]: *Domain evolution in ferroelectric materials: A continuum phase field model and finite element implementation.* Computer Methods in Applied Mechanics and Engineering, 196: 4365–4374.
- [213] SCHRADER, D.; MÜLLER, R.; XU, B.; GROSS, D. [2007]: *Domain evolution in ferroelectric materials: A continuum phase field model and finite element implementation.* Computer Methods in Applied Mechanics and Engineering, 196: 4365–4374.
- [214] SCHREFL, T.; FIDLER, J.; KRONMÜLLER, H. [1994]: *Remanence and coercivity in isotropic nanocrystalline permanent magnets.* Phys. Rev. B, 49(9): 6100–6110.
- [215] SCHRÖDER, J. [2009]: *Derivation of the localization and homogenization conditions for electro-mechanically coupled problems.* Computational Materials Science, 46: 595–599.
- [216] SCHRÖDER, J.; KEIP, M.-A. [2012]: *Two-scale homogenization of electromechanically coupled boundary value problems.* Computational Mechanics, 50(2): 229–244.
- [217] SCHRÖDER, J.; NEFF, P. [2003]: *Invariant formulation of hyperelastic transverse isotropy based on polyconvex free energy functions.* International Journal of Solids and Structures, 40(2): 401–445.
- [218] SCHRÖDER, J.; ROMANOWSKI, H. [2005]: *A thermodynamically consistent mesoscopic model for transversely isotropic ferroelectric ceramics in a coordinate-invariant setting.* Archive of Applied Mechanics, 74: 863–877.
- [219] SEKERKA, R. F. [2005]: *Analytical criteria for missing orientations on three-dimensional equilibrium shapes.* Journal of Crystal Growth, 275: 77–82.

- [220] SHANTHRAJ, P.; SVENDSEN, B.; SHARMA, L.; ROTERS, F.; RAABE, D. [2017]: *Elasto-viscoplastic phase field modelling of anisotropic cleavage fracture*. Journal of the Mechanics and Physics of Solids, 99: 19–34.
- [221] SHU, Y. C.; LIN, M. P.; C., W. K. [2004]: *Micromagnetic modeling of magnetostrictive materials under intrinsic stress*. Mechanics of Materials, 36(10): 975–997. Active Materials.
- [222] SHU, Y.; BHATTACHARYA, K. [2001]: *Domain patterns and macroscopic behaviour of ferroelectric materials*. Philosophical Magazine B, 81(12): 2021–2054.
- [223] SMITH, R. C.; DAPINO, M. J.; SEELECKE, S. [2003]: *Free energy model for hysteresis in magnetostrictive transducers*. Journal of Applied Physics, 93(1): 458–466.
- [224] SPALDIN, N. A. [2003]: *Magnetic Materials: Fundamentals and Device Applications*. Cambridge University Press, Cambridge.
- [225] SPENCER, A. J. M. [1971]: *Theory of invariants*. In Eringen, A. C. (Editor), *Continuum Physics*, Vol. 1, pp. 239–353. Academic Press, New York.
- [226] SRIDHAR, A.; KEIP, M.-A. [2019]: *A phase-field model for anisotropic brittle fracturing of piezoelectric ceramics*. International Journal of Fracture, 220: 221–242.
- [227] SRIDHAR, A.; KEIP, M.-A.; MIEHE, C. [2016]: *Homogenization in micro-magneto-mechanics*. Computational Mechanics, 58(1): 151–169.
- [228] STEIGMANN, D. [2004]: *Equilibrium theory for magnetic elastomers and magnetoelectric membranes*. International Journal of Non-Linear Mechanics, 39: 1193–1216.
- [229] SU, Y.; LANDIS, C. [2007]: *Continuum thermodynamics of ferroelectric domain evolution: Theory, finite element implementation, and application to domain wall pinning*. Journal of the Mechanics and Physics of Solids, 55: 280–305.
- [230] SUO, Z.; KUO, C.; BARNETT, D.; WILLIS, J. [1992]: *Fracture mechanics for piezoelectric ceramics*. Journal of the Mechanics and Physics of Solids, 40(4): 739–765.
- [231] SUO, Z.; KUO, C.-M.; BARNETT, D.; WILLIS, J. [1992]: *Fracture mechanics for piezoelectric ceramics*. Journal of the Mechanics and Physics of Solids, 40 No.4: 739–765.
- [232] SZAMBOLICS, H.; BUDA-PREJBEANU, L.; TOUSSAINT, J.; FRUCHART, O. [2008]: *A constrained finite element formulation for the landau-lifshitz-gilbert equations*. Computational Materials Science, 44(2): 253–258.
- [233] TAKEI, A.; ROMAN, B.; BICO, J.; HAMM, E.; MELO, F. [2013]: *Forbidden directions for the fracture of thin anisotropic sheets: An analogy with the Wulff plot*. Physical Review Letters, 110: 144301–1–5.
- [234] TANNER, E. T. [2001]: *Shock, vibration and acoustic isolation system*.
- [235] TEICHTMEISTER, S.; KIENLE, D.; ALDAKHEEL, F.; KEIP, M.-A. [2017]: *Phase field modeling of fracture in anisotropic brittle solids*. International Journal of Non-Linear Mechanics, 97: 1–21.
- [236] TIAN-HU, H.; ZI-YUAN, S. [1994]: *A new electric boundary condition of electric fracture mechanics and its applications*. Engineering Fracture Mechanics, 47(6): 793–802.
- [237] TORABI, S.; LOWENGRUB, J. [2012]: *Simulating interfacial anisotropy in thin-film growth using an extended Cahn-Hilliard model*. Physical Review E, 85: 041603–1–16.
- [238] TORABI, S.; LOWENGRUB, J.; VOIGT, A.; WISE, S. [2009]: *A new phase-field*

- model for strongly anisotropic systems.* Proceedings of the Royal Society A, 465: 1337–1359.
- [239] TOUPIN, R. [1956]: *The elastic dielectric.* Journal of Rational Mechanics and Analysis, 5(6): 849–915.
- [240] TRUESDELL, C.; NOLL, W. [1965]: *The nonlinear field theories of mechanics.* In Flügge, S. (Editor), *Handbuch der Physik Bd. III/3.* Springer-Verlag, Berlin Heidelberg.
- [241] TRUESDELL, C.; TOUPIN, R. [1960]: *The classical field theories.* In Flügge, S. (Editor), *Principles of Classical Mechanics and Field Theory*, Vol. III/1 of *Encyclopedia of Physics*, pp. 226–795. Springer-Verlag, Berlin.
- [242] VALLICOTTI, D.; SRIDHAR, A.; KEIP, M.-A. [2018]: *Variationally consistent computational homogenization of micro-electro-mechanics at finite deformations.* International Journal for Multiscale Computational Engineering, 16: 377–395.
- [243] VALLICOTTI, D.; SRIDHAR, A.; KEIP, M.-A. [2019]: *Variationally consistent computational homogenization of micro-magneto-mechanics at finite deformations.* in preparation.
- [244] WAALS, J. VAN DER [1894]: *Thermodynamische Theorie der Kapillarität unter Voraussetzung stetiger Dichteänderung.* Zeitschrift für Physikalische Chemie, 13(1): 657–725.
- [245] WAALS, J. VAN DER [1979]: *The thermodynamic theory of capillarity under the hypothesis of a continuous variation of density.* Journal of Statistical Physics, 20(2): 200–244.
- [246] VARAPRASAD, B. S. D. C. S.; TAKAHASHI, Y. K.; HONO, K. [2013]: *Microstructure control of l_0 -ordered fept granular film for heat-assisted magnetic recording (hamr) media.* The Journal of The Minerals, Metals & Materials Society, 65(7): 1543–1851.
- [247] VARGA, Z.; FILIPCSEI, G.; ZRÍNYI [2006]: *Magnetic field sensitive functional elastomers with tunable elastic modulus.* Polymer, 47: 227–233.
- [248] WANG, J.; KAMLAH, M. [2009]: *Three-dimensional finite element modeling of polarization switching in a ferroelectric single domain with an impermeable notch.* Smart Materials and Structures, 18(10): 104008.
- [249] WANG, J.; ZHANG, T.-Y. [2007]: *Phase field simulations of polarization switching-induced toughening in ferroelectric ceramics.* Acta Materialia, 55: 2465–2477.
- [250] WANG, J.; SHI, S.-Q.; CHEN, L.-Q.; LI, Y.; ZHANG, T.-Y. [2004]: *Phase field simulations of ferroelectric/ferroelastic polarization switching.* Acta Materialia, 52: 749–764.
- [251] WANG, X.-P.; GARCIA-CERVERA, C, J.; WEINAN, E, W. [2001]: *A Gauss-Seidel projection method for micromagnetics simulations.* Journal of Computational Physics, 171(1): 357–372.
- [252] WATSON, J. R. [1996]: *Method and apparatus for varying the stiffness of a suspension bushing.*
- [253] WEN, Y.; WANG, Y.; CHEN, L. [1999]: *Effect of elastic interaction on the formation of a complex multi-domain microstructural pattern during a coherent hexagonal to orthorhombic transformation.* Acta materialia, 47: 4375–4386.
- [254] XU, B.-X.; SCHRADER, D.; GROSS, D.; MÜLLER, R. [2010]: *Fracture simulation of ferroelectrics based on the phase field continuum and damage variable.* International journal of fracture, 166: 163–172.

- [255] XU, B.; SCHRADER, D.; MÜLLER, R.; GROSS, D. [2009]: *Micromechanical analysis of ferroelectric structures by a phase field method*. Computational Materials Science, 45: 832–836.
- [256] XU, B.; SCHRADER, D.; MÜLLER, R.; GROSS, D.; GRANZOW, T.; RÖDEL, J. [2010]: *Phase field simulation and experimental investigation of the electro-mechanical behavior of ferroelectrics*. Journal of Applied Mathematics and Mechanics, 90(7–8): 623–632.
- [257] YI, M.; XU, B.-X. [2014]: *A constraint-free phase field model for ferromagnetic domain evolution*. Proc. Roy. Soc. A, 470(2171): 20140517.
- [258] ZÄH, D.; MIEHE, C. [2013]: *Computational homogenization in dissipative electro-mechanics of functional materials*. Computer Methods in Applied Mechanics and Engineering, 267: 487 – 510.
- [259] ZHANG, J. X.; CHEN, L. Q. [2005]: *Phase-field microelasticity theory and micromagnetic simulations of domain structures in giant magnetostrictive materials*. Acta Materialia, 53: 2845–2855.
- [260] ZHANG, J. X.; CHEN, L. Q. [2005]: *Phase-field model for ferromagnetic shape-memory alloys*. Philosophical Magazine Letters, 85: 533–541.
- [261] ZHANG, J.; CHEN, L. [2005]: *Phase-field microelasticity theory and micromagnetic simulations of domain structures in giant magnetostrictive materials*. Acta Materialia, 53(9): 2845–2855.
- [262] ZHANG, W.; BHATTACHARYA, K. [2005]: *A computational model of ferroelectric domains. Part I: model formulation and domain switching*. Acta materialia, 53: 185–198.
- [263] ZHANG, W.; BHATTACHARYA, K. [2005]: *A computational model of ferroelectric domains. Part I: Model formulation and domain switching*. Acta Materialia, 53: 185–198.
- [264] ZHANG, W.; BHATTACHARYA, K. [2005]: *A computational model of ferroelectric domains. Part II: Grain boundaries and defect pinning*. Acta Materialia, 53: 199–209.
- [265] ZHANG, W.; ZHAO, M.; TONG, P. [2002]: *Fracture of piezoelectric ceramics*. Advances in Applied Mechanics, 38: 147–289.
- [266] ZHOU, M.; RAVICHANDRAN, G.; ROSAKIS, A. J. [1996]: *Dynamically propagating shear bands in impact-loaded prenotched plates - ii*. Journal of the Mechanics and Physics of Solids, 44: 1007–1032.
- [267] ZHOU, M.; ROSAKIS, A. J.; RAVICHANDRAN, G. [1998]: *On the growth of shear bands and failure-mode transition in prenotched plates: A comparison of singly and doubly notched specimens*. International Journal of Plasticity, 14: 435–451.

Curriculum Vitae

Personal Data

Name	Ashish Sridhar
Date of Birth	Jan 04, 1990
Place of Birth	Mumbai, India
Parents	Sridhar Jayaraman and Jayashri Sridhar
Sibling	Rohan Sridhar
Spouse	Ankitha Nagabushan

School Education

2005–2007	Secondary school: Baroda high school, Alkapuri: Vadodara, India
March 2007	General entrance examinations for university acceptance

University Education

2007–2011	Mechanical engineering, Manipal institute of technology
May 2011	Graduation as Bachelor of Engineering (B.E)
2011–2014	International masters program COMMAS, University of Stuttgart
April 2014	Graduation as Master of Science (M.Sc)

Professional Occupation

2014–2019	Research associate and assistant lecturer, Institute of Applied Mechanics (CE), University of Stuttgart
2017–2018	Course director of international Master of Science program COMMAS, University of Stuttgart
2019– 2021	Product specialist- EM solutions, Altair GmbH Böblingen.



Smart electromagnetic materials have been known to mankind since around 500 BC. But their use was limited to very specific usecases until the later part of the last century. However in recent decades, electromagnetic materials played a pivotal role in the information technology, industrial and automotive sectors, just to name a few. This is excluding their applications in numerous day to day applications that have almost become ubiquitous in our daily lives.

The focus of this work is to model the material behavior of such materials, specifically ferromagnets, magnetorheological elastomers (MREs) and piezoelectric materials. The overarching theme of the present contribution is to use appropriate phase-field formulations to better predict and understand their behavior. Mathematical and numerical modeling techniques using appropriate variational principles are employed to model these highly nonlinear electro-magneto-mechanically coupled problems, while naturally taking account of their microstructure evolution, taking place on smaller length scales.